# Ultrasonic sensing methods for sewer pipe inspection

Gomez Gutierrez, Francisco Jose

# ULTRASONIC SENSING METHODS FOR SEWER PIPE INSPECTION

FRANCISCO JOSE GOMEZ GUTIERREZ

Thesis submitted for the Degree of Doctor of Philosophy

Department of Mechanical Engineering

King's College London, University of London

*September 2005*

*I, Francisco Jose Gomez Gutierrez, confirm that the work presented in this thesis is my own. Where information has been derived from other sources, I confirm that this has been indicated in the thesis.*

*Abstract*

The work presented in this thesis focuses on investigating ultrasonic profiling methods for the inspection of the inner sections of partly filled and fully filled tubular structures, oriented primarily towards the inspection of sewers.

As part of this research, an analytical model based on linear systems theory employed for the simulation of ultrasonic scans inside water filled pipes is implemented. This modelling environment provides insight into the behaviour of pulse-echo ultrasonic waves inside tubular structures filled with liquid. An experimental validation comparing model predictions against experimental results shows the capability and accuracy of the modelling environment.

An advanced imaging technique incorporating the intensities of the received ultrasonic echoes to enhance the visualisation capabilities of inspected sewer pipes immersed in liquids is formulated. The proposed approach generates augmented three-dimensional graphs (surface-intensity maps) which represent the inner surface of tubular structures based on B-mode images acquired by rotational ultrasonic sensors. The proposed approach generates images of very high resolution and is superior to the commonly used time-of-flight profiling method.

Extending from the modelling and visualisation research, this thesis proposes an automatic defect recognition and localisation method based on artificial neural network techniques. A pre-processing technique, which is carefully adapted to the pipe inspection problem at hand, is incorporated, in order to achieve a clearer separation between defective and non-defective sections. The pre-processor scans the surface-intensity maps with a moving window and creates the input for the subsequent neural-network-based analysis. A comparative study shows that the chosen approach outperforms other methods.

The developed techniques were thoroughly validated through extensive simulations employing the developed modelling environment and laboratory experiments emulating operating conditions expected to be found in sewer pipes.

## ACKNOWLEDGEMENTS

I would like to start by acknowledging Dr. Kaspar Althoefer for all his support, guidance, contributions and encouragement, in order to bring this research work to what it is today. I am also thankful to Professor Lakmal Seneviratne, for his supervision and advice.

Thanks also go to System Technologies for providing the sensing system that made possible the assembly of the experimental platform used for conducting the experimental work. Special thanks to David, Hugh and Marcus for their technical support when debugging the interminable technical problems. Without their contribution and help this work would not have become a reality.

The list of acknowledgements would be incomplete, if I did not mention my gratitude to my fellow students: Paresh, Choo Pan, Leslie, Honghai and Martin for making the lab an enjoyable place to be.

## Dedication

***To my beloved wife Jelenyela. None of this would have been be possible without your love, support and understanding.***

***To Sebastian and Adrian who are my source of inspiration and happiness.***

***To my parents for all their hard work, dedication and for providing me with the tools and teachings to achieve this goal.***

# TABLE OF CONTENTS

# LIST OF FIGURES

## LIST OF TABLES

# Chapter 1

## INTRODUCTION

*This chapter provides an overview of the work conducted as part of this research project. An outline of the thesis is provided together with the motivations behind the research. The main objectives and contributions are presented at the end of this chapter.*

## 1.1. Introduction

Traditionally sewer inspection techniques are based on closed-circuit television only able to inspect the part of sewers filled with gaseous media. New techniques allowing the inspection of the flooded section of sewers, with minimal disruption, are of great interest to water and sewerage companies. Ultrasound imaging allows the visualisation of inner walls of pipes filled with liquid and the detection of abnormal conditions such as cracks, sediment accumulation, root intrusion and pipe wall deformations.

This thesis proposes and investigates novel ultrasonic sensing methods specifically applied to detect defects in inner walls of sewer pipes filled with liquid. The presented research work comprises the simulation of ultrasonic fields inside pipes, a novel visualization technique enhancing defect locations and an innovative, automated defect detection system based on artificial intelligence techniques.

This document is structured into 7 chapters.

**Chapter 1 - Introduction**

The sections of this introductory chapter outline the motivation for this research, the main aims and methodology of this work and, place the thesis in context. The introduction concludes with a summary of contributions made.

**Chapter 2 - Sewer Inspection**

This chapter provides background information on sewers, their characteristics and specifies the typical types of defects found in the sewer environment. The latest technological developments in multi-sensor inspection systems for sewers are reviewed.

**Chapter 3 - Experimental Platform**

This chapter describes the experimental platform employed for conducting all the experiments presented here, showing the capabilities and limitations of the created algorithms.

**Chapter 4 - Ultrasound Fields: Simulation and Experimental Validation**

This chapter introduces an ultrasound simulation environment and its development. This simulation environment models the behaviour of ultrasound beams emitted from a rotational ultrasonic sensor inside water-filled pipes and allows the generation of simulated sensor data comparable to the data obtained from a real sensor. This modelling environment, which was particularly constructed for the pipe inspection problem, is validated through an experimental study.

**Chapter 5 - Enhanced Visualisation of Ultrasound Images**

This chapter proposes a novel approach for enhancing the visualisation of defects in scans of rotational ultrasound sensors. The chapter comprises a discussion about the factors which determine the resolution of transducers used in ultrasonic imaging, a description of the proposed methodology and an experimental study based on simulations and experiments exploring the capabilities of the proposed methodology.

**Chapter 6 - AUTOMATIC DEFECT DETECTION**

This chapter proposes a new approach for the detection of defective sections inside acquired sensor images. The neural network based approach is capable of categorising the data acquired by the rotational ultrasonic sonar into defective areas and non-defective ones. The neural network based approach is thoroughly investigated and its capabilities explored through an experimental study.

**Chapter 7 – Conclusions and future work**

This chapter summarises and evaluates the results of this research work and, moreover, discusses possibilities for further research work.

## *1.2. Motivation*

Pipe inspection in recent years has become a serious issue for water companies around the world because environment offices in many countries have dramatically increased the regulations regarding damaged water pipes and sewers, aiming to reduce the loss of fresh water and pollution of the environment.

The sewerage systems are usually one of the biggest infrastructures in cities. Just in the UK, the sewerage network comprises about 502,000 km sewers (public and private sewers).

The age of the system is the main cause that undermines its structural integrity. It is thought that half of the UK sewers are more than 50 years old and a few of them were even built during the Victorian period. Statistics published by the Office of Water Sevices (OFWAT) indicated that 10% of public sewers are in a state in which a collapse is likely in the foreseeable future or collapse is imminent [2000]. In addition, the Department of Environment, Food and Rural Affairs (DEFRA) has reported that 17% of private sewers are in similar condition as the aforementioned [2003].

When a sewerage system fails, it poses a serious health and environmental risk. For instance, incidents where groundwater sources have been contaminated by leaking sewers have been reported in the past, and as a result, serious disease outbreaks have occurred [Short 1988]. Recently, a study conducted by the University of Sheffield showed that in groundwater sources as deep as 60 m, sewage-derived bacteria were present [Powella 2003]. As a consequence, most regulation agencies around the globe have imposed strong regulations to water companies in order to warranty the structural integrity of urban sewer systems.

Figures show that during the last 50 years, the demand for sewer systems has been increasing steadily but the maintenance programs have not been able to cope with it. As a matter fact, in the UK just about 0.1% of the sewer system is replaced every year. One way to improve the efficiency of the replacement works when resources are limited is by assessing the sewerage network, classifying the damage conditions and prioritizing the maintenance works.

The most widely used method of collecting information on the internal condition of sewers is CCTV inspection. It is used to assess sewer pipe defects in sewers where human visual inspection cannot be carried out due to size limitations. Makar [2000] stated that CCTV is likely to remain the preferred method of inspection in the near future. Nevertheless, the quality of the inspection of most of the CCTV methods relies on the skill and experience of the operator, together with the reliability and quality of the TV picture, which can be

misleading because vital defects can be concealed by mud and moss [Fenner, 2000]. Another disadvantage is that in order to inspect a section of a sewer, it commonly has to be blocked off and drained, if the whole pipe is to be viewed.

If sewers are to be inspected under normal, operational conditions, systems with a combination of sensors which can assess dry sections as well as wet sections have to be used. Ultrasound can propagate in gases and liquids but due to the attenuation characteristics of the sound in air, it is unlikely that a single frequency transducer can be used to assess dry and wet sections. On the other hand, if a visual inspection system is combined with and Ultrasound Scanner, part-filled of fully filled sewers could be inspected. Ultrasound has been widely used for medical imaging, non-destructive testing (NDT) and sonar applications. But, it has been modestly investigated in the context of sewer inspection, involving mainly heuristic strategies providing results which support the feasibility of ultrasonics for pipe inspection [Duran 2002b, Andrews 1998, Pace 1994].

This research work is aimed to investigate immersion ultrasonic sensing methods for the inspection of inner sections of part-filled and fully filled pipes, oriented primarily to the inspection of sewers. It should be noted that due to the unavailability of a single sensing technique that can be used for inspecting dry and wet sections, this work is part of a multidisciplinary programme aimed to develop an autonomous multi-sensor mobile platform for pipe inspection capable of working inside sewers during normal operation, equipped with sensors able to inspect dry and wet sections of pipes simultaneously.

## *1.3. Aims and Objectives*

The main objective of this work is to study ultrasonic inspection techniques for their suitability to investigate the conditions of liquid-filled sewer pipes. The intension is to create and research techniques that can be realised as lightweight sensing systems to be integrated in autonomous, multi-sensor, mobile mechatronics devices which can travel through sewer pipes under any condition and analyse the areas of the pipe covered with water or liquid. These techniques

should complement the existing inspection techniques available for the inspection of dry sections.

As mentioned above, ultrasound techniques have been modestly investigated in the context of sewer pipe inspection. As a result, the first objective of this work is to develop and study a modelling environment which has the capability of emulating the ultrasonic-based pipe inspection process. This modelling environment allows generating realistic simulation data under controlled conditions without incurring the high costs of running real experiments. The main idea is to create a computer-based modelling instrument that will provide insight into the behaviour of ultrasound waves emitted into the liquid contained within a tubular structure and facilitate the study of the factors that affect the ultrasonic pipe inspection process.

The second objective is focused on enhancing the capabilities of existing ultrasonic sensing devices, in particular, rotational ultrasonic sensors, for the visualisation and identification of defects. This research proposes and explores new post processing techniques taking in consideration the characteristics of the emitted ultrasound beams and use this knowledge to enhance the defect detection capabilities, aiming to match or exceed the capabilities of existing visual inspection techniques. The chosen approach exploits the intensity information of the sensor signals and the resultant images prove to be superior to images constructed from standard time of flight measurements. To the best knowledge of the author, this is the first time that such visualisation techniques have been applied to the ultrasonic data acquired in water-filled tubular structures.

In line with recent trends in sewer pipe inspection, researchers have noted that current visual inspection methods are based on the skills of the operator and as such not sufficient for a modern pipe inspection approach. Due to the subjectivity of the operator, the quality of the inspection process changes depending on the person who is assessing the images at a given time. Inspection experts and researchers are proposing that future pipe inspection systems should incorporate artificial intelligence techniques to increase the objectivity of the inspection process, and decouple the inspection process from the influence of the human being as much as possible. The third objective of this research is to

develop such an automatic classification system capable of detecting defective sections when fed with data gathered from ultrasound inspection of liquid filled sections. An in-depth experimental study compares different pre-processing techniques and neural network architectures. The most suitable approach for the problem at hand, a windows-based pre-processing technique coupled with an artificial neural network, is proposed and discussed in detail.

## 1.4. Contributions

This thesis describes a simulation and experimental investigation into the inspection process of liquid-filled pipes using rotational ultrasonic sensors. The contributions of this research are:

- A simulation environment for simulating the inspection process when using rotational ultrasonic sensors inside tubular structures. This has been achieved by extending a computer-based simulator for the generation of simulated signals propagating inside pipes partly or fully filled with liquid.
- The validation of the developed simulation environment by carrying out an extensive study, examining simulated and experimental data.
- A novel visualization technique for the visual inspection of pipe walls immersed in liquids: Surface Intensity Plots (SIP). This technique allows the identification of defects and changes in the inner pipe wall smaller than the resolution of the sensor.
- Determination of the capabilities and limitations of the proposed visualization technique (SIP) and its experimental validation by means of an extensive simulation and experimental study.
- Development of an automatic defect detection system. Feature extraction techniques that can be applied to the proposed visualisation technique were investigated and the most suitable one chosen. Neural Networks techniques were studied and a suitable architecture was proposed, trained, tested and optimised in order to develop a system that is capable of automatically recognising defective sections from non-defective ones.

During the course of this project, the findings and results of this research were published in international conference proceedings and journals. A list of these publications is provided below:

- Gomez F., et al. 2003a. Modelling of Rotating Ultrasonic Sensors for Pipe Inspection. *International Conference on Mechatronics (ICOM 2003)*, Loughborough, UK, 19-20 June, 2003.
- Gomez F., et al. 2003b. Modeling of Ultrasound Sensor for Pipe Inspection, *Proc. 2003 IEEE Int. Conf. on Robotics and Automation (ICRA 2003)*, pp 2550-2560, Taipei, Taiwan, 12-17 September, 2003.
- Gomez F., et al. 2004. An ultrasonic profiling method for sewer inspection, *Proc. 2004 IEEE Int. Conf. on Robotics and Automation (ICRA 2004)*, Volume: 5, April 26-May 1, 2004, Pages: 4858- 4863, New Orleans, 2004.
- Gomez F. et al. 2005. Simulation of ultrasound imaging inside fully charged pipes. *Automation in Construction*. Accepted 7 July 2005. In press.
- Gomez F. et al. 2005. An ultrasonic profiling method for the inspection of tubular structures. *Computer-Aided civil and infrastructure engineering*. (Conditionally accepted).

# Chapter 2

## SEWER INSPECTION

*This chapter provides a general overview of sewer inspection as well as sewer characteristics and classifications as defined by the water authorities. A discussion on the present trends in sewer inspection is given. The discussion is closed by reviewing the suitability of using ultrasonic techniques for inspecting the flooded section of sewer pipes, as a complement for current visual inspection methods that only can assess dry sections.*

## 2.1. Introduction

A sewer, as defined by the Water Industry Act 1991, is a system of pipework including manholes which serves buildings situated in more than one curtilage. Sewers provide an essential service to households and businesses in towns and cities, they usually remain unattended until something goes wrong.

In England and Wales there are 302,000 kilometres of public sewers and between 80,000 and 200,000 kilometres of private sewers. It has been reported that 17% of private sewers are in condition were a collapse is likely in the foreseeable future or the collapse is imminent. Data published by OFWAT has shown that 10% of public sewers were classified as grade 4 and 5, representing a similar condition as the aforementioned private sewers [NAO, 2004]. Studies have shown that there are 5000 collapses and 200,000 blockages per year and just 0.1 % of the sewer system is being replaced every year [WEF 1994] at a cost of £180 m. In 2002, 385 kilometres of public sewers were replaced or upgraded in England and Wales.

The environment agency reported that 16.4% (5,175) of all pollution incidents last year in England and Wales were caused by sewage, compared with 14.1% the previous year, these pollution incidents, most of which were caused by sewage, cost water companies almost £1m in fines in 2002.

## 2.2. Classification of sewers

There are three main types of underground drainage pipes: Drain, Public sewers and private sewers. A drain is a pipe that carries waste water (either foul or surface water) from just one property. A private sewer carries waste from two or more houses. It is owned by a group of people in a building and eventually joins a public sewer. Public sewers belong to the sewerage undertakers and carries sewerage from two or more properties. The sewerage undertakers have the responsibility for maintaining and extending the public sewer network. The main characteristics of private and public sewers are listed next [DEFRA, 2003].

**Private sewers**

- Belong to property owners.

- They are mostly situated in privately owned properties but may be partially in public highways.
- Minimum size: 100 mm.
- Buried at shallow depths to deal with relatively simple and smaller drainage areas.
- Pipes usually run closer to each other and under buildings.
- Change of directions by long radius bends.
- Communicate with other pipes through pipe junctions.
- Chambers are generally constructed in brickwork and with lightweight covers.

**Public sewers**

- Belong to water and sewerage companies.
- Usually are situated in or under public highways. But can also be routed through private land with permanent wayleave for the undertaker for maintenance and restriction on the landowners not to prejudice the integrity of the sewer.
- Deal with the drainage of large areas and may have pumping stations.
- Minimum pipe size: 150 mm.
- Are buried deeper to suit the complexity of topography of large drainage areas and to withstand vehicular loads in public highways.
- Pipes run further from buildings and usually not under them.
- Pipes change direction at manholes.
- Sewer pipes are joined to other sewers at manholes only, except for lateral connections at pipe junctions.
- Usually laid in straight lines.
- Manholes are made of concrete are covered with medium/heavy duty covers.

Public sewers are divided in critical and non-critical sewers depending on the possible impact on the surrounding environment in case of a failure. Critical sewers are those, whose collapse repairs will be expensive or disruptive or those,

which are considered to be strategically important. The principal structural criterion is that if a sewer should fail, the subsequent costs would be significantly higher than if rehabilitation was carried out before failure [WRC, 2001]. All other sewers not falling into this category are termed non-critical sewers. It should be noted that the categorization of a sewer as either critical or non-critical is not an indication of its physical condition. Similarly, the age of sewers does not necessarily give an indication of their condition [MMC, 1996].

## 2.3. Sewers common failures

Because flows through sewers are generally at low pressure the stresses on pipework are limited and degradation is usually very slow. Sewers may collapse or become blocked, but the seriousness of the consequences depends on the extent to which it causes other infrastructure such as roads to collapse or causes sewage to flood above ground or into water courses. Sewers also come under external pressures including heavy loads, ground conditions and tree root intrusion, and can be subject to blockages arising from siltation and the build up of fats from food outlets [NAO, 2004].

In practice, the most serious consequence for individual customers of a failure in the sewer network is sewer flooding. This may result from a sewer collapse or blockage related to deteriorating pipework, but is most commonly the result of the system becoming overloaded by heavy rainfall as surface water floods into sewers. If the system becomes overloaded in this way ("hydraulic overload") sewage backs up through drains and into houses and other buildings (internal flooding) or gardens, parks and roads (external flooding). And overflows of sewage may cause pollution incidents [NAO, 2004].

### 2.3.1. Classification of sewers regarding its structural condition

Sewerage companies are required to maintain their extensive networks of sewers so that they can provide services to current and future customers. As a result, sewers are assessed and their condition is classified in one of five possible categories, from grade 1 (no structural defects) to grade 5 (for example collapsed or severely deformed sewers, or extensive areas of missing fabric or bricks),

although grade 5 sewers may continue to function effectively for some time [NAO, 2004]. Table 2.1 list the characteristics for each one of the grades.

**Table 2.1**. Structural conditions of sewers, Internal Condition Grades (ICG) [WRC, 2001].

| Condition grade | General meaning |
|---|---|
| 1<br>Very good | No structural defects.<br><br>**Acceptable structural condition.** |
| 2<br>Good | For brick sewers:<br>Minor cracking or no deformation or loss of bricks and mortar loss confined to surface and line & level as built and connections satisfactory.<br><br>For other sewers:<br>Circumferential cracking or moderate joint defects, i.e. open joint (medium) or joint displaced (medium), spalling slight and wear slight.<br><br>**Minimal collapse risk in short term but potential for further deterioration.** |
| 3<br>Adequate | For brick sewers:<br>Deformation 0-5%, no fracture and only moderate mortar loss or displaced bricks or total mortar loss without other defects or occasional defective connections.<br><br>For other sewers:<br>Deformation 0-5% and cracked or fractured or longitudinal/multiple cracking or occasional fractures or severe joint defects or minor loss of level or badly made connections, i.e. open joint (large) or joint displaced (large). Spalling medium. Wear medium.<br><br>**Collapse unlikely in near future but further deterioration likely.** |
| 4<br>Poor | For brick sewers:<br>Deformation 5-10% and fractured or total mortar loss or small number of missing bricks or displaced/hanging brickwork or moderate loss of level or frequent badly made connections or dropped invert.<br><br>For other sewers:<br>Deformation 5-10% and cracked or fractured or broken or serious loss of level, i.e. Spalling large. Wear large.<br><br>**Collapse likely in foreseeable future.** |

| | |
|---|---|
| 5<br>Very poor | For brick sewers:<br>Already collapsed or deformation > 10% and fractured or extensive areas of missing bricks and/or displaced/hanging brickwork or missing invert.<br><br>For other sewers:<br>Already collapsed or deformation >10% and cracked or fractured or broken or extensive areas of missing fabric.<br><br>**Collapsed or collapse imminent** |

### 2.3.2. Structural defects

The sewerage rehabilitation manual states that the sewer structural defects can be classified as [WRC, 2004]:

- Open Joints: longitudinal movement between adjacent pipes.
- Displaced Joints: faulty alignment between consecutive pipes;
- Cracks: lines visible, pipe pieces all in place. They can be sub-classified as: longitudinal, circumferential, multiple
- Fracture: cracks visibly open, pipe pieces all in place;
- Hole
- Collapsed: loss of all structural integrity
- Spalling
- Wear
- Deformation: percent of pipe diameter loss (to nearest 5%).

### 2.3.3. Service codes

In addition to the structural condition defects, there are seven service condition codes [WRC, 2004]:

- Tree Root Penetration: Fine, mass, tap.
- Infiltration: Seeper, Dripper, /Runner, Gusher.
- Encrustation: typically dissolved salts deposited on pipe. walls. Heavy, medium, light.

- Obstruction: solid material causing hydraulic reduction.
- Debris: organic/silty material, typically sedimentation.
- Water Level: a short discontinuity in the pipe gradient.
- Line: a divergence to left or right.

## 2.4. Characteristics of sewers

There are three types of wastewater systems: storm drains, sanitary sewers and combined systems for both purposes. Sewers in general, were traditionally made of bricks, concrete, vitrified clay and cast iron. More recently, new materials are been introduced [WEF, 1994; Wirahadikusumah, 1998]:

- spirally wound HDPE
- Copper
- Galvanised steel
- PVC-U: solid wall, twin wall, ultrarib
- Polypropylene (PP)
- Polyethylene (PE)
- Styrene Copolymer
- blends (PVC + SAN)
- PVC-C

Most of the pipes used in municipal sewer networks are circular. The size of sewers varies greatly but most of them are between 200 mm and 600 mm, and thus are not apt for human inspection [Roth, 1998]. For instance, in the UK, 96% of the 250,000 Km of existing sewers have inner diameters smaller than 1 m [Duran, 2002a], and are considered not accessible by humans.

Sewers gather wastewater from buildings and transport it to sewage treatment works. They handle four categories of flow:

- Used water and foul water from domestic and business customers.
- Surface water running off properties after rainfall.
- Surplus surface water draining from roads, garden and other urban spaces after rain.
- Infiltration water which enters into the sewer network by defective areas such as cracks, flawed joints and manholes.

Sewage level inside sewer pipes may vary from dry through partially filled to fully filled. Typically, the lowest level to be expected inside a sewer is around 5% [Pace, 1994].

## 2.5. *Internal sewer pipeline assessment*

Automated sewer inspection is a relatively new area. Previously sewer inspection was a manual task based on visual inspection, limited to pipe sizes which can accommodate a human being. The first commercial attempts at unmanned inspection date back to the early nineties, using Closed Circuit Television (CCTV) cameras installed on mobile platforms pulled by wires. Still today, this is the most widely used inspection technique for sewers assessment, but instead of pulling the platform, tethered robots are used.

As research evolved and new sensor and robot technologies became available, the limitations of simple sensor systems were addressed and new requirements fulfilled. In recent years, research has focused on building multi-sensor systems for pipe inspection [Duran, 2002a]. For example, Kurt is a six wheel autonomous mobile platform with a sensor configuration consisting of two inclinometers and five ultrasound sensors for navigation, Figure 2.1. It also has a CCTV camera which has an on-board frame grabber with a radio link module to transmit images and relevant information to the outside world [Kirchner, 1997].

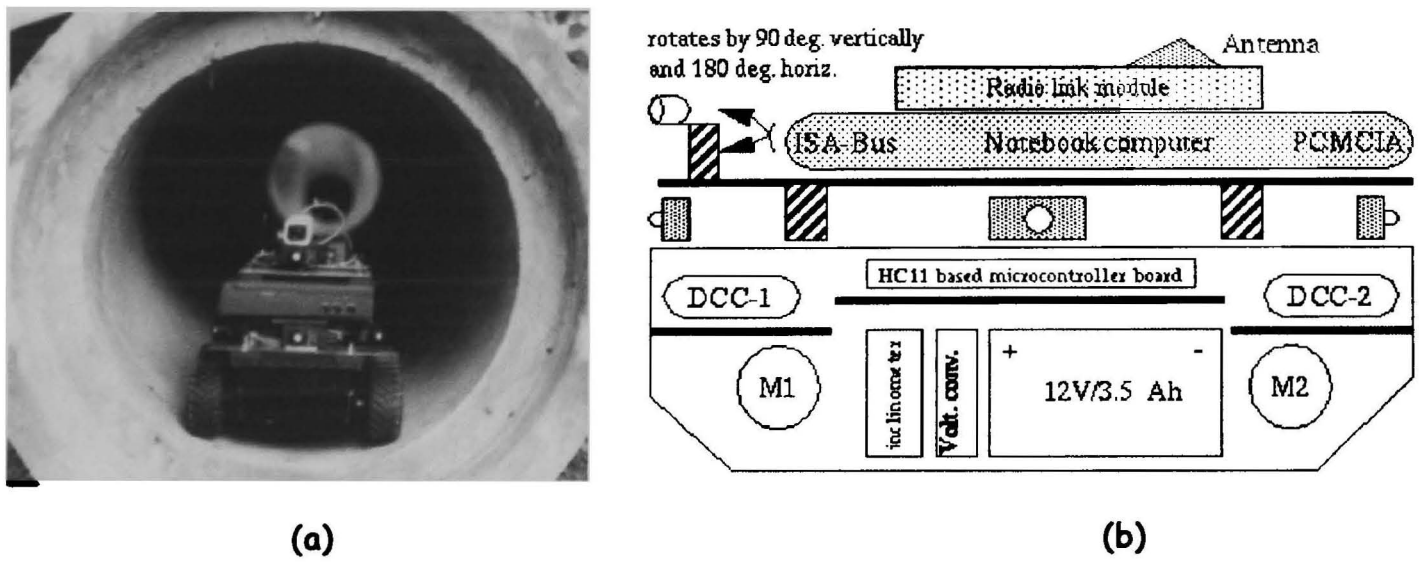


(a) (b)

**Figure 2.1** Kurt picture and schematic (a) travelling inside sewer pipe (b) Major components schematic diagram [Kirchner, F. and Hertzberg, J., 1997]

KARO, a remotely controlled and highly manoeuvrable robot inspection system, is designed to automatically assess sewer pipes; it is equipped with a 3D-optical sensor, ultrasonic sensors in the head for vehicle navigation and in the belly to measure wall thickness, Figure 2.2. It also has a microwave back scattering sensor for inspection of the soil surrounding the pipe wall [Kuntze 1998].

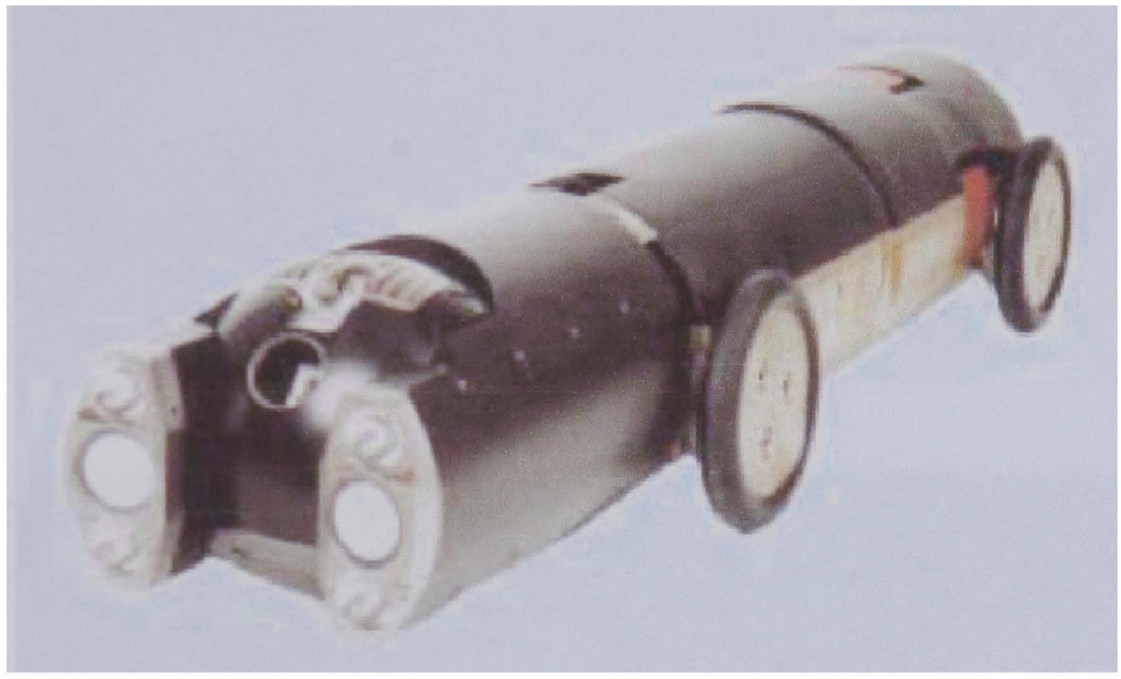

Figure 2.2 KARO picture

MAKRO is a five segment, articulated robot equipped with inclinometers in each member, Figure 2.3. In the front section, there are four ranging sensors (two ultrasound and two infrared) for obstacles detection, a stereo camera head, two laser projectors, and a lamp [Rome, 2001].

PIRAT (Pipe Inspection Real-time Assessment Technique) is a multi-sensor, tele-operated robot able to assess defects in sewers and other pipes, Figure 2.4. The PIRAT measurement system is composed of a laser scanner which repeatedly measures the pipe radius as its head rotates around the sewer axis to build up the geometry of cross-sections, leading to a 3D sewer surface map [Kirkham, 2000].

(a)

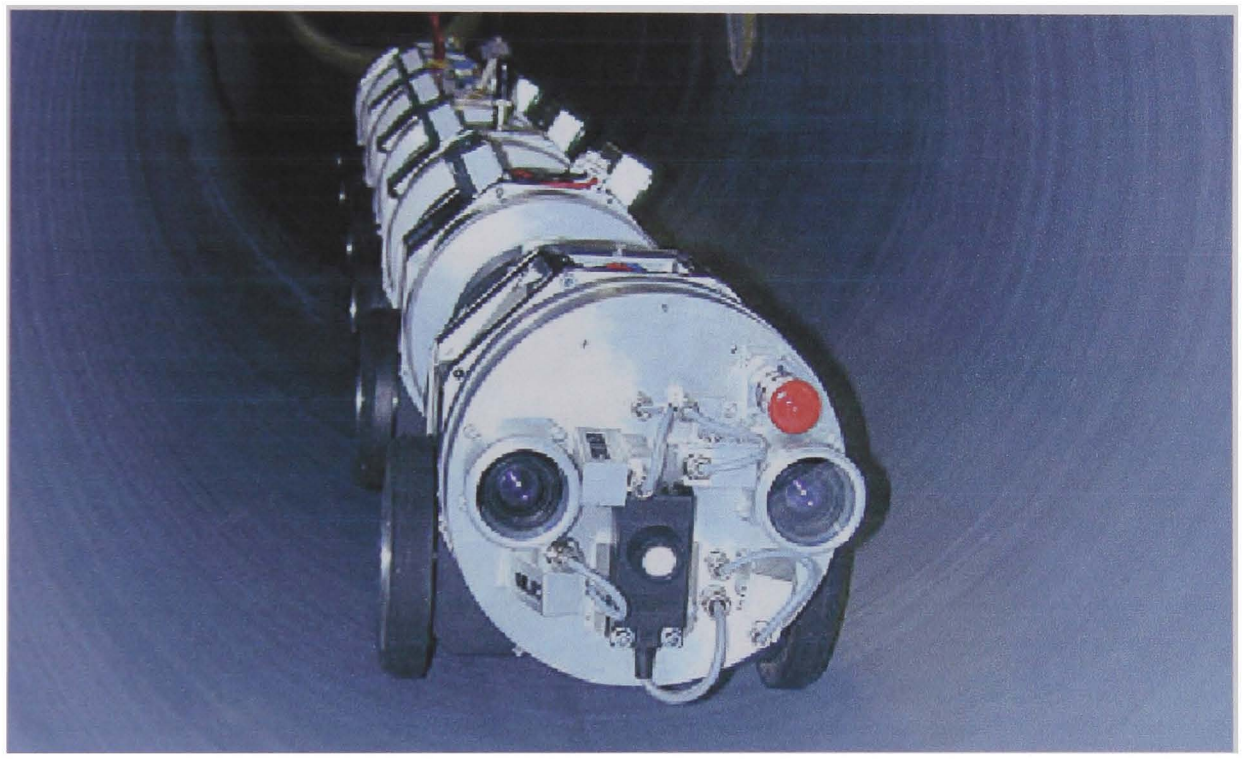

(b)

**Figure 2.3** MAKRO Pictures (a) Top View, (b) MAKRO Robot travelling inside sewer pipe

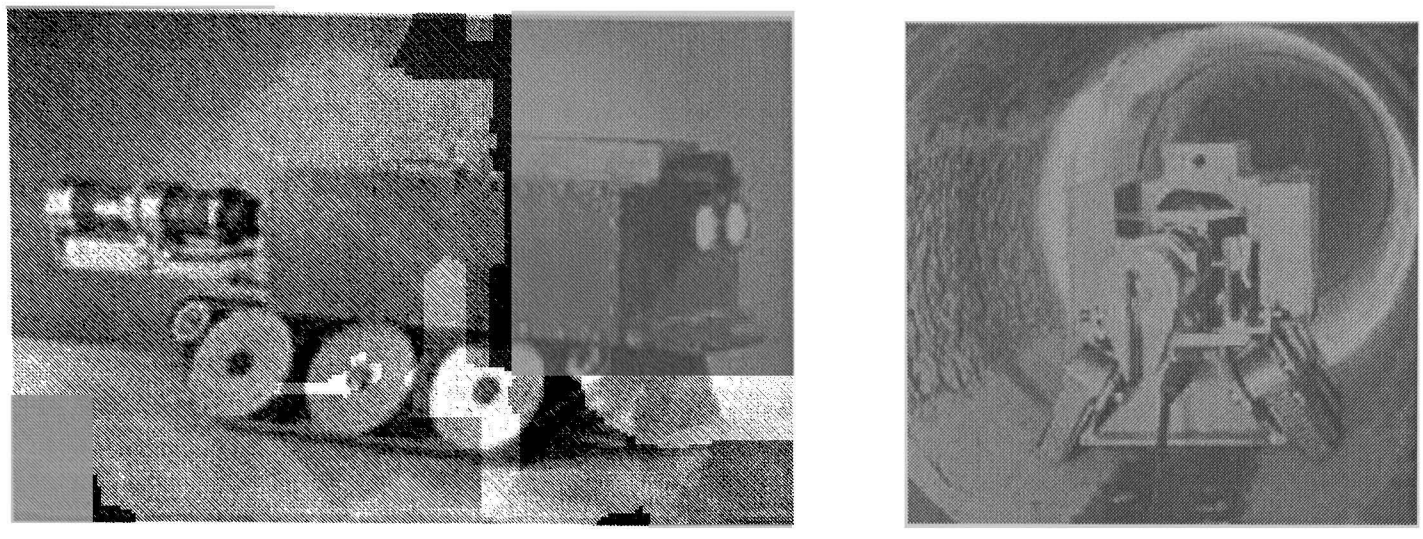

(a) (b)

**Figure 2.4** Pirat pictures (a) side view (b) Travelling inside sewer pipe

Another inspection system, Sewer Scanner and Evaluation Technology (SSET), is an autonomous robot equipped with an optical scanner with a fish-eye lens and a gyroscope, and it has the capacity to log images during the inspection, Figure 2.5. These images are post-processed by specialized routines to reveal defects and flaws which are finally analyzed by an expert [CERF, 2001].

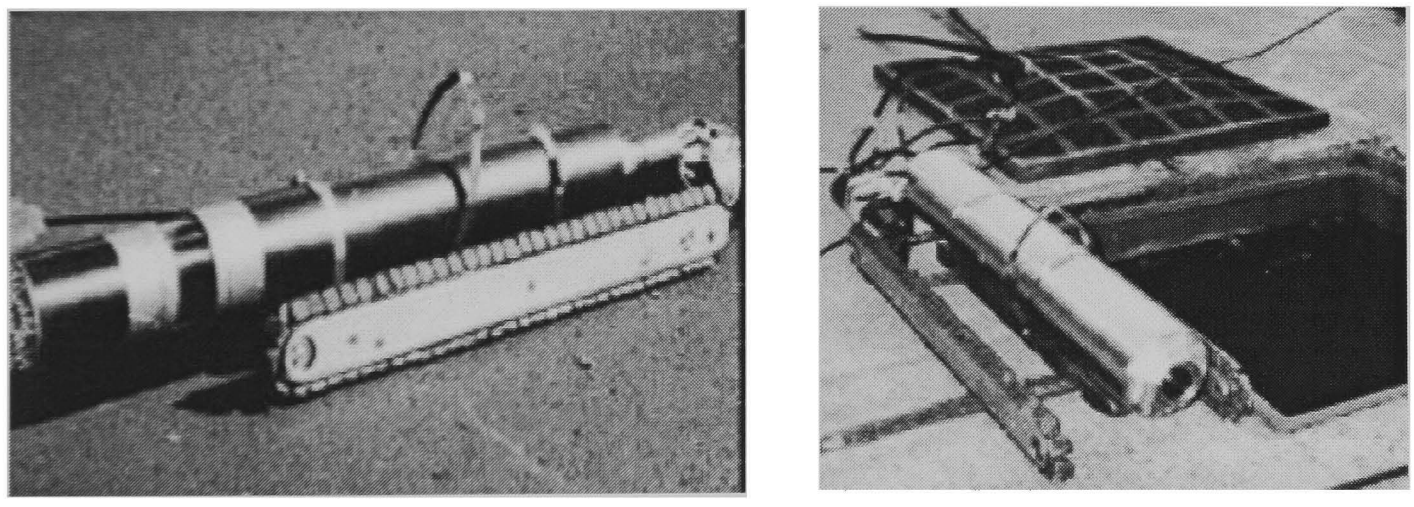

(a) (b)

**Figure 2.5** SSET Pictures. (a) side view (b) top view

In recent years, great advances have been made towards multi-sensor autonomous pipe inspection platforms. However, today's commercial sewer pipe inspection is still mainly camera based, being able to inspect only dry sections of pipes [Duran 2002a]. The work described in this thesis can be considered an important sensing module that could be integrated into existing or new multi-

sensor pipe inspection systems. The basic idea is to have a small, lightweight, rotational ultrasonic sonar as the underwater sensing system. It should be able to detect similar anomalies as those detected by means of visual inspection methods (Chapter 5). As a result, an integral sewer pipe inspection system which is able to assess defects in dry and wet sections can be developed. It is expected that this research work will contribute to expand the capabilities of rotational ultrasonic sonars in order to match the inspections requirements of the moment.

Tracking the progress of the developments in the sewer pipe inspection field, a point of agreement among experts is the automation of the pipe inspection process. As a matter of fact, it not only can save significant time and money, but also improve accuracy and consistency in diagnostics. Automating these processes can also provide an incentive for checking water and sewer mains regularly as a part of preventive maintenance programs [Moselhi, 1999]. In agreement, with the tendencies observed in the field, this research work considers as well, the study of artificial intelligence techniques as a mean for automatic defect location in wet sections of sewers (Chapter 6).

## *2.6. Ultrasonic Inspection of sewers*

Before inspecting a sewer, a section is commonly drained and blocked off, if the whole pipe is aimed to be viewed. The inspection of sewers in normal service, where a pipe can be partially or fully filled with water, is an incipient research area that is being addressed. A few efforts have been carried out using ultrasound techniques for the inspection of under water sections [Gomez2003a, Kirkham 2000, Pace, 1994]. Rotating ultrasonic sensors are being used to profile inner pipe walls immersed in sewage [Andrews, 1998; Pace, 1994]. Nevertheless, its capabilities have not been fully exerted.

The standard ultrasonic inspection process consists of moving a rotational ultrasonic sonar along the longitudinal axis of a sewer pipe, at defined steps, creating a series of consecutive profiles of its inner section which are recorded and later analysed. Rotational sonars can be installed on wheeled mobile platforms or floating ones.

The recorded profiles are analyzed by an expert or by an automatic diagnostic system to find anomalous conditions that might influence the structural characteristics and mechanical integrity of the pipe (see also Chapters 5). Analysing these profiles, conditions such as sediment accumulation, roots intrusion and deformation of the pipe wall can be detected. However, the quality of the assessment in wet sections does not match those of visual inspection systems employed in dry sections.

### 2.6.1. Acoustic properties of sewage

When dealing with underwater acoustic systems, there are two key parameters that have to be known in order to design such a system, the transmission loss and the back-scattering coefficient. When an ultrasound field propagates in a homogeneous medium, its energy suffers two types of losses: spreading and attenuation (see Chapter 5). The combination of these two is known as the transmission loss. It is noted that, if there are small objects or inhomogeneities in the medium where the acoustic field is travelling, such as suspended particles or bubbles, part of the field energy is going to scatter on such inhomogeneities (reverberation), adding an additional loss and incrementing the noise of the system. This is known as the back-scattering coefficient. Both parameters are vital when choosing the operating frequency of a sonar system. In particular, when the medium is sewage where solids in suspension and inhomogeneities in the fluid are present in normal conditions. If the proper frequency is not chosen, the scattering effect in the media will act as a filter, not allowing the ultrasound field to pass through it. As a consequence most of the emitted energy will be reflected back before reaching the pipe wall. By reviewing the literature it was seen that the only available information was reported by Pace [1994] after running a series of experiments in real sewers in order to determine the limitations that sewage will impose when using ultrasonic profilers.

Pace carried out an empirical study for determining the best frequencies for inspecting sewers. He conducted a series of experiments in open channel sewers, monitoring the characteristics of the sewage and measuring the losses and the backscattering coefficient for different frequencies. The experiments where

carried out in sewers that were usually two thirds full with a flow rate between 0.4 and 1.1 m/s with a suspended solid content between 0.142 and 0.232 kg/m$^3$. In the next table, results obtained by Pace are summarised.

**Table 2.2** Measured acoustic parameters of sewage

| Frequency (MHz) | Attenuation (dB) | Scattering strength (dB) |
|---|---|---|
| 0.7 | 9.0 | 17 |
| 1.4 | 1.8 | 8 |
| 2.1 | 0.5 | 11 |
| 2.9 | 1.5 | 16.5 |
| 3.5 | 2.5 | 19 |

In the above table, it can be seen that the lowest attenuation and backscattering strength were achieved at a frequency of 2.1 MHz. As the frequencies move away from the central value of 2.1 MHz, the attenuation increases. This effect is stronger when the frequency is decreased. For instance, when the frequency is shifted 700 kHz below the central frequency, the attenuation increases a 34% (1.3 dB). While, when the frequency is increased 800 kHz, the attenuation just increases 26%. Hence, the attenuation is more sensitive to reducing the frequency than increasing it.

Analysing the scattering strength data, it can be seen that the optimum is at a frequency lower than that for the attenuation, it is at 1.4 MHz. When, the frequency is decreased by 700 kHz, the backscattering strength increases almost 8 times. But, when the frequency is increased in the same amount, the backscattering just doubled.

From the data analysis, it can be concluded that the best frequency for transmitting an ultrasound signal inside sewage is between 1.4 MHz and 2.1 MHz. Due to availability of resources, the experiments in the present work were carried out using a rotational ultrasonic transducer at 3 MHz. This is not the optimum frequency, but this is not relevant, because the scope of this research was to carry out experiments in a lab environment, using water. But by knowing the

implications of changing the frequency, the proposed techniques should be able of being implemented in real sewers without considerable changes in the results.

## 2.7. Summary

Sewers are made of different materials; the most commonly used materials are: concrete, vitrified clay, cast iron and PVC. Virtually all pipes used in municipal sewer networks are circular with sizes varying greatly, but most of them are between 200 mm and 600 mm in diameter. They handle four categories of flow: used water and foul water from customers, surface water running off properties after rainfall, surplus surface water draining from roads, garden and other urban spaces after rain and infiltration water which enters into the sewer network by defective areas such as cracks, flawed joints and manholes. Sewage level inside sewer pipes may vary from dry through partially filled to fully filled. Sewers are divided in critical and non-critical sewers depending on the potential impact on the surrounding environment in case of a failure.

The most used technique for sewers assessment uses CCTV cameras installed on robots for recording the inner sections of pipes. This has the disadvantage that sewers has to be put out of service or only the sections above the water level can be inspected. Rotating ultrasonic sensors are being used to provide images of sections below the sewage level. Experiments carried out in real sewers have shown that between the frequency range of 1.4 and 2.9 MHz, the lowest attenuation and backscattering noise were reported, hence this range is the most suitable for ultrasound imaging in sewage.

# Chapter 3

## EXPERIMENTAL PLATFORM

*This chapter presents the experimental platform used for carrying out the experiments in the present work. The experimental platform was built to allow the ultrasound scanning of different types of pipes filled with water or any other fluid of interest.*

A few attempts have been done in the past to inspect sewers by using ultrasound sonar profilers. Sonars have been mounted in trolleys [Pace, 1994] and in floating platforms that are moved along open sewer channels or sewer pipes [Andrews, 1998]. In either case, the mobile units are pulled by means of traction cables.

Basically, for profiling a pipe using an ultrasonic sonar, the sonar has to be moved along the pipe while the transducer inside the sonar is scanning the inner pipe wall. The experimental setup was built with the idea of having the capability of moving the ultrasonic sonar along the longitudinal and axial axes of a pipe filled with liquid.

The experimental setup was built using a 300 litres water tank (100 x 60 x 50 cm), a rotational ultrasonic transducer, model SeaKing, manufactured by Tritech International, Aberdeen, UK and a SCARA robot manufactured by Universal Machine Intelligence, Oxford, UK. The experimental set up had two PC's. One for operating the sonar and the logging of the ultrasonic data, and the other, for operating the SCARA Robot, Figure 3.1.

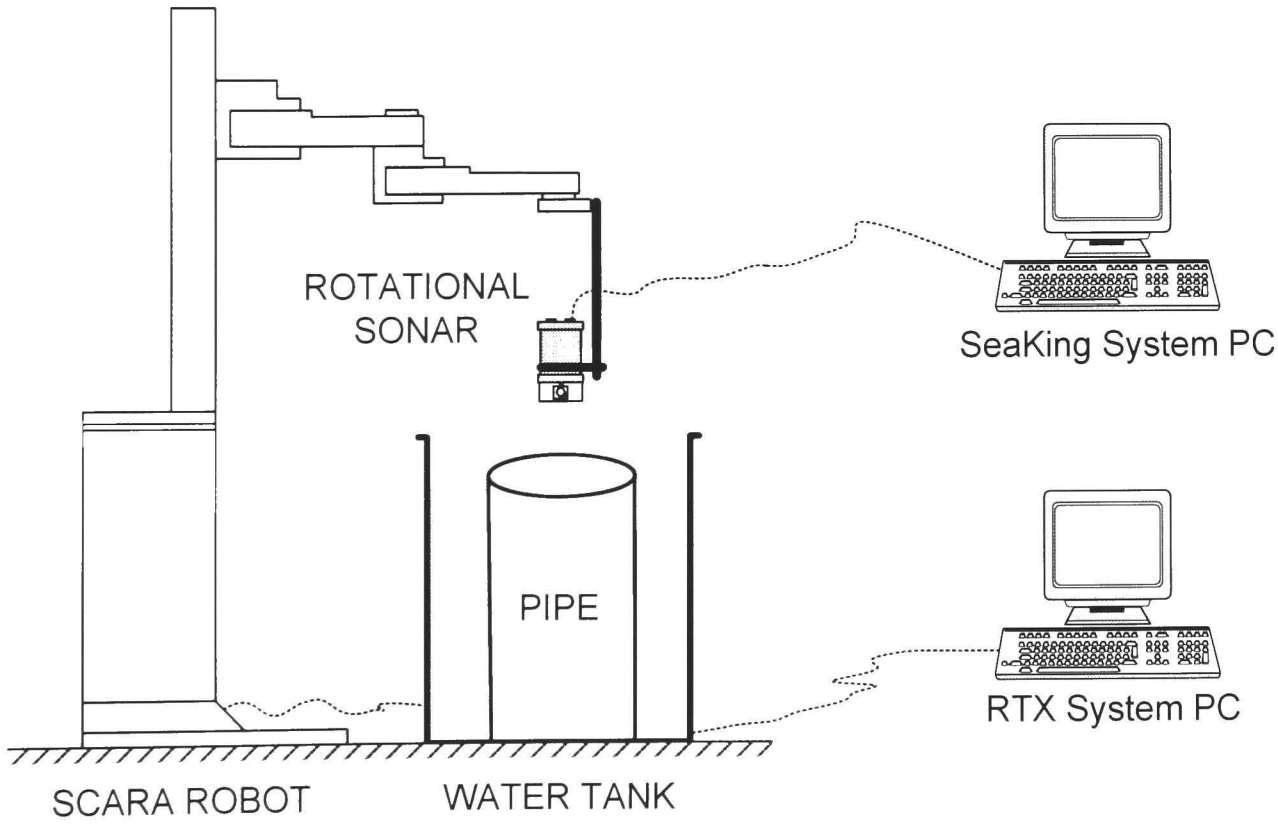


**Figure 3.1** Experimental set-up.

## 3.1. Sonar System

The sonar system was supplied by Systems Technologies, Ulverston, UK, one of the project sponsors. The supplied system is a rotational ultrasonic sonar with similar characteristics as the one intended to be used for real pipe inspections. The electronics are housed in the head of the sonar system; they are responsible for: generation and reception of the pulse/echo signal, measurement of the envelope amplitude of the echo, analogue to digital conversion, temporary storage of the data and communications via a high speed ARCNET serial link to a host computer. ARCNET is a highly integrated token ring network which can handle 255 nodes attached on a single loop. Each node has unique headers, identifiable by the SeaKing token ring network. Each node must take receipt of the token before it can send its data packets out (i.e. Sonar data transferred and addressed to the host computer).

The transducer which is also installed in the head of the sonar system is a single piston, unfocussed, piezoelectric transducer made of Lead Zirconate Titanate (PZT). It has a resonant frequency of 3 MHz, a 10 mm diameter and is mounted on a rotary stepper motor which can be controlled.

The transducer and the motor of the rotating head are protected from getting in contact with water or sewage by being housed inside a semi-rigid boot. The protecting enclosure is pressure compensated and filled with oil. The oil used to fill the boot is an inhibited mineral insulating oil commercially known as Shell Diala MX; detailed specifications can be found on appendix D.

There are 4 range resolutions available; Low, Medium, High and Ultimate. By adjusting the resolution, the mechanical step size can be changed from: 1.8, 0.9, 0.45 to 0.225 degrees respectively. The pulse duration is adjustable, with a minimum allowed pulse duration of 10 microseconds.

The rate at which signals are sampled can be adjusted, with a maximum sampling rate of 162 kHz. The amplitude of the received echo is converted by using a digital to analogue converter with 8 bit resolution. The maximum scan rate of the sonar system is 180 degrees per second. However, the maximum scan rate is limited by the physical acoustic limit. It is important to keep in mind, that the minimum time that the transducer can wait in a given position will be

determined by the depth of the observation, i.e. the time that will take the pulse to propagate through the medium until the observation target and the echo to return to the transducer:

$$t = 2\frac{d}{c}, \tag{3.1}$$

where $t$ is the time of flight, $d$ is the observation distance and $c$ is the speed of sound in the media. For instance, for scanning a B-mode image in a 300 mm pipe using the ultimate resolution (1600 steps per revolution), the minimum sampling interval can be calculated by using equation 3.1: 0.66 sec. This is well below the maximum speed of the sonar: 2 seconds per revolution. There is a trade off between scan speeds and resolution. Use of a lower resolution will give faster scan speeds, but with less detail.

### 3.1.1. Electronic boards

The SeaKing sonar is made of four electronic boards contained within a seal body tube in dry air at a pressure of one atmosphere. The sonar body is machined from aluminium alloy, and has a hard-anodised coating. The boards inside the enclosure are:

- ComDV3,
- CPUCV3,
- SOPCV3,
- SIPCV3.

A short description of the functionality of each board will be provided in the following sections, Figure 3.2.

#### 3.1.1.1. ComDV3 – Power and interface board

This board generates all voltages required for the system to operate, it has a socket to connect the sensor with the ARCNET card in the host computer and receive the power from the main power supply. In addition there is a column of diagnostic LED's situated on one side of the board. They are useful for fault tracing in the system.

#### 3.1.1.2. CPUCV3 – CPU board

This card contains "the brain" of the sensor system conducting and controlling all control functions. On this board, the TTL carrier signal, that later will be use for generating the electrical pulse for exciting the transducer, is generated by means of a 12 bit numerically controlled oscillator (HSP45102) [Intersil, California, USA]. The time varying gain control signal is generated by a high speed voltage output digital-to-analogue converter (CA3338) [Intersil, California, USA]. Another D/A converter is used as a local oscillator for synthesizing the mixing frequency that is used to reduce the frequency of the received echo to an intermediate frequency (IF). Once the echo has been received, demodulated and its amplitude measured (in the SOPCV3 board), an eight bit high speed analogue to digital converter (AD7821) [Analogue Devices, Massachusetts, USA] with a bandwidth of 100 kHz, located in this board, is used to digitise this signal.

#### 3.1.1.3. SOPCV3 – Sonar preamp and TX

This board decreases the frequency of the received echo to an intermediate frequency (IF), 455 kHz, by using the superheterodyne method [Stremler90]. After reduced to IF, the signal is filtered, amplified, its envelope detected and its intensity measured. All this is accomplished by using a high performance low power mixer FM IF system with a high-speed indicator for received signal strength - RSSI (SA627) [Phillips semiconductors, Eindhoven, The Netherlands].

#### 3.1.1.4. SIPCV3 – Sonar Output

This board is responsible for the amplification and transmission of the electrical pulse that will excite the transducer, the reception of the echo, pre-amplification of the received signal and compensation for losses due to distance by means of a time varying gain amplifier. The amplification of the TTL pulse containing the carrier signal, generated in the CPUCV3 board, is done by using dual input drivers (EL7242) [Intersil, California, USA] to switch two power MOSFETs which its outputs are connected to a transformer which finally drives the transducer. On the reception mode, this board is mainly responsible for pre-amplifying the received signal, and to compensate the transmission losses in the

medium by applying a time varying gain by means of a voltage controlled amplifier (VCA610) [Texas Instruments, Texas, USA].

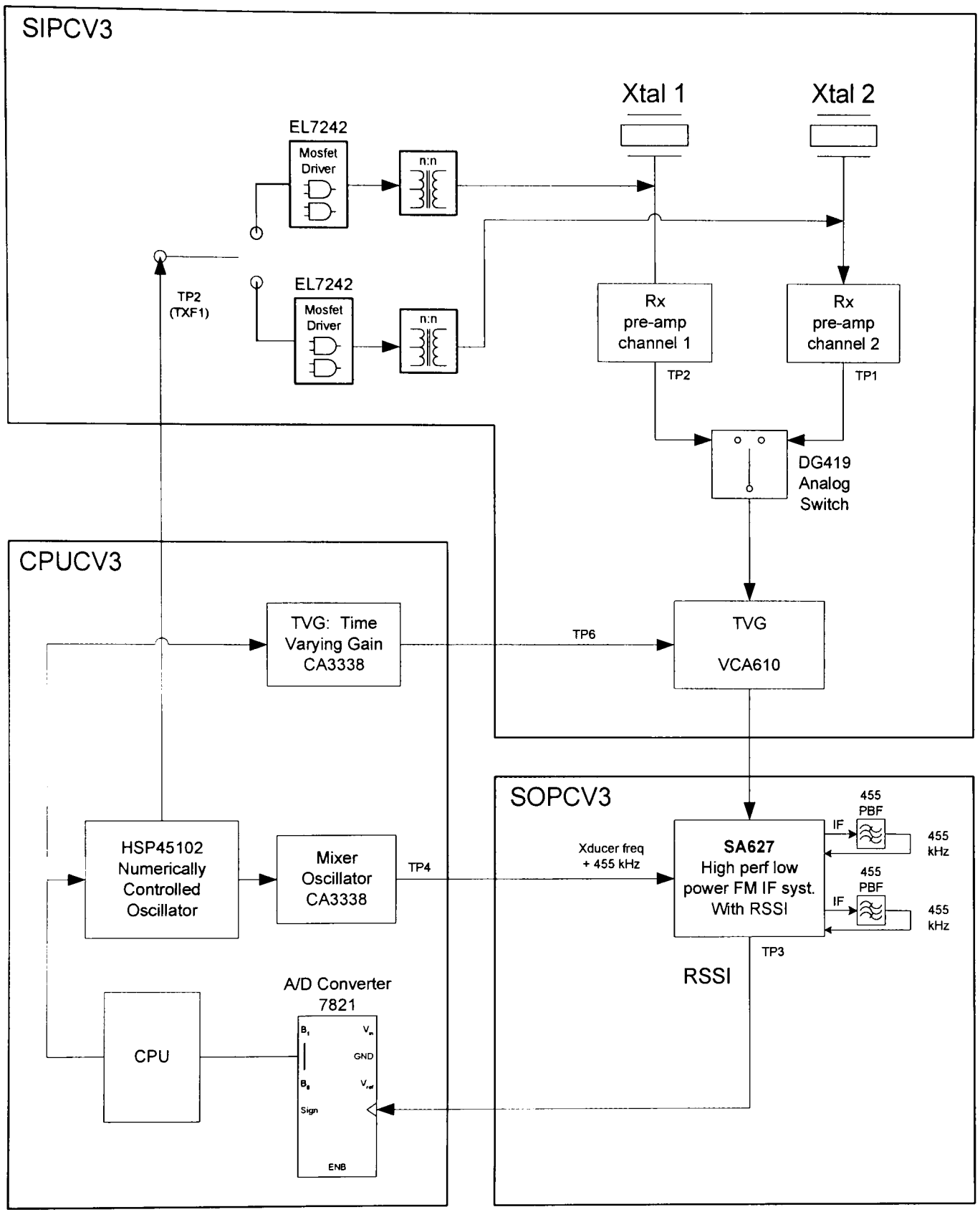


**Figure 3.2** Sonar System Internal electronic boards block diagram

## 3.1.2. DYNAMIC RANGE

The ultrasonic signals received by the sonar system have a wide dynamic range, due to the propagation characteristics of the sound. The sonar system has a

dynamic range that extends from 0 dB to 80 dB. There are two parameters that can be adjusted by the user: sensitivity and contrast. By adjusting these parameters, the observation window can be moved and re-sized to get the best sensitivity from the 8 bit Analogue-to-Digital converter, Figure 3.3. The contrast parameter lets the user change the size of the sampling window (analogous changing an amplifier gain) between 9 to 25dB. The sensitivity parameter is an offset that defines which area is going to be observed.

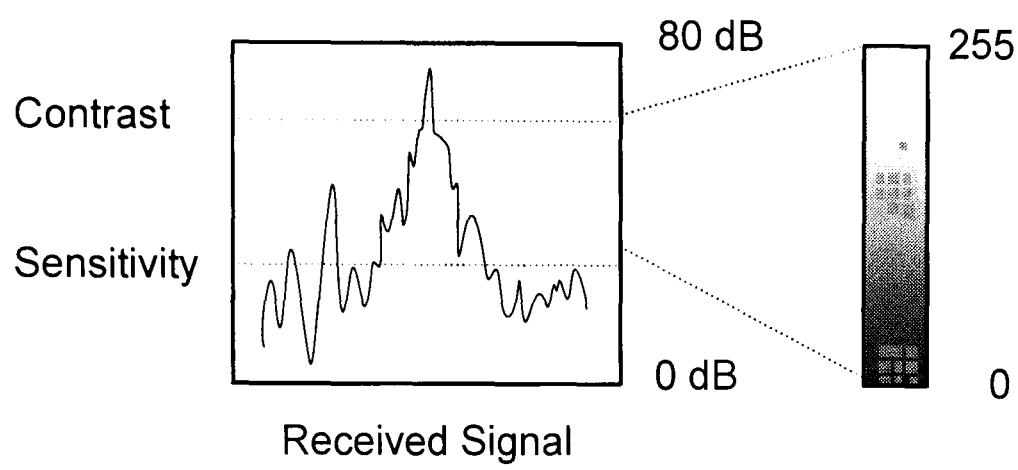


**Figure 3.3** Dynamic Range parameters that can be adjusted in the rotational ultrasonic sonar to enhance the quality of the received signal.

### 3.1.3. Time varying gain - TVG

The sonar system is equipped with an adjustable time varying gain in the receiver to compensate for the attenuation experienced by the emitted signal. The time varying gain increases the gain of the amplifier as a non-linear function of time. This is done to compensate for the attenuation per unit distance travelled by the ultrasound field. It can be changed among three predefined levels: Low, Med, High, being Med the default setting.

## *3.2. Robotic manipulator*

A robot arm was used to locate the sonar inside the pipe and to move it along in order to scan the inner surface. The employed manipulator was a UMI-RTX with a 6 degree of freedom robotic arm. The RTX robot is manufactured by OxIM Ltd., Oxford, England. The robot arm is designed to be

controlled from an IBM compatible Personal Computer (PC) via a RS232 serial link where the monitor and control application run on MS-DOS.

The RTX arm has seven motors which are controlled by two processing units called intelligent peripherals. The intelligent peripherals are controlled by a communications protocol called IPC – Intelligent Peripherals Communications which was specifically developed by Universal Machine Intelligence, Ltd., London, UK, to be used with the RTX manipulator. These intelligent peripherals are referred to as IP0 and IP1. Each IP is an Intel 8031 micro controller, with proportional, integral and differential (PID) control algorithm and velocity profiling. Each IP includes and Intel 8156 256-byte RAM with input/output, a 27128 EPROM (which contains each IP's 16 Kbytes firmware), and an 8243 input/output expander.

IP0 can control the position, speed, acceleration and force of up to five motors. IP1 can control up to four motors. The motors which are controlled by each IP are shown in table 3.1.

**Table 3.1** SCARA Robot - Motors table

| Movement | Motor | Intelligent Peripheral |
|---|---|---|
| shoulder | shoulder | 0 |
| elbow | elbow | 0 |
| up/down (z) | zed | 0 |
| wrist yaw | yaw | 0 |
| wrist pitch | wrist 1 | 1 |
| roll | wrist 2 | 1 |
| grip | grip | 0 |

The RTX robot is driven by seven precision 24 VDC motors. One motor with 20 W output power controls the vertical motion. Six other of 3 W output power control the other axes. For this experimental study of scanning a pipe immersed in water, just three motors were required: shoulder, elbow and zed.

The shoulder, elbow and yaw motors do not work against gravity when the arm manipulates load, as they drive joints that swing in the horizontal plane. The zed motor does work against gravity and can lift 4 kg in addition to the weight of the arm, at 100 mm/s. The wrist motors also work against gravity (the worst case is when the gripper is horizontal), and they can pitch and roll a 2 kg cylinder centrally held in the gripper at 60 degrees/s. Ranges of travel can be seen in Table 3.2.

**Table 3.2** SCARA Robot, ranges of travel for the arm axes

| Axis | endstop to endstop encoder counts | total range mm or degrees | encoder counts |
|---|---|---|---|
| Zed | 0 to -3554 | 948 mm | 3554 |
| zed | underside of wrist to baseboard | 881 mm | 3303 |
| shoulder | 2630 to -2630 | 180 degrees | 5260 |
| elbow | 2206 to -2630 | 331 degrees | 4836 |
| yaw | 1071 + e/3 to -1071 + e/3 | 220 degrees | 2142 |
| pitch | w1+w2 = 108 to -2642 | 102 degrees | 2750 |
| roll | w1 –w2 = 4882 to -3560 | 313 degrees | 8442 |

w1: is the encoder count for wrist 1
w2: is the encoder count for wrist 2
e: is the encoder count for the elbow motor

The motors are driven using pulse width modulation (PWM). The torques applied to the arm joints are regulated by the width of the pulse of current which is supplied to the motors every 16 ms. The width (w) of this pulse ranges from 0 to 64. With a value of 64, the motor sees a continuous supply of current. It should be noted that the current that can be drawn by the motor decreases in a linear way with an increase in motor speed. Motor torque is proportional to motor current. In table 3.3, the maximum linear and angular speeds for each one of the motors are shown.

**Table 3.3** SCARA Robot, maximum linear and angular speeds

| movement | maximum rate speed | at motor speed (rpm) |
|---|---|---|
| zed | 104.2 mm/s | 975 |
| shoulder | 42.8 degrees/s | 6250 |
| elbow | 85.6 degrees/s | 6250 |
| wrist yaw | 128.4 degrees/s | 6250 |
| wrist pitch and roll | 92.7 degrees/s | 6250 |

Each motor is fitted with a two-phase optical incremental encoder, so that the software can monitor how far the motor has moved and in what direction. In table 3.4, the ranges of travel for the arm axes from the initialised position are shown.

**Table 3.4** SCARA Robot, number of encoder counts needed to produce a specified movement

| motor | movement | encoder counts |
|---|---|---|
| zed | 1 mm | 3.74953 |
| shoulder | 1 degree | 29.2227 |
| elbow | 1 degree | 14.6113 |
| yaw | 1 degree | 9.73994 |
| wrist 1 | 1 degree | 13.4862 |
| wrist 2 | 1 mm | 13.4862 |

The repeatability of the movements of the RTX robot arm is typically +/- 0.5 mm at the writs pivot with the arm at full extension and with the dead bands parameter from the servo loop set to 1.

## 3.3. Summary

In the present chapter the setup used for carrying out the experiments of the present research has been shown. A rotational ultrasonic sonar can be moved by means of a SCARA robot inside liquid filled pipes. Both the sonar and the robot are remotely controlled by man machine interfaces running on personal computers.

The sonar is a sealed system that can be immersed in liquid and is composed of an unfocussed single ultrasonic transducer with a frequency of 3 MHz and a sampling rate of 162 kHz. The observed areas can be scanned using for different angular resolutions: 1.8, 0.9, 0.45 to 0.225 degrees.

The SCARA robot is used for positioning the transducer inside the pipe and to move it along the longitudinal axis of the pipe. The robot has six degrees of freedom but only 3 are being used: zed, shoulder and elbow. The robot has a movement repeatability of +/- 5 mm.

The presented platform has been able to emulate the sewer pipe inspection process carry out by a rotational sonar installed on top of a crawler robot travelling along a pipe filled with sewage.

# Chapter 4

## ULTRASOUND FIELDS:

## SIMULATION AND EXPERIMENTAL VALIDATION

*Traditionally sewer inspection requires sewers to be blocked, disrupting its normal operation, or to be inspected during late night when the flows are low and most of the wall can be inspected visually. New techniques allowing the inspection of sewers with minimal disruption are of great interest to sewer inspectors. Ultrasound imaging can show inner walls of pipes filled with liquid, being able to detect conditions such as sediment accumulation, roots intrusion, deformation of the pipe wall and cracks under water.*

*This chapter presents a modelling environment developed for the simulation of ultrasonic scans inside water filled pipes and its experimental validation. The comparison of model predictions against experimental results shows the capability of the simulations to generate realistic and accurate ultrasound images. The developed routines were particularly created to model rotating ultrasonic transducers inside tubular structures, allowing the simulation and visualization of ultrasonic wave propagation inside water pipes and sewers.*

## 4.1. Introduction

As reported in Chapter 2, the inspection of sewers is conventionally carried out using visual methods employing CCTV cameras. But, new inspection methods are gradually being developed to overcome the limitations of such purely optical methods which rely on the skills of an operator assessing recorded images while the camera is moving or still pictures.

The main advantage of ultrasonic inspection techniques applied to sewer inspection is their ability to inspect the water (liquid) filled parts of the sewers and pipes. Employing a multi-sensor system a complete view of the pipe above and below water level can be achieved while the pipe is in normal operation. A matter of concern to some researchers is that standard ultrasonic inspection methods can miss small defects. Extending from work conducted elsewhere, it can be shown that ultrasonics can be employed to provide a quick, quantitative assessment of sewer deformation and other problems, indicating not just the presence of a problem, but also its extent [Makar, 1999].

Ultrasonic inspection methods have been modestly investigated in the context of sewer inspection, involving mainly heuristic strategies providing results which support the feasibility of ultrasonics for pipe inspection [Duran, 2002; Andrews, 1996; Pace, 1994]. Modelling ultrasound fields for medical imaging approaches and in non-destructive testing is a relative mature research area. However, to the best knowledge of the author no attempt has been made to simulate ultrasonic imaging inside liquid-filled tubular structures.

Due to the ample benefits that are provided by a modelling environment for a given process, the starting point of this research focussed on the development of a software platform for the simulation of ultrasonic fields inside tubular structures. The main idea was to use the modelling platform for supporting the design and testing of new inspection techniques. This approach allows to shorten experimental test stages, and besides scientific benefits is expected to be beneficial for industry by reducing development costs and time, allowing the most appropriate sensor to be designed or selected for a given

inspection condition and operator training to be conducted in simulated environments.

The main contribution of this section of the research project is the extension of an ultrasound model originally developed for medical imaging applications, to simulate the behaviour of ultrasound fields generated by rotational ultrasonic scanners inside pipes. The developed modelling platform is validated through an extensive experimental study and is expected to bridge the existing knowledge gap in ultrasonic based sewer pipe inspection.

## 4.2. *Ultrasonic Inspection of sewers*

Rotating ultrasonic sensors have been used to provide images of inner sewer walls immersed in sewage [Andrews, 1998]. However, its capabilities have not been fully explored. The ultrasonic inspection process is carried out using rotational ultrasonic sonars similar to the ones used for obstacle avoidance and target recognition in underwater Remotely Operated Vehicles (ROV) and Autonomous Underwater Vehicles (AUV).

Only recently, ultrasound techniques are becoming popular as an option for the inspection of the water filled sections of sewers. The main purpose of the ultrasonic signal acquisition system is to be used as a submersible vision device which is not affected by the colour and turbidity of the media. Conditions such as sediment accumulation, roots intrusion, deformation of the pipe wall and cracks are of great interest to the sewer inspectors and all of them can be recognized by appropriate ultrasonic imaging techniques.

In order to scan a sewer section flooded with liquid, the scanner is to be moved along the area to be inspected by means of an autonomous or remotely controlled vehicle, keeping record of the position of the sensor at every instance. The idea is to scan series of consecutive axial views while the sonar moves along the longitudinal axis of the pipe in steps of defined lengths or at a defined speed, Figure 4.1.

In order to create the axial views or B-Mode images, the area of interest is swept at fixed angular intervals creating a B-Mode data file where the received echo intensity, for each angular transducer displacement, is stored in a compressed

8-bit logarithmic scale. After the scan, the transducer is translated a fixed distance to the next position along the longitudinal direction where a new scan is carried out. This procedure is repeated until the area to be inspected is completely covered.

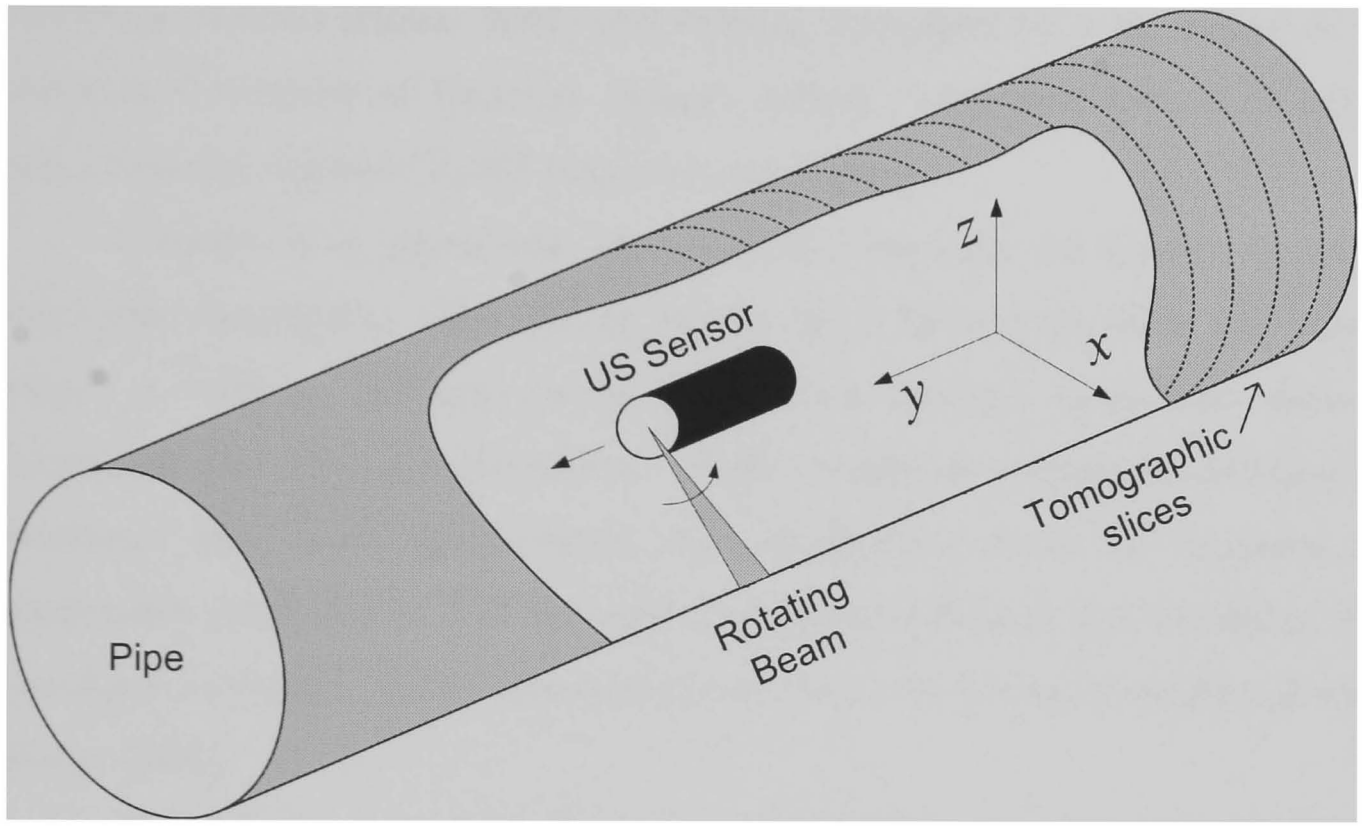


**Figure 4.1** Ultrasonic inspection of pipes. The ultrasonic head is rotated inside the pipe creating a tomographic slice (B-mode Image). To inspect a pipe section, the sensor is moved along the longitudinal axis of the pipe.

At the end, a set of files each containing a B-mode image in polar coordinates for each of the positions scanned along the *y*-axis, is obtained. The recorded axial views of the pipe can later be analyzed by an expert or by an automatic diagnostic system to find anomalous conditions that might influence the structural characteristics and mechanical integrity of the pipe. A flow diagram illustrating the scanning process is presented in Figure 4.7.

## 4.3. Modelling Methodology

Reviewing the literature with regards to available algorithms and routines for simulating ultrasonic fields, it was found that a number of general programs had been developed in the recent past. Virtually all available programs were of relatively generic nature however, most of them aimed at the medical sector for

the ultrasonic examination of internal organs or embryos. It was found that no routines were available for the simulation of rotary profiler sensors.

A number of simulation tools for medical ultrasound imaging have been developed in the past. Two high quality simulation tools were more closely considered for this research: Ultrasim, developed by Sverre Holm at the University of Oslo [Holm, 2001] and Field II, developed by J. A. Jensen at the Technical University of Denmark [Jensen, 1996]. Both tools have been amply used, cited and validated by the ultrasonic community.

Ultrasim is an interactive, menu-oriented simulator for finding the sound field from transducers. Ultrasim can handle 1D, 1.5D and 2D linear and phased arrays, as well as flat and curved arrays with different geometries such as rectangular and elliptical geometries. Each simulation consists of dividing the transducer into small sub-elements, the contribution of all the elements are numerically integrated to find the emitted or received field by the transducer. The transducer excitation can be either continuous wave or a broad-band pulsed wave [Holm, 2001].

Field II, is a set of routines for the simulation of ultrasound transducer fields and ultrasound imaging using linear acoustics. The pulsed ultrasound fields are calculated by using the Tupholme-Stepanishen method [Tupholme, 1969; Stepanishen, 1971]. Field II is capable of calculating the emitted and received fields for both the pulsed and continuous wave case for a large number of different transducers. It was created with the aim of simulating ultrasound imaging systems used in medical applications [Jensen, 1996].

It should be noted that these two software packages are realized as MATLAB toolboxes allowing easy integration into a new simulation environment and modifications and extensions to be implemented without too much complication. After carefully testing and studying the characteristics and capabilities of both toolboxes, the final decision was to use Field II. Even though both tools are able to simulate the emitted field for different kinds of transducers, Ultrasim does not have routines for the simulation of pulse-echo systems which is the cornerstone for the simulation of the ultrasound imaging system using during the experimental study.

In order to use the simulator and to create the required extensions for the simulation of ultrasound imaging inside fully-charged pipes, the modelling methodology employed by Field II was carefully studied.

The following section presents the derivation of the equations used by Field II to model a pulse echo system [Jensen, 1999].

### 4.3.1. Field II model

Field II was developed based on linear acoustic theory. A shift invariant linear system can be characterized by applying a Dirac delta function and registering its response. This is known as the impulse response. From the impulse response, the response of such system to any stimulus can be predicted. The pulse-echo system modelled by Field II is presented in Figure 4.2. An electric excitation pulse is applied to a piezoelectric crystal that made the transducer, the crystal transforms the electric signal into mechanical vibrations in the transducer's surface, generating a pressure field that is irradiated into the surrounding medium. The pressure field propagates through the medium until it reaches a boundary where it reflects, refracts or both, depending on the incidence angle and the density difference between the two media. The scattered field travels back to the transducer's face, where the pressure variations are converted into an electric signal.

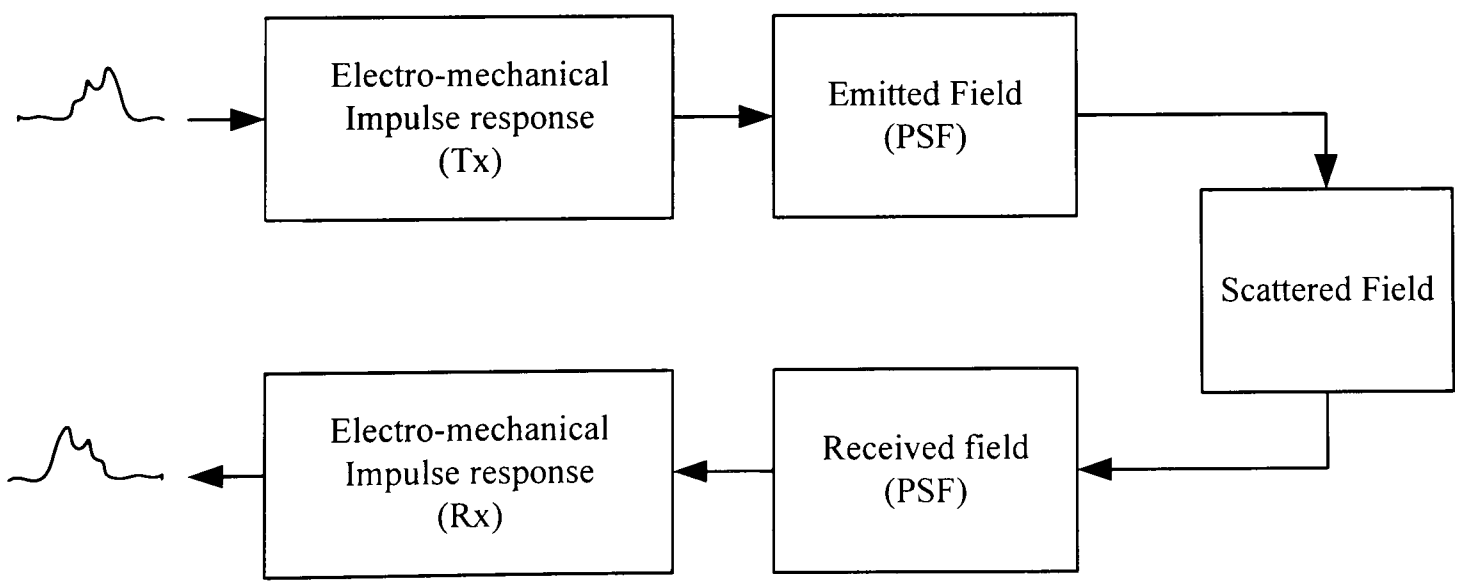


**Figure 4.2** Block diagram illustrating the simulation process

In order to derive the equations used in the model, an appropriate coordinate system was defined. The transducer was assumed to be mounted in an

infinite rigid baffle and it was divided into smaller elements whose locations are given by $\vec{r}_2$ , Figure 4.3. The transducer is assumed to radiate into a homogeneous medium and the point in the space were the acoustic field is calculated is described by $\vec{r}_1$.

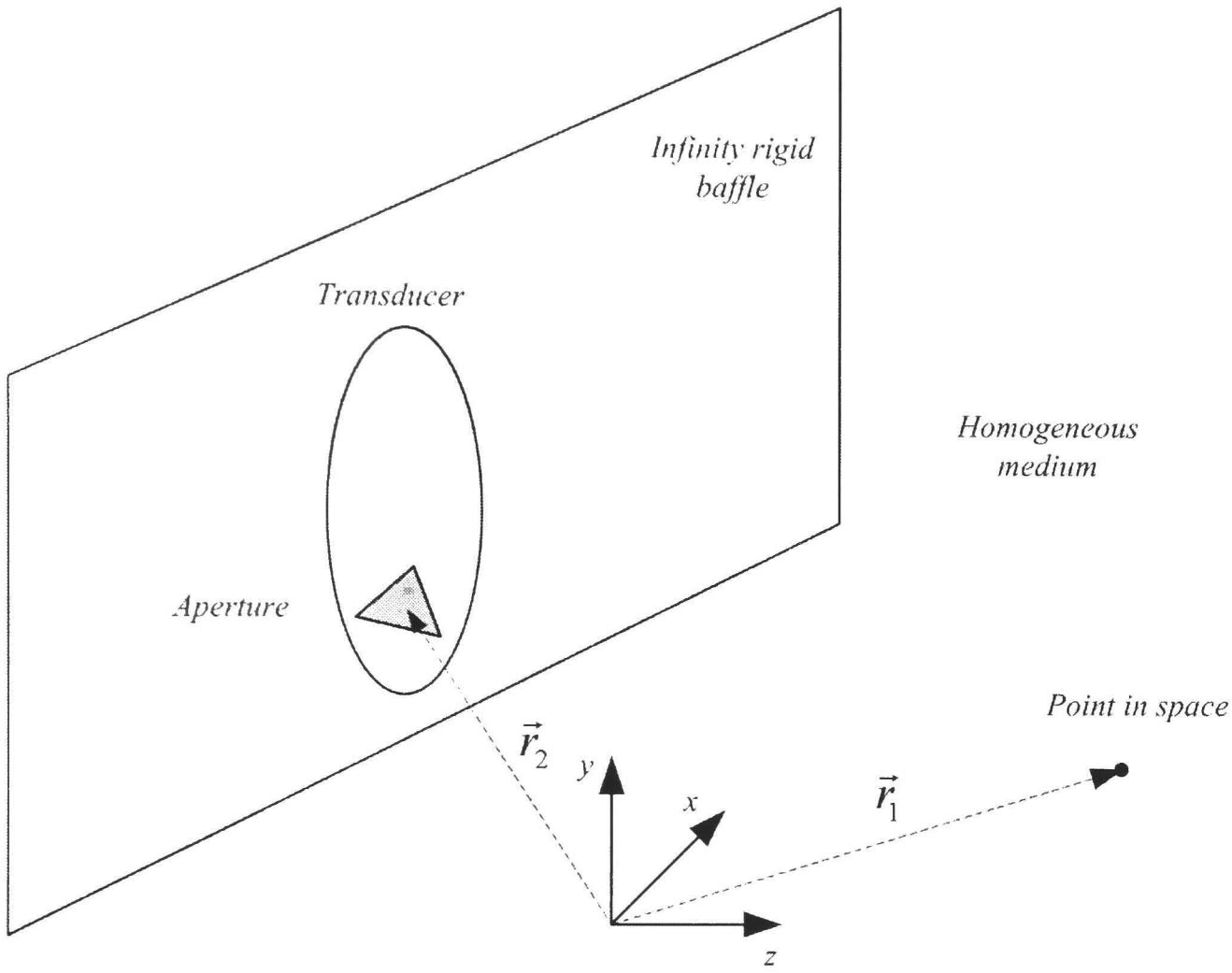


**Figure 4.3** Illustration of variables used in the model.

#### 4.3.1.1. Derivation of the spatial impulse response

The Spatial Impulse Response (SIR) was an approach developed by Tupholme and Stepanishen as an alternative to simplify the complex problem of determining the ultrasound field that reaches a reflector. The spatial impulse response is a function of the relative position between the transducer and the observation point,

$$h(\vec{r}_1, t) = \int_S \frac{\delta\left(t - \frac{|\vec{r}_1 - \vec{r}_2|}{c}\right)}{2\pi|\vec{r}_1 - \vec{r}_2|} dS \,, \tag{4.1}$$

where $\vec{r}_1$ and $\vec{r}_2$ describe the location of the observation point and the source respectively, $c$ is the speed of sound in the media, $S$ is the surface of the transducer and $t$ is time. It characterizes the three-dimensional extent of an ultrasonic field for a given transducer [Tupholme, 1969; Stepanishen, 1971].

Equation 4.1 can also be found in the literature under the name of Point Spread Function (PSF). It represents the output of an ultrasound system during the scanning of an ideal point target located in space; this term is usually used to refer to two dimensional representations. The PSF is a function of the relative position between the location of the transducer elements and an observation point in space. Once the impulse response is known, the field for any kind of excitation can be computed by convolving the spatial impulse response with the excitation function, Figure 4.2.

Using the Huyghen's principle, the face of the transducer is divided into small triangular elements that vibrate independently. As a consequence, each element can be analysed separate from the others. The small triangle aperture is assumed to be located on an infinite rigid baffle where the velocity normal to the plane in all the locations outside the aperture is zero. The point in the space, where the emitted field is observed, is described by the vector $\vec{r}_1$ and the position of the aperture by $\vec{r}_2$. Using the coordinate system presented in Figure 4.3, the emitted pressure which is a scalar field, is calculated by using the Rayleigh integral [Pierce, 1989]:

$$p(\vec{r}_1,t) = \frac{\rho_0}{2\pi}\int_S \frac{\dfrac{\partial v_n\left(\vec{r}_2, t-\dfrac{|\vec{r}_1-\vec{r}_2|}{c}\right)}{\partial t}}{|\vec{r}_1-\vec{r}_2|}\,ds\,, \tag{4.2}$$

where $v_n$ is the velocity normal to the face of the transducer, $c$ is the speed of sound in the medium and $\rho_0$ is the density of the medium. As mentioned before, this integral is a statement of Huyghen's principle, which says that the pressure field can be determined by integrating the contributions of all the small infinitesimal elements that compose the source. For formulating the integral, the following assumptions were made: the waves propagate in a homogeneous

medium with no attenuation, the aperture is flat and no re-radiation from scattering and reflection takes place.

From the linear Euler's equation, it can be shown that the particle velocity is irrotational, $\nabla \times \vec{u} = 0$ [Morse, 1969; Kinsler, 2000]. This means that it can be expressed as the gradient of a scalar function $\Phi$,

$$\vec{u} = -\nabla\Phi(\vec{r},t)\,, \tag{4.3}$$

which is known as the velocity potential. The physical meaning is that the acoustic excitation of an inviscid fluid involves no rotational flow. A real fluid has finite viscosity and therefore the particle velocity is not curl free everywhere, but for most acoustic processes, the rotational effects are small and confined to the vicinity of the boundaries. They have little influence on the propagation of sound. By substituting equation 4.3 in Euler's equation gives

$$p(\vec{r},t) = \rho_o \frac{\partial\Phi(\vec{r},t)}{\partial t}\,, \tag{4.4}$$

by substituting 4.4 in 4.2, it is seen that the surface integral is equal to the velocity potential,

$$\Phi(\vec{r}_1,t) = \int_S \frac{v_n\left(\vec{r}_2, t - \dfrac{|\vec{r}_1 - \vec{r}_2|}{c}\right)}{2\pi|\vec{r}_1 - \vec{r}_2|}\, ds\,. \tag{4.5}$$

In order to separate the excitation pulse from the transducer geometry a time convolution with a Dirac delta function ($\delta$) is introduced,

$$\Phi(\vec{r}_1,t) = \int_S \int_T \frac{v_n(\vec{r}_2,t_2)\delta\left(t - t_2 - \dfrac{|\vec{r}_1 - \vec{r}_2|}{c}\right)}{2\pi|\vec{r}_1 - \vec{r}_2|}\, dt_2\, ds\,, \tag{4.6}$$

To make the particle velocity independent from $\vec{r}_2$, it is assumed that the surface velocity is uniform along the aperture. By applying the time convolution definition, equation 4.6 becomes:

$$\Phi(\vec{r}_1,t) = v_n(t) * \int_S \frac{\delta\left(t - \frac{|\vec{r}_1 - \vec{r}_2|}{c}\right)}{2\pi|\vec{r}_1 - \vec{r}_2|} ds\,, \tag{4.7}$$

As can be seen, the right hand term of equation 4.7 is the spatial impulse response presented in equation 4.1 that will be used to determine the incident field in each one of the scatterers composing the digital phantom, in this particular study, the pipe wall.

#### 4.3.1.2. Wave equation

In the previous section, the spatial impulse response was derived. It is used for determining the incident field in two scenarios: into a scatterer being irradiated from a transmitter and into the receiver from the field being reflected back from a scatterer. The wave equation will be used to derive the reflected field from the digital phantom representing the study object in the next section.

The wave equation used in Field II was derived following a similar methodology than Chernov [1960]. In order to solve the wave equation the following assumptions were made:

- The instantaneous pressure is equal to the mean pressure of the medium plus the pressure disturbance caused by the ultrasound wave.
- The instantaneous density is considered to be equal to the density of the undisturbed medium plus the density change caused by the passing of the wave.
- The pressure and density changes created by the ultrasonic wave are considered first-order small quantities.
- No heat conduction or conversion of ultrasound energy into thermal energy takes place.

From the above assumptions, the instantaneous acoustic pressure and density at any point in space can be expressed as:

$$p_{ins}(\vec{r},t) = P + p_1(\vec{r},t)\,, \tag{4.8}$$

$$\rho_{ins}(\vec{r},t) = \rho + \rho_1(\vec{r},t)\,, \tag{4.9}$$

where $P$ is the mean pressure of the medium and $\rho$ is the density of the undisturbed medium, $p_1$ and $\rho_1$ are the pressure and density perturbations caused by the ultrasonic field.

Since the entropy of the ultrasonic system is constant, the acoustic pressure and the density satisfy the adiabatic equation [Chernov, 1960]. For describing the travelling of a sound wave, there are two possible descriptions: The Lagrange description,

$$\frac{dP_{ins}}{dt} = c^2 \frac{d\rho_{ins}}{dt} \tag{4.10}$$

and the Euler description,

$$\frac{1}{c^2}\frac{\partial p_1}{\partial t} = \frac{\partial \rho_1}{\partial t} + \vec{u} \cdot \nabla \rho\,, \tag{4.11}$$

where $u$ is the particle velocity, $\nabla$ is the gradient operator and $\cdot$ is the scalar product. The latest is more appropriate because the coordinate system is fixed in space and the equation describes the properties of any particle of fluid at a given location and time [Morse, 1968; Chernov, 1960].

Another constraint is that the pressure, density and particle velocity must also satisfy the hydrodynamic equations [Chernov, 1960]: the dynamic equation,

$$\rho_{ins} \frac{d\vec{u}}{dt} = -\nabla P_{ins} \tag{4.12}$$

and the equation of continuity,

$$\frac{\partial \rho_{ins}}{\partial t} = -\nabla \cdot (\rho_{ins}\, \vec{u})\,. \tag{4.13}$$

Now using the equations for the instantaneous pressure (4.8) and density (4.9) and discarding higher order terms, the following relationships are obtained:

$$\rho \frac{\partial \vec{u}}{\partial t} = -\nabla p_1 \text{ and} \tag{4.14}$$

$$\frac{\partial \rho_1}{\partial t} = -\nabla \cdot (\rho \vec{u})\,. \tag{4.15}$$

Differentiating 4.15 with respect to $t$ and inserting 4.14 into 4.15 gives

$$\frac{\partial^2 \rho_1}{\partial^2 t} = -\nabla \cdot \left( \rho \frac{\partial \vec{u}}{\partial t} \right) = -\nabla \cdot (-\nabla p_1) = \nabla^2 p_1 , \tag{4.16}$$

differentiating 4.11 with respect to $t$

$$\frac{1}{c^2} \frac{\partial^2 p_1}{\partial t^2} = \frac{\partial^2 \rho_1}{\partial t^2} + \frac{\partial \vec{u}}{\partial t} \cdot \nabla \rho , \tag{4.17}$$

and inserting 4.16 and 4.14 gives

$$\nabla^2 p_1 - \frac{1}{c^2} \frac{\partial^2 p_1}{\partial t^2} = \frac{1}{\rho} \nabla \rho \cdot \nabla p_1 . \tag{4.18}$$

Assuming that the propagation velocity and the density only vary slightly from their mean values,

$$\rho(\vec{r}) = \rho_0 + \Delta\rho(\vec{r}) , \tag{4.19}$$

$$c(\vec{r}) = c_0 + \Delta c(\vec{r}) , \tag{4.20}$$

where $\rho_0 >> \rho$ and $c_0 >> \Delta c$

$$\nabla^2 p_1 - \frac{1}{(c_0 + \Delta c)^2} \frac{\partial^2 p_1}{\partial t^2} = \frac{1}{(\rho_0 + \Delta\rho)} \nabla(\rho_0 + \Delta\rho) \cdot \nabla p_1 . \tag{4.21}$$

Ignoring small quantities of second order and using the approximation ($\Delta << 1$):

$$\frac{1}{1+\Delta} \approx 1 - \Delta , \tag{4.22}$$

gives

$$\nabla^2 p_1 - \left( \frac{1}{c_0^2} - \frac{2\Delta c}{c_0^3} \right) \frac{\partial^2 p_1}{\partial t^2} = \left( \frac{1}{\rho_0} \nabla(\Delta\rho) - \frac{\Delta\rho}{\rho_0^2} \nabla(\Delta\rho) \right) \cdot \nabla p_1 . \tag{4.23}$$

Neglecting the second order term $(\Delta\rho/\rho_0^2)\nabla(\Delta\rho)\cdot\nabla p_1$ yields the wave equation which describes the waves propagation in three dimensions:

$$\nabla^2 p_1 - \frac{1}{c_0^2} \frac{\partial^2 p_1}{\partial t^2} = -\frac{2\Delta c}{c_0^3} \frac{\partial^2 p_1}{\partial t^2} + \frac{1}{\rho_0} \nabla(\Delta\rho) \cdot \nabla p_1 , \tag{4.24}$$

where $\nabla p_1$ and $\nabla \rho$ are the pressure and density variations, respectively, caused by the displacement of the ultrasonic wave. The density of the medium is $\rho_0$ and the speed of the sound in the medium is $c_0$, $\nabla^2$ is the Laplacian operator, $\nabla$ is the gradient operator and $(\cdot)$ is the scalar product.

#### 4.3.1.3. Scattered Field

The scattered field is determined for a small inhomogeneity inside a homogeneous medium, see Figure 4.4.

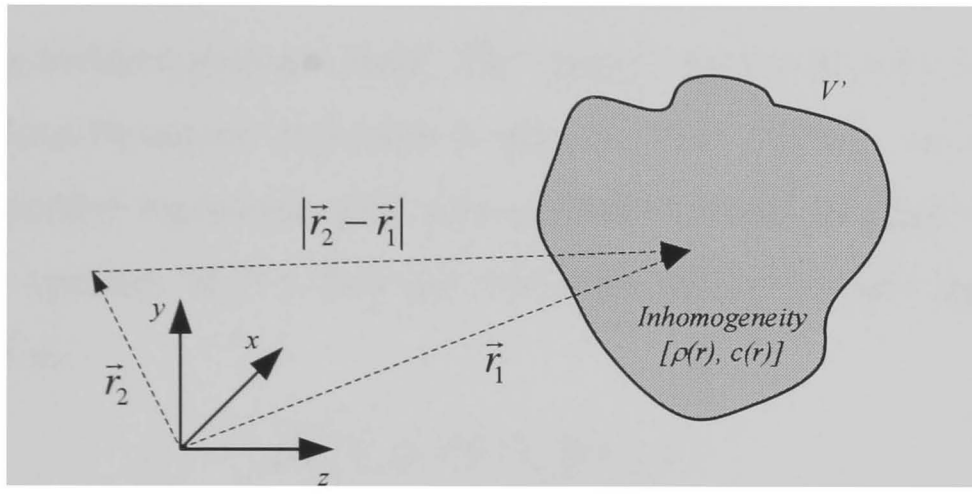


**Figure 4.4** Coordinate system used for determining the scattered field.

The inhomogeneity is enclosed inside the volume $V'$ and its location is described by $\vec{r}_1$. The scattered field is calculated at the point indicated by $\vec{r}_2$ by integrating all the spherical waves emanating from the scattering region $V'$ using the time dependent Green's function for unbounded space. Thus, the scattered field is [Morse, 1968; Gore, 1977]:

$$p_s(\vec{r}_2,t) = \int_V \int_T \left[ \frac{1}{\rho_0} \nabla(\Delta\rho(\vec{r}_1)) \cdot \nabla p_1(\vec{r}_1,t_1) - \frac{2\Delta_c(\vec{r}_1)}{c_0^3} \frac{\partial^2 p_1(\vec{r}_1,t_1)}{\partial t^2} \right] G(\vec{r}_1,t_1|\vec{r}_2,t)\, dt_1 d^3\vec{r}_1 , \quad (4.25)$$

where G is the free space Green's function:

$$G(\vec{r}_1,t_1|\vec{r}_2,t) = \frac{\delta\left(t - t_1 - \frac{|\vec{r}_2 - \vec{r}_1|}{c_0}\right)}{4\pi|\vec{r}_2 - \vec{r}_1|}, \quad (4.26)$$

$d^3\vec{r}_1$ means integrating w.r.t. $\vec{r}_1$ over the volume $V'$, and $T$ denotes integration over time.

The scattering operator can be denoted by:

$$F_{op} = \frac{1}{\rho_0}\nabla(\Delta\rho(\vec{r}_1))\cdot\nabla p_1(\vec{r}_1,t_1) - \frac{2\Delta_c(\vec{r}_1)}{c_0^3}\frac{\partial^2 p_1(\vec{r}_1,t_1)}{\partial t^2}, \tag{4.27}$$

and the pressure field inside the scattering region

$$p_1(\vec{r},t) = p_i(\vec{r},t) + p_s(\vec{r},t), \tag{4.28}$$

where $p_I$ is the incident pressure field. The integral can not be solved directly. To solve it, the Born-Neumann expansion is applied [Press, 1992]. Let $G_i$ symbolize the integral operator representing the Green's function and the integration and $F_{op}$ the scattering operator (4.27), then the first order Born-Neumann approximation can be written as:

$$ps_1(\vec{r}_2,t) = G_i F_{op} p_i(\vec{r}_1,t_1) \tag{4.29}$$

$p_s$ has been set to zero in equation 4.29. Inserting $p_{sI}$ in equation 4.28 and then in equation 4.25, yields:

$$\begin{aligned} p_{s_2}(\vec{r}_2,t) &= G_i F_{op}\left[p_i(\vec{r}_1,t_1) + G_i F_{op_i} p_i(\vec{r}_1,t_1)\right] \\ &= G_i F_{op} p_i(\vec{r}_1,t_1) + \left[G_i F_{op_i}\right]^2 p_i(\vec{r}_1,t_1) \end{aligned}. \tag{4.30}$$

It is important to remember that *Gi* indicates an integral over $\vec{r}_1$ and $t_1$, and not the pressure at point $\vec{r}_1$ and time $t_1$ but over the volume of $V'$ and time $T$ indicated by $\vec{r}_1$ and $t_1$.

The general expression for the scattered field then is:

$$\begin{aligned} p_s(\vec{r}_2,t) = \quad & G_i F_{op} p_i(\vec{r}_1,t_1) \quad + \\ & \left[G_i F_{op}\right]^2 p_i(\vec{r}_1,t_1) + \\ & \left[G_i F_{op}\right]^3 p_i(\vec{r}_1,t_1) + \cdots \end{aligned} \tag{4.31}$$

Terms involving $\left[G_i F_{op}\right]^N p_1(\vec{r}_1,t_1)$ where N>1, describe multiple scattering of order N. Usually the scattering from small obstacles is considered weak so higher order terms can be neglected. Thus, a useful approximation is to employ only the

first term in the expansion. This corresponds to the first order Born-Neumann approximation.

Using this, equation 4.25 can be approximated by:

$$p(\vec{r}_2,t) \approx \iint \left[ \frac{1}{\rho_0} \nabla(\Delta\rho(\vec{r}_1)) \cdot \nabla p_i(\vec{r}_1,t_1) - \frac{2\Delta c(\vec{r}_1)}{c_0^3} \frac{\partial^2 p_i(\vec{r}_1,t_1)}{\partial t^2} \right] G(\vec{r}_1,t_1|r_2,t) dt_1 d^3\vec{r}_1 \tag{4.32}$$

So in order to calculate the scattered field, the sound pressure of the incident field for the homogeneous medium must be calculated.

#### 4.3.1.4. Incident Field

For deriving the equation for calculating the incident field, the coordinate system presented in Figure 4.5 is going to be used. The incident field is generated by the ultrasound transducer assuming no other sources exist in the medium. The field is conveniently calculated by employing the velocity potential $\Phi(\vec{r},t)$ introduced in section 4.3.1.1 and enforcing appropriate boundary conditions [Tupholme, 1969; Stepanishen, 1971]. The velocity potential satisfies the following wave equation for a homogeneous medium,

$$\nabla^2\Phi - \frac{1}{c_0^2}\frac{\partial^2\Phi}{\partial t^2} = 0\,, \tag{4.33}$$

once the velocity potential is known then the pressure is calculated using equation 4.4.

The particle velocity normal to the transducer surface is denoted by $v(\vec{r}_3+\vec{r}_4,t)$, where $\vec{r}_3$ identifies the position of the transducer and $\vec{r}_4$ a point on the transducer surface relative to $\vec{r}_3$. The solution to the homogeneous wave equation is [Stepanishen, 1971]:

$$\Phi(\vec{r}_1+\vec{r}_3,t) = \int_S \int_T v(\vec{r}_1+\vec{r}_3,t_3) g(\vec{r}_1,t_1|\vec{r}_3+\vec{r}_4,t_3) dt_3\, d^2\vec{r}_4\,, \tag{4.34}$$

where $S$ denotes the transducer surface and $g$ is the Green's function for a bounded medium:

$$g(\vec{r}_1, t_1 | \vec{r}_3 + \vec{r}_4, t_3) = \frac{\delta\left(t - t_3 - \frac{|\vec{r}_1 - \vec{r}_3 - \vec{r}_4|}{c_0}\right)}{2\pi|\vec{r}_1 - \vec{r}_3 - \vec{r}_4|}, \tag{4.35}$$

where $|\vec{r}_1 - \vec{r}_3 - \vec{r}_4|$ is the distance from $S$ to the point where the field is calculated and $c_0$ the mean propagation velocity. The field is calculated under the assumption of radiation into an isotropic, homogeneous non-dissipative medium.

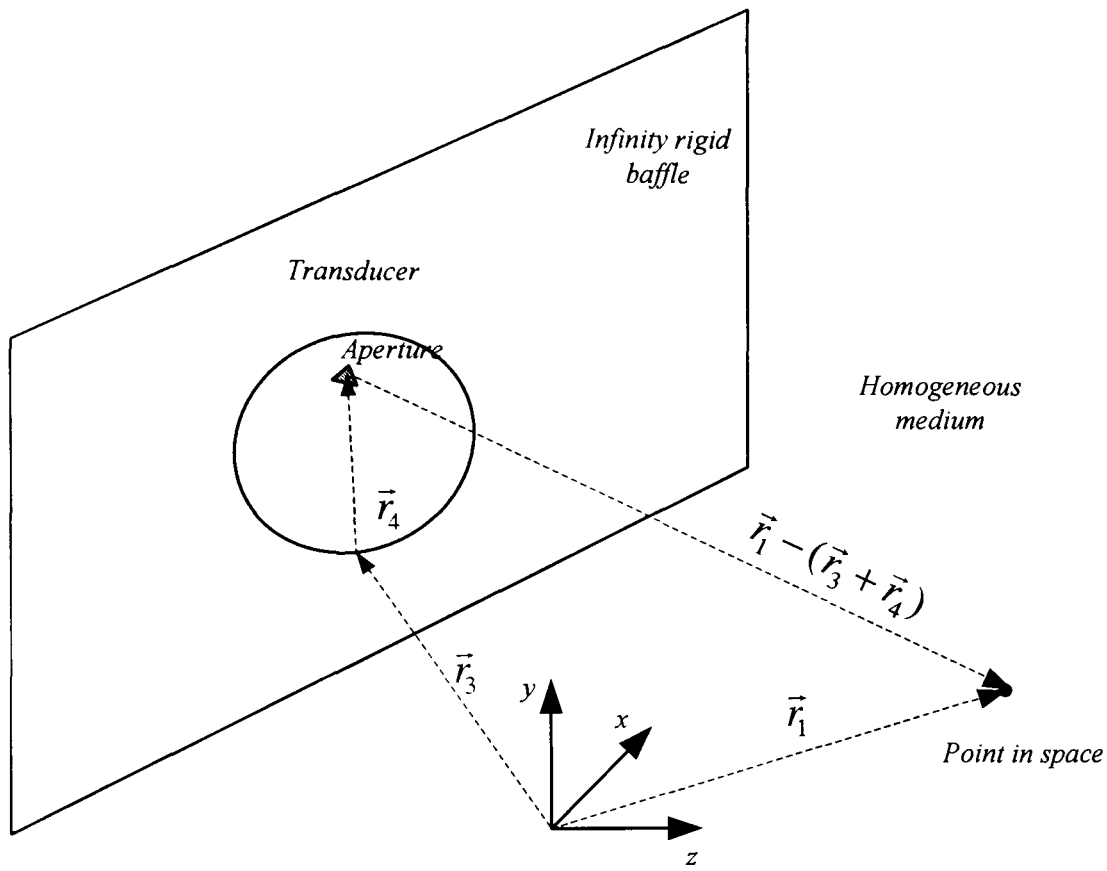


**Figure 4.5** Coordinate system used for calculating the incident field.

If the particle velocity is assumed to be uniform over the surface of the transducer, equation 4.34 can be reduced to [Stepanishen, 1971]:

$$\Phi(\vec{r}_1, \vec{r}_3, t) = v \int_T u(t_3) \int_S g(\vec{r}_1, t_1 | \vec{r}_3 + \vec{r}_4, t_3) d^2\vec{r}_4 dt_3 \tag{4.36}$$

This is the spatial impulse response previously derived, and the sound pressure for the incident field then is:

$$p(\vec{r}_1, \vec{r}_3, t) = \rho_0 \frac{\partial \Phi(\vec{r}_1, \vec{r}_3, t)}{\partial t} = \rho_0 v(t) \otimes \frac{\partial h(r_1, r_3, t)}{\partial t} \tag{4.37}$$

or

$$p(\vec{r}_1,\vec{r}_3,t)=\rho_0\frac{\partial v(t)}{\partial t}\otimes h(r_1,r_3,t) \tag{4.38}$$

#### 4.3.1.5. The received signal

The received signal is the scattered pressure field integrated over the transducer surface, convolved with the electromechanical impulse response, $E_m(t)$, of the transducer. The transducer is located at $\vec{r}_5$ and the location of the element in the transducer face that is receiving the scattered field is $\vec{r}_6+\vec{r}_5$, see Figure 4.6. The received signal is:

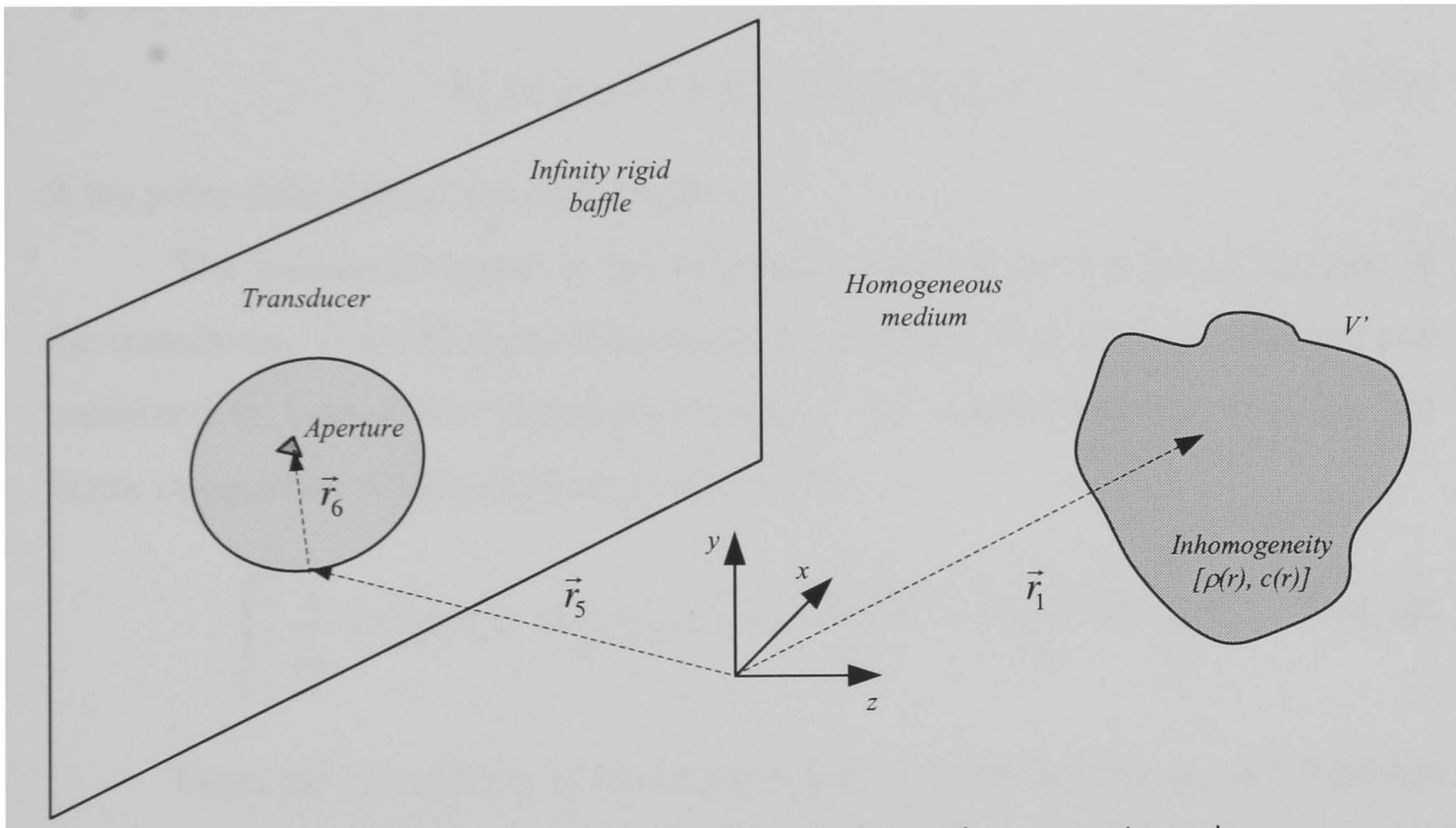


**Figure 4.6** Coordinate system for calculating the received signal

$$p_r(\vec{r}_5,t)=E_m(t)\otimes\int_S p_s(\vec{r}_5+\vec{r}_6,t)d^2\vec{r}_6\,. \tag{4.39}$$

The scattered field is:

$$p_s(\vec{r}_6+\vec{r}_5,t)=\frac{1}{2}\int_{V'}\int_T F_{op}[p_i(\vec{r}_1,t_1)]\frac{\delta\left(t-t_1-\dfrac{|\vec{r}_6+\vec{r}_5-\vec{r}_1|}{c_0}\right)}{2\pi|\vec{r}_6+\vec{r}_5-\vec{r}_1|}dt_1d^3\vec{r}_1\,, \tag{4.40}$$

combining this with equation 4.39 and comparing with equation 4.1, it can be seen that $p_r$ includes the Green's function for bounded space integrated over the transducer surface, which is equal to the spatial impulse response. Inserting the

expression for $p_i$ and integrating over the transducer surface and over time, results in:

$$p_r(\vec{r}_5,t) = E_m(t) \otimes \frac{1}{2}\int_{V'} F_{op}\left[\rho_0 \frac{\partial v(t)}{\partial t} \otimes h(\vec{r}_1,\vec{r}_3,t)\right] \otimes h(\vec{r}_5,\vec{r}_1,t) d^3\vec{r}_1 \quad (4.41)$$

Because the position of the transmitting and the receiving transducer is the same ($\vec{r}_3 = \vec{r}_5$), equation 4.41 can be rearranged into:

$$p_r(\vec{r}_5,t) = \frac{\rho_0}{2} E_m(t) \otimes \frac{\partial v(t)}{\partial t} \otimes \int_{V'} F_{op}\left[h_{pe}(\vec{r}_1,\vec{r}_5,t)\right] d^3\vec{r}_1 \quad (4.42)$$

where

$$h_{pe}(\vec{r}_1,\vec{r}_5,t) = h(\vec{r}_1,\vec{r}_5,t) \otimes h(\vec{r}_5,\vec{r}_1,t) \quad (4.43)$$

is the pulse-echo spatial impulse response.

The calculated signal is the response measured for one given position of the transducer. For a B-mode scan image a number of scan lines is measured and combined to form a two dimensional image. To analyse this situation, the last factor in equation 4.42 is explicitly written out

$$\int_{V'}\left[\frac{1}{\rho_0}\nabla(\Delta\rho(\vec{r}_1))\cdot\nabla h_{pe}(\vec{r}_1,\vec{r}_5,t) - \frac{2\Delta_c(\vec{r}_1)}{c_0^3}\frac{\partial^2 h_{pe}(\vec{r}_1,\vec{r}_5,t)}{\partial t^2}\right] d^3\vec{r}_1 . \quad (4.44)$$

From the calculation of the incident field it is known that $h_{pe}$ is a function of the distance between $\vec{r}_1$ and $\vec{r}_5$, while $\Delta\rho$ and $\Delta c$ are only functions of $\vec{r}_1$ (equation 4.34). So when $\vec{r}_5$ is varied over the volume of interest, the resulting image is a spatial non stationary convolution between $\Delta\rho$, $\Delta c$ and a modified form of the pulse-echo spatial impulse response.

Assuming that the pulse-echo spatial impulse varies slowly then the spatial frequency content is constant over a finite volume, hence equation 4.44 can be rewritten

$$\int_{V'}\left[\frac{1}{\rho_0}\nabla(\Delta\rho(\vec{r}_1))\nabla^2 h_{pe}(\vec{r}_1,\vec{r}_5,t) - \frac{2\Delta_c(\vec{r}_1)}{c_0^3}\frac{\partial^2 h_{pe}(\vec{r}_1,\vec{r}_5,t)}{\partial t^2}\right] d^3\vec{r}_1 \quad (4.45)$$

$h_{pe}$ is a function of the distance between the transducer and the scatterer or equivalently of the time given by

$$t = \frac{|\vec{r}_1 - \vec{r}_5|}{c_0} \tag{4.46}$$

The Laplace operator is the second derivative w.r.t. distance, assuming only small deviations from the mean propagation velocity, it can be approximated with the second derivative w.r.t. time:

$$\nabla^2 h_{pe}(\vec{r}_1, \vec{r}_5, t) = \frac{1}{c_0^2} \frac{\partial^2 h_{pe}(\vec{r}_1, \vec{r}_5, t)}{\partial t^2}. \tag{4.47}$$

Using these approximations, equation 4.42 can be rewritten:

$$p_r(\vec{r}_5, t) = \frac{\rho_0}{2c_0^2} E_m(t) \otimes \frac{\partial v^3(t)}{\partial t^3} \otimes \int_{V'} \left[ \frac{\Delta\rho(\vec{r}_1)}{\rho_0} - \frac{2\Delta c(\vec{r}_1)}{c_0} \right] h_{pe}(\vec{r}_1, \vec{r}_5, t) d^3\vec{r}_1. \tag{4.48}$$

Symbolically this could be written as

$$p_r(\vec{r}_5, t) = v_{pe}(t) \otimes f_m(\vec{r}_1) \underset{r}{\otimes} h_{pe}(\vec{r}_1, \vec{r}_5, t), \tag{4.49}$$

where $\otimes$ is time convolution, $\underset{r}{\otimes}$ is the spatial convolution calculated using $\int_V f(r_1)\, d^3 r_1$ and $p_r$ is the received signal.

The function, $v_{pe}(t)$, describes the transducer excitation and the electro-mechanical impulse response during emission and reception of the pulse,

$$v_{pe}(t) = \frac{\rho_0}{2c_0^2} E_m(t) \otimes \frac{\partial^3 u(t)}{\partial t^3}. \tag{4.50}$$

The term, $f_m$, accounts for the inhomogeneities in the medium due to density and propagation velocity perturbations which give rise to the scattered signal,

$$f_m(\vec{r}_1) = \frac{\Delta\rho(\vec{r}_1)}{\rho_0} - \frac{2\Delta c(\vec{r}_1)}{c_0}. \tag{4.51}$$

The modified pulse-echo spatial impulse response, $h_{pe}$, that relates the transducer geometry to the spatial extent of the pressure fields is

$$h_{pe}(\vec{r}_1,\vec{r}_2,t) = h(\vec{r}_1,\vec{r}_5,t) \otimes h(\vec{r}_5,\vec{r}_1,t) \ . \tag{4.52}$$

## 4.4. Simulating a rotary ultrasound sensor inside a tubular structure

The pipe inspection process was described in section 4.2; it requires that an ultrasonic transducer is to be rotated around the longitudinal axis of the inspected pipe (here: the *y-axis*) and be translated along it, see Figure 4.1. In order to simulate the pipe inspection process, a set of routines emulating the behaviour of the ultrasonic sonar, its movement along the pipe, the data manipulation and finally the generation of a three dimensional inner pipe profile were created, implemented and validated. Figure 4.7, shows a flow diagram describing the scanning process. The set of developed routines expanded the capabilities of Field II.

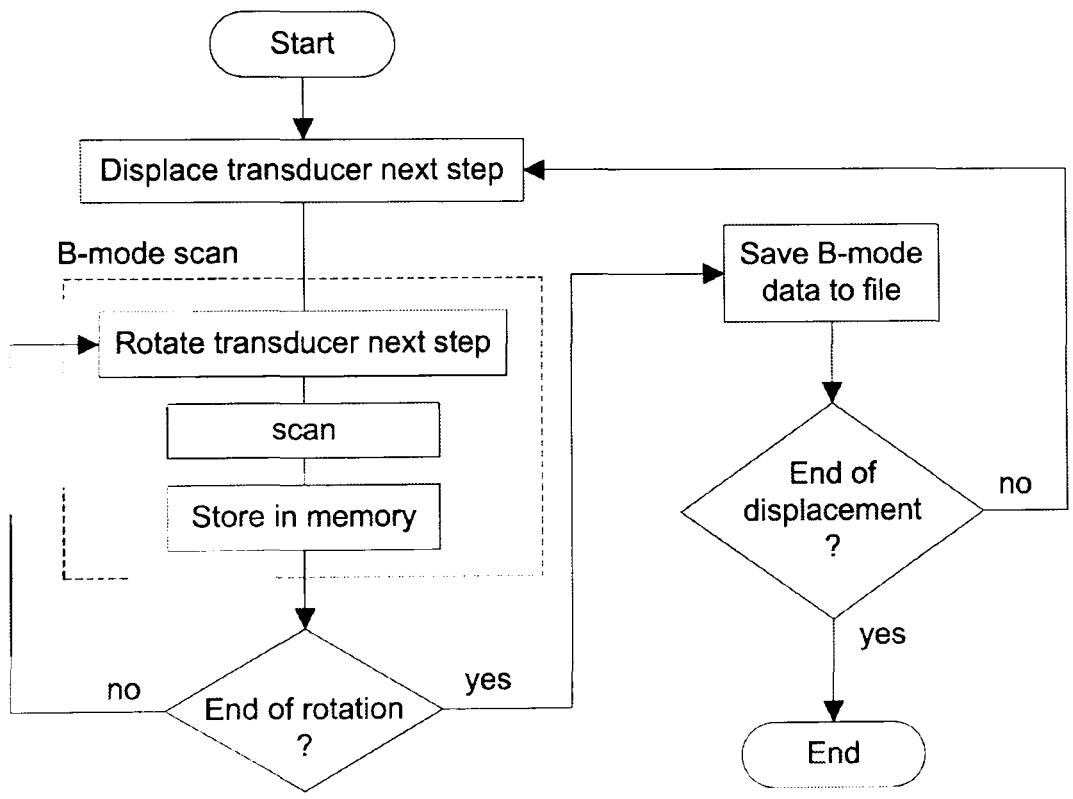


**Figure 4.7** Diagram flow showing the scanning process for a pipe

In order to simplify the simulation process and reduce the computational load of the model, the model was developed locating the centre of the transducer at the origin of the coordinate system with its front face aligned with the *x-y* plane, Figure 4.8.

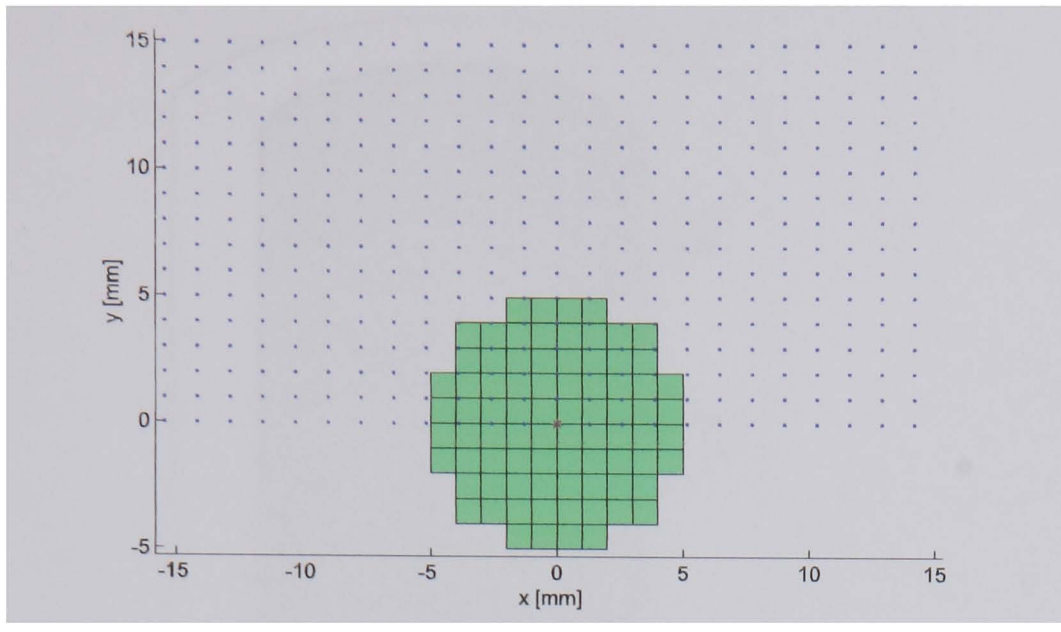


**Figure 4.8** *Circular transducer located at origin on x-y plane*

It should be noted that due to the approach used by Jensen [1996] when developing the Field II's routines, any movement of the transducer is not possible. As a consequence, instead of moving the transducer in order to simulate the scanning of a sewer pipe where a transducer has to be rotated and translated in order to sweep an interest section, the phantom representing the pipe will be moved accordingly. Hence, routines for rotating and translating the object under observation while the transducer is kept still at the origin of the coordinate system were developed [Gomez, 2003 and 2004].

In addition to the basic parameters required for describing a pulse-echo ultrasonic scanning system, the added routines require information such as the initial position along the pipe were the transducer is going to be located, the size of the steps used for displacing the transducer (longitudinal observation resolution) and the distance that the transducer is going to be moved.

Due to the extensive computing requirements that the simulator demands, in some cases the scanning of a small pipe section can be simulated only. The parameters required are: initial angle ($\theta_{start}$), final angle ($\theta_{end}$) and the angular resolution ($\theta_{step}$). The initial and final angles are measured with respect to the *z-axis*, Figure 4.9.

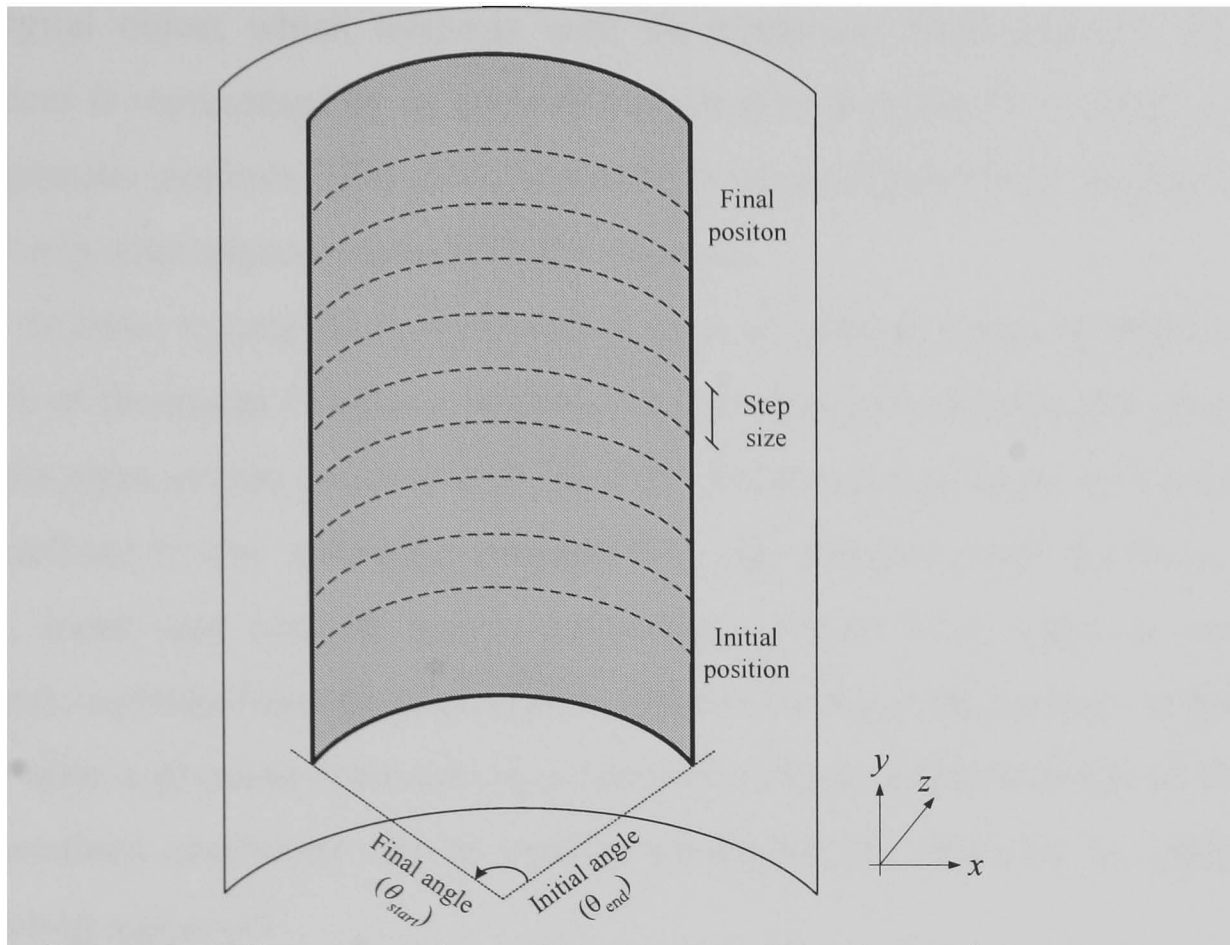


**Figure 4.9** Illustration of input parameters used by the simulation system.

In Figure 4.10 a summary of the most important input-output parameters of the simulator is shown. In addition, a full list with all the routines developed in Matlab as part of this research is presented in appendix A.

Input parameters:

- Transducer centre frequency (*f*)
- Transducer radius (*r*)
- Size of mathematical elements (*w, h*)
- Sampling frequency (*fs*)
- Speed of sound in medium ($c_0$)
- Phantom (pipe dimensions, defect)
- Pulse duration
- Area to be scanned
  - Initial longitudinal position
  - Final longitudinal position
  - Longitudinal step size (long. resolution)
  - Initial angle
  - Final angle
  - Angular step size (angular resolution)

Output:

- B mode images:
  - RF lines (θ, *t*)
  - Position (*y*)

**Figure 4.10** Input/Output parameters for the simulation algorithms

## 4.5. Phantoms

The basic idea of the simulator is to ultrasonically scan an object, hence a digital representation of the study object has to be created in order to be studied.

The digital object which interacts with the ultrasonic field emitted from the transducer is represented by an array of evenly spaced scatterers, located inside a homogeneous medium. The set of scatterers representing the inner surface of the pipe or any other object is referred to by phantom.

In order to ease the burdensome process of creating a pipe by defining the location of thousands of points, routines for creating three dimensional phantoms of whole pipes or pipe sections were created. These routines allow the creation of pipes defined by the following parameters: pipe diameter, wall thickness, pipe length, mesh size and arc size. Additional routines were added to remove geometric sections from the phantoms in order to facilitate the creation of defects. Hence after a phantom representing a sewer is created, different kinds of defects or anomalous conditions can be created modifying the phantom by adding or subtracting scatterers.

The distance between scatterers (individual reflecting points inside the phantom) must be chosen appropriately. Reducing distances between scatterers (equivalent to reducing the mesh size) leads to an increase in the number of scatterers per axial section of pipe, which in turn impacts directly on the processing requirements. As a consequence, it demands more memory and increases the processing time required to run the model. However, if the distance between scatterers is increased in excess, the resulting image may appear as a discontinuous object, see Figure 4.11. The optimum value for the mesh size parameter to properly represent a pipe is mainly defined by the beam width of the transducer which is a function of its frequency (wavelength) and geometry. The minimum scatterer separation to represent a pipe wall is also determined by the size of the defects to be studied. The defect size cannot be smaller than the mesh size.

In Figure 4.11 results from a simulation where two phantoms with mesh sizes of 0.2 mm and 4 mm were scanned by rotating the transducer a full rotation, are shown. As can be seen, when the mesh size is too big (inset b), the scanned pipe appears as a discontinued object

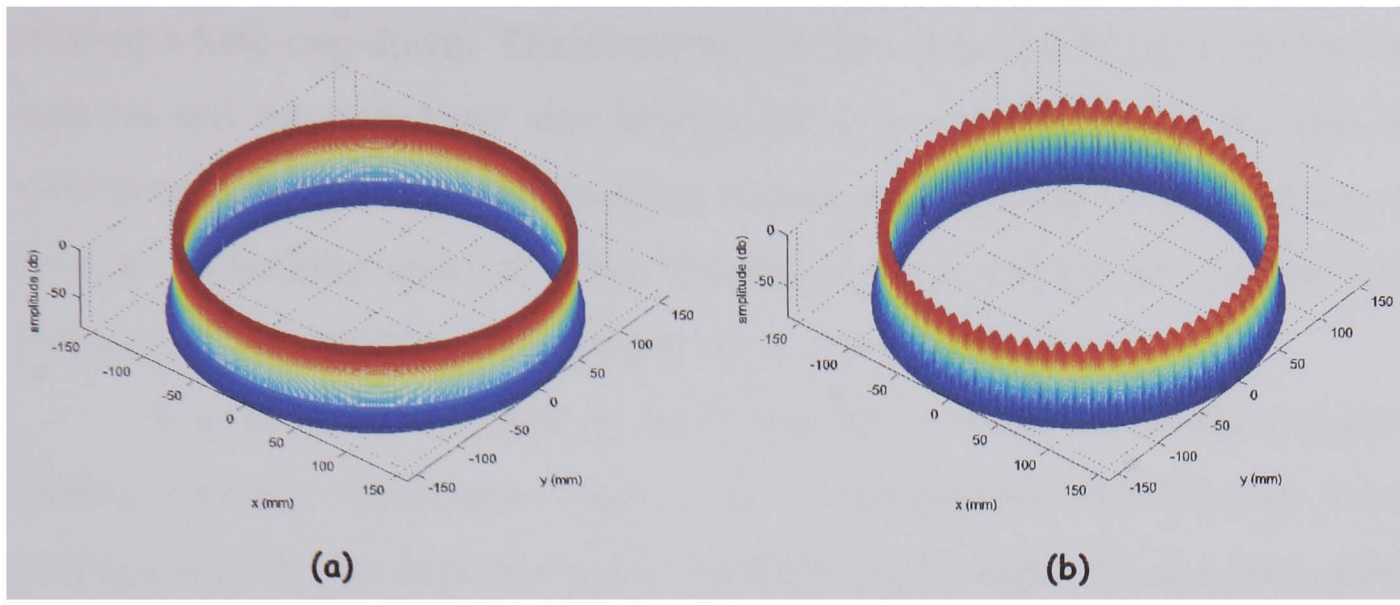


**Figure 4.11** Scatterers separation comparison plot. Echoes obtained by simulating a full rotation of a transducer located in the centre (origin of the coordinate system) of a 300 mm pipe are shown. Phantoms with different scatterers separation were used: (a) 0.2 mm (b) 4 mm. While a continuous representation is achieved in (a), in (b), the image of the wall becomes discontinuous.

The best scatterer separation for the experiments carried out in the present research was determined by trial and error, varying distances over a large range and analyzing its corresponding responses. For the particular case of simulating ultrasonic fields for inspecting 300 mm diameter pipes, a scatterer separation in the range from 0.1 mm to 1.0 mm was found to give good results. It was found that, as a rule of thumb for the used sensor with a beamwidth of 2.66 degrees, the distance between the scatterers should be at least half of the minimum size of any simulated defect.

## *4.6. Backing material modelling*

The investigated transducer used for the validation of the simulations was a single piston transducer with a frequency of 3 MHz. As mentioned in section 4.4, the centre of the transducer is located at the origin of the coordinate system and its front face is aligned with the *x*-*y* plane. It should be noted, that the premises used to develop the model by Jensen [1996] assume that the transducer is mounted on an infinitely rigid baffle, and as a consequence, the ultrasound field is emitted from the front and rear faces of the transducer, generating ultrasound fields which travel in the positive as well as negative *z* directions.

Standard ultrasonic transducers used in pulse-echo applications are mounted on backing materials to reduce the undesirable effects caused by the mismatch in the impedance between the transducer and the medium, usually

creating a long ring-down. The simulation of the interaction between the backing material and the transducer was beyond the scope of this work. Because the simulation considers that the ultrasonic transducer is located in the medium and there is no backing material, when the transducer is excited, the emitted field propagates from both the front and rear faces of the transducer.

It is important to keep in mind that the transducer is located inside a tubular structure filled with water. As a consequence, the pressure waves propagating from the rear face of the transducer in the negative $z$-direction reflect in the section of the pipe located in the negative $z$ half-space (behind the transducer). The echoes coming from the rear side of the transducer get mixed with the echoes returning from the front face, distorting the signals of interest [Gomez, 2003a and 2003b].

In order to overcome this limitation which arises when creating images from pipes immersed in water, a scatterer filter function was developed and implemented. This function analyzes the phantom and the location of the transducer before starting the simulation of the ultrasonic field and removes all the scatterers located in the negative $z$ half-space [Gomez, 2003a and 2003b].

## 4.7. Simulation Optimization – Scatterer reduction

Due to the nature of the equations which describe the ultrasound phenomena, the computing time is an important issue to consider. Determining the spatial impulse response for each scatterer, calculating the scattered field using the wave equation and finally determining the received field by the transducer is a highly demanding task for the used processor. It is noted that the simulation time is proportional to the number of scatterers used to represent an object [Jensen, 2000].

For instance, to run a simulation on a Pentium IV, 1.8 GHz with 256 Mbytes of RAM, modelling a phantom representing a ring formed by just 3600 scatterers, rotating the transducer 180 degrees in 1 degree steps, takes around 12 minutes. However, this example is just a 2D simulation with scatterers located in the axial-elevation plane only. To simulate the same sweep of 180 degrees, with a pipe section of 100 mm long, built by consecutive, equally spaced rings, the

resulting phantom will be composed of 360,000 scatterers; this simulation will take at least 20 hours. The aforementioned simulation just generates a single B-mode image. In order to inspect a pipe section, the transducer has to be moved along the pipe. Scanning a 5 mm section of the previous phantom, at 1 mm intervals, would increase the simulation time by a factor of 5 to 4.2 days.

Improving the simulation time has been a key issue when simulating ultrasonic images in pulse echo systems. The following approach was created aiming to reduce the simulation time when scanning whole pipes. The original routines determine the scattered field from all the scatterers which compose the phantom located inside the media. For the particular case of three dimensional phantoms, the number of scatterers is usually over 100,000. However, a good portion of them lie in an area where the ultrasound-field energy of the incident field is very weak, being equal to or less than the background noise level. If the radiation pattern of the transducer is known a priori then the scatterers located in the area where the energy levels are very weak can be ignored. Removing them, before calculating the response, reduces considerably the computational time [Gomez, 2003a and 2003b].

The investigated single piston transducer has a far field radiation pattern that can be described by a translated sin(x)/x function propagating in all directions ($x$, $y$ and $z$) from the front face of the transducer. As the wave front moves away from the centre of the transducer, its amplitude decreases, falling quickly below the background noise level. This means that not all the scatterers who compose the phantom receive an ultrasound field with enough intensity to generate a detectable echo.

With the aim to reduce the simulation time, the new approach was to define a conic surface which describes a volume containing most of the energy radiated by the transducer. This volume is used as a pre-processing stage where all the scatterers which fall outside of the boundaries of the conic surface are removed and then the reduced new phantom is passed to the simulation routines, i.e., such a cone defines a volume and only the scatterers located inside of it, are used to calculate the scattered field, see Figure 4.12. It should be noted that the

scatterer reduction function is applied to the original phantom every time the transducer is rotated or moved to a new position during the simulation process.

The scatterer reduction function was realised with a variable aperture that can be adjusted to deal with different kinds of transducers with different radiation patterns. In order to incorporate transducers with different sizes and geometries, besides changing the aperture of the cone, its vertex can be translated to any location behind the transducer (negative *z-axis*), in order to align the illuminated area (grey area Figure 4.12) of the cone with the radiation pattern of the transducer, see Figure 4.12.

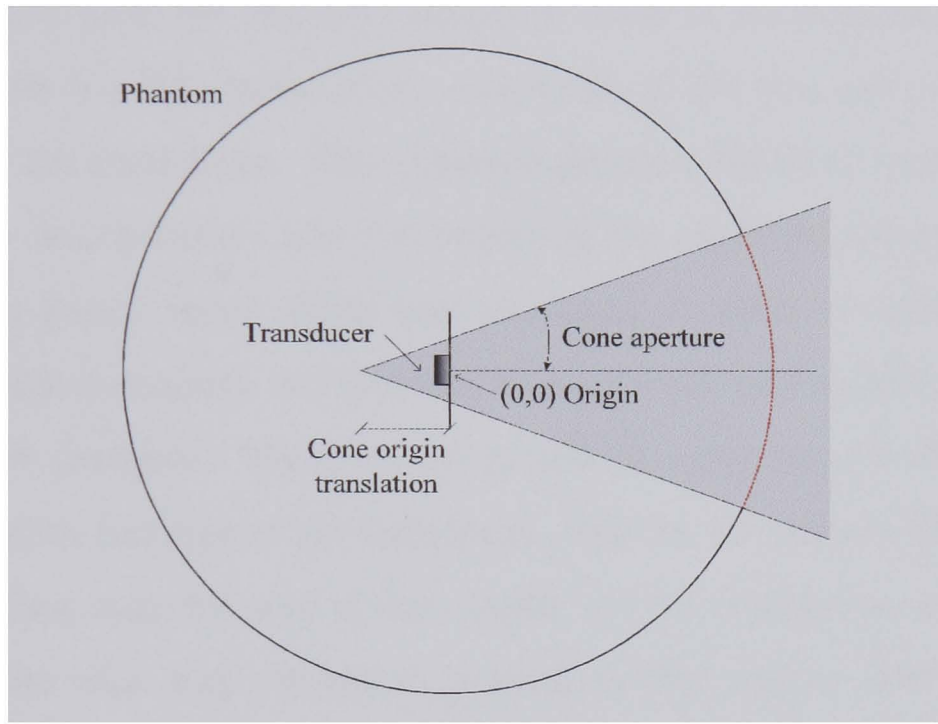


**Figure 4.12** Scatterer reduction function. The grey area represents the optimization cone used to select the scatterers from the phantom to be used for subsequent field calculations. The original phantom before optimization is represented by the entire circle. The reduced phantom (after applying the optimization algorithm) is represented by the red arc (dotted line).

## *4.8. Validation*

In order to validate the developed algorithms for ultrasonic-based pipe profiling, simulations and comparative experiments were conducted. Three experiments were carried out. Firstly, in an attempt to determine the lateral beam width of the employed system, a 0.5 mm copper wire immersed in clear water was scanned by using the experimental platform described in chapter 3. The corresponding results of real experiments and simulation were quantitatively compared to validate the accuracy of the simulations through a lateral beam width measurement. Furthermore, two experiments using Polyvinyl Chloride (PVC-U)

pipes, like those used for sewers, with precisely carved defects were carried out. In all cases, experiments and numerical simulations were conducted and results compared.

### 4.8.1. Lateral beam width measurement

The main objective of this study was to measure the radiation pattern of the transducer and compare it with the predicted one obtained from simulations. The basic parameter to characterize the radiation pattern of a given transducer is the beam width, which is defined as the angular distance between the points in the radiation pattern were the intensity drops to -3 dB of its maximum value. The radiation pattern is a 3D characteristic, symmetric to the axis and perpendicular to the surface of the transducer. The radiation pattern originates from the centre of the transducer and describes how the energy of the emitted field radiates into the medium. The lateral beam width was measured in water by rotating the sonar head and recording position and intensity of the echoes generated by a thin copper wire of 0.5 mm diameter. The wire was located at a distance of 440 mm and was aligned parallel to the face of the transducer. For the simulation, the centre of the transducer's face was located at the origin of the coordinate system and the phantom of the wire was positioned parallel to the $y$-axis. The phantom was created with a mesh size of 0.1 mm and composed of 240 scatterers. The $z$-axis was the reference axis for the rotation of the sensor; for instance, the zero degree position of the transducer lies on the positive $z$-axis, Figure 4.13. The sensor was rotated around the $y$-axis, from -10 to 10 degrees about its centre using a step resolution of 0.225 degrees.

In order to facilitate the comparison of the experimental and simulated results, the simulated results were down-sampled to match the sampling frequency of the used sonar system. The simulator tool generates sampled data at a frequency of 100 MHz, while the sonar system samples at a maximum rate of 162.5 kHz. The excess samples acquired at 100 MHz lying between two 162.5 kHz samples were averaged.

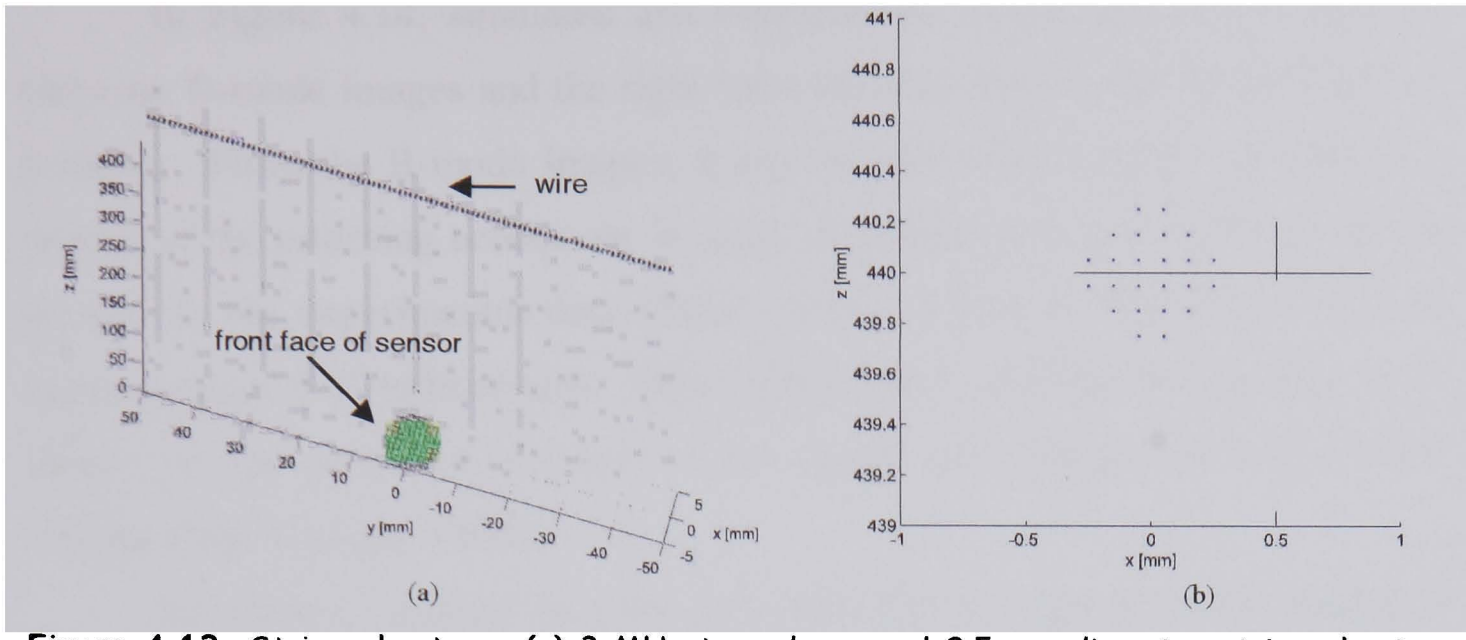


**Figure 4.13** String phantom. (a) 3 MHz transducer and 0.5 mm diameter string phantom (b) magnified view of the phantom in the x-z plane.

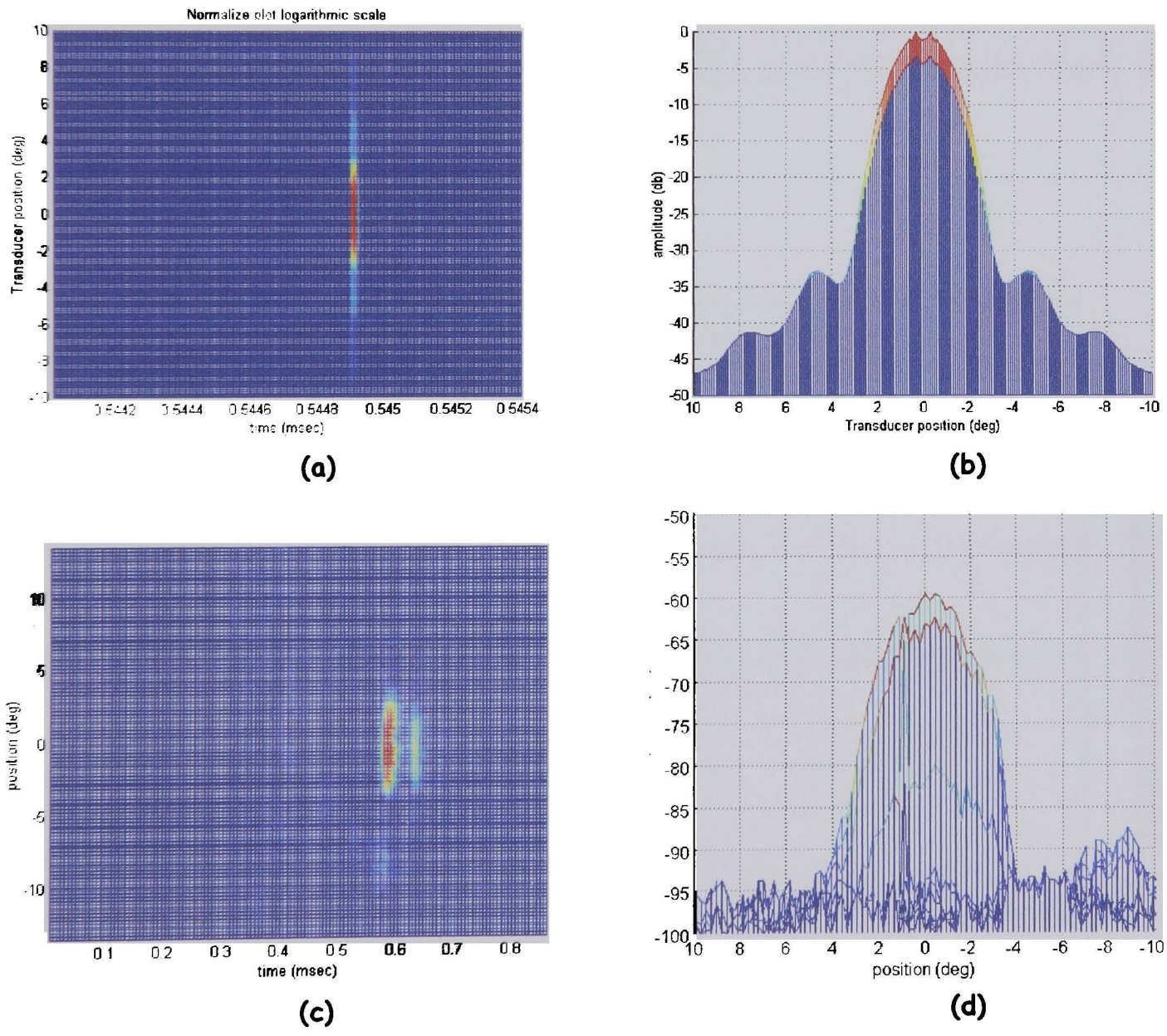


**Figure 4.14** Beamwidth experiments comparison. 3-D mesh plot, received echoes from 0.5 mm copper wire. Simulated data: (a) axial-lateral plane view; (b) lateral view. Experimental data: (c) axial-lateral plane view ; (d) lateral view

In Figure 4.14, simulated and experimental signals are shown; the left plots are B-mode images and the right ones are plots of intensity against angular position. From the B-mode images, it can be seen that the shape and intensity profile of the returning echoes are in good agreement with just slight deviations present in the experimental data (Figure 4.14c), where a shadow is visible at approximately 0.65 milliseconds. This artefact can be attributed to the ring-down effect, i.e. the period of vibration of the crystal after being struck by a short voltage pulse [Gustav, 1998].

By closely studying the pulse generated by the employed sonar system, it was found that even though the electrical pulse which excites the transducer perfectly resembles a square pulse, the emitted pressure pulse shows a main peak which concentrates most of the energy inside it, then decreases monotically and is sometimes accompanied by a tail-peak (ring-down). The duration of the ring-down is about 5 times the duration of the emitted pulse (10 microseconds), see Figure, 4.15.

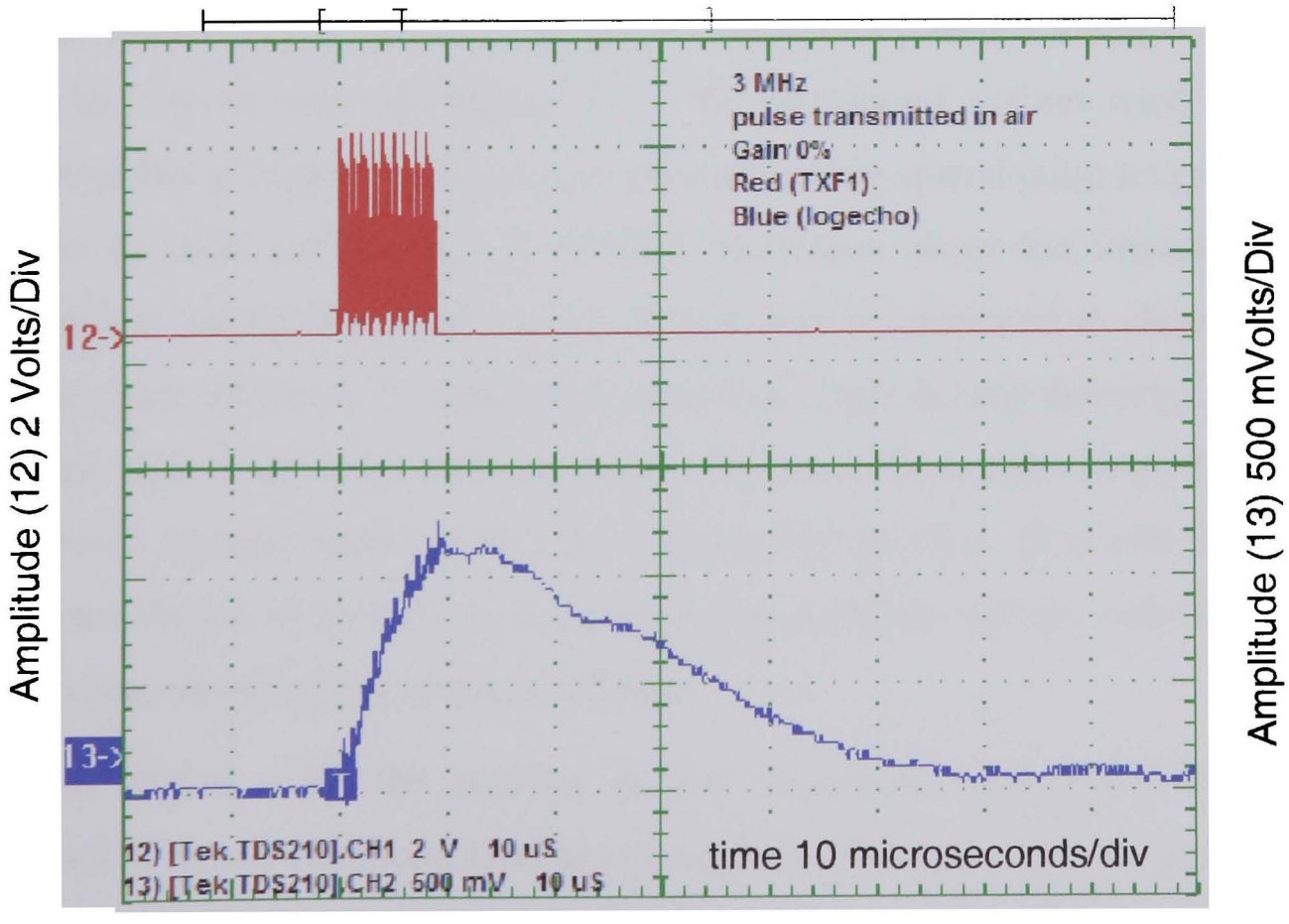


**Figure 4.15** Ring down characteristic of the SeaKing system used for the experiments. Top waveform, electric excitation pulse. Bottom waveform, emitted pulse

In ultrasound imaging there is a factor which describes the "quality" of the sound emanating from an ultrasound transducer after being struck by a short voltage pulse, usually named the $Q$ factor [Gustav, 1998]. The $Q$ factor depends on the bandwidth of the transducer and is defined as:

$$Q = \frac{f_0}{f_1 - f_2}, \tag{4.53}$$

where $f_0$ is the resonant frequency, $f_2$ is the frequency above resonant where the intensity reduces by 3 dB and $f_1$ is the frequency below resonant where the intensity reduces by 3 dB. The $Q$ factor refers to two characteristics of the transducer: the purity of the sound (bandwidth) and the persistence (ring down time). It should be noted that bandwidth and pulse duration are related. The beginning and end of an ultrasound pulse introduce a range of frequencies; the shorter the pulse, the wider its frequency spectrum. A "high Q" transducer will respond to a short voltage pulse with a relatively long lasting vibration, emitting ultrasound with a narrow bandwidth (nearly "pure" sound). A "low Q" transducer, on the other hand, will vibrate for only a short time period, emitting a short pulse of ultrasound consisting of a broad range of frequencies [Gustav, 1998].

As can be seen in Figure 4.15, the ultrasound system used for the experiment has a “high Q” and as a consequence a long spatial pulse length which degrades its axial resolution. A detailed discussion about the impact of the bandwidth in the resolution of a sonar system will be presented in chapter five. The ring down effect can be reduced by attaching a high density damping material to the rear side of the transducer to extract and absorb ultrasonic energy from the piezoelectric element once the excitation signal has finished. It should be noted that the simulation of the backing material and its coupling with the transducer has not been considered in this research project.

In Figure 4.16, the profiles of the simulated (continuous line) and experimental beams (diamond line) are presented. As can be seen, only the main lobe of the profiles can be compared because the background noise of the experimental platform is around -30 dB. As a consequence, the echoes caused by the side lobe radiation cannot be seen.

In table 4.1, the measured beam widths for the experimental and simulated cases are shown. The difference between them is calculated using the experimental data as reference. Even though the numerical results show an average difference of 26% between the simulated and the experimental beam width, the graphical results show a reasonable and consistent match between the radiation patterns in both cases.

**Table 4.1** Beam width table, experimental and simulated measurements

| BEAM WIDTH (dB) | EXPERIMENTAL (degrees) | SIMULATED (degrees) | DIFFERENCE (%) |
|---|---|---|---|
| -3 | 2.66 | 2.2 | 28 |
| -6 | 2.17 | 1.42 | 30 |
| -9 | 2.52 | 1.75 | 26 |
| -12 | 3.00 | 2.02 | 26 |
| -24 | 3.71 | 2.79 | 22 |

As shown in Figure 4.16, the simulated radiation pattern tends to be slightly narrower than the experimental one. The difference between the experimental and simulated results is likely to be caused by refraction artefacts occurring at the interface between the transformer oil, the rubber cap and the water which was not considered by the simulation. This will be elaborated next.

If an acoustic wave travelling in one medium traverses a boundary to another medium with a different characteristic acoustic impedance, the original wave can be reflected, transmitted (refracted) or both. The amount of reflected and transmitted energy depends on: the characteristic acoustic impedance of each medium and the impingent angle. Depending on the impingent angle, the transmission of an ultrasonic wave from one fluid to another can be normal or oblique. In the case of a normal incident wave arriving at a boundary between two media, the amplitude of the transmitted wave will be smaller than the amplitude of the incident wave but the beam shape will not be modified. On the other hand, if an oblique incident beam with a given cross-sectional area arrives at a boundary, the cross-sectional area of the transmitted beam will be different from

the incident beam [Kinsler, 2000]. Refraction takes place due to the different velocities of the acoustic waves within the two media. In the case of oblique incidence, the transmitted wave front will diverge or converge depending on the relationship between the speed of sound of both media.

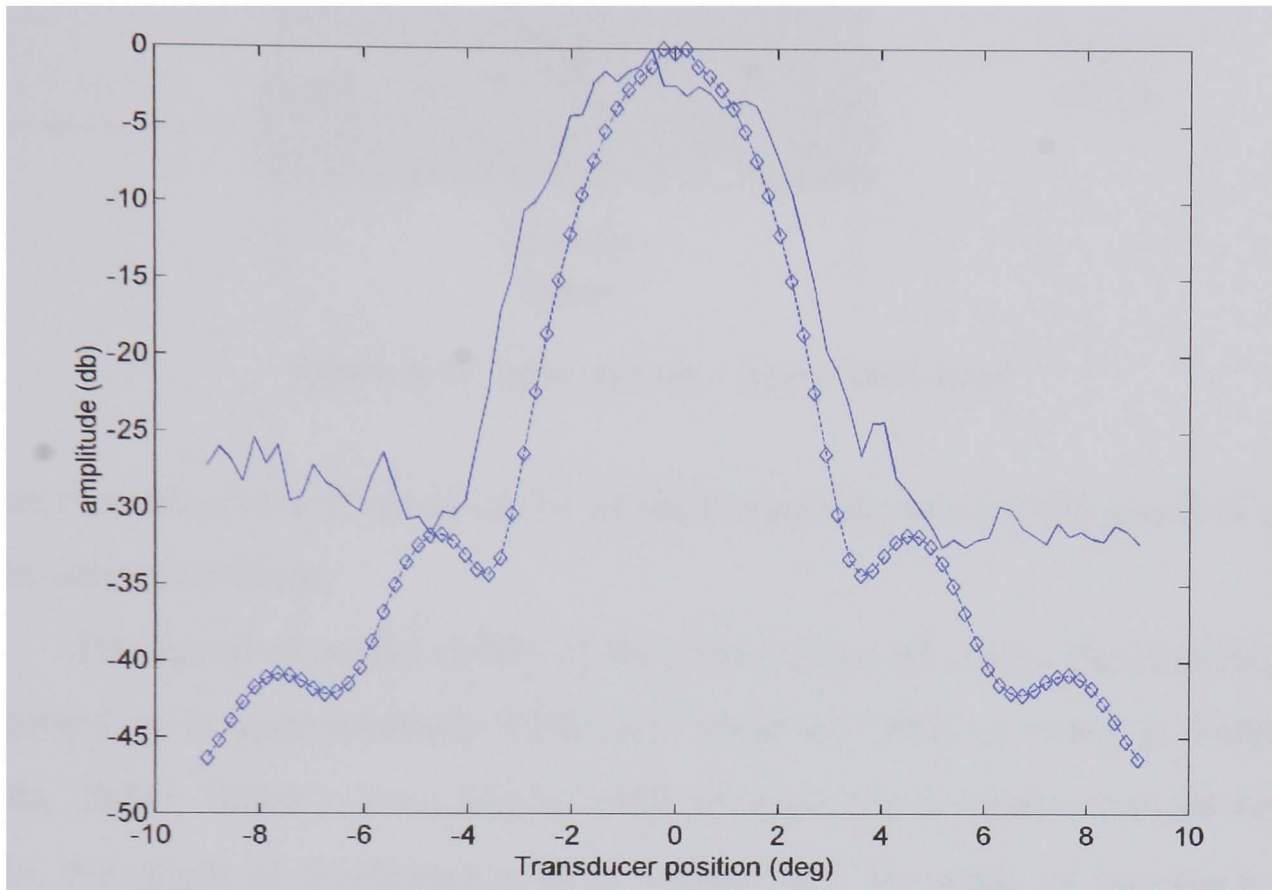


**Figure 4.16** Beam widths comparison: Experimental data (continuous line), simulated data (diamond line).

Since the thickness of the rubber cap of the used sensor system is very small (less than 1 mm, see Figure 4.17) and its characteristic impedance is larger than the characteristic impedance of the two fluids involved (oil and water), it can be assumed that the effect of the rubber cap in modifying the cross-sectional area of the incident wave is negligible. However, since the transformer oil and the water have different acoustic properties, the refracted beam is modified.

The angle of refraction depends on the impingent angle of the beam when it enters the new medium. As the angle of the incident wave gets smaller, the angle of refraction gets closer to the boundary. When the incident angle reaches a certain point, called the critical angle, the refraction is parallel to the boundary between the media. The critical angle is defined as:

$$\theta_C = \sin^{-1}\left(\frac{c_1}{c_2}\right), \tag{4.54}$$

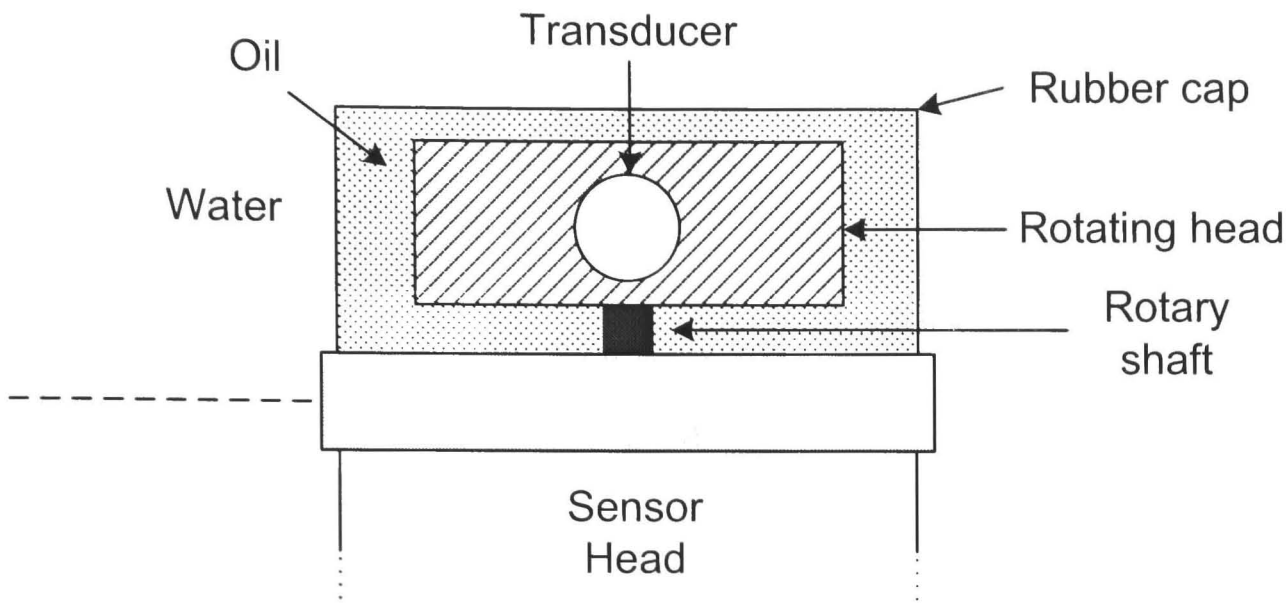


**Figure 4.17** Sonar system - Sensor head detail

where $c_1$ is the speed of sound of the incident medium and $c_2$ is the speed of sound in the second medium.

The speed of sound (SOS) of the transformer oil where the transducer is immersed in is approximately 1390 m/s while the SOS in water is 1480 m/s [Onda, 2004]. Since $c_1 < c_2$, and the angle of incidence is smaller than the critical angle, the angle of transmission $\theta_t$ is greater than the angle of incidence. To determine the refraction angle, Snell's law is used:

$$\frac{\sin\theta_i}{c_1} = \frac{\sin\theta_t}{c_2}, \tag{4.55}$$

where: $\theta_i$ is the incident angle, $\theta_t$ is the transmitted angle, $c_1$ is the speed of sound in the medium where the incident wave is travelling and $c_2$ is the speed of sound in the second medium.

In order for refraction to take place, the beam incidence has to be oblique. It should be noted that the rubber boot protecting the transducer has a cylindrical shape. The incidence angle will be the angle formed between the longitudinal axis of the beam and the tangent line at the point of contact between the beam and the rubber boot. Provided the boot was a perfect cylinder and the sound source was a point, the incidence angle will be normal and therefore the emitted beam will propagate from one medium to the other without distortion.

However, the used transducer is not a point source but its front face is a circular surface with a 10 mm diameter; it is not rotating exactly at the centre of

the cylinder and the rubber boot is not a perfect cylinder. Considering, these factors, it is unlikely to have a perfect normal incidence angle. Small incident angles are to be expected for the real sonar.

The divergence of the emitted field can be estimated by using equation 4.55. It is assumed that the beam is emitted into the transformer oil and traverse through the protective boot into the water. For this analysis, the divergence effect, caused by the protective boot, are ignored. It was found that for incident angles greater than zero and below twenty degrees; the transmitted wave will diverge by around 7%. This deviation is in agreement with the difference registered from the comparison of experimental and simulated results. However, it just accounts for a fraction of the total difference registered. It is noted that the speed of sound in the transformer oil was taken from a table of acoustic properties [Onda, 2004], choosing a generic transformer oil. No information was available from the oil or sensor manufacturers. A more quantitative study was not possible in the given lab environment.

### 4.8.2. Ultrasonic scanning of Square Defect

Experimental and simulation studies concerning a Polyvinyl Chloride (PVC-U) pipe with a precisely carved square defect were conducted. The plastic pipe had a nominal diameter of 300 mm and a measured inside diameter of 296 mm. The carved defect investigated was a carefully cut square hole. The hole dimensions were 10 x 10 mm, Figure 4.18. The hole was centred over the $x$-axis and extended along the $y$-axis from 70 to 80 mm. The hole and the surrounding area were scanned by displacing the transducer along the longitudinal axis of the pipe ($y$-axis) for a distance of 42 mm at 3 mm intervals, sweeping from -10.0 to 10.0 degrees at 1 degree intervals. The resulting scan area is a rectangular surface of approximately 63 by 42 mm. The scanning process generated fourteen B-mode images, representing tomographic slices of the pipe.

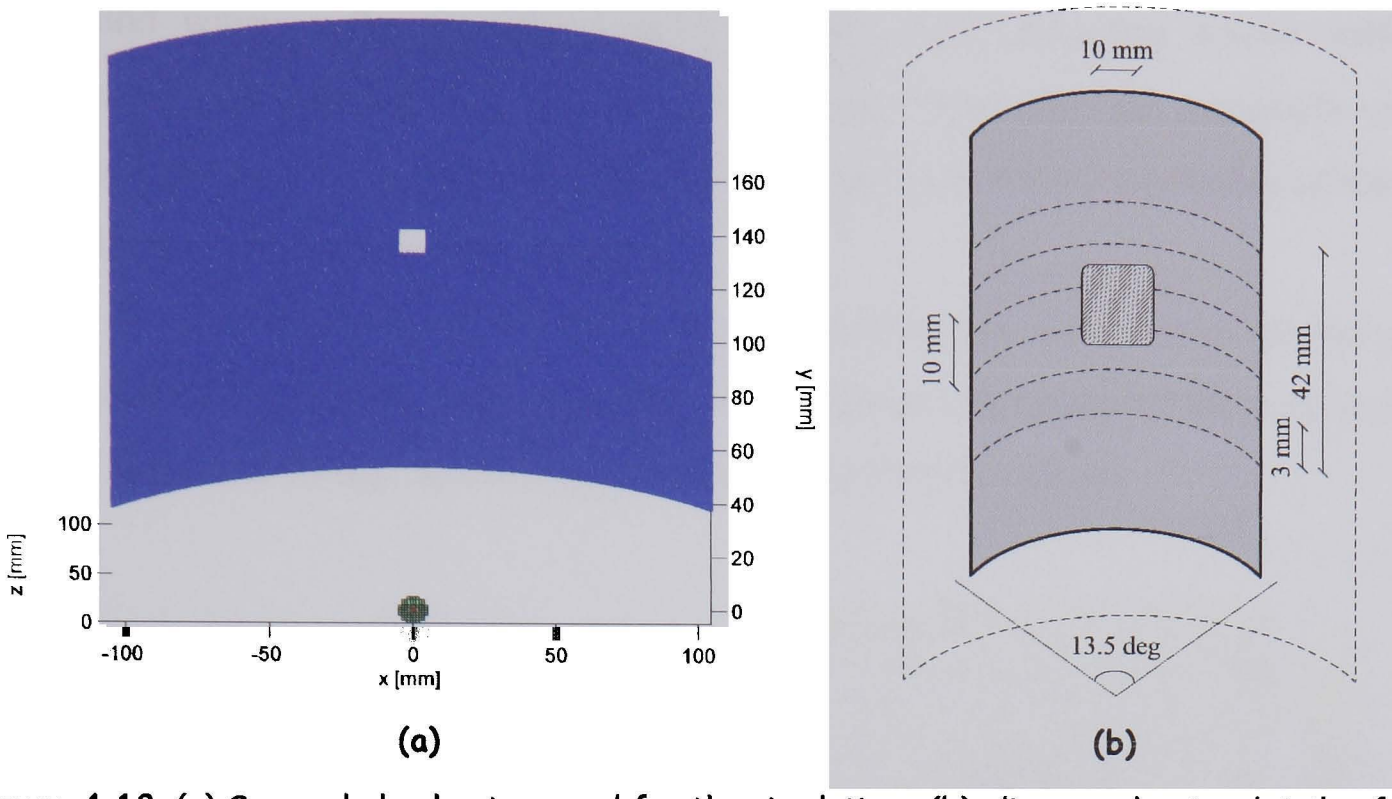


**Figure 4.18** (a) Square hole phantom used for the simulation. (b), diagram showing details of the scanned pipe section used for experimental tests.

To compare the experimental data and the simulation results, an appropriate visualization methodology is employed. From the set of consecutive B-mode images acquired during the scanning process, a three-dimensional image representing the inner surface of the pipe is created. The profile is created by measuring the time of flight of the ultrasonic pulse and registering the maximum intensity of the received echo. As a consequence, four variables are obtained: $x$, $y$ and $z$ indicating the position of the reflector (scatterer) that generated the echo and, in addition, the echo intensity. A useful way to represent these profiles is through the use of three-dimensional colour plots that will be referred to as surface-intensity plots, showing the inner surface of the pipe and the received intensity. This visualization technique was created specifically for this purpose [Gomez, 2004] and its functionality and capabilities will be explained in detail in Chapter 5.

In Figure 4.19, surface-intensity plots for simulated and experimental data are presented. For the simulated case presented in Figure 4.19a, the removed section can be easily identified as the area where the intensity decreases until reaching a minimum (dark area). Even though, the hole is a perfect square, the resulting image is not a square. It is noted that the corners of the square in the scanned image are rounded. This is due to wave interaction occurring when the

ultrasound waves reflects at the corners. When two interacting waves with different origins interact, they superimpose on each other, and the amplitude of the sound pressure at any point of interaction is the sum of the amplitudes of the two individual waves (see also chapter 5).

A closer analysis of the acquired image shows that the contrast between the intensity from echoes returned by the intact wall and the centre of the removed section is around 14 dB, decreasing smoothly from 0 dB to -14 dB.

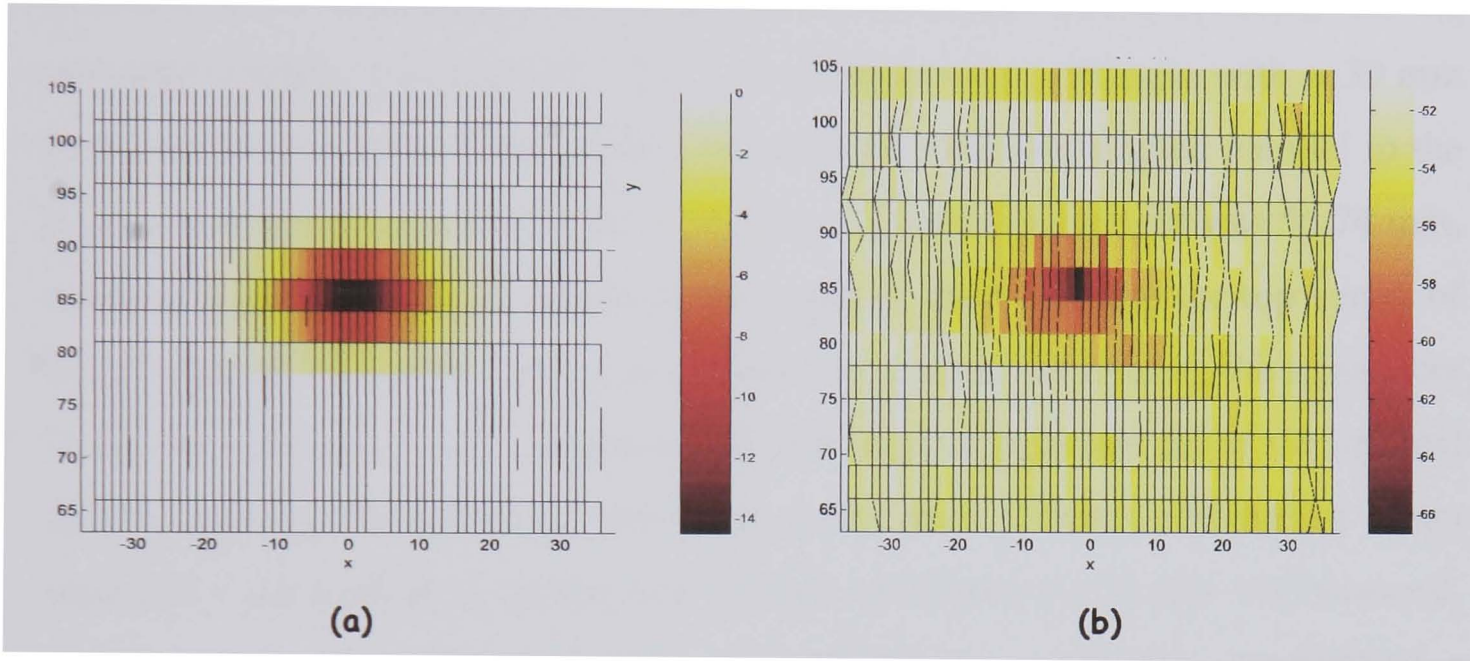


**Figure 4.19** Surface-intensity plots for square defect (a) simulation (b) experiment

In Figure 4.19b, the corresponding experimental result is presented. The experimentally acquired signals are notoriously noisier than the simulated signals, as expected for experimental data. In the presented case, the defect is easily recognizable in the surface-intensity plot as the area where the intensities of the returning echoes decrease until reaching a minimum in agreement with the simulated case. Comparing the echo intensities returning from the surface of the pipe wall and the centre of the hole, a contrast of 14 dB can be appreciated showing very good agreement with the simulation.

It is noted that, the defect size present in the experimental data is smaller than the one visible in the simulated one. This can be attributed to the difference in the beam width size between the sonar system and the simulator as was explained in the previous section. A wider beam width results in a poorer resolution which can be seen in the smaller dark area in the surface-intensity plot presented in Figure 4.19b. The deformations appreciated in the plot can be

attributed to the differences between the lateral resolution of the stepper motor and the longitudinal resolution of the SCARA robot. From the results of this study case, it can be concluded that the simulation tool is representing the physical phenomenon in an accurate and acceptable way.

### 4.8.3. Scanning a Triangle Defect

For this part of the project, a PVC-U pipe with a nominal diameter of 300 mm and a measured inside diameter of 296 mm with a precisely carved isosceles triangle was studied. The carved shape was a triangle with a 39 mm base and 60 mm sides, Figure 4.20. The triangle base was aligned parallel to the *x*-axis, extending from -19.5 mm to 19.5 mm. The triangle height was 56.74 mm, the base was located at 20 mm from the origin of the *y*-axis and the top vertex of the triangle at 76.74 mm. The pipe section was scanned by rotating the transducer from -11.7 degrees to 11.7 degrees at 0.225 degrees intervals (B-mode images) and by moving the transducer along the *y*-axis from 10 mm to 88 mm at 3 mm intervals. As a result, a rectangular surface of 60 mm by 78 mm was scanned. The scanning process generated 27 B-mode images, each one representing a tomographic slice of the pipe.

The internal surface of the pipe was profiled using the set of acquired B-mode images by applying a time of flight (TOF) profiling algorithm. A TOF profiling algorithm detects the location of the first reflection inside the acquired RF lines using a pre-fixed threshold; this technique is discussed in detail in Chapter 5. For this particular case the threshold value was fixed at -10 dB. Results are presented in the form of surface-intensity plots, with dashed lines superimposed representing the removed section, Figure 4.21. In the presented surface-intensity plots, the white section in the centre of the triangle shows the segment of the pipe where the reflected echoes were very weak or no echoes were detected. It is noted that the sides of the triangle in both cases, were detected as stepped lines instead of straight lines. This artefact can be attributed to the interval size used when scanning the pipe along the *y-axis*. It can be seen as a quantization error and its presence does not affect the aim of the study.

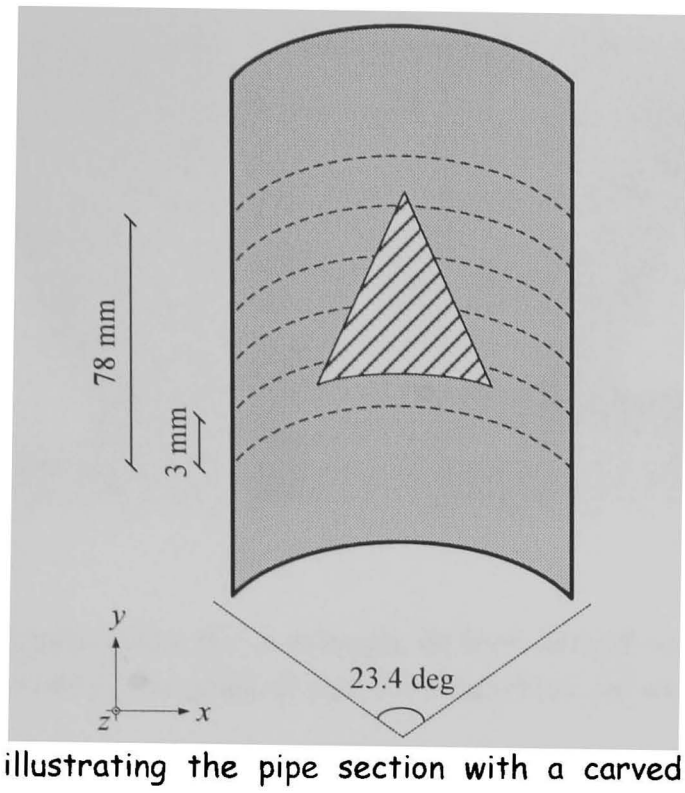


**Figure 4.20** Diagram illustrating the pipe section with a carved triangle used for the experiment.

As discussed in section 4.8.1, the beam width of the experimental transducer is larger than the simulated one, as a consequence, its resolution is lower. The size of the area where echoes are not reflecting (white area) in the experimental case (Figure 4.21b) is smaller than in the simulated case (Figure 4.21a). The impact of resolution on the surface-intensity plots is elaborated on chapter 5.

During experiments, it was observed that the off-centre location of the transducer inside the pipe is a key parameter that affects the quality of the resulting images. In this particular experiment, the transducer was slightly misaligned towards the positive $x$ direction. As a result, the plot, in Figure 4.21b, shows a slight asymmetry when representing the triangular hole. The misalignment results in a grey scale transition along the boundary on the left side (12 mm) which is wider tan the one on the right side (9 mm). Another indication of the off-centre condition of the scanner are the tenuous shadows present at the top-right quadrant of the plot.

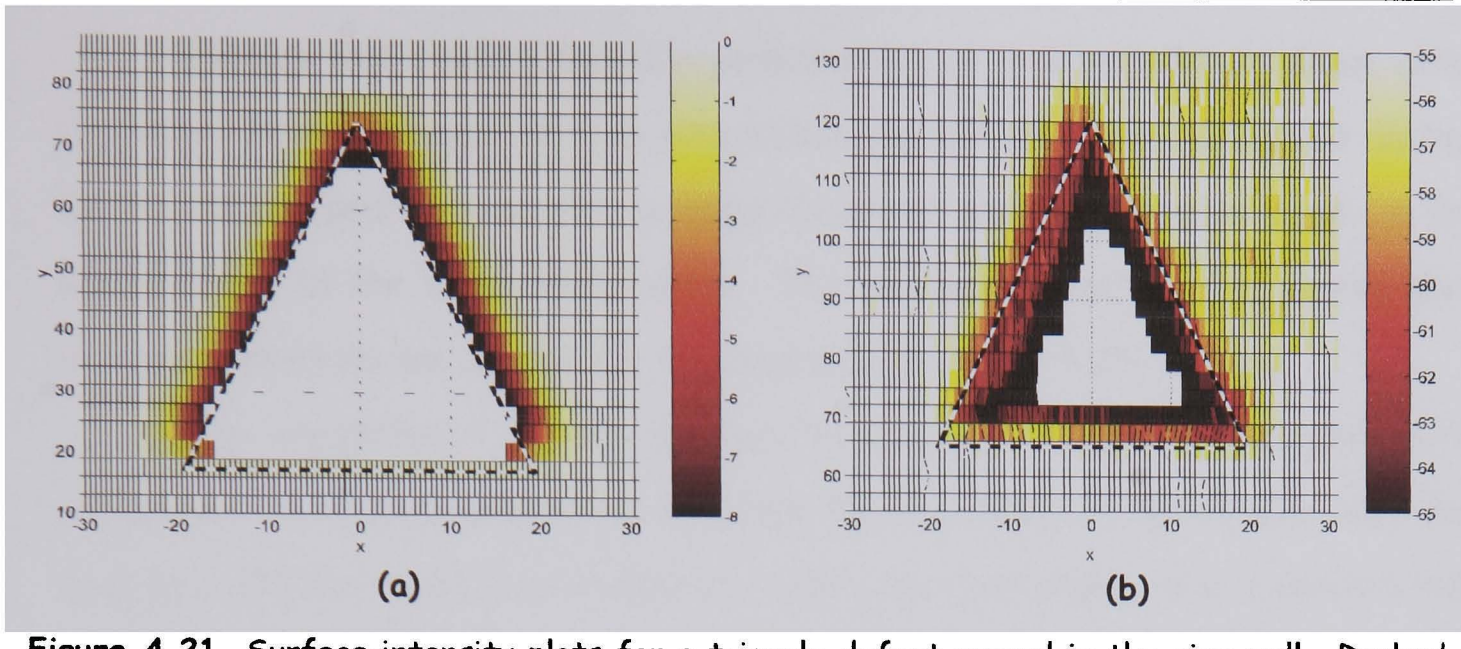


**Figure 4.21** Surface-intensity plots for a triangle defect carved in the pipe wall. Dashed lines show the removed section in the original pipe (a) simulation, (b) experiment

From the visual analysis and comparison of results from simulations and experiments, it can be said that the simulation environment can be used to create simulated images of defective pipes immersed in liquids.

## 4.9. Summary

In this chapter, an environment for the simulation of the ultrasonic inspection of water filled pipes has been presented. The simulation environment was developed as an extension of the Filed II routines that have been amply used for the simulation of medical imaging.

The developed simulator is oriented towards the generation of simulated data from rotating ultrasonic sonars scanning the inner wall of pipe sections filled with liquid. It allows the creation of simulated two dimensional (B-mode) and three dimensional images of the inspected objects.

Three study cases have been presented in order to validate the capabilities of the developed simulation environment through the comparison of simulated data with real data. The first case compared the radiation pattern of a real transducer with a simulated one. The second and third cases compared results from scanning two pipe sections with defects such as a square hole and triangular hole. Numerical comparisons (beam width and contrast intensity) and visual inspection of inner pipe profiles were used to determine the suitability of the developed environment for the desired aim. Results have shown a good agreement between experimental and simulated data.

Factors that could affect the performance of real transducers from ideal ones have been analysed. It was concluded that the deviations observed during the validation process are due to simplifications and assumptions used in the development of the ultrasound model. The conducted analysis has shown that such deviations do not impede the developed simulator to fulfil its goal.

The presented work can be used to conduct in-depth investigations of ultrasonic based pipe inspection systems, by providing an invaluable tool for studying ultrasound wave propagation in fully charged pipes. It is expected that the present research will facilitate the design of future pipe inspection systems by allowing the execution of sensitivity analysis before attempting time-consuming measurements in a real-world scenario. In addition, the system can be used to generate artificial data that can be used for training purposes.

# Chapter 5

## ENHANCED VISUALISATION OF ULTRASOUND IMAGES

*This chapter presents a visualisation technique which creates three-dimensional profiles integrated with intensity information from the scanning process. The proposed methodology allows the visualization of defects smaller than the sensor resolution when using single unfocussed circular transducers. A discussion about the factors which determine the resolution of transducers used in ultrasonic imaging, the description of the proposed methodology, an experimental study based on simulations an experiments exploring the capabilities of the methodology are presented.*

## 5.1 Introduction

In the near future, it is expected that sewers can be inspected by autonomous mobile inspection systems carrying a multitude of sensors including small sonars. These systems will travel through the sewage network during normal sewer operation providing a "complete" view of the inspected pipe segment.

Scanning beam sonars are made of a single element. Such sonar systems have the advantage of being small and employing only simple processing electronics. However, their resolution is range dependent due to the beam divergence, unless lens or concave shaped transducers are used for focussing the beam at a given range. The use of focussed beams has the disadvantage that different transducers will have to be used for inspecting pipes with different sizes. Another option for improving resolution is to use sonars made of arrays with multiple elements. These have the advantage of electronic beam forming which allows dynamic focussing which greatly improves the resolution of the sonar at different ranges, but in contrast, they require complicated electronics and enormous computational power. As a result, the use of un-focussed scanning beam sonars will allow the construction of small-scale inspection systems with small transducers and miniaturized (on-board) electronics circuits.

While camera-based systems are usually limited to the inspection of the dry parts of a pipe, this research aims to use scanning beam sonars to create detailed images which can be used for the detection of defects located in the inner sections of pipes filled with liquid.

The standard approach for pipe profiling, consist of creating three-dimensional pipe wall representations namely surface profiles, by measuring the time that it takes for the echo created at the pipe wall to arrive at the transducer (time of flight). Time of flight images are acquired and converted to depth profile images using equation 5.1, which allows the calculation of the distance knowing the velocity of the sound in the medium [Roth, 1999]. Pipe profiles can also be extracted from sets of consecutive B-mode images employing gating and thresholding techniques. Once the echo is detected, the time of flight (TOF) is

recorded and together with the sensor location information (axial and radial position) a three-dimensional profile of the inner pipe surface can be constructed. Even though, a 3D profile of the inner pipe wall is a powerful tool for the inspection of the inner section of pipes, providing information on structural damage, blockages, sediment, large cracks, and the location of incoming lateral lines, it has the disadvantage that defects with sizes smaller than the sensor resolution are missed. In this chapter, a visualization technique which allows the detection of defects that can not be appreciated in pipe profiles which are smaller than the sensor resolution will be presented. The proposed approach was validated through lab experiments and simulations and its capabilities for the inspection of sewer pipes were determined

## 5.2 Background – Acoustic imaging

Acoustic imaging techniques are used in connection with visual inspection or analysis of all of the three phases of materials, i.e., solids, liquids and gases. Examples of applications of such techniques include industrial non-destructive evaluation in metals and liquids, medical ultrasound imaging, underwater imaging and echo ranging in the atmosphere. In the development of such techniques several classes of acoustic imaging systems have been constructed. Acoustic imaging devices perform two basic tasks: data acquisition and data display. Such systems display the gathered data in one, two or three dimensions.

Acoustic imaging systems can be grouped in two types: direct imaging systems such as acoustic cameras or pulse-echo devices and indirect reconstructed imaging devices such as acoustical holographic devices, synthetic aperture and computed tomographic systems.

The most important one-dimensional imaging technique which has been the cornerstone of many other acoustical imaging techniques is referred to as A-mode. In this technique, a piezoelectric transducer transmits a short burst of acoustic energy into a medium and then receives and displays the amplitudes of echoes as a function of time.

In the two-dimensional world, the most widely used technique is the B-mode imaging, where a transducer is mechanically or electronically steered

sweeping the area of interest. As the transducer is moved, an acoustical pulse is transmitted at each one of the swept locations and the intensities of the received echoes returning to the transducer are displayed as brightness levels proportional to the echo amplitude. The intensity levels are amplified using a time varying gain in order to compensate the attenuation experienced by the acoustic field as it travels through the medium. On the display, usually a computer monitor, the brightness levels are displayed with reference to echo range and transducer position or orientation providing cross-sectional images of the studied object.

Furthermore, there are three dimensional acoustic imaging systems. Devices in this class include C-mode pulse-echo scanners, acoustic three-dimensional scanning systems, transmission or reflection acoustic cameras and acoustic holographic imaging systems. In these devices a three-dimensional volume of the object is scanned by flooding it with acoustic emissions from different directions and moving the transducer or beam formed pulses. Data from the volume is processed and displayed in several different ways.

The most common of these systems is the C-mode where a single transducer or an array operates in the pulse-echo mode. The transducers are physically or electronically scanned through a rectangular raster format so that a three-dimensional volume of the object is interrogated by the ultrasonic beam, or the front surface of the transducer is fixed at a single point and the body of the transducer is moved in a spiral motion so that the transducer irradiates a conical three-dimensional volume in a spiral format. In each case only echo data from a pre-selected range is displayed as brightness levels proportional to echo amplitude, in an analogous way as B-mode information is presented. Due to the use of a fixed focus lens and an electronic range gate, a C-scanner presents two-dimensional data in an orthoscopic display in which the display coordinates are the $x$ and $y$ Cartesian coordinates of the targets at a fixed depth in the object.

### 5.2.1 Image Resolution Considerations – Limiting factors

B-mode images are created when a transducer transmits a short pulse of duration $\Delta t$ into a medium. The emitted ultrasonic beam has a width $\Delta\theta$, where most of the energy is concentrated, see Figure 5.1. After the pulse is transmitted,

the system waits a predetermined time, recording the amplitudes of the received echoes from obstacles located along the travelled path of the beam (RF Line), and transmits another pulse in another direction until a given area is swept. The scanning process for generating a B-mode image is carried out by displacing a transducer in straight line or rotating it. In both cases the linear or angular step size is constant.

The echoes received by the transducer are processed and filtered. After being filtered, the envelope is detected by using the Hilbert transform [Schlaikjer, 2003], the amplitude of the signal is measured and digitized. The amplitudes of the received signal are stored in a set of arrays (RF lines) that will later be used to create a two dimensional image. It should be noted that the dynamic range of acoustic signals is large due to losses of this kind of signals. Losses are a consequence of the geometric spreading (intensity decreases according to the square of the distance from the source). Hence, logarithmic scales are used to present the intensities in an appropriate way. Finally, a two dimensional image is created by plotting the values stored in the arrays as bright dots, using an appropriate coordinate system (Cartesian or Polar). The brightness of each dot is determined by the echo amplitude.

In order to inspect the inner wall of a pipe, an ultrasonic transducer is rotated about and linearly displaced along the longitudinal axis of the pipe. The area of interest is swept creating a set of B-Mode data files (one for each location along the longitudinal axis). Subsequently, the transducer is translated in the longitudinal direction (which is here the $y$-direction as defined in chapter 4) a fixed distance to the next position where a new scan is carried out creating another B-mode file. This procedure is repeated until the area to be inspected is completely covered, Figure 4.7. At the end of the scanning process, a set of files associated with every scanned position along the longitudinal axes is obtained. Each file contains a B-mode data set, in the form of a matrix containing the intensities of the received echoes for each one of the emitted pulses $\{ I_{ij} , i = 1,..., (\theta_{start} - \theta_{end})/\theta_{step}, j = 1,..., n \}$, where $I_{ij}$ is the intensity matrix, $i$ is the line corresponding to an emitted pulse at a given position, $\theta_{start}$ and $\theta_{end}$ are the starting and ending angular positions of the scanned area and $j$ is the number of samples

acquired on each line (the observation depth or range along the longitudinal axis of the beam), Figure 4.9.

For the creation of a three dimensional image of the inside pipe wall, the pipe profile is extracted from the set of B-mode images. To achieve this, the main reflection for each RF line is detected by means of thresholding techniques. A common method to detect the main echo is to compare the amplitude of the received signal with a user-defined threshold. Once the echo has been detected, the elapsed time since the transmission of the pulse until its return to the transducer is measured. The proper choosing of the threshold value is a vital parameter which affects the quality of the resulting profile [Roth, 1999]. The measured time is also known as time of flight (TOF) and it is used to determine the distance from the transducer to the pipe wall. The distance between transducer and the pipe wall is determined by measuring the time of flight of the detected echo and by multiplying it with the velocity of the sound in the medium,

$$d = \frac{t \cdot c}{2}, \tag{5.1}$$

where $t$ is the time of flight and $c$ is the velocity of the sound in the medium. It should be noted that the distance has to be halved because the time of flight is measuring the time that takes the pulse to travel from the transducer to the object and back.

The profiles resulting from the approach explained above allow 3D visualisation of the inner pipe surface. However, the capabilities of the mentioned profiling approach to detect small changes in the inner geometry of the pipe wall or detect small defects are limited by the resolution of the transducer.

The ability of an ultrasound imaging system to discern between two scatterers (reflecting objects in the path of the ultrasonic beam) lying close to each other, as well as differences in depths, is determined by the axial and lateral resolution, see Figure 5.1.

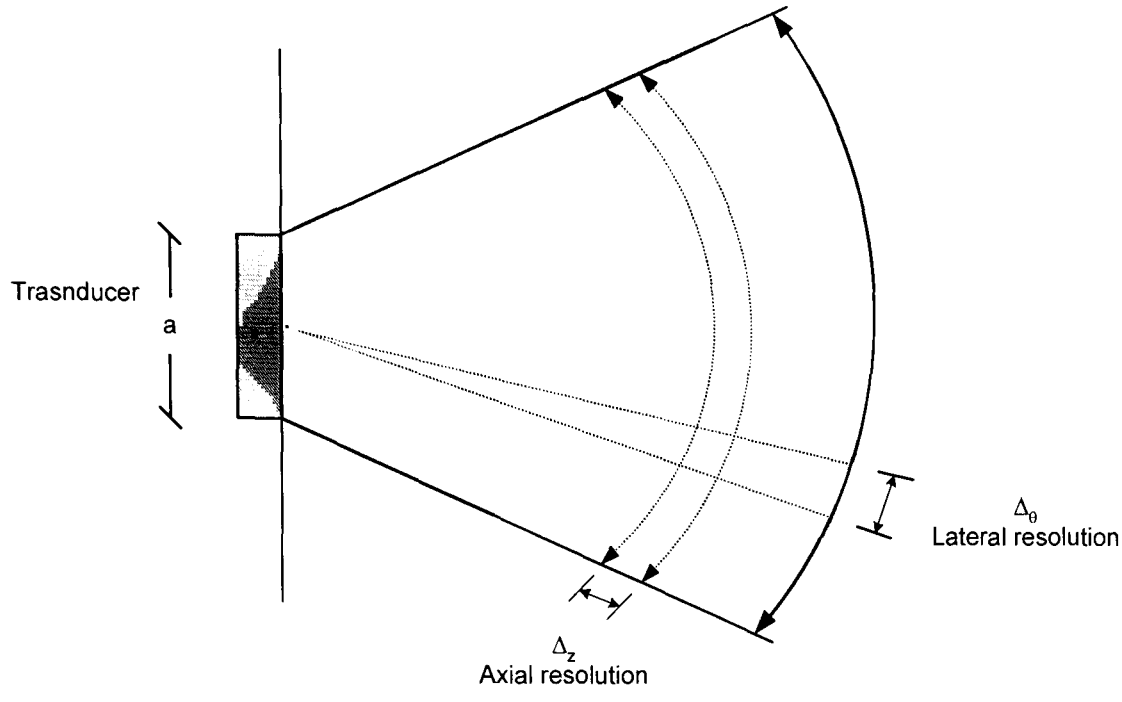


**Figure 5.1** Lateral and axial resolution parameters

The detectability of defects or other irregularities, in the 3D representation of the inner pipe wall, is mainly determined by the axial and lateral resolution, which mostly depend on two sensor parameters, bandwidth ($B$) and aperture size ($a$), respectively. The higher the resolution in the axial and lateral directions, the smaller the size of defects that can be distinguished.

#### 5.2.1.1 Axial resolution

The axial resolution is defined as the spatial resolution of ultrasound in the direction of the ultrasound beam, and is also known as the depth, linear, longitudinal or range resolution [Gustav, 1998]. The axial resolution is the minimum distance in the direction of the beam between two scatterers or reflectors which can be identified as separate echoes. The axial resolution is mainly determined by the bandwidth of an ultrasonic sensor and depends to a certain extend on the sensor's damping characteristics. The larger the bandwidth, the smaller are the variations ($\Delta z$) in the axial direction, that can be distinguished, Figure 5.1. Owing to their physical characteristics, ultrasonic transducers are only capable of generating and detecting frequencies within some limited range around the transducer's centre frequency, $f_c$.

The following excitation function represents an ultrasonic pulse centred on $t = 0$ with a carrier frequency $f_c$:

$$pulse(t) = \begin{cases} 0 & if |t| > \dfrac{\Delta t}{2} \\ \cos(2\pi f_c t) & \text{otherwise} \end{cases}. \tag{5.2}$$

Using Fourier analysis, the frequencies required to support such a pulse can be obtained and the corresponding bandwidth can be determined. The Fourier transform $P(f)$ of the pulse described in equation 5.2 is

$$P(f) = \int_{\Delta t/2}^{\Delta t/2} \text{pulse}(t)\, e^{-i2\pi f t} dt = \frac{\Delta t}{2} \text{sinc}[\pi(fc - f)\Delta t)] + \frac{\Delta t}{2} \text{sinc}[\pi(fc + f)\Delta t)], \tag{5.3}$$

where $f$ is frequency and $sinc(x) = sin(x)/x$.

From equation 5.3, it can be noted that most of the energy of the pulse can only be transmitted if the transducer has a bandwidth extending to the first zeros of the *sinc* function. The first zero occurs when the argument of the function is equal to $\pi$ and thus

$$\pi(fc - f)\Delta t = \pi \Rightarrow \frac{1}{\Delta t} = \Delta f, \tag{5.4}$$

and the bandwidth ($B$), is given by

$$B = 2\Delta f = \frac{2c}{\Delta z} = \frac{2}{\Delta t}. \tag{5.5}$$

Equation 5.5 shows the relationship between bandwidth and pulse duration. If the bandwidth is to be increased in order to improve the axial resolution then the duration of the pulse has to be reduced. However, the minimum duration of the pulse is limited by the transducer resonant frequency, which is equal to one period of the carrier frequency ($1/f_c$).

In addition, when a piezoelectric transducer is excited with a high energy electric pulse, the pressure field generated by the transducer does not have the same shape and duration that the excitation signal. Usually, the duration of the

pulse is longer because the transducer keeps vibrating after the electrical excitation pulse has been applied. This undesirable effect, known as ringing, depends on the material that the transducer is made of and the damping characteristics of the mounting material (backing material).

It has been found that the axial resolution is slightly greater than half the spatial pulse length, which is the number of waves in the transmitted ultrasound pulse multiplied by their wavelength [Gustav, 1998]. For a pulse duration $\Delta t$, the depth variation $\Delta z$ can be calculated as follows,

$$\Delta z = c \cdot \Delta t , \tag{5.6}$$

where $c$ is the velocity of the sound in the medium. For the particular case of pipe inspection where the inner pipe wall is profiled by measuring the time of flight of the echo, the minimum detectable change in the inner surface along the axial axis will be determined by the size of the pressure pulse and the time resolution (sampling rate) of the ultrasound sonar. Whichever is the longest will determine the resolution of the system.

#### 5.2.1.2 Lateral resolution

Lateral resolution is usually defined as the ability of a transducer to distinguish between two adjacent objects or reflectors. It refers to the ability to discern two separate objects perpendicular to the ultrasound beam direction. For a single element transducer, lateral resolution is mainly determined by the width of the ultrasound beam - the narrower the beam the better the lateral resolution, Figure 5.1. In the case of B-mode imaging, the resolution is also affected by the number of scan lines per image [Gustav, 1998].

Typically the face of the transducers is circular or rectangular in shape. The face of the transducer is the aperture through which the acoustic field passes in order to be measured. It can be a single element or divided into multiple elements. In pipe profiling, single transducers instead of arrays are used due to size and design constraints. Flat circular transducers are mostly used because they produce a conical beam, having as a result a circular illumination area which has similar characteristics in the lateral and elevation directions. In the following, the radiation of a plane circular piston is studied.

An aperture with radius $a$, mounted on a flat rigid baffle of infinite extent is emitting an acoustic field to a receiver located in front of it, Figure 5.2. The transducer oscillates at frequency $f_c$ and the receiver location is described by the vector $r$ and the angle $\theta$ between the vector and the $z$ axis. The ideal scenario for having high lateral resolution is to have a radiation pattern where most of the acoustic energy is concentrated around $\theta = 0$.

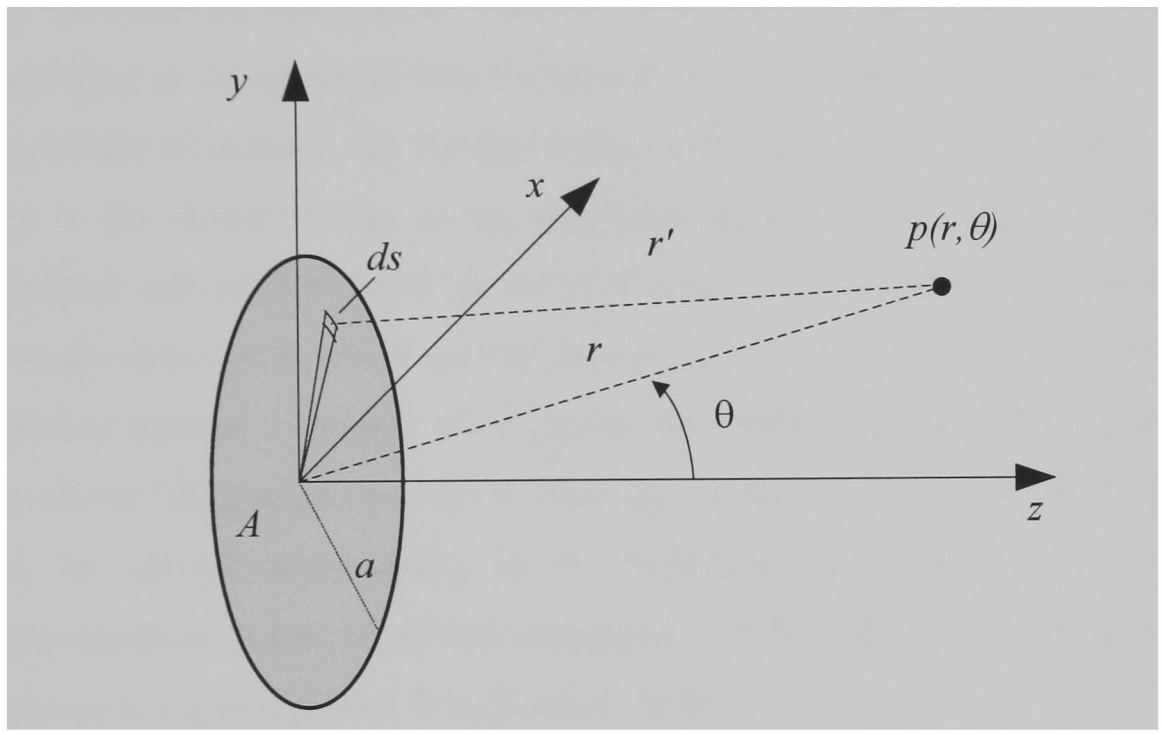


**Figure 5.2** Determination of the beam profile using an arbitrary point for an unfocussed circular piston transducer

For circular piston transducers, the beam pattern can be determined by assuming the radiating surface moves uniformly with speed $v_0$ and dividing the face of the transducer into infinitesimal elements, each one acting as a baffled simple source [Kinsler, 2000]. The differential pressure of the simple source is,

$$dp = \frac{j\omega\rho_0 c}{2\lambda r} e^{i(kr-\omega t)} dQ, \tag{5.7}$$

where $dQ$ is the differential strength of the infinitesimal elements ($dQ = v_0\, ds$), $\omega$ is the angular frequency ($2\pi f$), $k$ is the wave number, $\rho_0$ is the density of the medium, $c$ is the speed of sound in the medium and $r$ is the distance to the observation point. From Huygens' Principle, the total pressure field emitted by

the radiator can be obtained by integrating over the surface of the face of the radiator,

$$p(r,\theta,t) = j\rho_o c \frac{v_0}{\lambda} \int_S \frac{1}{r'} e^{j(wt-kr')} ds\,, \tag{5.8}$$

where $v_0$ is the amplitude velocity and $r'$ is the distance from the differential element to the observation point $r$, Figure 5.2. By solving the integral in equation 5.8, the radiated field can be studied. Two main regions can be distinguished depending on the distance from the transducer to the point of observation, near the face of the transducer, the Fresnel region and far from it, the Fraunhofer region. Due to the characteristics of the inspection process under study, the area to be inspected will be located in the far field region. In this region, the emitted field diverges spherically and it can be approximated as a point source with a given radiation pattern. In order to determine the radiation pattern for a single piston transducer, the integral shown in equation 5.8 has to be solved. This expression can be solved numerically, or if employing the Fraunhofer or far field approximation, it can be solved analytically. After solving the integral, the total pressure at a given point $r, \theta$ is [Kinsler, 2000]

$$p(r,\theta,t) = \frac{j}{2}\rho_0 c v_0 \frac{a}{r} ka \left[\frac{2J_1(ka\sin\theta)}{ka\sin\theta}\right] e^{j(wt-kr)}. \tag{5.9}$$

As can be seen in equation 5.9, all the angular dependence is in the bracketed term, and the expression can be written as

$$\left|p(r,\theta)\right| = p_0(r)D(\theta)\,, \tag{5.10}$$

where,

$$p_0 = \frac{1}{2}\rho_0 c v_0 (a/r)ka\,, \tag{5.11}$$

$$D(\theta) = \frac{2J_1(\xi)}{(\xi)}, \tag{5.12}$$

and

$$\xi = ak\sin\theta\,. \tag{5.13}$$

Equation 5.10 shows that the acoustic field is a spherical wave modified by the directivity function which represents the angular dependence, where $p_0$ is the pressure amplitude which reaches its maximum when the directivity function, $D(\theta)$, is equal to unity. This happens when angle theta $\theta$ equals zero.

As can be seen from equation 5.12, the far field of an ultrasound beam produced by a single piston transducer has a form similar to a Bessel function of the first kind, Figure 5.3. It can be assumed that most of the energy is concentrated inside the main lobe of the function which is limited by the first zero of the function which occurs at $\xi = 3.83$, Figure 5.3. The beam width is defined as the angle at which the intensity reduces by a half or -3 dB, and it can be obtained by finding the angle where the Bessel function is approximately equal to 1.62. Hence, the beam width can be calculated as follows,

$$\Delta\theta \approx 2\sin^{-1}\left(\frac{0.26c}{af}\right). \tag{5.14}$$

Equation 5.14 shows that the only way to reduce the beam width of a single piston transducer is by increasing its aperture size or its frequency. Usually, a large aperture or transducer diameter, results in a small angular resolution ($\Delta_\theta$).

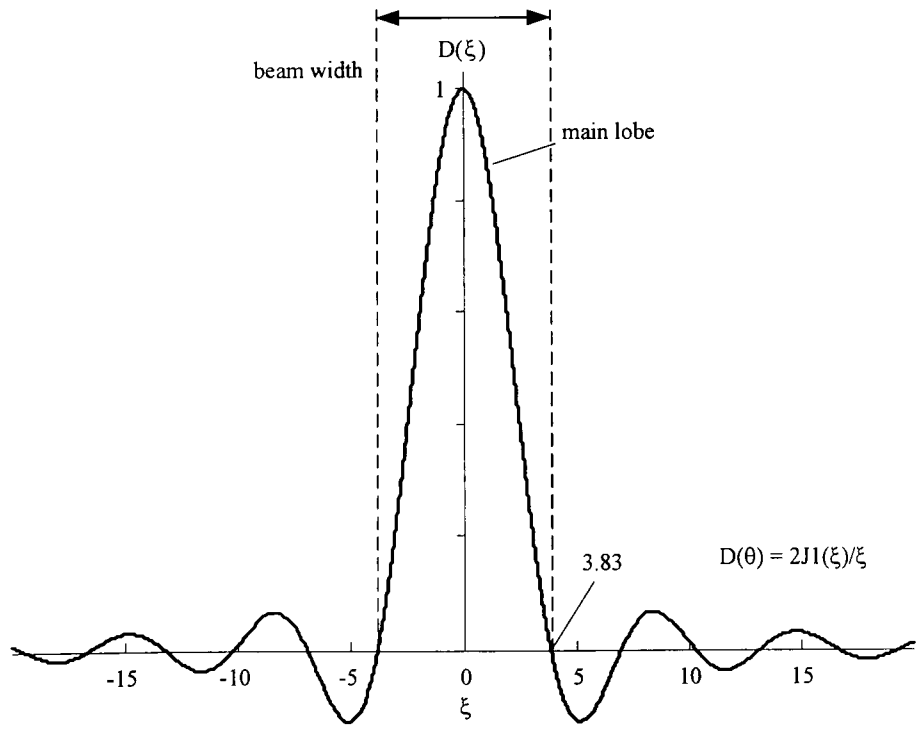


**Figure 5.3** Beam pattern for a single piston transducer

For a given angular resolution, the corresponding lateral resolution will be the length of the arc at the distance between the observation point and the transducer face (range). As a consequence, the lateral resolution is function of range,

$$\Delta x_\theta = r\Delta_\theta , \tag{5.15}$$

where $\Delta x_\theta$ is the lateral resolution at a given range, $\Delta_\theta$ is the angular resolution in radians and $r$ is the distance from the aperture to the object.

It is noted that many factors influence the pattern of the acoustic field, not all can be taken into account analytically. In order to gain a good understanding of the behaviour of a particular transducer, it is often necessary to resort to direct measurements and numerical simulations.

As discussed above, axial and lateral resolution are mainly determined by intrinsic characteristics of the transducer such as diameter, frequency and bandwidth. But in the case of the axial resolution, it should be noted that the time resolution of the system, i.e. the sampling frequency, is a key parameter which can degrade the physical resolution achievable by a transducer. The sonars available in the market at the moment which are being used for pipe profiling were originally designed for bathymetric applications. Such sonars were designed to be used in small sized, portable systems connected via an umbilical cable to a host computer. As a result, such systems have usually low speed data acquisition devices due to size and communication channel constraints. Here lies the importance of introducing post-processing and visualization techniques which can be used with existing equipment to enhance the detection of defects in the acquired data.

## *5.3 Methodology*

As presented in the introduction, this research aims to overcome the limitation of conventional profiling techniques, expanding the capabilities of sonar based pipe profilers to detect cracks and defects smaller than the sensor resolution. The research focuses on scanning relatively even pipe walls with ultrasonic transducers whose beam is kept at a constant distance and normal to the inspected surface. The beam profile of a transducer has a main lobe and side lobes, but usually the intensity of the side lobes is quite small due to the

directivity characteristics of the transducer, Figure 5.3. As a consequence, the reflections caused by side lobes are not usually detected in pulse-echo systems because they are covered by background noise. The proposed approach exploits the change of the target reflective characteristics due to the presence of an anomaly in the observed surface. Lets introduce the sonar equation:

$$SL + DI + TS - 2TL - NL = DT\,, \tag{5.16}$$

where the Source Level (SL) is a measure of the emitted acoustic intensity. This parameter assumes that the acoustic energy spreads omni-directionally outwards away from the source. However, most acoustic sources are designed to focus the acoustic energy into a narrower beam, represented here by the directivity index (DI). The Detection Threshold (DT) is a parameter defined by the system, in order to detect an echo; i.e. the observed signal has to be above the DT. The Transmission Loss (TL) is the reduction in the acoustic signal as it moves away from the source due to the combined effects of spreading and attenuation. The Noise Level (NL) represents an isotropic sound which is present in the media and the Target Strength (TS) represents the quality of the target (target reflective characteristics).

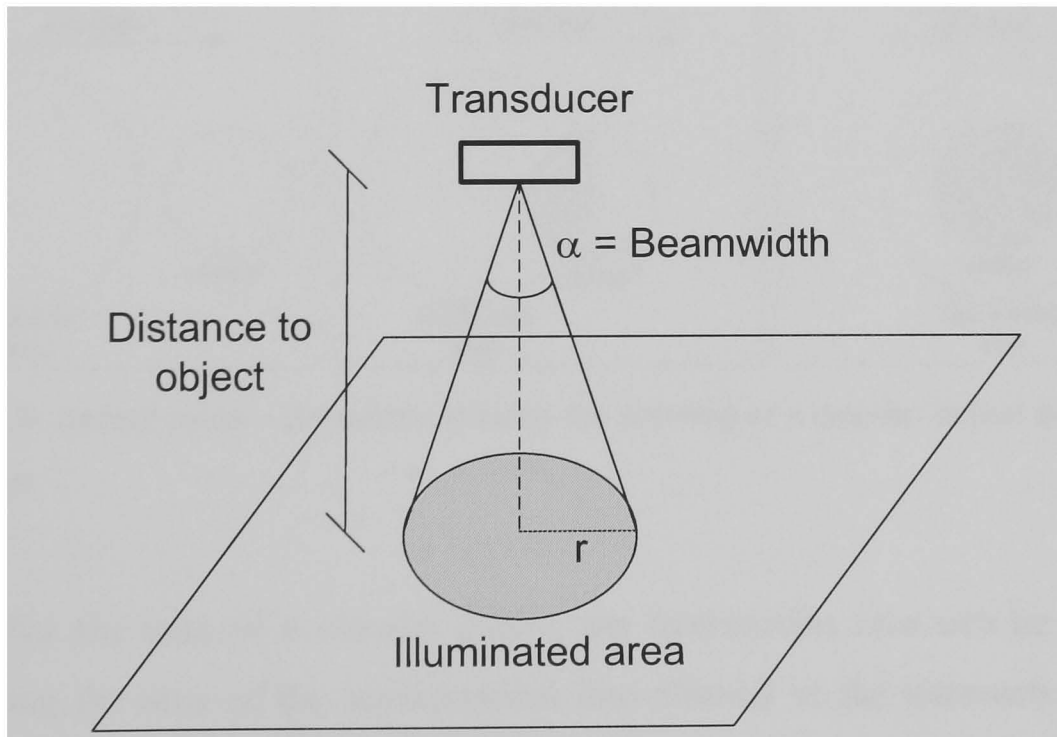


**Figure 5.4** Illuminated area of a transducer

The transducer of the ultrasound sonar system is not an isotropic source but an oriented source, irradiating in a given direction, as can be seen in Figure 5.4. For a circular transducer, the emitted field can be described as a cone. If a flat surface is irradiated, the projected field on the surface will be a circular area with radius $r$.

When a hole located in such a flat surface is scanned by a circular flat transducer, Figure 5.5, and the size of the defect is smaller than the illuminated area irradiated by the transducer and the surface have constant properties such as roughness, density and shape (typical inner wall characteristics of pipes and sewers), then the target strength (TS) is going to be fairly constant while scanning the area outside the defect. However, when the beam reaches the border of the defect, the TS inside the illuminated area is going to start decaying until reaching a minimum. The change in the TS is going to be a weighted average of the TS of the non-defective area ($TS_{NDA}$) and the TS of the defective area ($TS_{defect}$).

$$TS = TS_{NDA}(A_{IA} - A_{intersect}) - TS_{defect}A_{intersect}, \quad (5.17)$$

where $A_{IA}$ is the Illuminated area, and $A_{intersect}$ is the intersection of the circles.

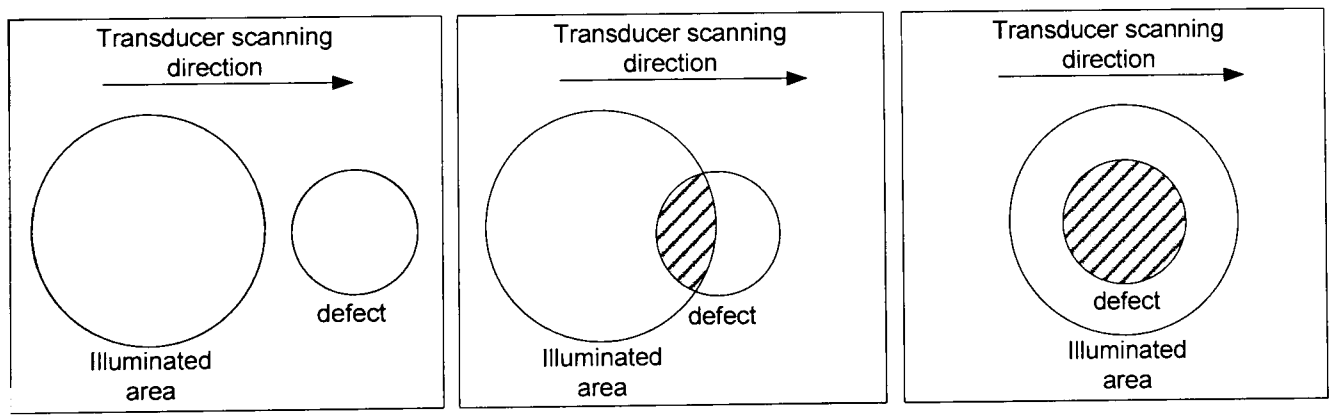


**Figure 5.5** Defect model - Schematic showing the scanning of a circular defect by a circular transducer.

For the case of a circular defect, the intersection area can be found by calculating the area of the asymmetrical lens formed at the intersection of two circles with different radii, see Figure 5.6.

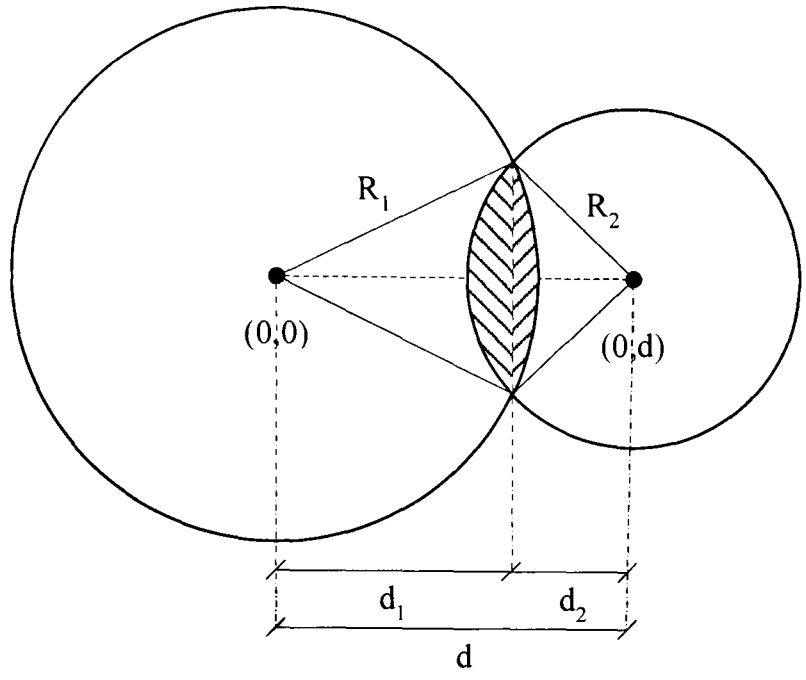


**Figure 5.6** Schematic showing the coordinate system used for finding the area of the asymmetrical lens formed at the Circle -circle intersection.

The area is calculated by adding the area of the two circular segments that form the lens. The area of a circular segment is [Harris, 1998]:

$$A(R',d') = R'^2 \cos^{-1}\left(\frac{d'}{R'}\right) - d'\sqrt{R'^2 - d'^2}\,, \tag{5.18}$$

and the asymmetrical lens area is [Weisstein, 2005],

$$\begin{aligned} A &= A(R_1,d_1) + A(R_2,d_2) \\ &= R_2 \cos^{-1}\left(\frac{d + R_2^2 - R_1^2}{2dR_2}\right) + R_1^2 \cos^{-1}\left(\frac{d + R_1^2 - R_2^2}{2dR_1}\right) - \\ &\quad \frac{1}{2}\sqrt{(-d + R_2 + R_1)(d + R_2 - R_1)(d - R_2 + R_1)(d + R_2 + R_1)}\,. \end{aligned} \tag{5.19}$$

There are two limiting cases, when $R_1+R_2$ is greater or equal to the distance between the two circles then the area is zero, and when the distance is smaller than $R_1$-$R_2$ then the area is the area of $R_2$.

In order to illustrate the behaviour of the model, a target strength change when a circular transducer of 0.8 mm radius scans a hole in a surface with 0.5 mm radius was calculated and the result is shown in Figure 5.7.

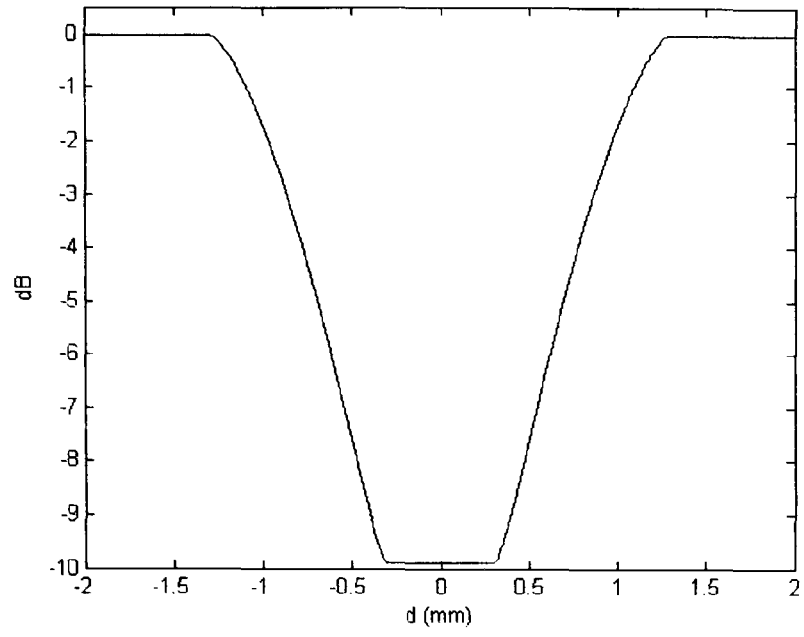


**Figure 5.7** Simulation of the change of the target strength when scanning a hole of radius 0.5 mm with a circular transducer of radius 0.8 mm. Target strength change expressed in dB assuming a defect TS = 0 and using as reference the TS of the non defective area.

When the emitted beam approaches a defect such as a hole or crack in an otherwise flat surface, the intensity of the reflected echoes will start decaying. The proposed approach assumes that the average characteristics of the surface (roughness, density and shape) are fairly constant over a given inspection segment. As a consequence, variations in the surface characteristics, specifically shape variations such as protuberances, holes and cracks below the resolution threshold of a given sensor can be visualized and detected when the intensity variations are registered in a three dimensional map. The proposal is to add a fourth variable to the "positional" three dimensional profiles traditionally generated by profiling sonars using the time of flight only. The additional variable integrates the intensity of the received echoes with the 3D coordinates ($x$, $y$ and $z$) in a three dimensional plot.

The distance from the boundary of the defect, where the intensity begins to decrease, will be defined by the characteristics of the beam. When the defect is bigger than the beamwidth, the intensity of the returning echo will reach a minimum, when the distance from the boundary of the defect to the centre of the beam is equal to half the beamwidth. On the other hand, if the defect is smaller than the beamwidth, the minimum will be reached when the beam is illuminating the whole of the defect, Figure 5.5. The minimum value that the intensity can

decrease in any case is equal to the background noise level. Once the minimum has been reached, the intensity will stay at that value until the border of the beam reaches the boundary of the defect for the first case (defect bigger than beamwidth) or when the defect starts coming out from the illuminated area in the second case (defect smaller than the beamwidth). In both cases, the intensity will keep increasing until reaching the same value as when it was illuminating the non defective area.

The minimum reflected intensity will be a function of the characteristics of the defect (shape, size and depth). In case of a protuberance (i.e. a defect sticking out towards the pipe inside), the intensity of the received signal will increase during a sideways scan. Summarizing, if a variation from average conditions in the relatively flat surface is present, such as changes in the shape of the surface or changes in the material properties (density or roughness), an intensity change in the received signal can be detected.

In Figure 5.8, a simulation carried out using the ultrasound field simulation tool, Field II, is presented. A flat surface with a 1 mm hole is scanned using a 3 MHz, 10 mm ultrasound transducer, Figure 5.8(a). The transducer is located at a distance of 150 mm from the surface and it is moved parallel to the surface from a position 10 millimetres in front of the hole until a position 10 millimetres after the hole. The intensity of the received signal is presented in Figure 5.8(b). In the presented plot, it can be seen how the intensity of the reflected echo diminish as the transducer approach the hole, even though the hole is smaller than the transducer resolution at the given distance which is 5.76 mm for a -3 dB beamwidth at 150 mm.

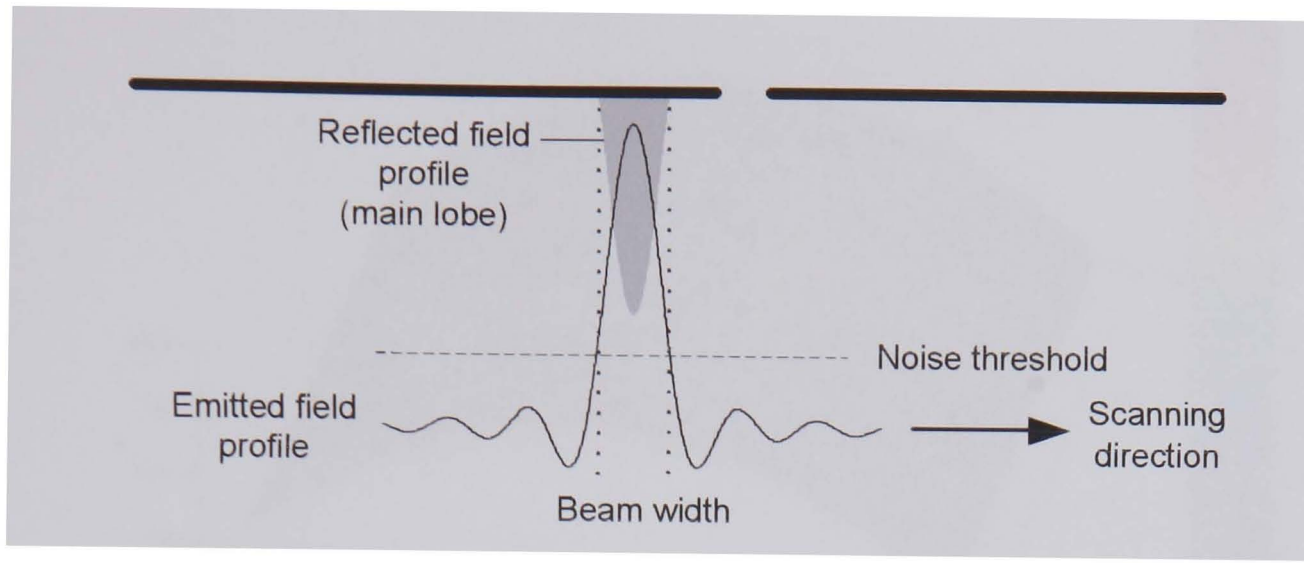


(a)

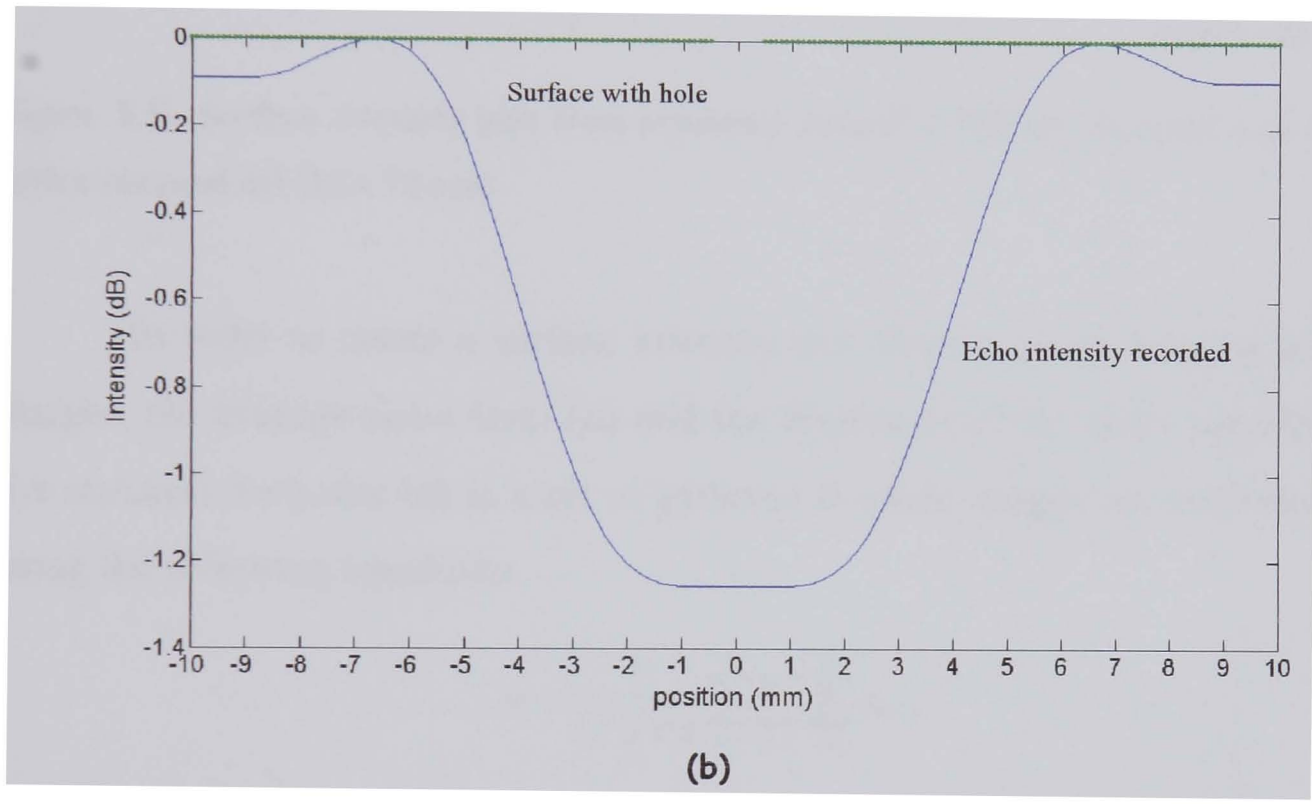


(b)

**Figure 5.8** Illustration of the surface intensity plot method. (a) Diagram (b) simulation: echo intensity when scanning a flat surface with a 1 mm gap, located at a distance of 150 mm from a 10 mm circular transducer. The transducer frequency is 3 MHz.

As mentioned above the proposed approach combines the $x$, $y$, and $z$ coordinates of the profile of the surface with the intensity of the echoes returned from the pipe wall at each illuminated location. These four variables can be presented in an appropriate graphic way, by means of a colour three-dimensional plot where echo intensities are overlaid using a colour logarithmic scale. This type of plot is here referred as surface-intensity plots (SIPs), Figure 5.9.

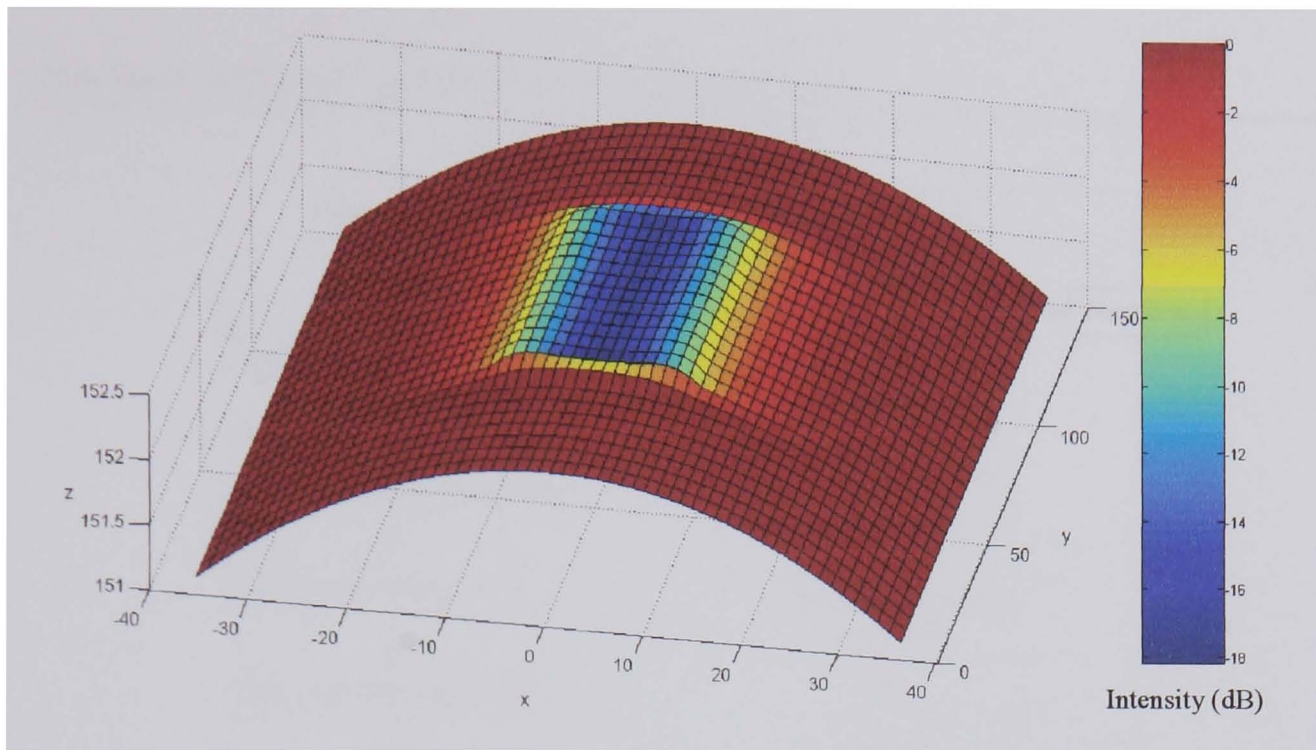


**Figure 5.9** Surface intensity plot from simulated data of a 300 mm diameter pipe section with a removed slit (10 x 70 mm).

In order to create a surface intensity plot from a set of scanned B-mode images, the average noise level ($\mu$) and the dispersion of the noise calculated as the standard deviation ($\sigma$) in a set of gathered B-mode images are determined by using the following equations:

$$\mu = \frac{1}{i \times j \times n} \sum_{z=1}^{n} \sum_{k=1}^{i} \sum_{l=1}^{j} x_{kl} \,, \tag{5.20}$$

$$\sigma_i^2 = \frac{1}{(i \times j \times n) - 1} \sum_{z=1}^{n} \sum_{k=1}^{i} \sum_{l=1}^{j} (x_{kl} - \mu)^2 \,, \tag{5.21}$$

where $i$ and $j$ are the length and width of the B-mode image, n is the number of B-mode images to use for creating the surface intensity plot and $x_{kl}$ is the intensity of a given pixel in the B-mode image.

The standard deviation and the mean noise level are added up to define a threshold to locate the echoes in the B-mode images. The intersection of the threshold and the leading edge of the echo are used to precisely locate the corresponding sample. Because the sonar is a discrete system, by counting the number of samples before the gate and dividing it by the sampling frequency, the time of flight (TOF) is determined:

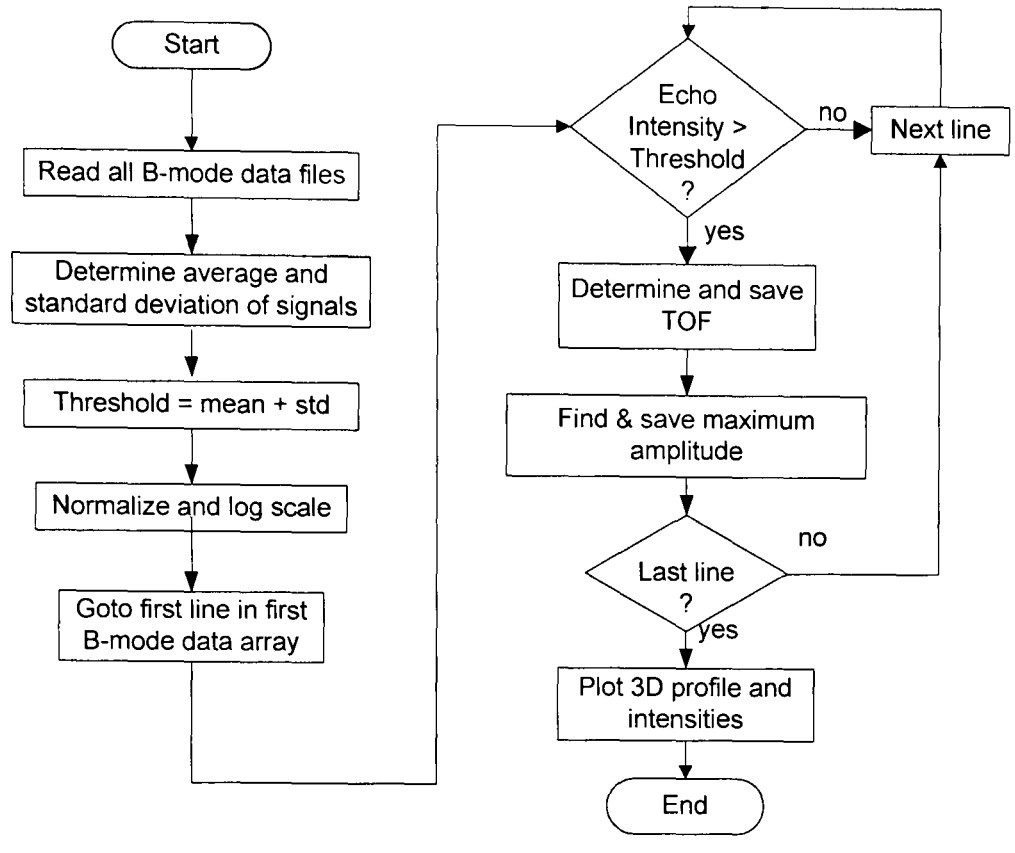


**Figure. 5.10** Flow diagram illustrating the surface-intensity plots method

$$TOF = \frac{N}{fs} \quad . \tag{5.22}$$

Then the TOF and the speed of the sound in the medium are introduced in equation 5.1 to compute the distance from the sensor to the inner pipe wall.

After the echo has been detected and the TOF measured, the peak intensity of the echo is found by calculating the maximum intensity inside a window with a predefined size, starting at the sample that went above the threshold. Finally, using the sensor location information (angle and displacement) and the TOF, the $x$, $y$ and $z$ coordinates are calculated and stored together with the peak intensity, Figure 5.10.

It should be noted that pipe profiling only uses the positional information obtained from the TOF measurements. This is the first time that intensity information has been integrated with three dimensional positional data in ultrasound pipe profiling. The presented approach improves the capabilities of sonar systems, built with non-focused, single transducer, to detect changes in the assessed surface which are below the sensor resolution. This will contributed to the development of smaller and more powerful survey equipment for sewers pipe

assessment. In the next section, simulations and experiments will show the visualization enhancement that can be achieved by using the proposed methodology.

## *5.4 Determination of the capabilities of the method*

The aim of this experimental work was to find the minimum defect size that can be reliably detected when a pipe wall (or generally a relatively even surface perpendicular to the ultrasound beam) is scanned. In a first stage, a sensitivity analysis was conducted through simulated experiments to find the minimum defect sizes, later these values were validated through real experiments. The simulations were carried out using a simulation tool developed and tested in the previous stage of the project [Gomez, 2003a; Gomez, 2003b; Jensen 1996] presented in chapter 4. The experimental validation was conducted by scanning sections of plastic pipes immersed in water by using the experimental platform described in chapter 3.

### 5.4.1 The Simulator

The simulator employed for the validation and determination of the capabilities of the method, allows the user to create simulated three dimensional ultrasonic profiles of inner sections of pipes with artificially created defects [Gomez, 2003a].

The modelling tool was primarily used to validate the proposed approach saving valuable resources and time. It has many advantages such as: high accuracy, fast sampling rate and access to the raw RF signal, a characteristic hard to obtain in sonar systems available in the market nowadays. A detailed explanation about how the simulator work and its capabilities can be found in Chapter 4.

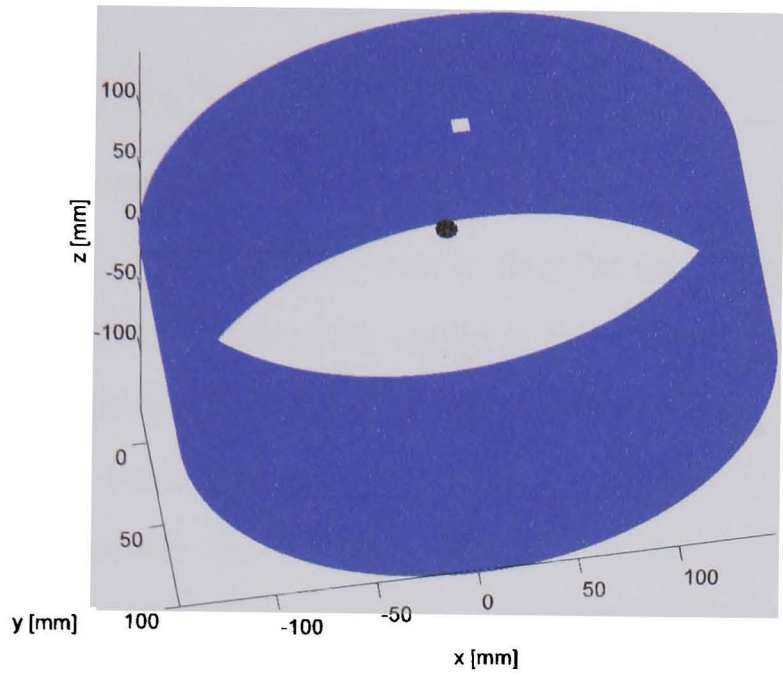


(a)

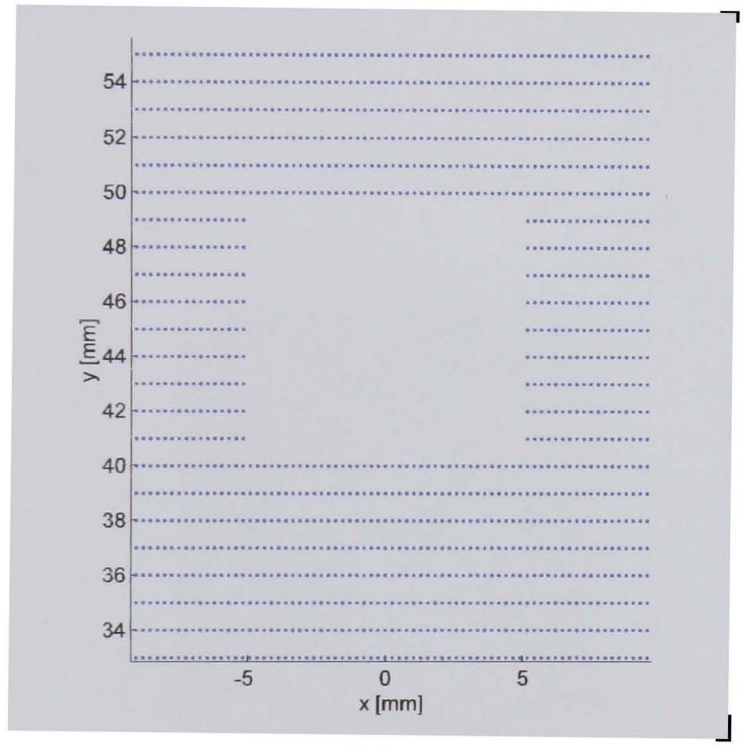


(b)

**Figure 5.11** (a) Digital Phantom for a 300 mm PVC pipe. (b) Expanded view of the phantom showing the mesh grid and square defect.

For all the simulations, a section of a 300 mm nominal diameter pipe, immersed in water, was scanned simulating a 3 MHz, 10 mm diameter, unfocussed single piston transducer equivalent to the real sensor used in the experiments. The simulated experiments were carried out using the same sampling frequency as the experimental platform: 162 kHz. Digital phantoms representing the pipe section with given defects were created for each of the cases by removing scatterers and using appropriate mesh grids, Figure 5.11.

### 5.4.2 Lateral resolution

The objective of this study was to find the minimum defect size along the lateral axis that can be detected by applying the proposed method. The scanning of a 300 mm diameter pipe segment with three precisely cut out rectangles was simulated. The three cut out rectangles were centred over the *x*-axis and positioned sequentially along the *y-axis* with 20 mm separation between each other. For referencing purposes, the three shapes were identified as rectangles *A*, *B* and *C*, see Figure 5.12. The height of the three rectangles is the same, 10 mm, but the width of the base is reduced to a half in each subsequent one, with being *A* the biggest one.

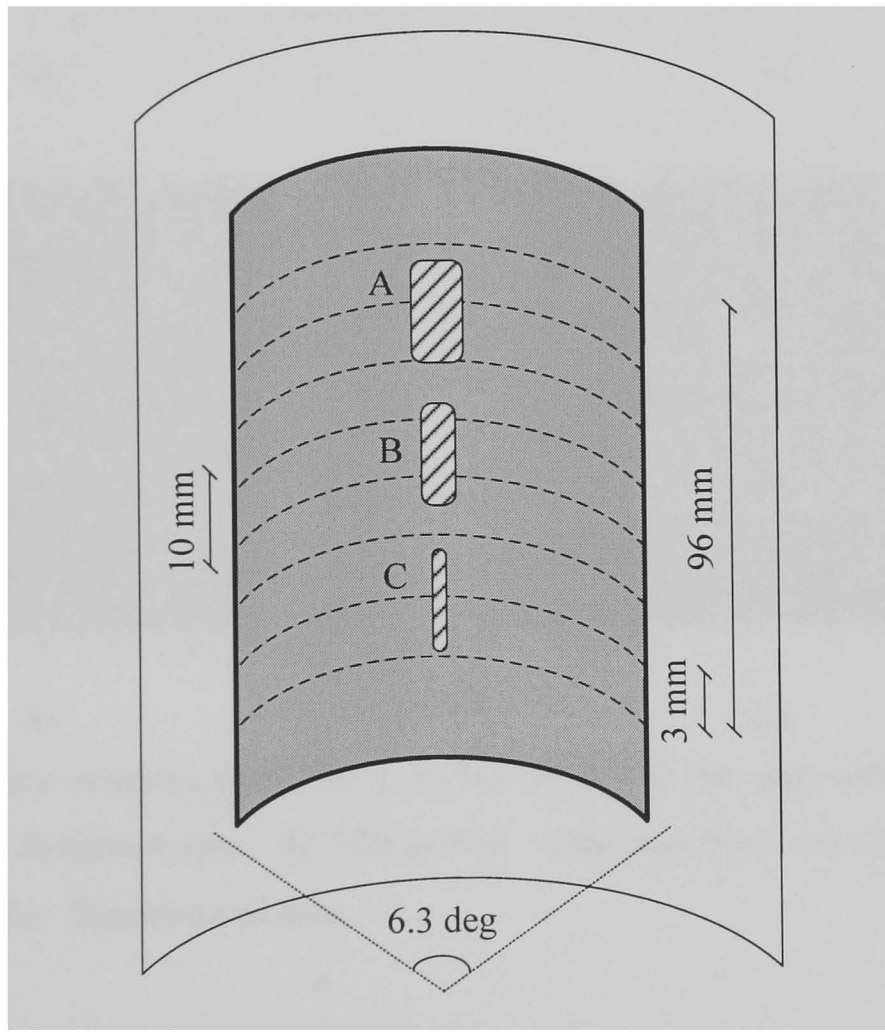


**Figure 5.12** Pipe section with the three cut-out rectangles used for the simulation.

The base of rectangle *A* is 2 mm long, centred over the *x*-axis, and extends from -1.0 mm to 1.0 mm. The base of rectangle *B* is 1 mm long, being half of the base size of *A*. It extends from -0.5 mm to 0.5 mm. Rectangle *C* is 0.5 mm long and extends from -0.25 mm to 0.25 mm.

The rectangles were scanned translating the transducer along the $y$-axis from 10 mm to 106 mm at 3 mm steps and rotating the transducer 6.3 degrees, from -3.15 degrees to 3.15 degrees at 0.225 degrees intervals. Hence, the scanned surface was a 16.3 mm by 96 mm rectangle. The scanning process generated 33 B-mode images.

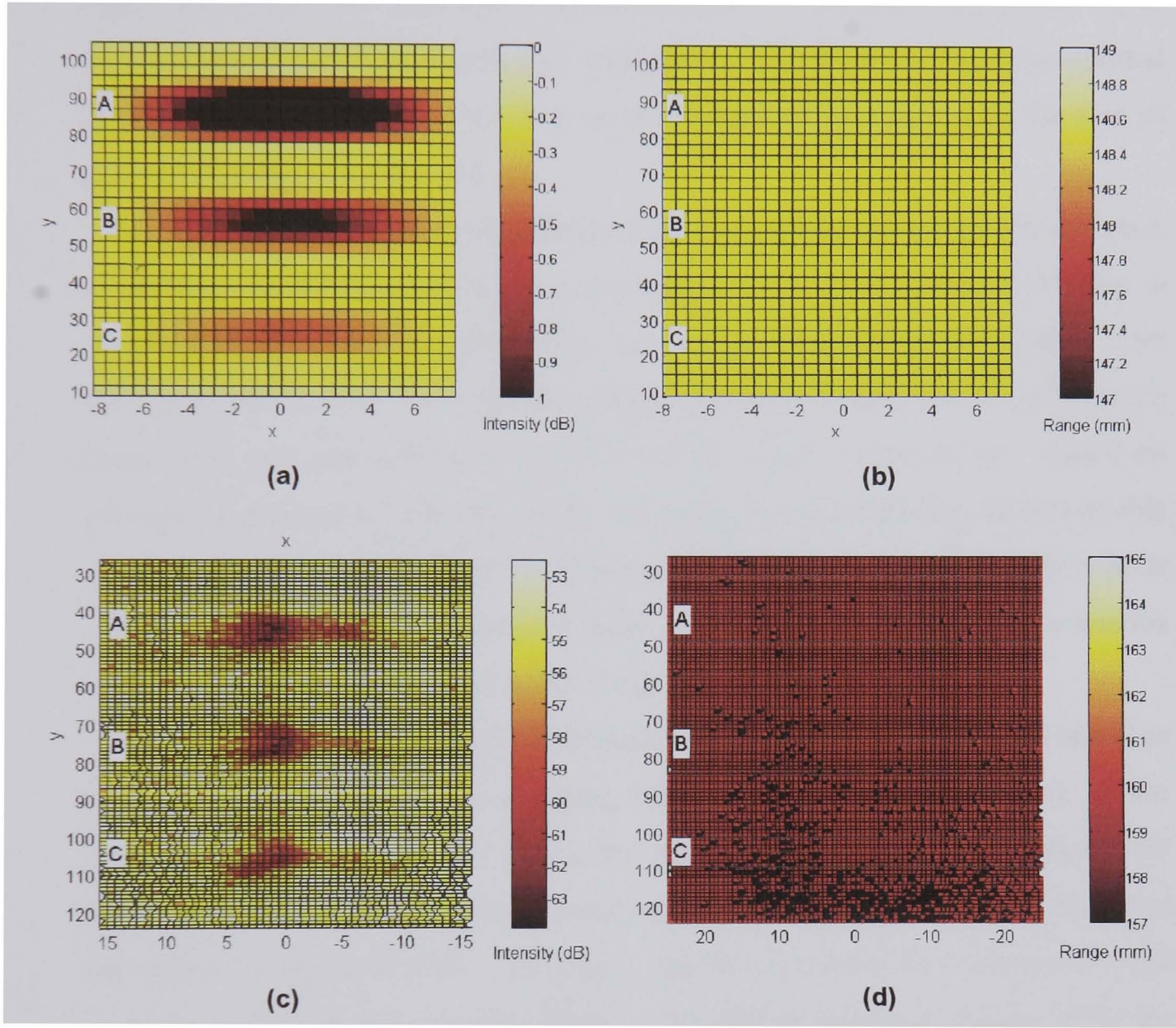


**Figure 5.13** Surface-intensity plots for a section of a 300 mm pipe with three cut-out rectangles. (a) SIP Simulated data. (b) TOF profile - Simulated data. (c) SIP- Experimental data. (d) TOF profile - Experimental data.

Once the proposed method was applied to the set of simulated B-mode images, the internal surface of the pipe was visualised. Following the procedure explained in section 5.3, the threshold value used for the detection of the echoes, was -9.1 dB. The resulting surface-intensity plots are presented in Figure 5.13.

When holes are present in a pipe wall immersed in water, they are usually appreciated in TOF profiles as holes or white sections – i.e. pipe sections from

where no echoes are returning. In the resulting TOF plots, there are no areas showing the absence of echoes or, in other words, holes. This means that using the TOF method only, it is not possible to visualize any of the holes present in the pipe wall. The TOF only method was not able to visualize any of the three rectangular defects in the inner pipe wall because the beam width of the emitted field, at such distance from the face of the transducer, is bigger than the size of any of the defects investigated.

In order to determine the minimum lateral dimension that can be detected, a condition has to be defined. A performance measure was defined in order to decide if a defect was recognizable or not in a surface-intensity plot (SIP). The parameter chosen was the intensity contrast between echoes returning from the intact pipe wall and echoes returning from the centre of the defect. Based on previous experiences with the sonar used for the experiments, an acceptable minimum contrast to visually recognize a defect in a surface-intensity plot is 0.5 dB. It should be noted that this value may have to be increased in scenarios where the acoustic background noise levels are higher.

The surface intensity plot in Figure 5.13(a) shows rectangles *A*, *B* and *C* as a reduction in intensity in the returning echoes (darker zones in the plot). In the case of rectangle *C* (0.5 mm wide), the smallest of all the studied defects, the intensity contrast between echoes returning from the pipe wall and the centre of the defect is around 0.5 dB. Therefore, this is considered the minimum lateral resolution of the proposed methodology. To validate the results generated by the simulator, an experiment with a real pipe with the same characteristics, defects and conditions as used for the simulation was carried out. These results can be seen in Figure 5.13(b), the three defects are easily recognizable in the SIP, whereas in the graph created using the TOF only technique, Figure 5.13(c), neither of the defects can be seen.

Summarising, in order to quantitatively determine the improvement achieved by using the SIP technique, simulations were carried out to find the minimum size in the lateral dimension that can be detected by the TOF technique. The results show that by using the surface-intensity plot technique, defects eleven times smaller than those seen with the TOF technique can be detected.

### 5.4.3 Axial resolution

The objective of this study was to find the minimum distance variation along the axial axis that can be detected by employing the proposed method for inner pipe-wall inspection. For this experiment, a pipe section with a nominal diameter of 300 mm and 3 mm wall thickness was scanned. The digital phantom was created by means of three circular layers each separated by 1 mm. The separation between scatterers was, like in the previous simulation, 1 mm. In the pipe wall, three 10 mm squares were precisely carved at different depths. The three squares were labelled squares *A*, *B* and *C*, Figure 5.14.

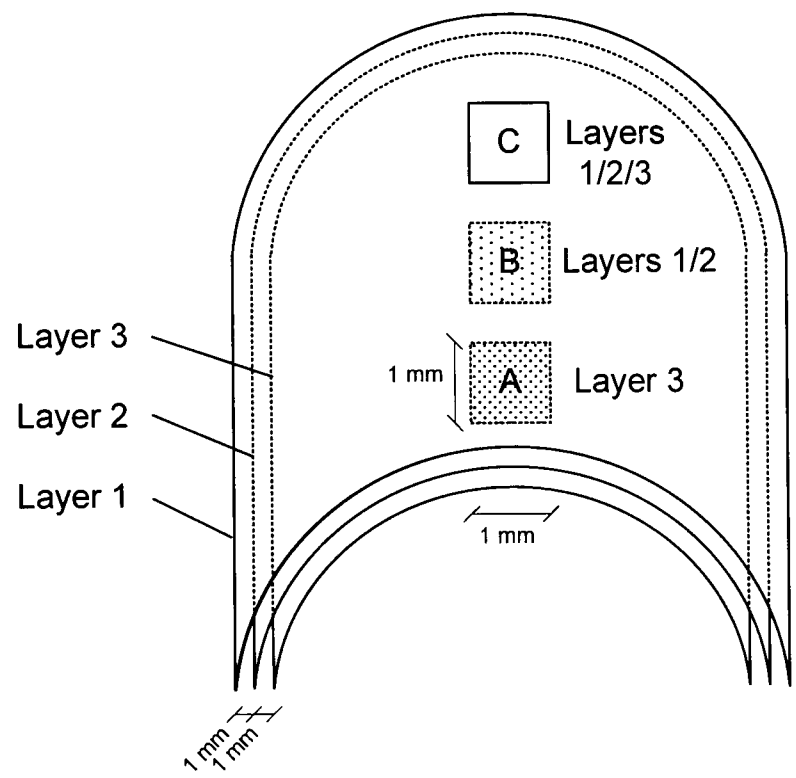


**Figure 5.14** Pipe section with the three carved squares used for the simulation.

Squares *A* and *B* have a depth of 1 mm and 2 mm, respectively, and extend along the *y* axis from 20 mm to 30 mm and from 50 mm to 60 mm respectively. Square *C* was a square hole passing through all 3 layers. The three carved squares were centred along the *x*-axis extending from -5 mm to 5 mm and positioned sequentially along the *y*-axis with a separation of 20 mm between each other.

The three squares were scanned translating the transducer along the *y*-axis from 9 mm to 105 mm in 3 mm steps and rotating the transducer 13.5 degrees,

from -6.75 degrees to 6.75 degrees in 0.225 degrees intervals. The scanning process generated 33 B-mode images.

Once the proposed method was applied to the set of simulated B-mode images, the internal surface of the pipe was visualised. The threshold used for the detection of the returning echoes was -11.44 dB and it was determined by applying the methodology presented in section 5.3. Results are presented in the form of surface-intensity plots, Figure 5.15.

It is important to mention, that if the TOF profiling method was used only to reconstruct the inner surface of the pipe and map the defects (squares A, B and C) a focused sensor and a fast sampling rate would have been needed to satisfy the resolution requirement. For instance, in order to achieved a 1 mm axial resolution, a sampling rate of at least 1.5 MHz would be needed. In contrast, in the present study an unfocussed transducer with a sampling rate of 162 kHz, almost an order of magnitude less, is being employed.

One of the main advantages of the surface-intensity plots is that changes in the pipe wall can be detected even in the presence of noise. In Figure 5.15(a), square *C* can be identified in the surface-intensity plot as a faint shadow. The shadow area at the bottom of the plot (square *C*) is indicative of a reduction of the echo intensity from its average value. The intensity information complements the axial information generated by the TOF method. As can be seen in Figure 5.15, the contrast in the intensities of the echoes between the intact pipe wall and the centre of segment *A* is around -2 to -3 dB. This is a good contrast value, clearly better than the 0.5 dB threshold determined in section 5.4.2.

In conclusion, using this approach based on surface-intensity plots, it is possible to detect changes in the inner wall of pipes which are 1 mm deep. Due to limitations of the available simulation and experimental platform a validation for defects less than 1 mm deep could not be carried out. Nevertheless, comparing the axial resolution of the employed system, when using the TOF only method (4 mm) and the results from the surface intensity plots (1 mm), it can be concluded that the proposed methodology allows the detection of changes in the axial direction which are four times smaller than the standard TOF technique.

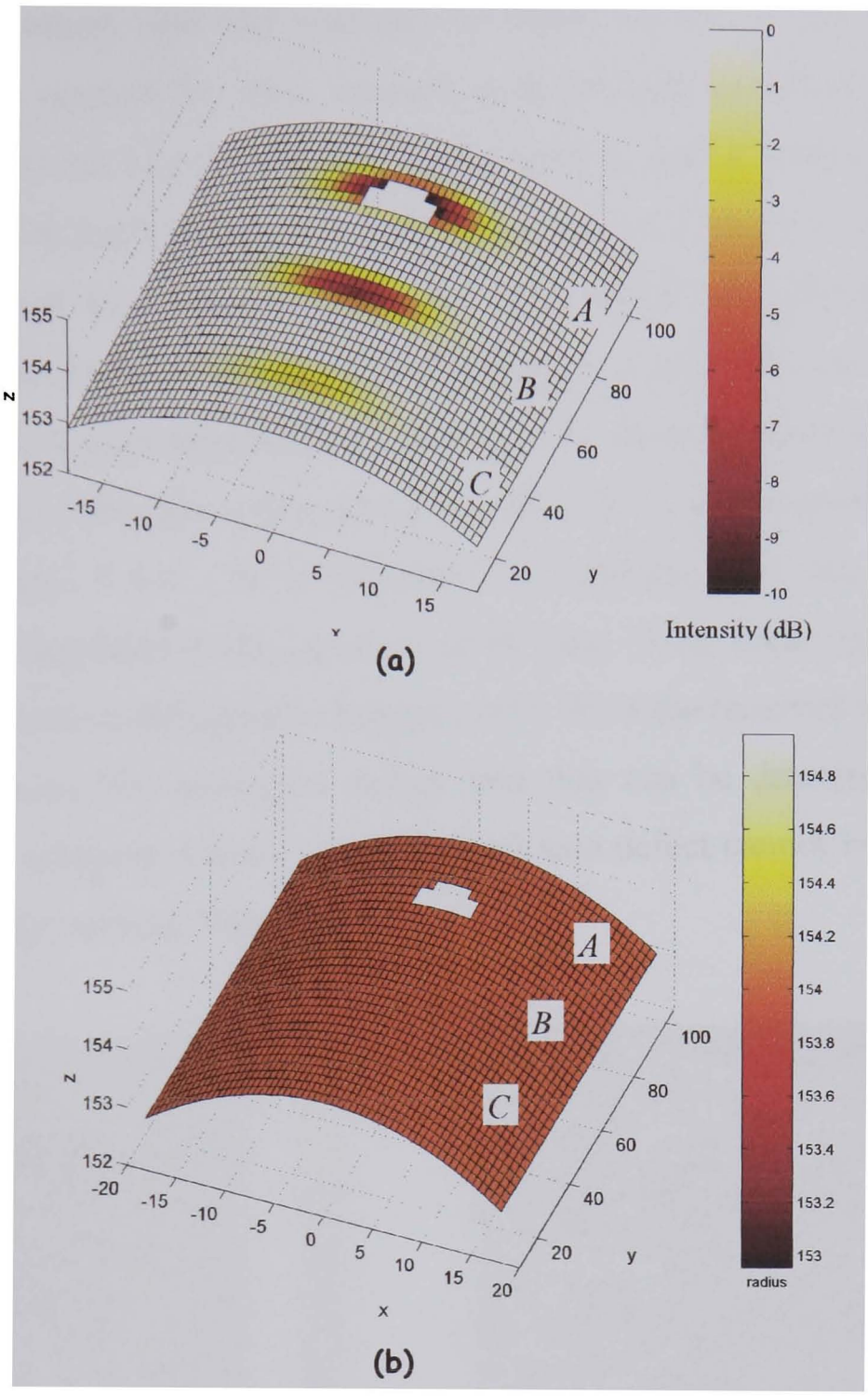


**Figure 5.15** Surface-intensity plot used to determine the axial resolution. A pipe section with two carved squares at 1 mm, 2 mm depth and a through square hole were scanned. All three squares have the same width (10 mm) and length (10 mm). Using the TOF method, only the top square hole, which penetrates through the entire pipe wall, was detected, while the other two with depths 2 mm and 1 mm did not show in the resulting TOF plot. (a) SIP (b) TOF profile

### 5.4.4 Combined lateral and elevation resolution

The objective of this study was to find the minimum surface area of a hole that can be detected by employing surface-intensity plots. In section 5.4.2 the minimum lateral resolution was found by keeping the size of the defect in the

elevation axis, constant and big enough, in order to not affect the lateral resolution. In this section the main concern is to find the combined minimum lateral and elevation resolution. For this, a pipe section with a nominal diameter of 300 mm with a through square defect was scanned. A 2 mm by 2 mm square section was removed from the pipe phantom. The defect was centred over the $x$-axis and extended from 20 mm to 22 mm along the $y$-axis. As can be seen in Figure 5.16, the dark area represents the defect. The intensity contrast from the centre of the defect to the pipe wall is about 0.5 dB. This is an acceptable value as explained in section 5.4.2. It is important to mention, that this resolution parameter can be degraded if the signal to noise ratio of the sonar system is not small enough in order to distinguish changes of 0.5 dB in the received signals.

In conclusion, the minimum defect area that can be detected with this approach is approximately 4 $mm^2$. Such a small area defect cannot be visualised using the TOF only method, Figure 5.16(b).

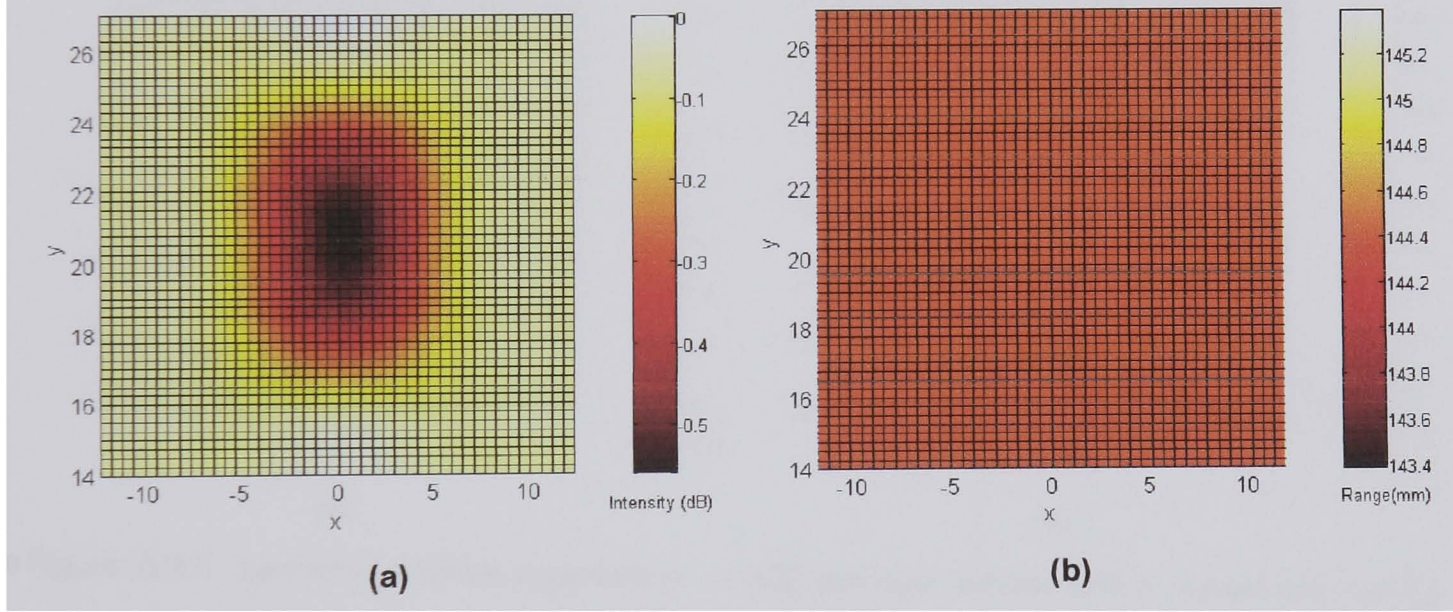


Figure 5.16 Lateral and elevation resolution experiment - A scanned 300 mm pipe section with a 2x2 mm square area is shown. (a) Surface-intensity plot, 3D view (b) TOF 2D View

### 5.4.5 Determination of the minimum spatial resolution

Finally, the spatial resolution or the combined lateral-elevation-axial resolution was determined. In this case the results from all the previous sections were combined in order to find the minimum defect volume detectable by the proposed method. A sensitivity analysis was conducted, varying the width of a

square defect, keeping the depth size constant to the minimum achievable value of 1 mm. In Figure 5.17, a surface-intensity plot showing the smallest defect that generated a detectable contrast is presented. The dark area in the centre of the plot shows the intensity reduction of the received echoes, indicating the presence of the defect. The contrast between the intensities registered on the pipe wall and the centre of the defect is about 0.8 dB. The measured contrast is an acceptable figure for a commercial sonar scanning system as defined in section 5.4.2.

When scans are conducted, in noisy environments or at low sampling rates, as it is the case with the SeaKing sonar used in the present study, the surface-intensity plots are a useful alternative. They are a perfect complement for the TOF methodology, due to its capabilities to show defects under these restraining conditions. The minimum defect that could be detected was a 2.5 mm x 2.5 mm square, with a depth of 1 mm, Figure 5.17.

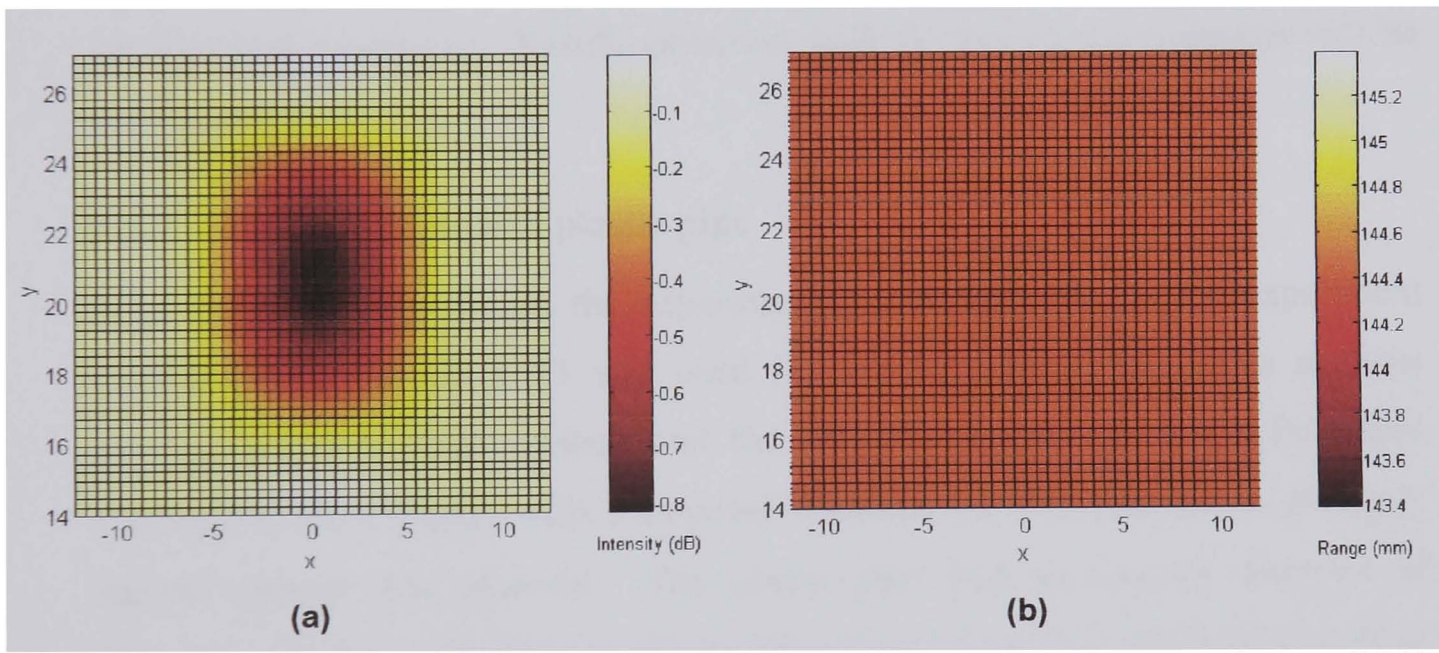


**Figure 5.17** Spatial resolution experiment. A 300 mm pipe section with a carved area of 2.5 x 2.5 mm and 1 mm depth is shown. (a) Surface intensity plot (b) TOF profile

As a result, it can be concluded that the minimum defect volume that can be detected by the proposed method is around 6.25 cubic mm. In table 1, an overview of the results obtained is shown.

**Table 5.1** Overview of simulation experiments

| Simulation Experiment | Result |
|---|---|
| Lateral/Elevation resolution | 0.5 mm |
| Axial resolution | <1 mm |
| Lateral-elevation resolution (combined) | 2.0 mm x 2.0 mm |
| Lateral-elevation-axial resolution (combined) | 2.5 mm x 2.5 mm |

## 5.5 *Further Experiments*

This section investigates the ability of the proposed methodology to detect defects smaller than the sensor resolution by carrying out lab experiments which emulate real conditions. Results obtained from the previous simulations will be corroborated.

### 5.5.1 Carved Triangle in plastic pipe

For this experiment the experimental data gathered for the experiment carried out in section 3.9.3 was used for conducting a comparative analysis between the TOF only method and the surface intensity plots. A Polyvinyl Chloride (PVC-U) pipe with a nominal diameter of 300 mm and a precisely carved triangle was scanned. The plastic pipe had an internal diameter of 296 mm. Figure 5.18 shows a 3D profile created by a time-of-flight algorithm with an overlaying triangle (black-white dotted lines) showing the size and position of the removed section in the real pipe.

In order to compare the TOF profiling method and the SIP, a methodology for identifying the removed section has to be defined. Two approaches can be used. First, the white area in the middle of Figure 5.18(b), where no returning echoes were detected can be defined as the removed section. If this method is employed, the identified triangle will be considerably smaller than the original one, having a height and a base which is 41% and 53% respectively smaller than height and base of the original defect. Second, the changes in depth can be used to identify the removed surface. For this case, the height and the base dimensions

of the identified defect will be 26% and 22% smaller than the corresponding dimensions in the original defect, see table 5.2.

In both cases, the area of the identified section is smaller than the actually removed triangular section. This shows how the beamwidth tends to mask defects and slight changes in the observed surfaces. Observing the vertices in Figure 5.18(a), it can be seen that the resolution is very poor. The sides of the triangle are not represented by continuous and smooth lines but by stepped lines with rough edges. The stepped edges are not of interest for the present analysis because they are a consequence of the step size, along the longitudinal axis of the pipe, used during the scanning process (3 mm). They can be eliminated by using a finer resolution in the scanning process when translating the sonar inside the pipe.

The ability to detect a removed section from a pipe using a TOF based profile relies basically on the lateral and elevation resolution (radial resolution) of the transducer employed for carrying out the scanning. For this case, because a circular single piston transducer was used, the lateral ($x$-axis) and elevation ($y$-axis) resolution are the same, being around 8 mm.

Observing the vertex of the triangle in Figure 5.18(b), the ability of the TOF method to detect details smaller than the sensor resolution can be seen. In the first approach, when the distance between the sides of the triangle gets below 13.57 mm, the main lobe of the ultrasonic signal reflects on both sides of the pipe, creating a detectable echo, hiding the vertex. In the second approach, the removed section is delimited by an area that shows a deviation from the inner diameter of the pipe, Figure 5.18. It should be noted that such change was not present in the original pipe. This is because the echo is not caused by a reflection from the centre of the beam but from its sides. As a result, the pulse is travelling a longer distance and the TOF increases. The change in distance detected by the TOF algorithm is translating the vertex in the positive direction along the *y-axis*, increasing the height of the identified triangle in comparison with the one identified in the previous approach. In the side vertices, the same behaviour is seen, contributing to reduce the overall differences in the height and base between the removed section and the identified one, table 5.2.

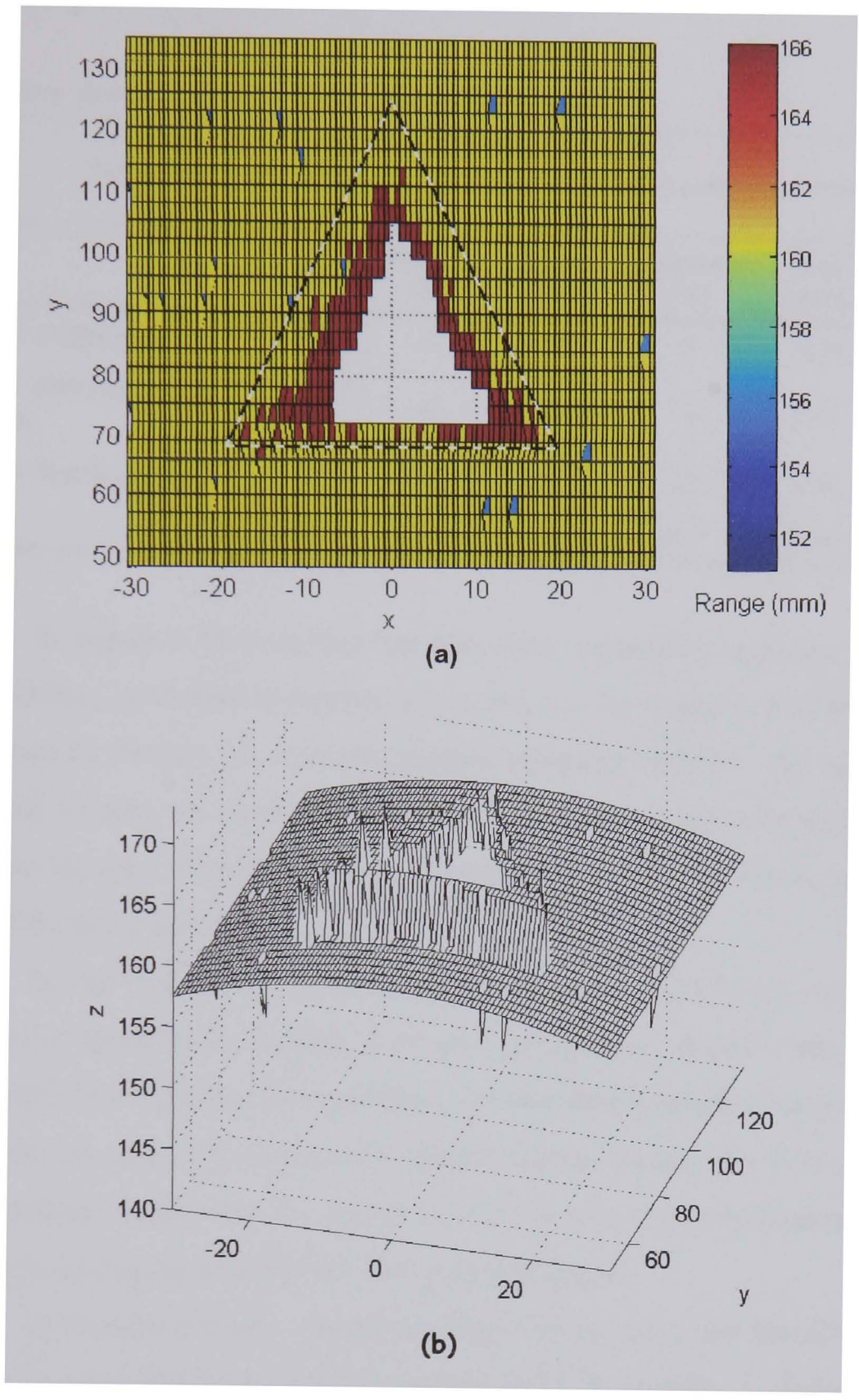


**Figure 5.18** Triangle defect experiment: Pipe profile created by using a time of flight algorithm. (a) TOF profile, 2D view. Removed area shown by dashed lines. (b) TOF - 3D view

**Table 5.2** Triangular defect visualisation methods comparison table.

| | Height (mm) | Difference (%) | Base (mm) | Difference (%) | Area ($mm^2$) | Difference (%) |
|---|---|---|---|---|---|---|
| **Defect (reference)** | 56.74 | 0 | 39 | 0 | 1106 | 0 |
| **TOF: non returning echoes** | 33 | 40 | 18.15 | 53 | 299 | 72 |
| **TOF: depth change** | 42 | 26 | 30.3 | 22 | 636 | 42 |
| **SIP** | 60.16 | 6.0 | 38 | 2.6 | 1143 | 3 |

In Figure 5.19 a surface intensity plot, created by applying the proposed methodology presented in section 5.3, is shown. As in the case of the TOF plots, a method to identify the removed section should be defined. For identifying the removed section, an intensity threshold of -59 dB was set in order to delimit the removed section. The echoes with intensities below -59 dB will be assumed to be part of the removed section.

In Figure 5.19, the removed section and the identified removed section are shown by black-white dashed lines and green-black dashed lines respectively. Qualitatively comparing both triangles, the identified triangle is very similar to the removed one, the vertices are more clearly defined than in the TOF case, the base looks similar in size but the height is slightly bigger as consequence of the top vertex being displaced in the positive *y-axis* direction.

Now quantitatively comparing them, the height of the identified triangle is 6 % bigger than the reference and the base is 2.6 % smaller. Comparing the areas of the identified triangles using the TOF method and the SIP method, a difference about 40 % can be seen. It can be said that for this particular example, the SIP has achieved an improvement of approximately 10 times when compared with the TOF method.

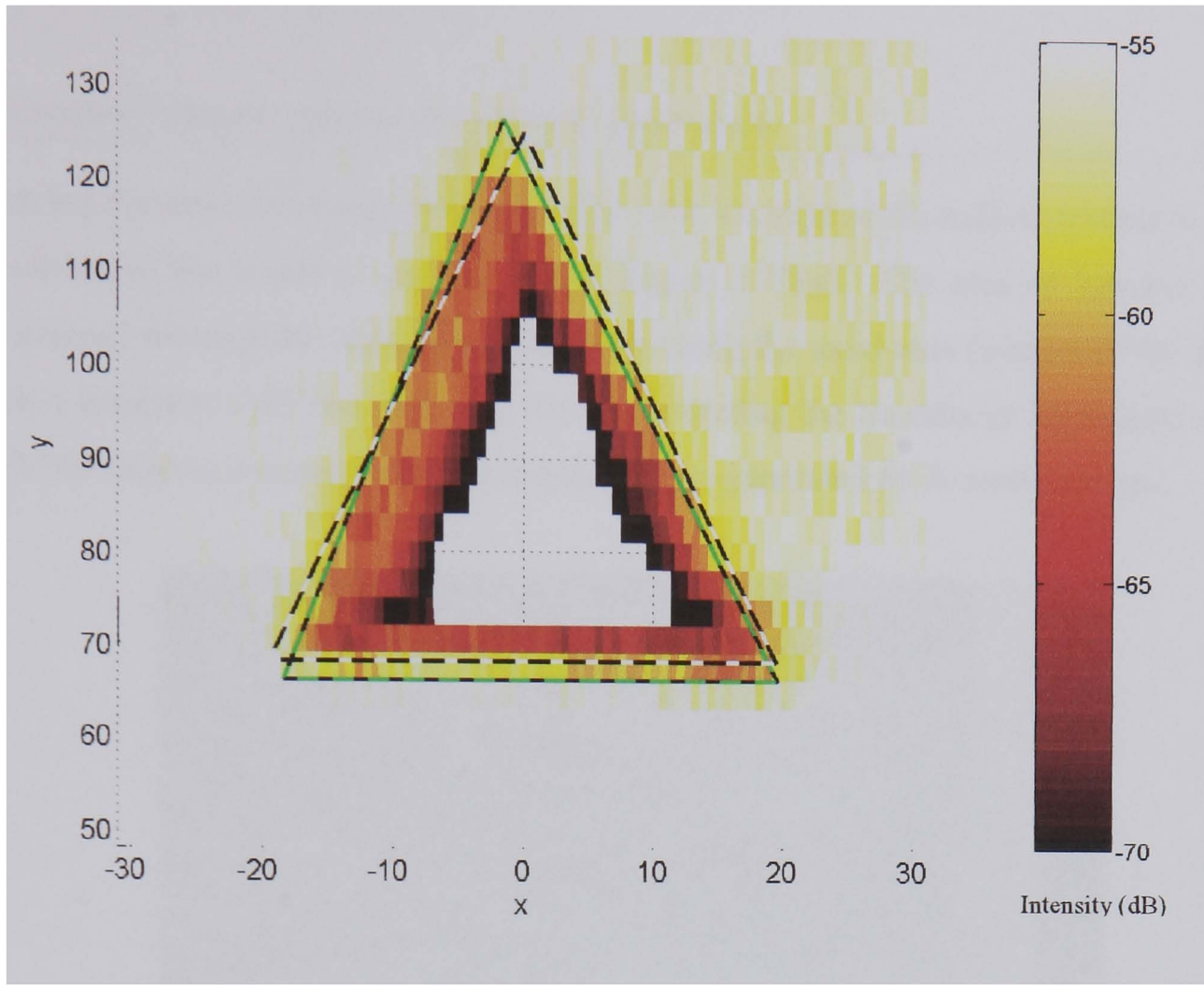


**Figure 5.19** 2D view of a surface-intensity plot obtained from scanning a 300 mm diameter pipe section immersed in water with a carved triangle. The white-black dashed- lines show the removed section and the green-black dashed-lines show the removed section recognised from the surface-intensity plot data.

### 5.5.2 Experiment: Perforated clay pipe

In this experiment, a DN300 vitrified clay pipe with a drilled hole and a splintered area around the hole was scanned (see picture in Figure 5.20(a)). The aim of the experiment was to do a qualitative analysis between the two profiling methods, TOF-only and intensity-surface plots. The analysis will show the capabilities of the proposed method to detect variations and defects in the inner pipe wall of pipes. The pipe used for the experiment had an internal diameter of 312 mm and a wall thickness of 34 mm. In one section of the pipe a 7 mm hole was drilled from the outside. While drilling the hole an excessive force was applied, leading to a fracture by compression of the pipe inside. As a result, an irregular hollow section of approximately 80 mm x 50 mm size and 10 mm in depth around the hole was created, Figure 5.20.

A small crack which appeared at a north-west location of the hollow section is just visible in the acquired camera image, Figure 5.20(a). The area of interest was scanned moving the ultrasonic transducer along the axial axis ($y$-axis) of the pipe at a distance of 65 mm at 1 mm steps and rotating the transducer 31.5 degrees at 0.225 degrees intervals. The scanning process generated 65 B-mode images.

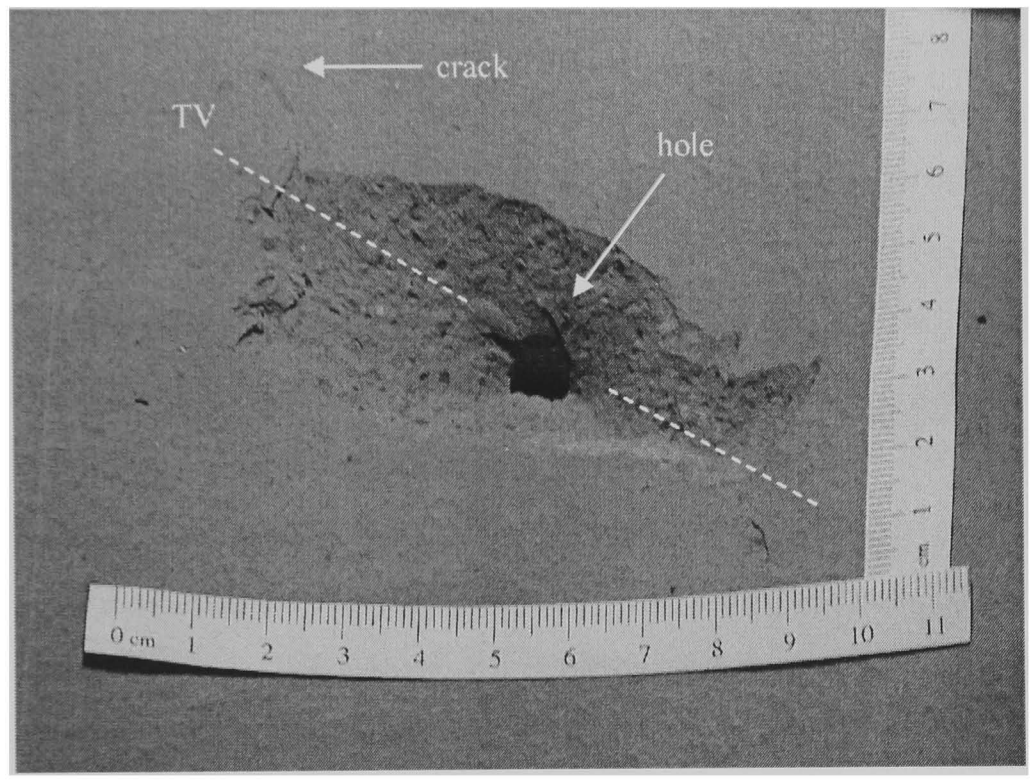


(a)

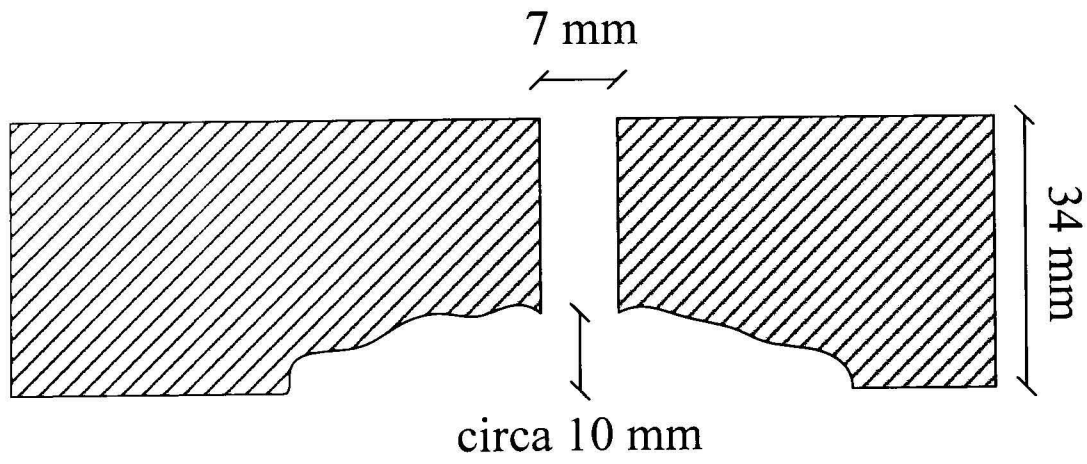


(b)

**Figure 5.20** Clay pipe with perforated hole and hollow section (a) Photograph of the study area, (b) schematic drawing of the transverse section.

It is noted that the profiles depicted in Figures 5.21 and 5.22 are mirror images of the photographic picture shown in Figure 5.20. This was done to present the ultrasonic results from the best possible angle. In Figure 5.21, a 3D

profile of the inner surface of the pipe, solely based on TOF measurement is shown. In this profile a hollow section, at two discrete depth levels can be seen. The first one is around 4 mm in depth and the second section, which is smaller in area than the previous, is about 8 mm in depth (depth is the measured distance from the longitudinal axis of the pipe).

In this TOF profile only two step changes, from the inner surface of the pipe wall, can be seen. These steps correspond to the discrete axial resolution of the transducer (4 mm). Even though, the area under investigation has a hole penetrating through the entire wall and a carved out hollow section in the inner wall, which could be described as a roughly 10 mm deep depression surrounding the through hole and containing minute defects in the micrometer range, most of these details are missed in the TOF-only 3D profile shown in Figure 5.21. It should be noted that even though the theoretical lateral resolution of the transducer is 5.76 mm (section 5.3), the hole, 7 mm diameter, cannot be seen in the TOF profile. In addition "false" positive and negative peaks not associated with any change in the geometry of the inner pipe wall are present. These peaks are created by acoustical and electrical noise present in the environment and the sensor system.

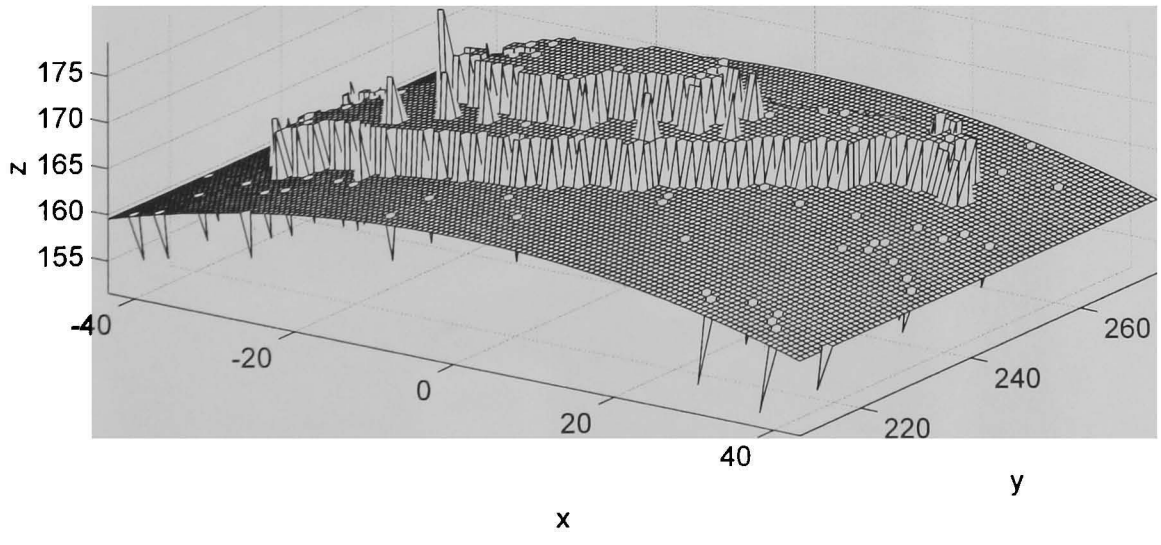


**Figure 5.21** 3D profile generated by means of the TOF method

In Figure 5.22, a 3D view and a top view of an intensity-surface map created by means of the proposed method are presented. Since, the presented

images are mirror images of the picture presented in Figure 5.20(a), the crack defect located at the top defect side of the original image is now located at the bottom side. In the greyscale surface-intensity plot of Figure 5.22(a), the intensity changes, on each overlaying section at different depths, can be associated with variations in depth which are not appreciated by the TOF-only method.

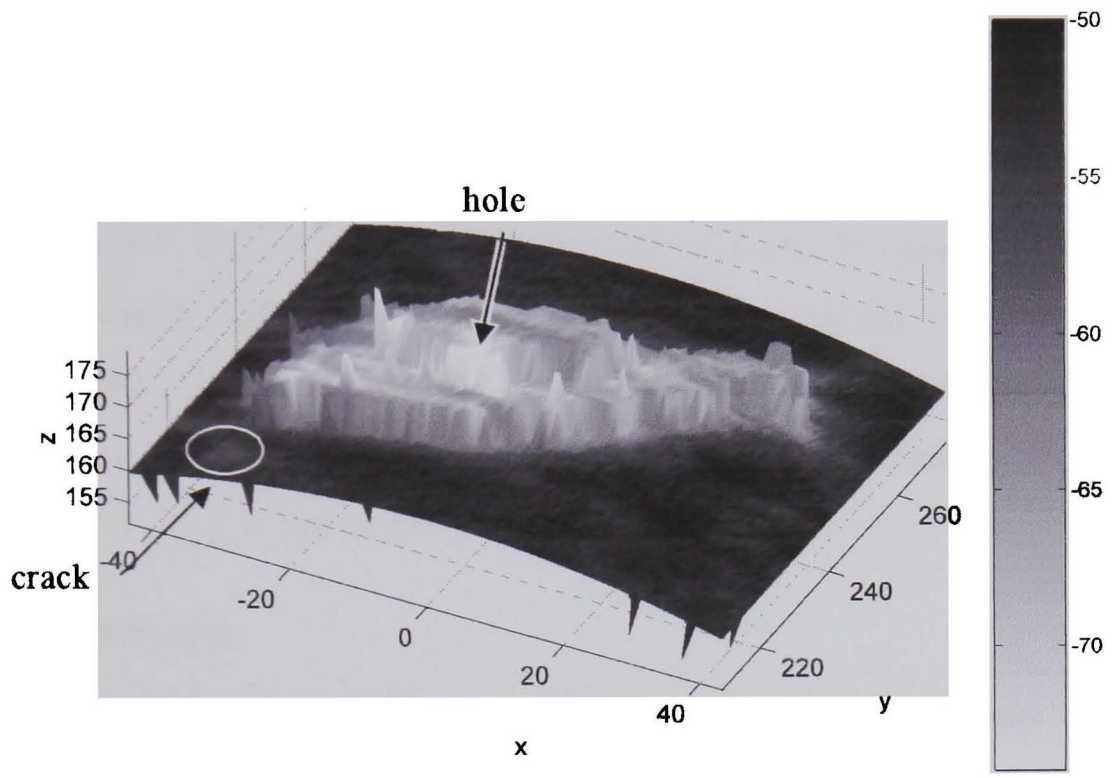


**Figure 5.22** Surface intensity plot of a clay pipe with a defect. The plot was created by means of the proposed method. (a) 3D profile inverse grey scale, (b) plan view colour scale

Although, changes in intensity can be caused by variations in the properties of the material which the pipe is made of, such as density and roughness, for the particular case of pipe inspection, these changes are mainly caused by variations in distance to the sensor. In the surface intensity plot, Figure 5.22(a), the brightest spots represent the deepest areas, and, the dark areas represent the areas closer to the sensor. In the plot shown in Figure 5.22(a), the two reference defects, crack and hole, are easily identified. The hole is depicted by the whitest spot close to the centre of the plot and the crack as a white shadow in the bottom left corner of the plot. The detected crack has a size of approximately 0.5 mm x 12 mm. It is important to mention, that the employed, unfocussed sensor would have only been able to capture defects of at least 8 mm width and at least 4 mm depth using the TOF approach.

## 5.6 Summary

An inspection method for the visualization of defects in structures immersed in liquid, scanned at fixed distance, has been presented. The proposed method is capable of creating 3D profiles of the inside wall of pipes through the use of consecutives B-mode images acquired by means of rotational ultrasonic sonars. The proposed method is able to detect anomalous conditions on the inside pipe wall which could not be detected by employing traditional profiling methods.

The proposed inspection method has been illustrated by means of simulation and experiments and its capabilities have been determined through the conduction of simulations. In the simulation experiments, pipe deformations such as indentations or protuberances in the order of 1 mm and square defects as small as 2.0 by 2.0 mm wide were detected using a 3 MHz unfocused transducer. In the experiments carried out using a 3 MHz unfocused sensor with a sampling rate of 162 kHz, defects such as a crack as small as 0.5 mm x 12 mm and a 7 mm diameter hole were successfully been detected.

When the Time-of-Flight (TOF) method is used in combination with the aforementioned sensor, it has a theoretical lateral resolution of 5.76 mm at 150 mm and an axial resolution of 4 mm. Comparing the aforementioned values, with the defect sizes that have been seen when applying the new proposed

methodology, an improvement of 11 times in the lateral resolution and 4 times in the axial resolution have been achieved.

During the validation process, it was found that for the inspection of pipes, the scanner has to be precisely located at the centre of it. In order to address this problem, future research would focus on compensating the attenuation of the returning echoes when the transducer is located at an off-centre position and on control strategies for centring the sensor inside the pipe.

# Chapter 6

## Automatic Defect Detection

*The research described in this chapter focuses on the creation of an automatic defect detection system that will overcome the limitations of a manual inspection system with respect to subjectivity, varying standards and high costs. In this chapter a classification technique based on neural networks is investigated for the detection of defects in ultrasonic scans of inner sections of pipes immersed in liquids.*

## 6.1 Introduction

Manual inspection for surface defects in sewers has a number of drawbacks, including subjectivity, varying standards, and high costs. Automatic inspection systems based on artificial intelligence techniques can overcome many of these disadvantages by offering utility companies the opportunity to significantly improve quality of inspection and reduce costs.

Relevant research has been carried out in the field of automated sewer inspection most of it applied to CCTV images. Moselhi and Shehab-Eldeen [1999, 2000] are working on a model for automating the process of identifying and classifying several surface defects from digitised video images of sewers by using image analysis and neural networks. Sinha has developed a neuro-fuzzy algorithm to recognise and classify cracks in images from sewers [Sinha, 2002; 2003, 2004]. The Commonwealth Scientific and Industrial Research Organisation (CSIRO) in Australia, developed a system called PIRAT, for assessing sewers in real time. It is a multisensor system that builds a cylindrical-polar geometric model of the interior of the sewer using a laser scanner which automatically recognises, classifies and rates defects based on artificial intelligence tools [Kirkham, 2000]. Shehab-Eldeen [2002] and Moselhi [2000] developed a system, AUTO-DETECT, which automatically analyzes CCTV videotapes that depict the conditions of the surveyed pipes and consequently detects and classifies defects by using five sets with three separate neural networks in each set. Each set is specialized for one type of defect: Deposit, Cross sectional reduction, misalignment, infiltration and crack. Most recently, Duran [2004] developed an automatic classification system for defects in sewer walls. Her approach consists of detecting and categorizing defects according to their type. The input information is extracted from raw images; extracted intensity and position signals as well as the combination of both are transformed in a signature space where defective and non-defective signals are separated independent of their radial location.

As can be seen the most popular pattern recognition system used so far for sewer assessment is based in neural networks fed by CCTV images. This is a

consequence of the little or no availability of sensing systems for the inspection of liquid filled sections of sewers as was presented in chapter 2.

During the revision of related work, it was noted that the automatic inspection process, based on intelligent classification techniques, described by Duran [2003, 2002], Zhuang [1998] and Kirkham [2000], use light intensity variations and positional information gathered from images to feed a neural classifier. From the mentioned works, the approach proposed by Duran [2003] making use of the light intensity variations has shown to be highly reliable and robust.

It should be noted that even though the sensing methods in this research and those shown in [Duran 2003, 2002] are different, the behaviour of the intensities in the surface intensity plots are analogous to the intensity changes observed in the projected rings.

### 6.1.1 Chapter Overview and test procedure

In this chapter a classification technique based on neural networks is investigated for the detection of defects in ultrasonic scans of inner sections of pipes immersed in liquids, Figure 6.5. The chapter is organised in six parts. In section 6.2 a brief tutorial of classification techniques is presented. Sections 6.3 and 6.4 are related to the pre-processing stage of the automatic defect detection system. Surface intensity plots are presented as an intermediate step between the raw data gathered by the sonar and the data passed to the feature extraction technique. In addition, the use of filters and input normalisation for improving the quality of the data are discussed. Section 6.5, develops possible feature extraction techniques that can be applied to the present problem, explores their potential and shows a comparative analysis based on preliminary experiments, at the end choosing the most suitable one. In section 6.6, after having chosen the most appropriate feature extraction technique, the training set is tweaked in order to contain representative signatures of defective and non-defective sections. Finally, the base neural network architecture is optimized by varying the number of elements in the hidden layers of the neural network until the smallest and fastest one that can perform the classification task is found. Section 6.7 concludes the

chapter by discussing results from experiments carried out to determine the performance and the limits of the proposed system.

The following three-stage test procedure was adopted to explore the capabilities of the proposed classification scheme and, at the same time, to keep the number of experiments/trials to a minimum. In view of the involved components constituting the overall classification scheme, the emphasis of the first set of experiments was on finding the most appropriate pre-processing technique. Different widely used pre-processing techniques were exposed to data from the ultrasonic sensor and the outputs were fed into a neural network. These experiments were repeated varying the number of hidden layers and nodes. The best classification capabilities achieved with any of the subsequent networks were recorded and used for comparison with the other pre-processing techniques.

The performance measure was the capability of a pre-processing technique and subsequent network to distinguish between defective and non-defective pipe sections using training data and unseen data. The number of generated false positives and negatives were also compared. Further performance issues, such as processing speed were not investigated at this stage.

The second stage of this study was to optimise the network architecture for the chosen pre-processing technique. Two performance aspects were explored: (a) success rate and (b) processing time. Once again, the proposed system composed of a pre-processing stage and a neural network were exposed to a range of seen and unseen data from different PVC pipe segments, in order to establish the optimum architecture and explore its generalisation capabilities. In the final stage, the developed and optimised system was tested on data from different types of pipes to investigate the limitations of the system in very different environments.

## 6.2 *Classification and machine learning techniques.*

Pattern recognition is the science that concerns itself with the description or classification of measurements [Schalkoff, 1992]. Objects of unknown class such as a crack in a wall pipe, a root intrusion or a misalignment are sensed by an appropriate sensor, the sensed signals are pre-processed and observable features of the object are extracted, Figure 6.1.

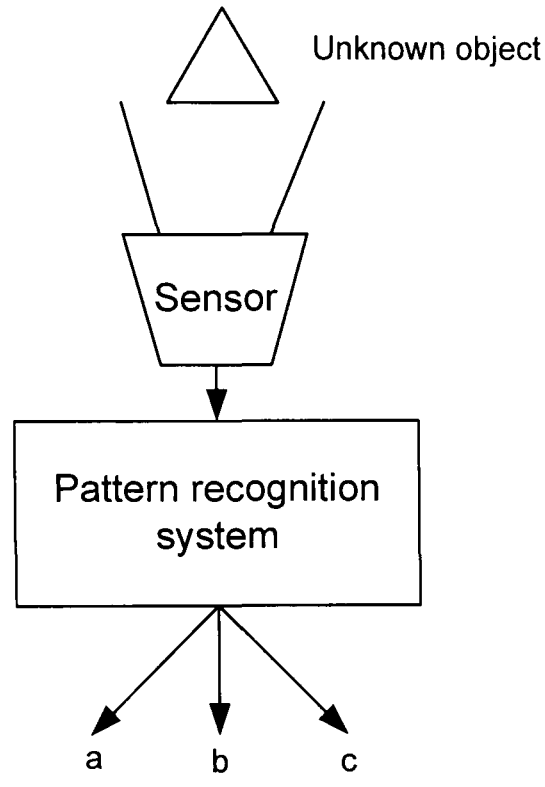


**Figure 6.1** Pattern recognition system

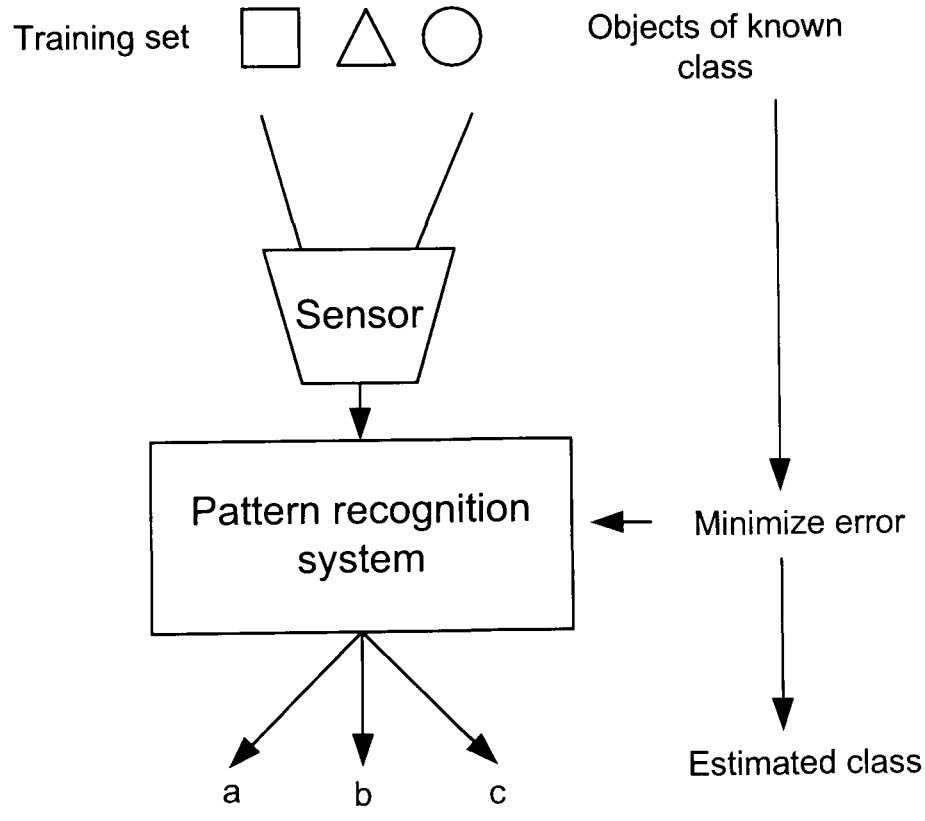


**Figure 6.2** Supervised Learning.

A Pattern Recognition system is able to estimate the class of an object, sometimes even with a measure of confidence (e.g. the object belongs to class A=80%, B=15%, C=5%).

In many Pattern Recognition applications, systems that learn from examples are used. In cases that the teaching is done by an expert, the system is named a "Supervised Learning" system. In Figure 6.2, an example of a supervised learning system in "training mode" is shown. A training set that has been previously classified by an expert is fed into the system, the system produces a result that at the beginning is likely to be wrong but iteratively through a learning methodology, the error between the training set and the estimated class is minimised. Other systems use unsupervised learning schemes. They are capable of determining classes in an input set without supervision. Two very simple classic examples of unsupervised learning are clustering and dimensionality reduction.

The key principle in pattern recognition systems is that the extracted features of the object are mapped into a feature space. The dimensionality of this space is as large as the number of features used. Figure 6.3 shows a feature space: objects with two measured features, $x$ and $y$, are represented as a point $P$ in a two dimensional space. If a linear function is suitable to discriminate between the two classes, then the learning set can be used to estimate the parameters of this line. The line equation will be used to classify newly observed samples between classes $A$ and $B$. However, due to the linearity of the classifier used for this example, this system is bound to make errors if classes are entangled or, worse, overlap.

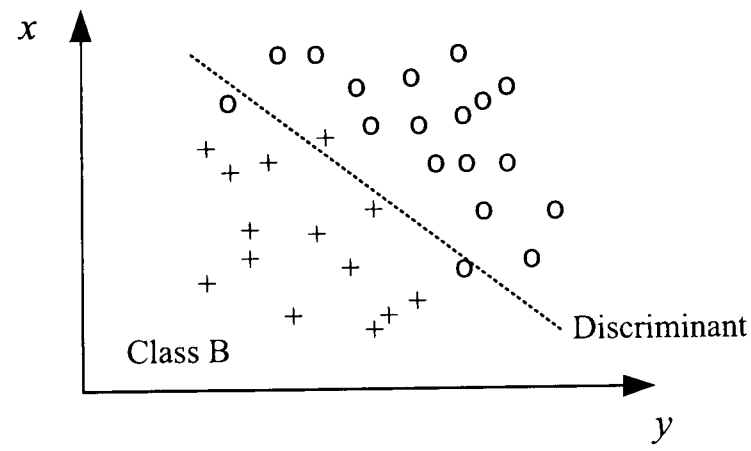


**Figure 6.3** Feature space and a linear discrimination function

There are several methods to obtain the discriminant function or approximate it. The fastest method is to use the features in a decision tree. In this

way the discriminant function is approximated with line segments parallel to the feature axes. This yields a fast but moderate performance. Moreover, it is a difficult procedure to find the threshold values for each feature in the decision tree.

The K-nearest neighbour classifier [Dasarathy, 1991] is another approach. It works by labelling an unknown object with the label of the majority or the K nearest neighbours. The discrimination function implemented by this classifier will in general be a jagged, piece-wise linear function since it is influenced by each object available in the learning set. A disadvantage of this method is its large computing power requirement, since for classifying an object, its distance to all the objects in the learning set has to be calculated [Bishop, 2003].

It can be said that the most popular classifier is based on artificial neural networks. An artificial neural network (ANN) attempts to emulate, in a simple way, the human mental neural structure and functions [Hsieh, 1993]. For the reader not familiar with neural networks, a tutorial about neural networks techniques can be found in appendix E.

In the following sections, an in depth study of the application of neural networks for the detection of defects in pipes inspected by using ultrasonic scanners is presented and its overall performance as a system, Figure 6.5, is assessed.

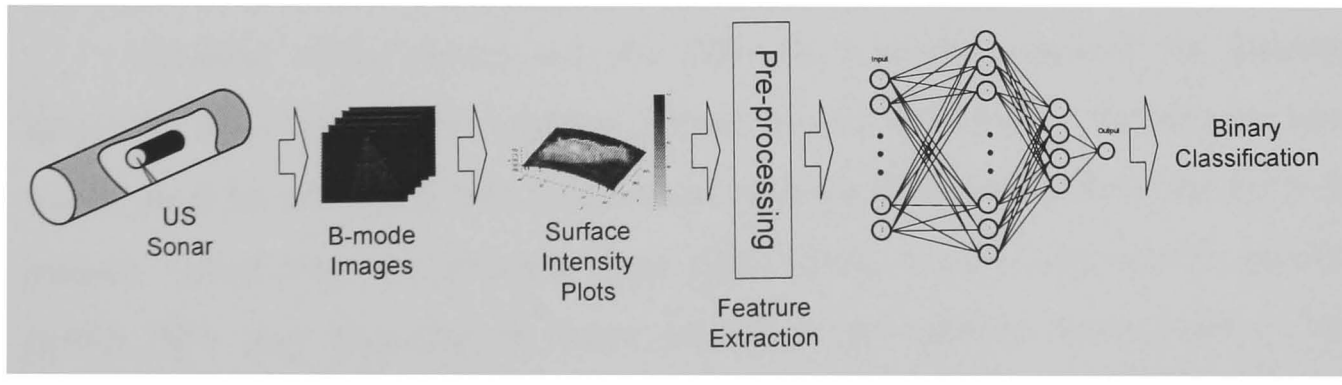


**Figure 6.4** Architecture of the automatic defect detection system.

## 6.3 *Surface Intensity Plots (SIP) - Representation*

As discussed in chapter 5, surface intensity plots (SIP) are the result of a non linear transformation applied to a set of B-mode images. SIPs are a graphic

representation of a sewer inner wall created by plotting the peak intensity of each echo in a three dimensional plot. The $x$, $y$ and $z$ coordinates where the echo is plotted, correspond to the point in the pipe wall which generated the echo. Such coordinates are calculated by means of the position of the sensor and the measured time of flight of the echo. SIPs are not only a graphical representation of the inner pipe wall, but can also be used to analyse the behaviour of the intensity information. This information can be exploited for the detection of minute defects. As discussed in chapter 5, they are capable of enhancing the presence of defects that are smaller than the sensor resolution.

It is proposed here to use the intensity information from the surface intensity plots in the form of a N by N matrix, pre-process the intensity information, extract the most relevant features into an input vector and feed it to a binary neural classifier.

## 6.4 Data Pre-processing

As shown in chapter 3, the sewer assessment system consists of a rotational ultrasound sonar scanning the submerged parts of sewers. This scanning procedure generates raw data in the form of B-mode images, see Figure 4.1. These images are then processed to extract a three dimensional profile of the inner section of the sewer keeping also record of the intensity of the returned echo for each point in space, namely surface intensity plots (SIP).

Chapter 4 has shown that the SIPs are powerful methods for locating defects in three dimensional profiles of inner sections of sewers. The original idea was to feed the automatic detection system with the SIPs created from the B-mode images. Observing data gathered from experiments, it was noted that the quality of the SIPs was degraded by noise present in the sensing system and in the surrounding environment. There are a number of different tools and methods that are normally used for pre-processing data before it is fed to a neural network: sampling, which selects a representative subset from a large population of data; transformation, which manipulates raw data to produce a single input; denoising, which removes noise from data; normalization, which organizes data for more efficient access; and feature extraction, which pulls out specific data that is

significant in some particular context. For this research, denoising, normalisation and feature extraction were studied. In the following section, denoising and normalization are to be discussed and feature extraction methods will be discussed in section 6.5.

### 6.4.1 Denoising

Noise is defined in the English Oxford dictionary as: random or irregular fluctuations or disturbances which are not part of a signal, or which interfere with or obscure a signal; oscillations with a randomly fluctuating amplitude over a usually continuous range of frequencies. In our case the noise present in the original signal, the echoes returning from the pipe wall, passes through a non-linear transformation that is used for creating the surface intensity plots. Due to the nature of the transformation, noise is seen in the surface intensity plots, degrading the quality of the position and intensity components. For the approach proposed in this work, where the intensity variations are going to be fed into a neural classifier in order to detect sharp edges caused by defects, it is desirable that noise present in the SIPs is removed or minimised. In Figure 6.5, a three dimensional plot showing the intensity variations for each one of the returned echoes, created from a scanned section of a plastic pipe with a cut slot, is presented. The $z$ axis represents the maximum intensity of the received echoes. The positive and negative peaks are caused by high frequency noise superimposed on the intensity data. In order to remove the noise, two filters techniques were explored: mean and median filter.

The mean filtering replaces each intensity value in the SIP with the mean value of its neighbours, including itself. This has the effect of eliminating values which are unrepresentative of their surroundings. Mean filtering is usually thought of as a convolution filter. Like other convolutions it is based around a kernel, which represents the shape and size of the neighbourhood to be sampled when calculating the mean. The size of the kernel depends on the amount of smoothing required.

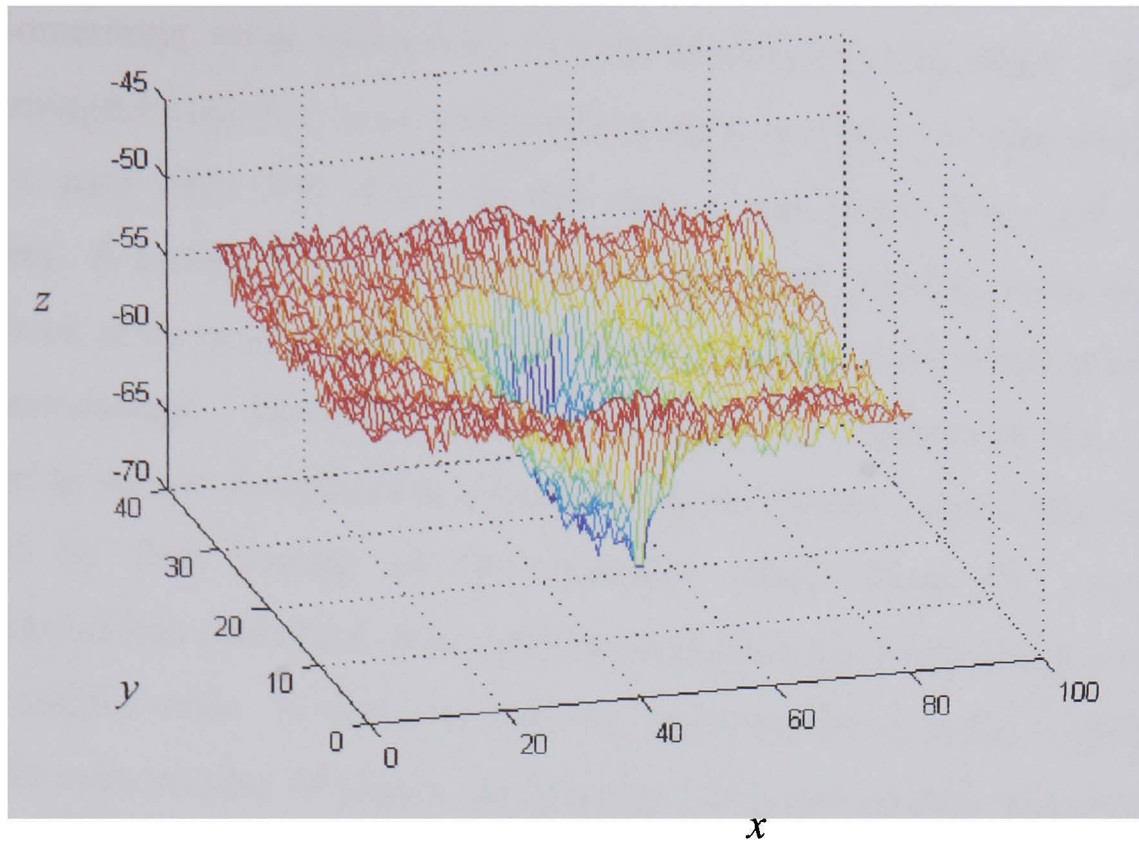


**Figure 6.5** Surface intensity plot showing a scanned section of a 300 mm PVC pipe with a slit. Raw data

A trial and error study was carried out, evaluating different kernel sizes and different kinds of data. It was seen that for most of the cases, a 5x5 kernel give an acceptable smoothing, see Figure 6.6. It should be noted that the size of the kernel will be determined by the resolution of the SIP and the signal to noise ratio.

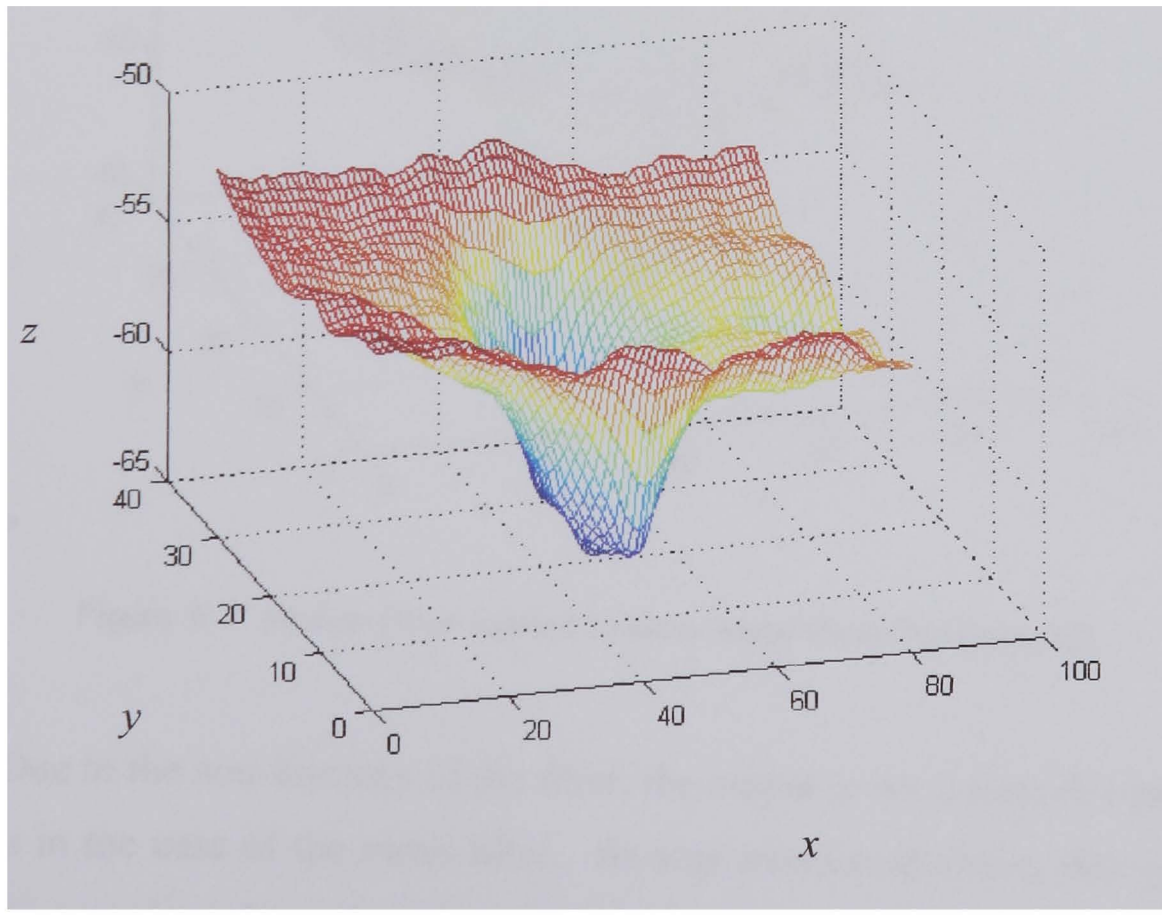


**Figure 6.6** Mean filter applied to noisy image shown in Figure 6.5

Sometimes, when processing two-dimensional signals, those signals can have meaningful high frequency components, such as edges and fine details that a linear low pass filter will alter. In this case a non linear filter will be more appropriate. A median filter, in this case, will take each intensity value in the SIP and will look at its nearby neighbours to decide whether or not it is representative of its surroundings. Instead of simply replacing the value with the mean of neighbouring values, it replaces it with the median of those values. The median is calculated by first sorting all the intensity values from the surrounding neighbourhood into numerical order and then replacing the value being considered with the middle value. In the case that the neighbourhood under consideration contains an even number of pixels, the average of the two middle intensity values is used. For this case, a square kernel was implemented as well. Using a trial and error methodology, it was found that a 5x5 kernel gives an acceptable cleaning of the signal, see Figure 6.7.

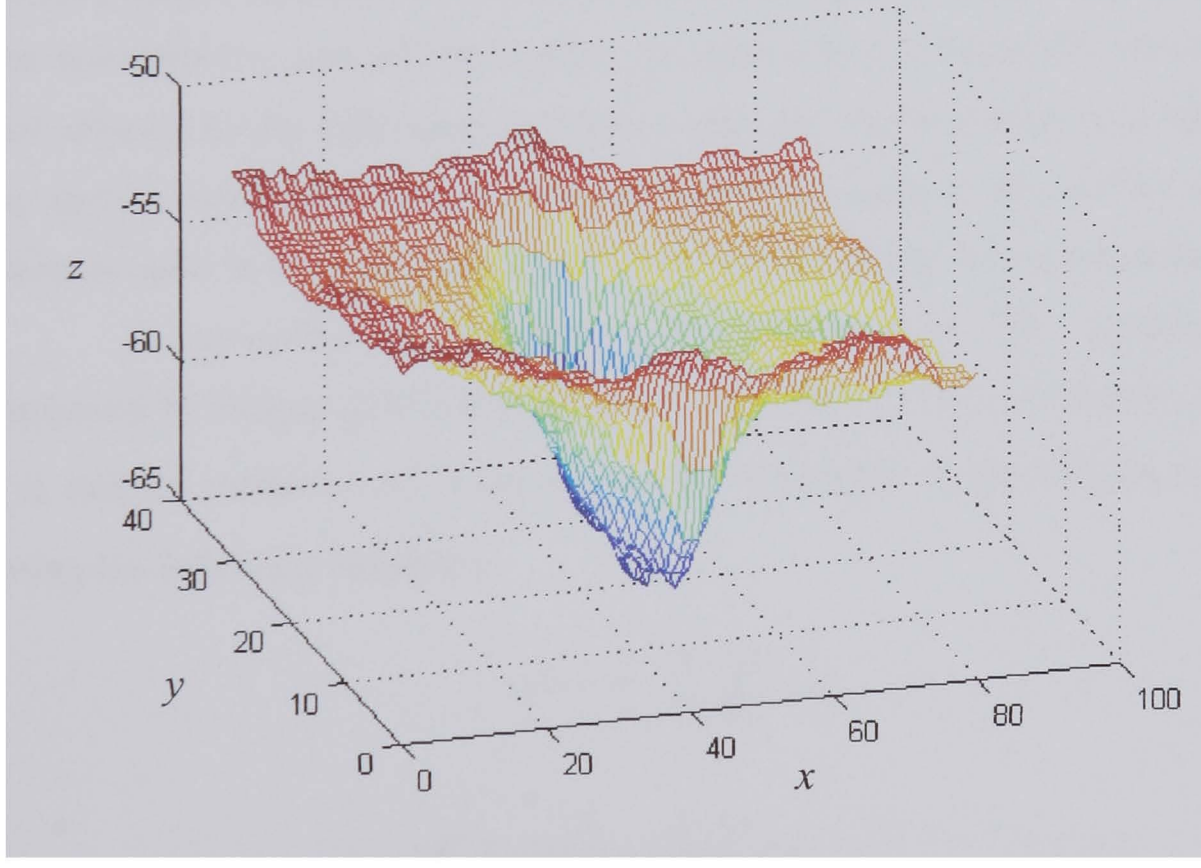


**Figure 6.7** Median filter applied to noisy image shown in Figure 6.5

Due to the non-linearity of the filter, the output is not a smooth continuous signal as in the case of the mean filter. As was mentioned above, this could be advantageous when detecting edges but on the other hand, it can mask small

defects due to the stepped behaviour of the output. Based on previous experience, the mean filter works well in most of the cases, but when it fails, a median filter has shown to be a good alternative.

### 6.4.2 Input normalization

One of the most common forms of data pre-processing is input normalization. Normalisation leads to the rescaling of the input variables. This is crucial when the range of the input variables differ considerably. In the particular case of this research where the intensities of three dimensional surface maps are being processed, the absolute values for the intensities are not important but their variations with respect to the average conditions of the pipe wall. Different scenarios (i.e. different pipe surfaces, different pipe diameters) will give different absolute intensity values but when defects are present in such pipes, the behaviour of the intensity information inside the defective area with respect to the values of the non-defective area will be similar. In order to have a diagnostic system that is not affected by the differences in sensors and pipe characteristics, it is mandatory to apply a linear transformation to the intensity values of the surface intensity plots in order to normalize its values before they are fed to the neural classifier.

To normalize the intensity values present in a SIP, a methodology proposed by Bishop [2003] will be used. For a SIP with $i$ x $j$ elements, the mean ($\mu$) and the variance ($\sigma_i^2$) values of all the intensities in the SIP are calculated using the following equations,

$$\mu = \frac{1}{i \times j} \sum_{k=1}^{i} \sum_{l=1}^{j} x_{kl} \,, \tag{6.1}$$

$$\sigma_i^2 = \frac{1}{(i \times j) - 1} \sum_{k=1}^{i} \sum_{l=1}^{j} (x_{kl} - \mu)^2 \,. \tag{6.2}$$

Then a new SIP with normalised intensities ($\tilde{x}_{kl}$) will be created by

$$\tilde{x}_{kl} = \frac{x_{kl} - \mu}{\sigma_i} \quad for\ k = 1,...,i; l = 1,...,j \,. \tag{6.3}$$

The intensities in the resulting SIP will have zero mean and unit standard deviation over the transformed set.

## 6.5 *Feature extraction*

In many classification problems, it is unclear which are the relevant features to consider. A common problem in pattern recognition systems is the choosing of the number of features to be used to describe a sample. Given a limited number of samples, the number of features has to be restricted in order to be able to construct sensible classifiers. This problem is usually referred to as the curse of dimensionality [Jain, 1978], keeping the number of samples fixed and increasing the number of available features will eventually lead to badly performing classifiers, Figure 6.8.

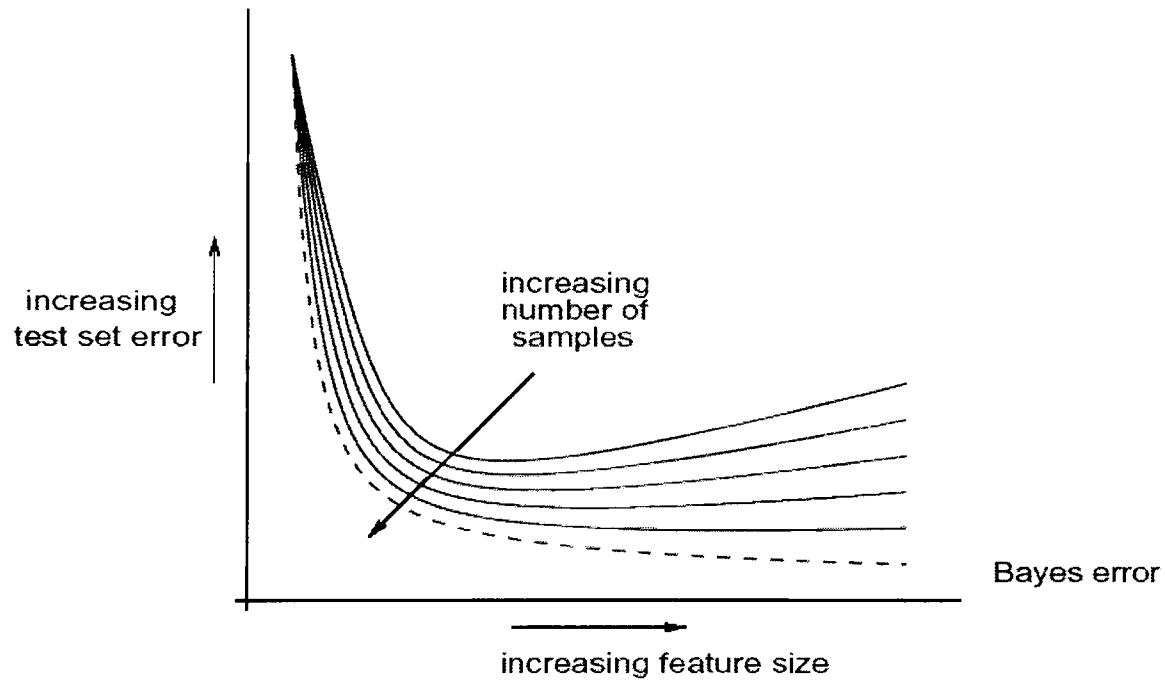


**Figure 6.8** The curse of dimensionality. For a fixed number of samples the error of a classifier will eventually increase when increasing the number of features.

Often a large set of $k$ potentially useful features is collected and two approaches can be used: feature reduction or feature extraction. In the first case, the $k$ most suitable features are chosen, creating a subset of the original feature set. Using feature extraction, new features are derived from the original features. All the original features are used and no reduction is obtained in the number of elements passed to the neural network, but in many cases, the optimization is easier [Chen, 2005].

Feature extraction is an important stage for any pattern recognition task and the studied case is no exception. Pipe defects are highly variable and finding reliable and robust features that can be used to identify them is a challenging task. The salient features of a data set can be extracted through a mapping, such as Fourier transform, discrete cosine transform, Karhunen–Loeve transform, or principal component method, usually reducing a higher dimensional input space to a lower dimensional representation space [Sinha, 2002].

For the case studied here, the raw data delivered by the sonar is pre-processed and converted into a new representation to facilitate the detection of defects, as presented in chapter 5. This transformation greatly reduces the amount of data to be handled by extracting relevant information from the B-Mode images. The reduction in the number of inputs and data points, will considerably improve the response time of the envisaged automatic defect detection system. Instead of processing a series of B-mode images, each one containing $x$ by $y$ data points, the detection system just has to process a series of vectors with $x$ points.

The information stored in the surface intensity plots can be either passed directly to the neural network or it can be further processed and its most important characteristics fed to the neural network. It should be noted that if a SIP is going to be fed directly into a neural network, it will have to have always the same dimensions, because, the number of inputs in the input layer of the network is usually fixed. However, the size of the SIP will depend on the width of the swept area (chapter 5). In order to have a neural classifier which is able to identify defects in SIPs regardless of the size of the SIP, it is desirable to have a methodology that can extract information and put it into a vector of constant size. The key issue is to have a technique that will create a data subset of the SIP with a fixed number of values to be fed into the neural network. The following sections describe the experiments carried out to find the most suitable technique for this purpose.

### 6.5.1 Sorting Algorithm

As mentioned in the introduction of this chapter, when a section of a pipe is scanned and a SIP is generated, the intensity values in the SIP behave in an

analogous way to the changes in intensity observed using the camera laser profiler approach described in Duran [2003]. Due to the affinity between both methods, it was decided to adapt and try this approach and to study its applicability to our study case.

Duran used a sorting algorithm as the feature extraction technique for processing the intensity information from the projected ring sensed by the CCTV camera. Once an intensity profile is extracted from the image by using image processing techniques, the first derivative of the signal along the longitudinal axis is calculated to emphasize intensity variations. Even though this data could perfectly be fed directly to the neural network, Duran proposed to create a signature as follows.

The intensity data received from each pipe section is made of individual samples, which are sorted by signal amplitude in descending order using a quicksort algorithm [Hoare, 1962]. As a result, any defective section having one or more intensity peaks, will be converted into a monotonically decreasing sequence. A normalisation step is then applied by subtracting the maximum value on the section from all the other data points. This is done for all the sections. The resulting signature is a monotonically increasing sequence starting from zero, where the non-defective sections will appear as flat signals with values very close to the origin. Defective sections, however, will appear as signals with a sharp slope at the beginning before reaching a high plateau, Figure 6.10 [Duran, 2003].

The sorting algorithm was implemented and tried with a SIP containing three holes with different sizes, in order to evaluate its potential to be used as a feature extraction methodology for the ultrasound pipe inspection. The intensity matrix of the SIP used as input for the feature extraction algorithm is shown in Figure 6.10(a) and the vector array corresponding to the output of the sorting algorithm is presented in a three dimensional plot in Figure 6.10(b). In Figure 6.10(b), each $y$ row corresponds to a sorted vector obtained after applying the sorting algorithm to the corresponding row in the intensity matrix (Figure 6.10a)). As can be seen in Figure 6.10(b), there are three mayor peaks which stand above the rest of the data. They are located at $y$ rows: 96, 51 and 25 respectively. They can be matched with the locations of the three holes present in the test set.

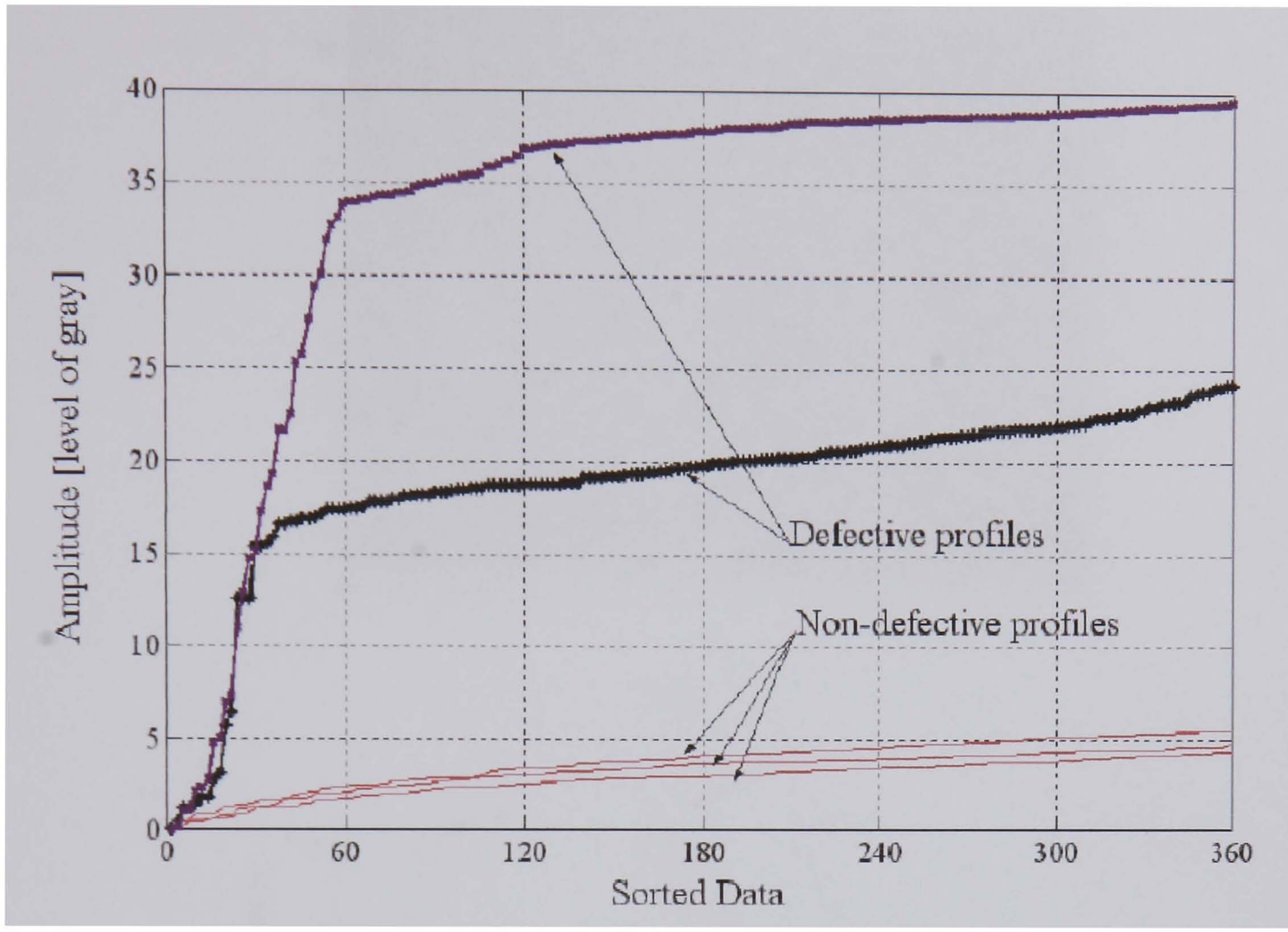


**Figure 6.9.** Normalised signature of defective and non-defective profiles gathered from using a laser base profiler. Defective Profiles irrespectively of the angular position of the defect produce a similar signature and differ considerably from non-defective profile signatures [Duran, 2003].

These results show the potential of the sorting algorithm for being used as a feature extraction technique. The capabilities of the sorting algorithm will be evaluated in more detail at the end of this section by feeding the feature vector generated by the sorting algorithm into a prototype neural classifier.

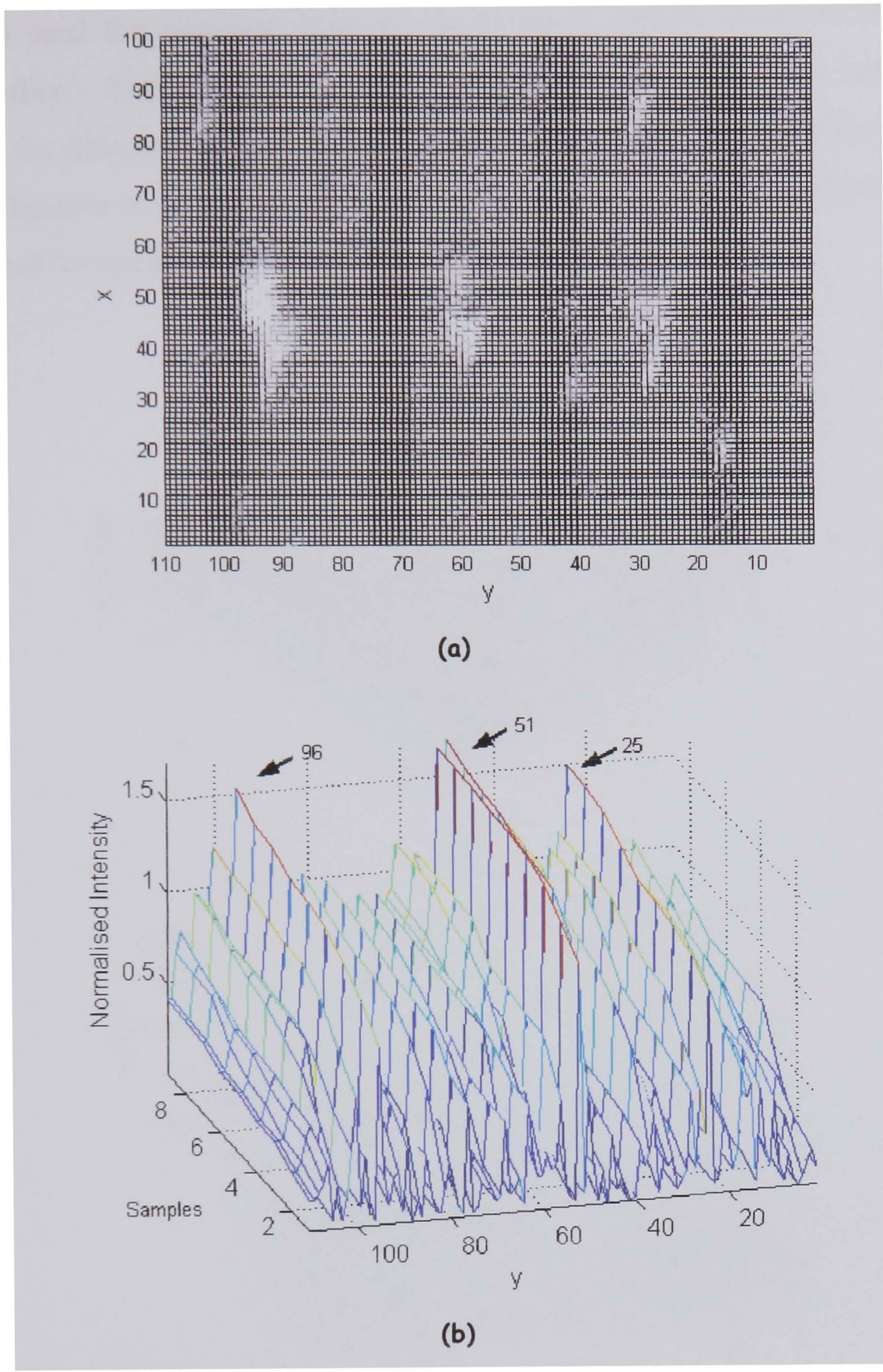


**Figure 6.10** Feature extraction, evaluation of sorting algorithm. (a) Test set: surface intensity plot with three defects located at 25, 51 and 96. (b) Output of sorting algorithm.

### 6.5.2 Fast Fourier Transform (FFT)

The FFT is a well known technique that has been extensively discussed in the literature as a method for extracting features from images [Weaver, 1983; Pratt, 1991]. In the case of the SIPs, the system will be dealing with intensities in a plane which makes it suitable for the application of the FFT. Recently, FFTs

have been used for detecting intensity variations in surface maps created by a Laser profiler. The intensity variations of the Laser profiler were used as a technique for detecting defects in images independent from their location [Duran, 2002c]. Because of its potential, the FFT technique was evaluated using the same test set used for testing the sorting algorithm section 6.5.1.

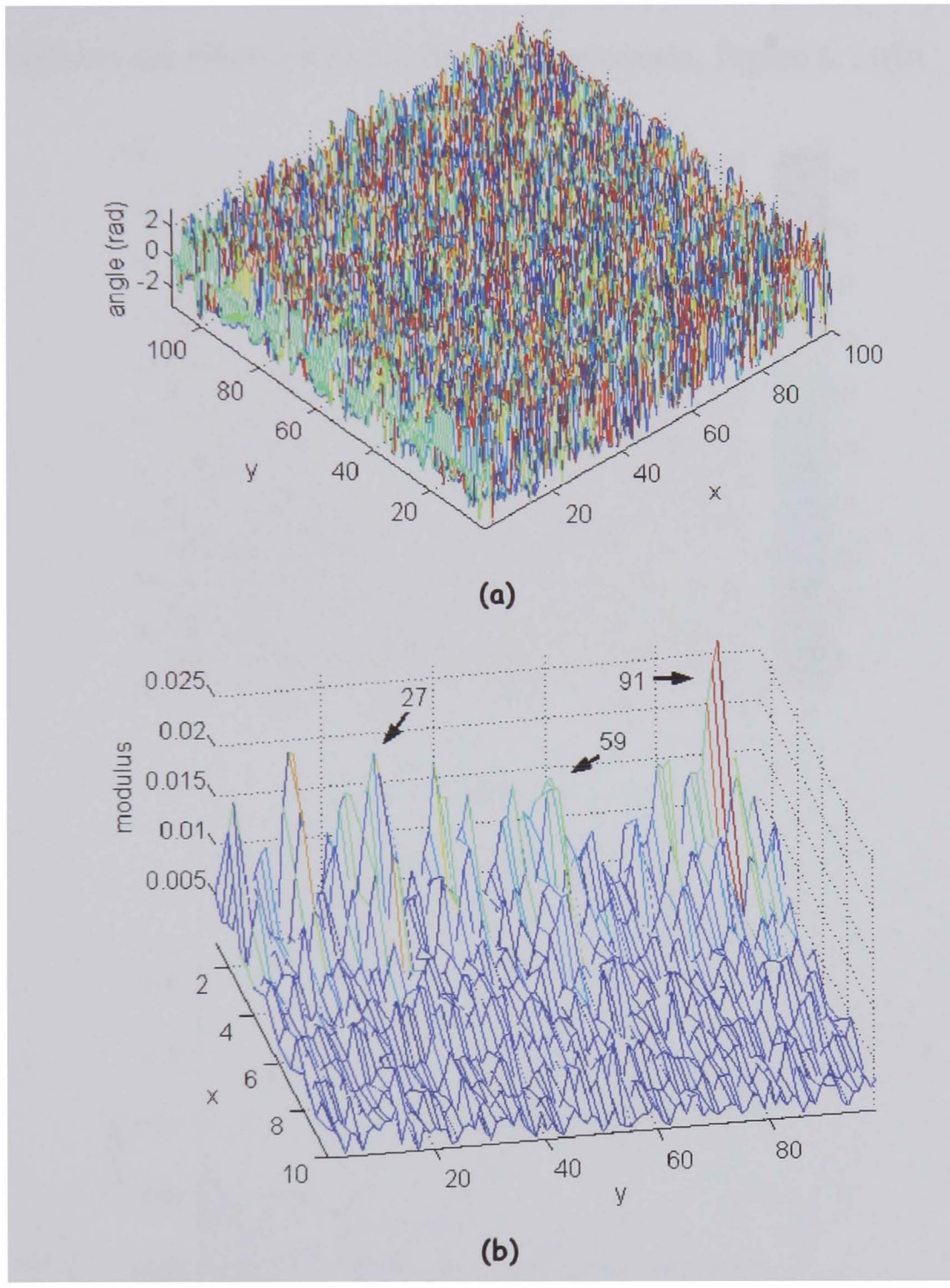


**Figure 6.11** Fast Fourier transform evaluation as feature extraction technique for automatic defect identification. The FFT was calculated from a test set with three defects and the output is plot in mesh graphs (Figure 6.9(a)). (a) Phase (b) Complex modulus.

In Figure 6.11, the phase (a) and the modulus (b) of the complex output of the FFT calculated from the test set are shown. The same test data as used in section 6.5.1 was used, Figure 6.10(a). As can be seen, the phase does not show any correlation with any of the defects present in the test set. However, in the section corresponding to the lower frequencies, the first components show some variations that could be matched with the presence of the defects in the test set. These variations are observed in the first 6 components, Figure 6.11(b).

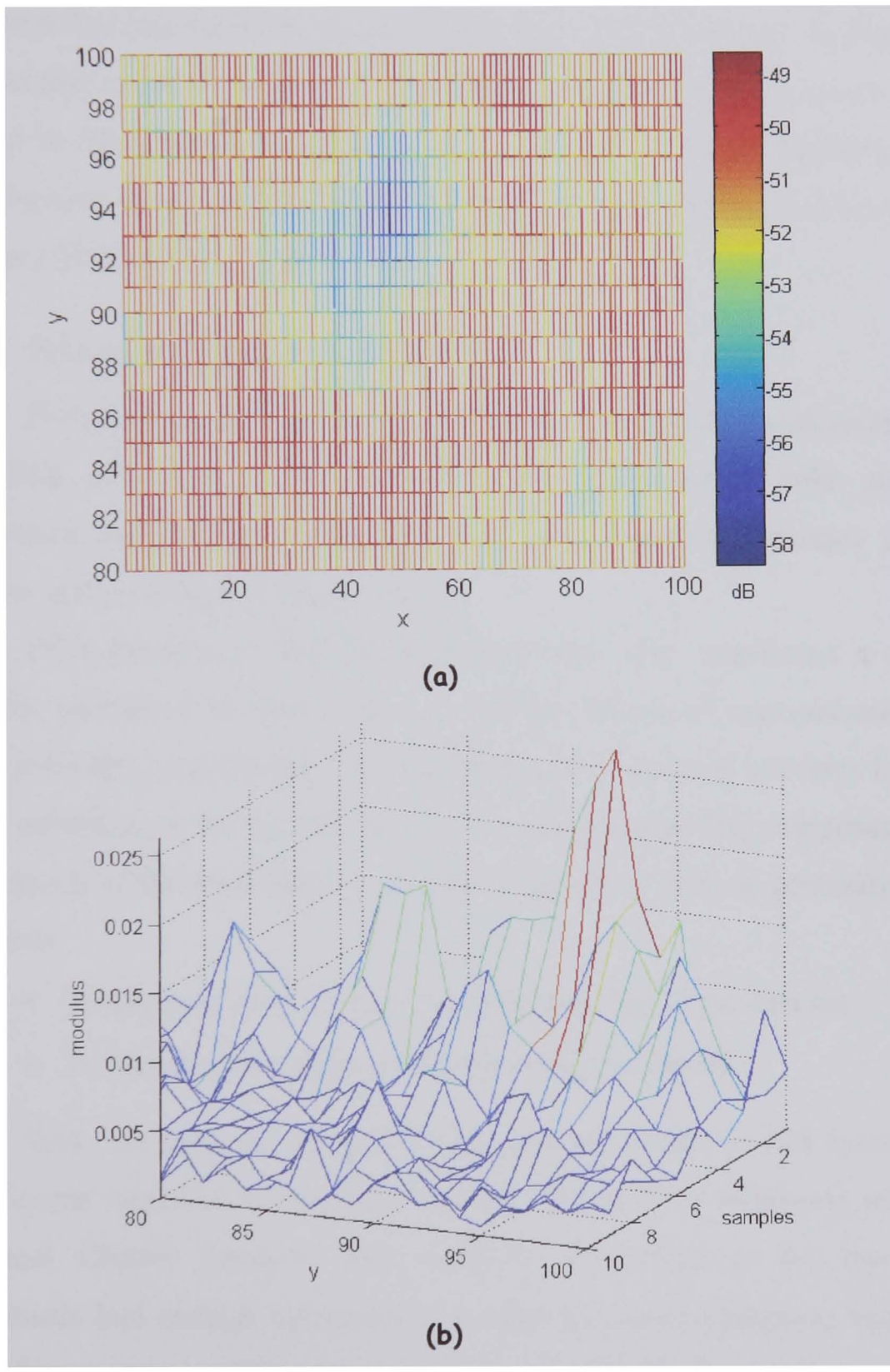


**Figure 6.12** FFT analysis. Expanded view of the area from 80 to 100 where the biggest defect in test set is located. (a) SIP two dimensional view (b) FFT - Complex modulus.

Carrying out a close analysis of Figure 6.11(b), it is seen that there are three peaks at locations 91, 59 and 27 than can be associated with the occurrence of the defects in the test set. There are other five peaks at locations: 2, 14, 40, 46 and 80 with lower amplitude that could be associated with the intensity changes caused by misalignments and noise. In Figure 6.12(a), an expanded view of the biggest defect present in the test set (rows 80 to 100) is shown. In Figure 6.12(b) the complex modulus of the FFT calculated from the test set is shown. The peak present in the complex modulus at line 91 (Figure 6. 12(b)) perfectly correlates with the area around line 91 in Figure 6.12 where the intensity is low due to the presence of the defect.

### 6.5.3 Principal Components Analysis

Principal components Analysis (PCA) is a standard statistical technique [Hotelling, 1933; Rao, 1964] that has found application in fields such as face recognition and image compression, and is a common technique for finding patterns in data of high dimensionality.

PCA involves a mathematical procedure that transforms a number of possibly correlated variables into a smaller number of uncorrelated variables called principal components. The first principal component accounts for as much of the variability in the data as possible, and each succeeding component accounts for as much of the remaining variability as possible. PCA is generally used with two aims:

- To discover or to reduce the dimensionality of the data set.
- To identify new meaningful underlying variables.

Here, the capacity of the PCA of creating a reduced data set maintaining the relevant information from the original SIP will be evaluated and applied. Statistical Cluster Analysis was used for evaluating if the two principal components had enough information in order to classify defective sections from non-defective ones. This technique was specifically designed for classifying observations on behalf of their relative similarities with respect to a multidimensional array of variables [Peneder, 2005; Kaufmann and Rousseuw, 1990]. Statistical cluster analysis allows to [Jerran and Cheadle, 2000]:

- Automate the procedure of classification, making it objective and stable; analyse very large data sets in a short period of time and quantify complex data.
- Discern and quantify group associations that are not readily identifiable by the naked eye, providing unbiased methods to recognize clusters.
- Explore how group associations vary within a data set.

The aim of this study is to evaluate the potentiality of PCA for being used as a feature extraction technique for the binary classifier. As a result, the most common and simplest cluster analysis technique was used, single linkage [Florek et al, 1951]. Single linkage is known as well as nearest neighbour and is one of the simplest agglomerative hierarchical clustering methods. Such methodology consists of three phases: First, a matrix that computes pair-wise Euclidean distances between all possible input pair combinations in the n-dimensional input space is created. Second, a cluster hierarchy is built using the smallest distance ($D(r,s)$) between one of the individuals within one cluster to one of the individuals in adjacent clusters. This is computed as,

$$D(r,s) = Min(d(i,j)) \tag{6.4}$$

where $d(i,j)$ is the Euclidean distance of object $i$ in cluster $r$ and object $j$ in cluster $s$. At each stage of hierarchical clustering, the clusters $r$ and $s$, for which $D(r,s)$ is minimum, are merged. Third, the linkage data is used to force the data into a predefined number of clusters. It should be noted that as an agglomerative technique, the first time the algorithm is run, the number of clusters is going to be equal to the number of data points. If a predefined number of clusters is not specified, the algorithm is going to keep running until one cluster grouping all the data points is formed.

The first and second principal components were classified into four clusters using the previously described procedure. Results are presented in the form of a scatter plot in Figure 6.13.

Each one of the data points grouped in the clusters was checked to see if they correspond to a defective or non-defective section. The idea behind this

analysis is to evaluate if the clusters that are being created from the features extracted by the PCA can be used for identifying defective sections. From this analysis, it was observed that Cluster 1 is grouping the values associated with non-defective sections, and clusters 2, 3 and 4 are grouping values associated with two of the three holes present in the test set. Only the biggest and medium holes are being grouped by the PCA technique, the smallest of the defects is not being separated from the cluster grouping the non-defective sections.

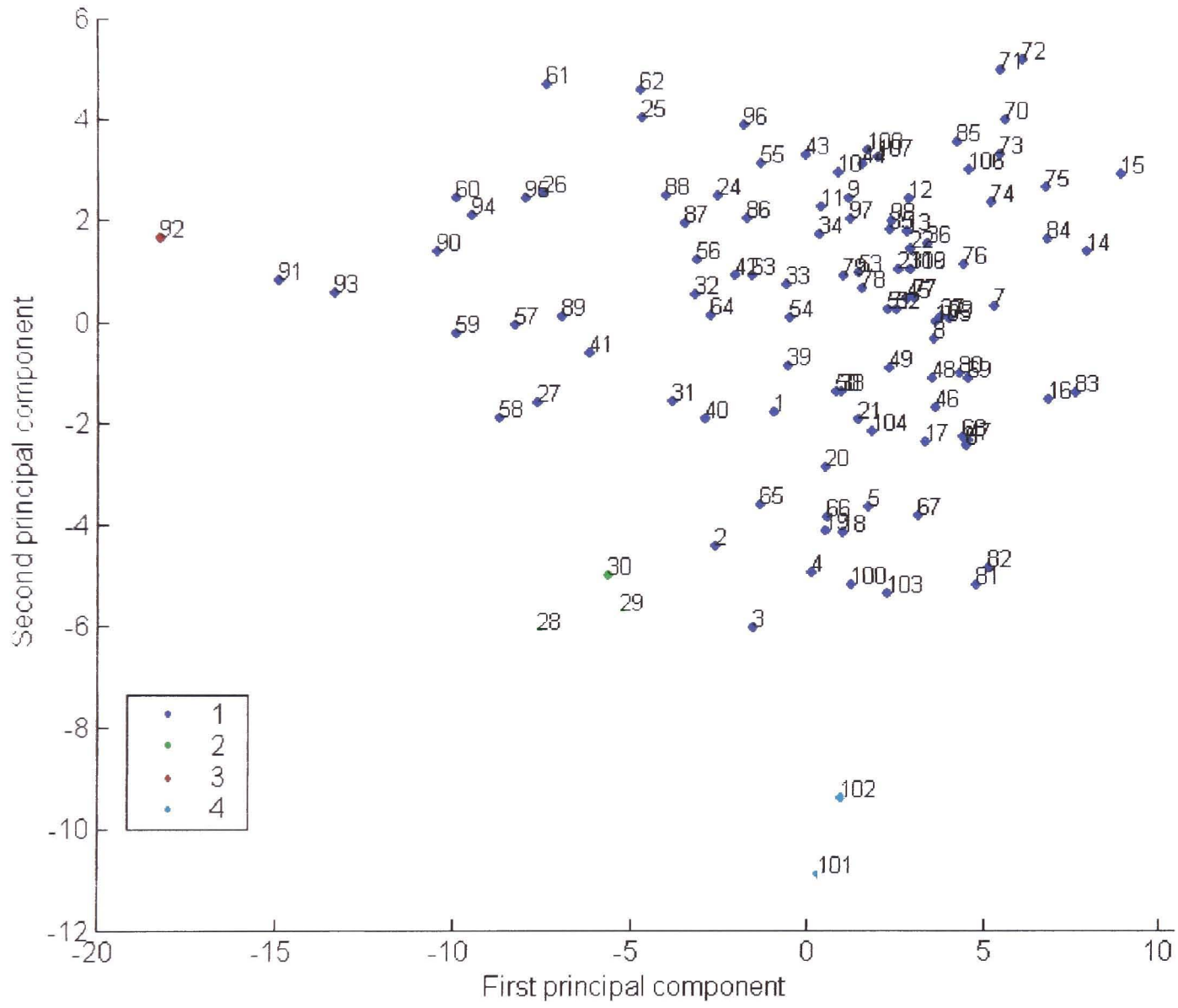


**Figure 6.13** Cluster analysis of Principal components. The first and second principal component of a surface intensity plot with three defects (holes) are shown in a scatter plot. Cluster 1 is grouping the values associated with non-defective sections, and clusters 2, 3 and 4 are grouping values associated with two of the three holes present in the test set (medium and large holes).

The previous results show that the PCA method has potential for extracting features containing relevant information for detecting defects in SIPs.

However, the disadvantage of using the PCA technique in this way is that the size of the features vector obtained from the first two principal components will depend on the size of the image being analysed. As a consequence, the number of neurons in the input layer of the ANN will have to be variable for each different scenario, making not possible to use a neural network.

The proposal to overcome this limitation is to use the PCA technique in a subset with fixed dimensions, in order to transform the data into two feature vectors with fixed dimensions. In this way, the topology of the neural network can be fixed.

It should be noted that a linear componential technique, such as PCA, widely used for learning the statistical structure in images, forms distributed representations that are well suited to high dimensional data. These models are linear and assume fixed statistics over the entire ensemble of the data. The goal of these technique is to separate out the independent components in a signal but the resulting representation could exhibits residual dependencies and non-stationary statistics [Karling and Lewicky , 2005]. As a consequence, the size of the subset is an important parameter to consider. There is a compromise between the size of the subset and the significance of the generated feature vectors, the smaller the subset, the less information that can be extracted from them.

In order to have the maximum amount of data points possible, The subset will be a rectangular moving window which is grouping together a pre-defined number of rows of the intensity matrix $I$ with size $p$ x $q$,

$$I_{(p,q)} = \begin{bmatrix} I_{(1,1)}, \cdots, I_{(1,q)} \\ \vdots \quad \ddots \quad \vdots \\ I_{(p,1)}, \cdots, I_{(p,q)} \end{bmatrix}. \tag{6.5}$$

A window, $W_{(m,q)}$, will be sweeping the intensity matrix from the first row until the row ($p$-$w$+1), Figure 6.14 where $p$ is the number of rows in the intensity matrix and $w$ is the size of the window,

$$W_{(m,q)} = \begin{bmatrix} I_{(m,1)}, \cdots, I_{(1,q)} \\ \vdots \quad \vdots \\ I_{(m+w-1,1)}, \cdots, I_{(m+w-1,q)} \end{bmatrix}; \quad \begin{matrix} w = window\,size \\ m = 1, 2, \cdots, (p-w+1) \end{matrix}. \tag{6.6}$$

A PCA will be applied to each window *W(m,q)* and the resulting first principal component vector ($PC_1$) and the second principal component vector ($PC_2$) will be organized into a feature vector (*PCO*),

$$PCO(m) = [PC_1(z), PC_2(z)];\ z = 1, 2, \cdots, w, \tag{6.7}$$

which later will be fed to the neural network.

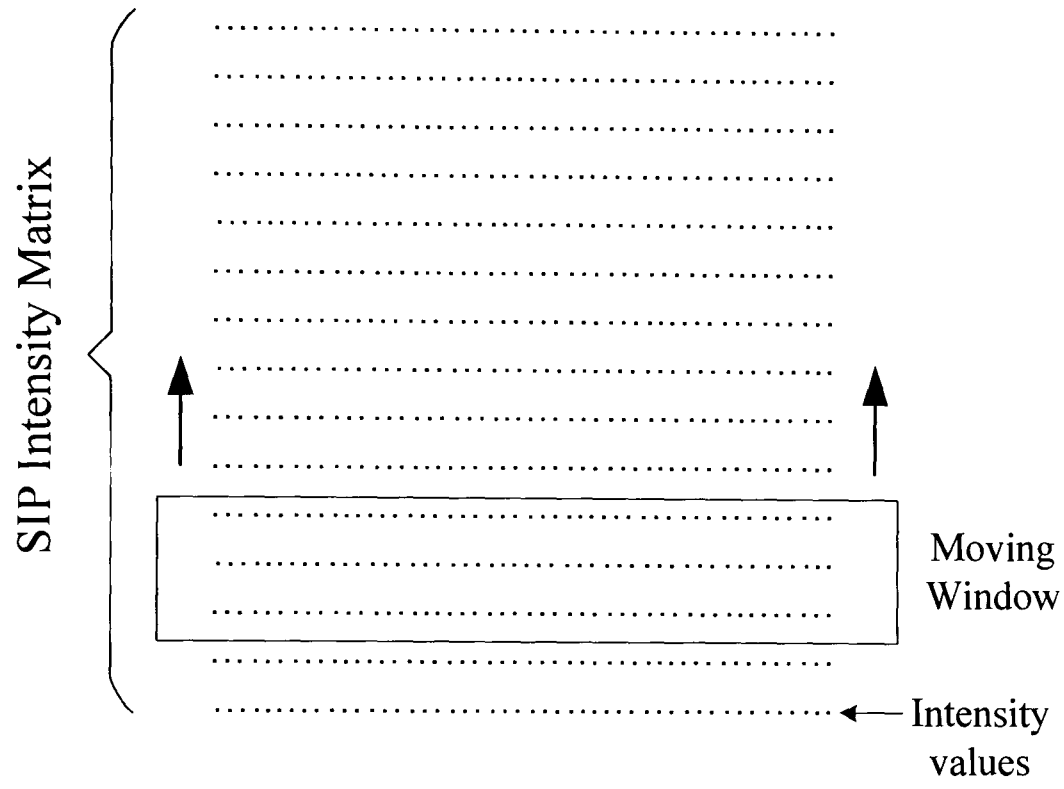


**Figure 6.14** Principal component analysis, moving window. Illustration of the method

The proposed methodology was applied to the test set by using a rectangular moving window which is grouping five rows at a time and generating a first and second principal component vectors with 5 elements each one. All the first and second principal component vectors were analysed by using the cluster analysis technique described above and by forcing it to group the data into four clusters. Results are presented in the scatter plot in Figure 6.15.

For generating the scatter plot, all the calculated principal components were organised sequentially in the same order as they were generated, creating two vectors, one with all first principal components and other with the second. Because the set was made of 110 rows with 100 elements each one, 106 principal components were calculated, each one containing 5 elements. After grouping them, two vectors with 530 elements on each one were created.

In order to find the starting position of the moving window which generated each pair of principal components, the element number in the vector that is grouping the given principal components is to be divided by the size of the moving window, in this study case: 5. This was done for determining the positions of the windows that generated every element grouped in clusters 2, 3 and 4. It can be seen that the cluster 1 is grouping all the non-defective areas of the intensity profile, cluster 2 is associated with the non-defective areas where the intensity is changing due to noise or misalignments and clusters 3 and 4 are grouping the values associated with the biggest hole.

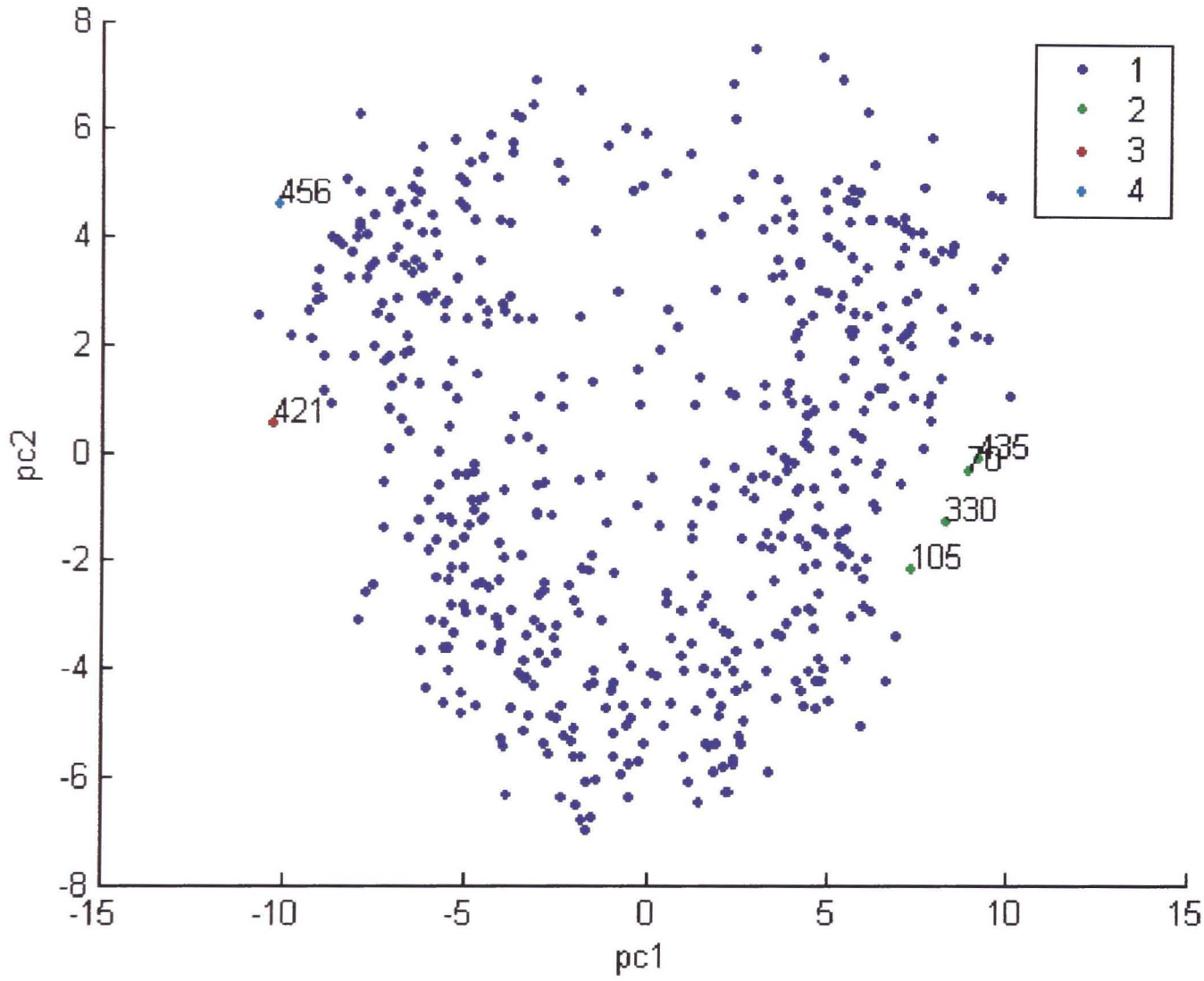


**Figure 6.15** Principal component analysis pre-processing method implemented as a moving window. A moving window grouping five rows at a time was used to calculate the PCA from the test set, a surface intensity plot with three defects. The element number is plotted next to each value present on clusters 2, 3 and 4. Cluster 1 is grouping all the non defective areas, cluster 2 is associated with non defective areas with noisy values and clusters 3 and 4 are associated with the third defect (biggest hole).

It should be noted that the small and the medium defects were not distinguished from the non-defective sections and that cluster 2 and 3 have only one element each one. Comparing the results from applying PCA to the whole image or to a moving window, it can be seen that in the latest case, the methodology produces poor results that cannot be relied upon the classification of non-defective sections from defective ones.

### 6.5.4 Moving window

In the previous case, a rectangular moving window grouping rows of the intensity matrix was used to calculate a series of principal components for extracting features from the intensity matrix of a SIP, regarding its size. The new proposal for creating an input vector with a fixed size is much simpler. The idea is to use a square moving window that will be reorganised into a feature vector with a constant number of elements that later can be feed to a neural network.

The square window is defined as follows:

$$.W_{(i,j)} = \begin{bmatrix} I_{(i,1)}, \cdots, I_{(i,j+n-1)} \\ \vdots \qquad\quad \vdots \\ I_{(i+n-1,j)}, \cdots, I_{(i+n-1,j+n-1)} \end{bmatrix}; \quad \begin{matrix} n = window\,size \\ i = 1, 2, \cdots, (p-n+1), j = 1,2, \cdots, q-n+1 \end{matrix} \quad (6.8)$$

The window $W$ of size $n$ x $n$ will be moved along the intensity matrix $I(p,q)$ with $p$ x $q$ elements, equation 6.6. The rows of each moving window will be transformed into $m$ input vectors $S$,

$$\begin{aligned} S_{(m)} = \; & [W_{(1,1)}, \cdots, W_{(1,j)}, \\ & W_{(2,1)}, \cdots, W_{(2,j)}, \\ & \vdots \qquad \vdots, \\ & W_{(i+1)}, \cdots, W_{(i,j)}] \end{aligned}, \quad (6.9)$$

where $m$ = 1, 2,..., $(P\text{-}i)*(Q\text{-}j)$. With this approach the set of output vectors will always have the same size regardless of the size of the intensity matrix. This is the simplest pre-processing approach of all the mentioned in the present discussion. The key issue is to find the appropriate window size which will supply enough information, in order to enable the neural network to learn the intensity change patterns associated with defects.

### 6.5.5 Feature extraction: Selection process

In the previous section four feature extraction techniques were studied. In order to explore their potential as feature extraction technique for the final automatic defect detection system, a comparative study was carried out.

Experiments were conducted using a generic neural network, training set and a test set to determine the performance of these techniques for the desired aim of distinguishing between detective and non-defective sections in surface intensity plots. The training set and the test set were data scanned from a clay pipe with three holes with different diameters. The test set is shown in Figure 6.16.

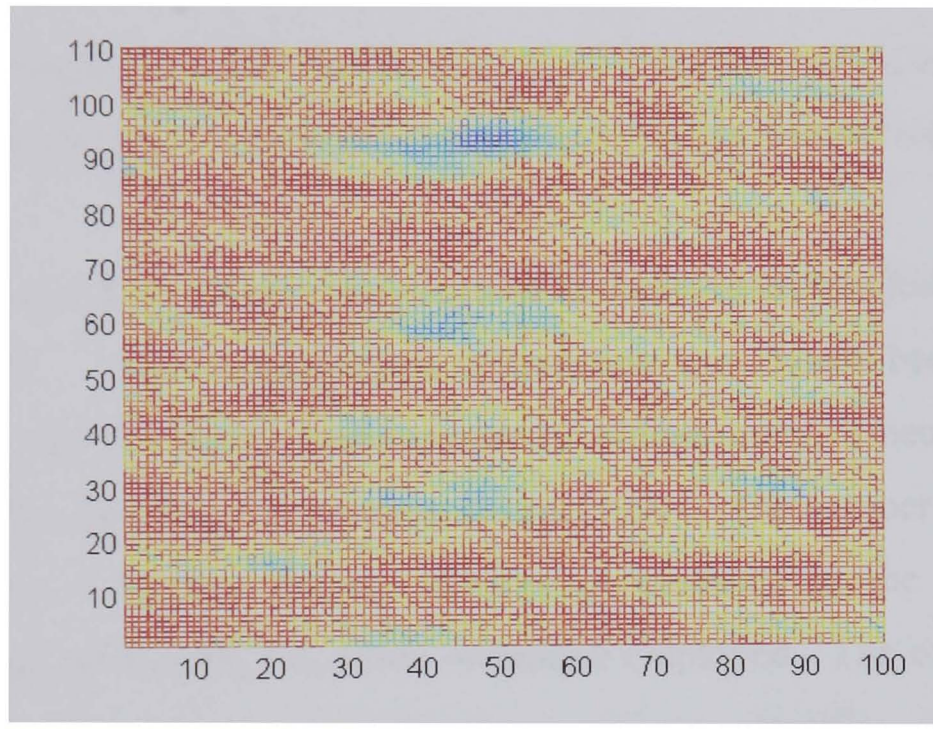


**Figure 6.16** Training set used for the selection of the feature extraction technique. Surface intensity plot from a section of a clay pipe with three perforated holes.

The test set was similar to the training set but contained holes with different sizes, see Figure 6.17.

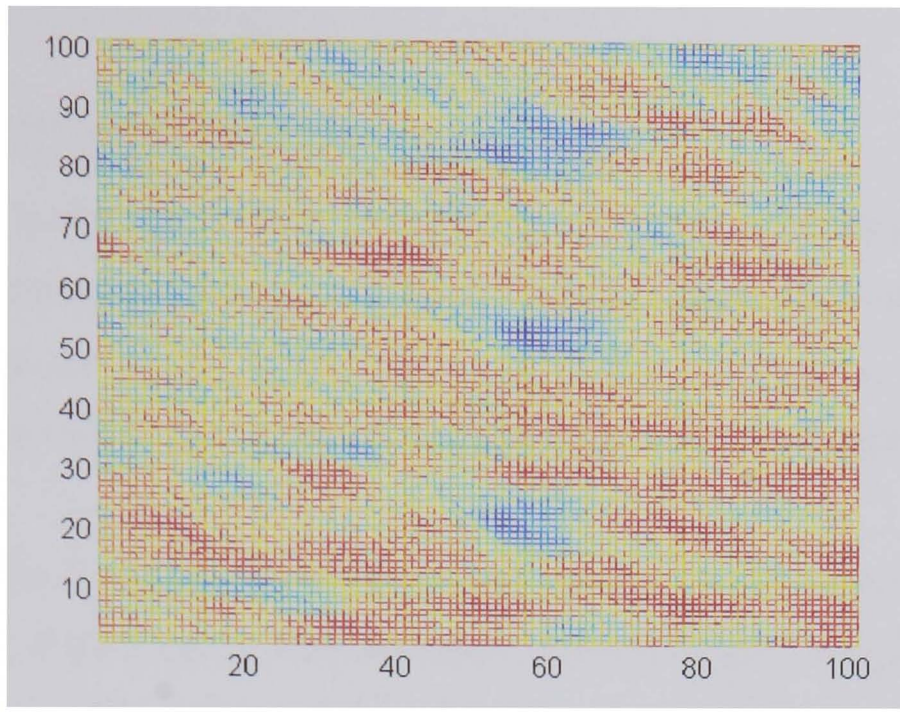


**Figure 6.17** Training set used for the selection of the feature extraction technique. Surface intensity plot from a section of a clay pipe with three perforated holes.

The initial network was composed of an input layer, two hidden layers and an output layer. A two hidden layers architecture was chosen because with this configuration and the appropriate number of hidden units, a neural network is capable of approximating any function [Hertz, 1991]. The number of elements of the input layer was fixed by the number of elements in the feature vector generated from the feature extraction technique employed. The output layer had one element because the system is to act as a binary classifier. The number of elements in the hidden layers were empirically selected by running experiments and altering the size of both layers until having a network which sum squared error converges in a reasonable amount of time to a value below a pre-defined threshold of $1\ 10^{-6}$. After carrying out this trial and error tests, it was found that the most suitable network was one with 16 elements in the first hidden layer and 8 elements in the second hidden layer.

Carrying out a comparative study of different pre-processing techniques can be a demanding and challenging task, because it might require to find suitable architectures for each one of the techniques to evaluate, as well as the optimization of the network for each one of the study cases, including the creation of representative data sets. The approach used in this comparative study, was to pre-select a suitable architecture where the input layer is changed for each one of the cases to evaluate, and each case is evaluated using the same test set.

In some cases, during the training of the neural network, arise that the chosen architecture did not converge. Hence, adjustments to the number of elements in the hidden layers were made. This was done as the last resource before concluding that a tested methodology was not suitable for the given problem.

Once a feature extraction method was chosen, an extensive optimisation study was carried out to find the smallest network that can give an acceptable performance. This was carried out by exposing the neural network to a broader range of unseen data and adjusting the number of elements in the hidden layers.

#### 6.5.5.1 Sorting algorithm

The sorting algorithm was applied to the training set presented in Figure 6.16, it generated 10 outputs from which the first one was removed because as result of the normalisation process, it was always zero. The neural network input layer was adjusted to accept a vector signature with nine elements, in order to receive the feature vector generated by the sorting algorithm. This pre-processed SIP was used as the training set and the targets (red dots on Figure 6.18(a)) +the defective and non-defective sections were assigned by visual inspection. The output of the neural network after been trained and presented with the training set is shown in Figure 6.18(a) as a continuous blue line.

The neural network was presented with unseen data, in order to evaluate how representative were the signatures generated by the pre-processing method. The output of the neural network was capable of detecting 5 defective rows from 23 in total (18 false negatives). In addition, there were 10 lines with no defects that were identified as defective ones (false positives). The effectiveness of the method to recognise the defects is about 22% (16% of false positives). It should be noted that the test set with the unseen data has similar characteristics to the set used for the training of the network. The loss in generalisation capability of the neural network when presented with unseen data, indicates that the sorting technique is not being capable of categorising the most important features from the original data.

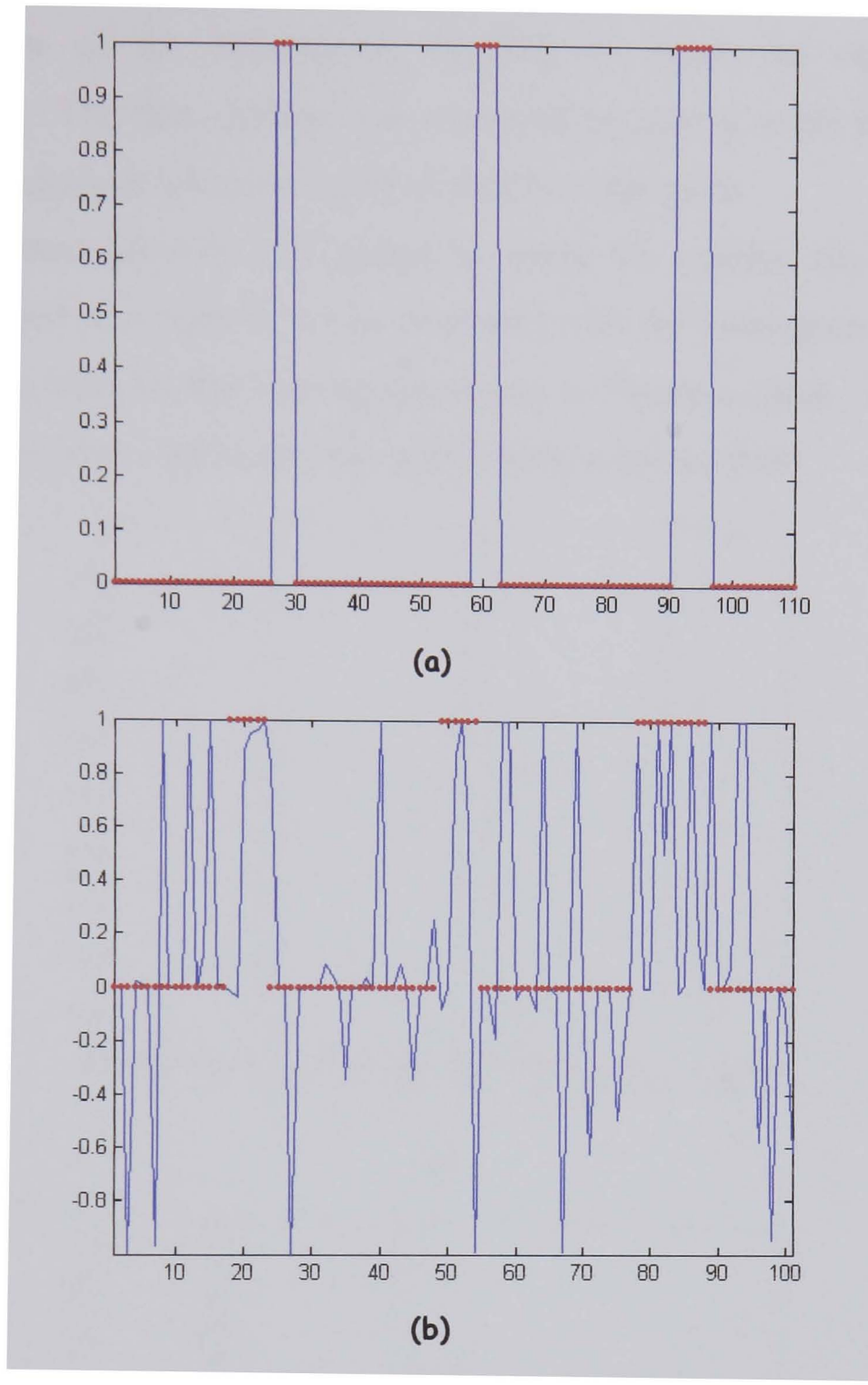


**Figure 6.18** Sorting algorithm processing method. Training set (a) the targets used for training the neural network are shown as red dots. The output of the neural network when presented with the training set is shown as the continuous blue line. Test set (b) Output of the neural network when presented with the test set is shown as a continuous blue line. The defects present in the test set are overlaid as red dots.

### 6.5.5.2 Fast Fourier Transform (FFT)

This section explores the capabilities of the FFT as a pre-processing technique in the context of classification using a neural network. For this evaluation, the FFT was calculated from the training and test sets, and the complex modulus of the FFT was fed into the neural network. As seen in section 6.5.2, from all the frequency components, the first 11 have the biggest variability,

providing most of the information required to create the signatures, see Figure 6.11(b). The first element was discarded because it is the dc component and it does not provide information about intensity variations.

The neural network was trained by using the training set, Figure 6.16. After the network was trained, it was presented with the training set. The output and the targets used for the training are shown in Figure 6.19(a). The output is represented by a blue continuous line and the targets by red dots.

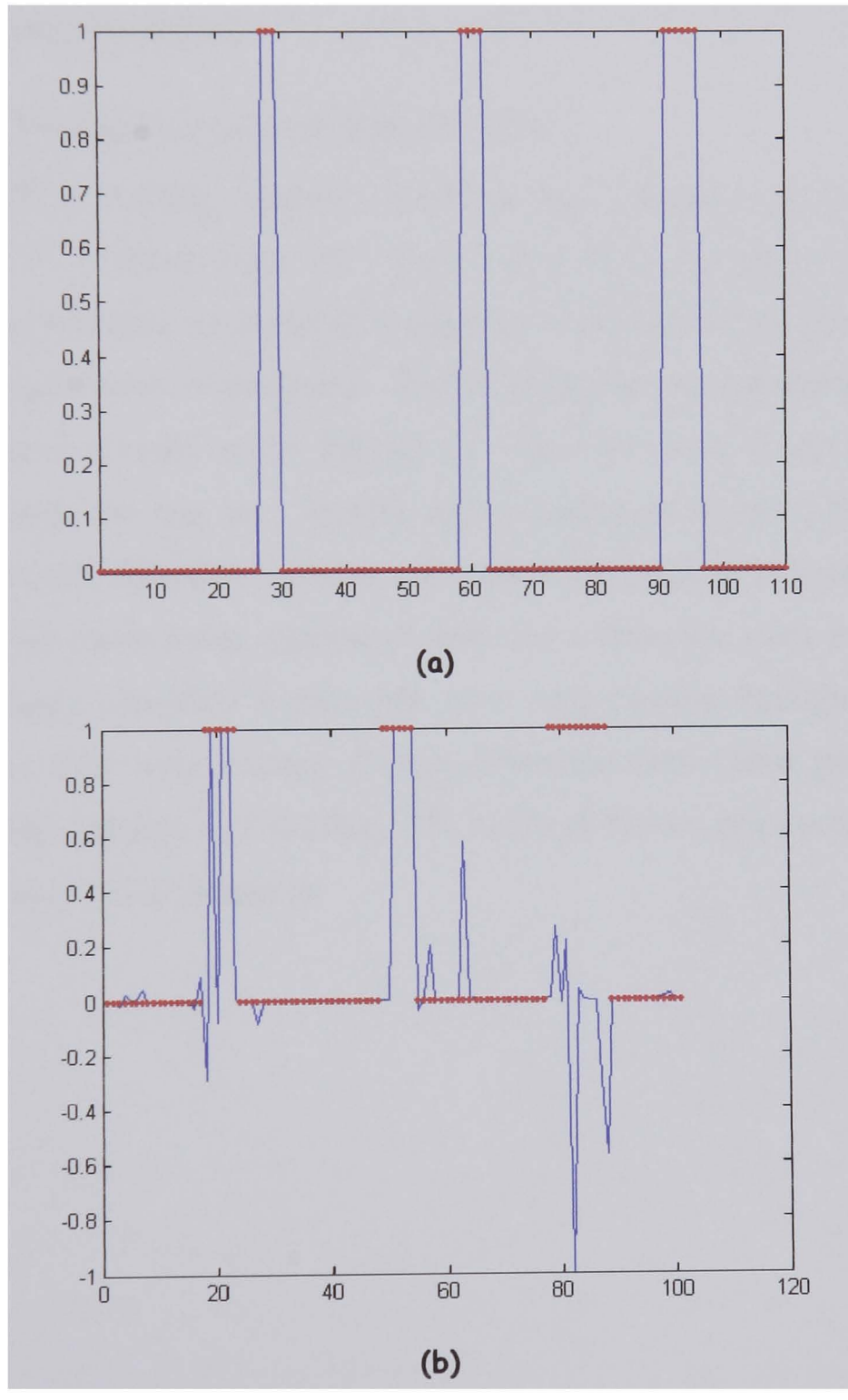


**Figure 6.19** Fast Fourier transform, pre-processing method. The training set (a) represented by the blue line with the targets over imposed as red dots. Output of the neural network when presented with the test set (b) represented by a continuous blue line. The defects present in the test set are overlaid as red dots.

The neural network was then presented with the test set, Figure 6.17. Comparing the output with the detected defects classified by visual inspection, it was observed that the trained network was able to detect 7 defective rows from 23 in total (16 false negatives). On the other hand, there were no false positives. The FFT algorithm was able to detect 30% of the rows in the surface intensity matrix where defects were present.

#### 6.5.5.3 Principal Component Analysis (PCA)

A PCA moving window algorithm was implemented as described in section 6.5.3. A window size of 5 rows was used for pre-processing the test set and the two principal components, containing 5 elements each, were grouped into a feature vector with 10 elements. The set of feature vectors generated were fed into the neural network as the training set. Once the network was trained, it was presented with the test set. Results are presented in Figure 6.20, where rows passing through defective sections are marked by black dots (overlaid over the image). This method was capable of detecting 5 defective rows from 23 in total and it wrongly classified 5 rows that were only passing through non-defective sections, as they were passing though defectives ones (false positives). This approach was capable of detecting 23% of the defective lines present in the test set with a 4% of false positives.

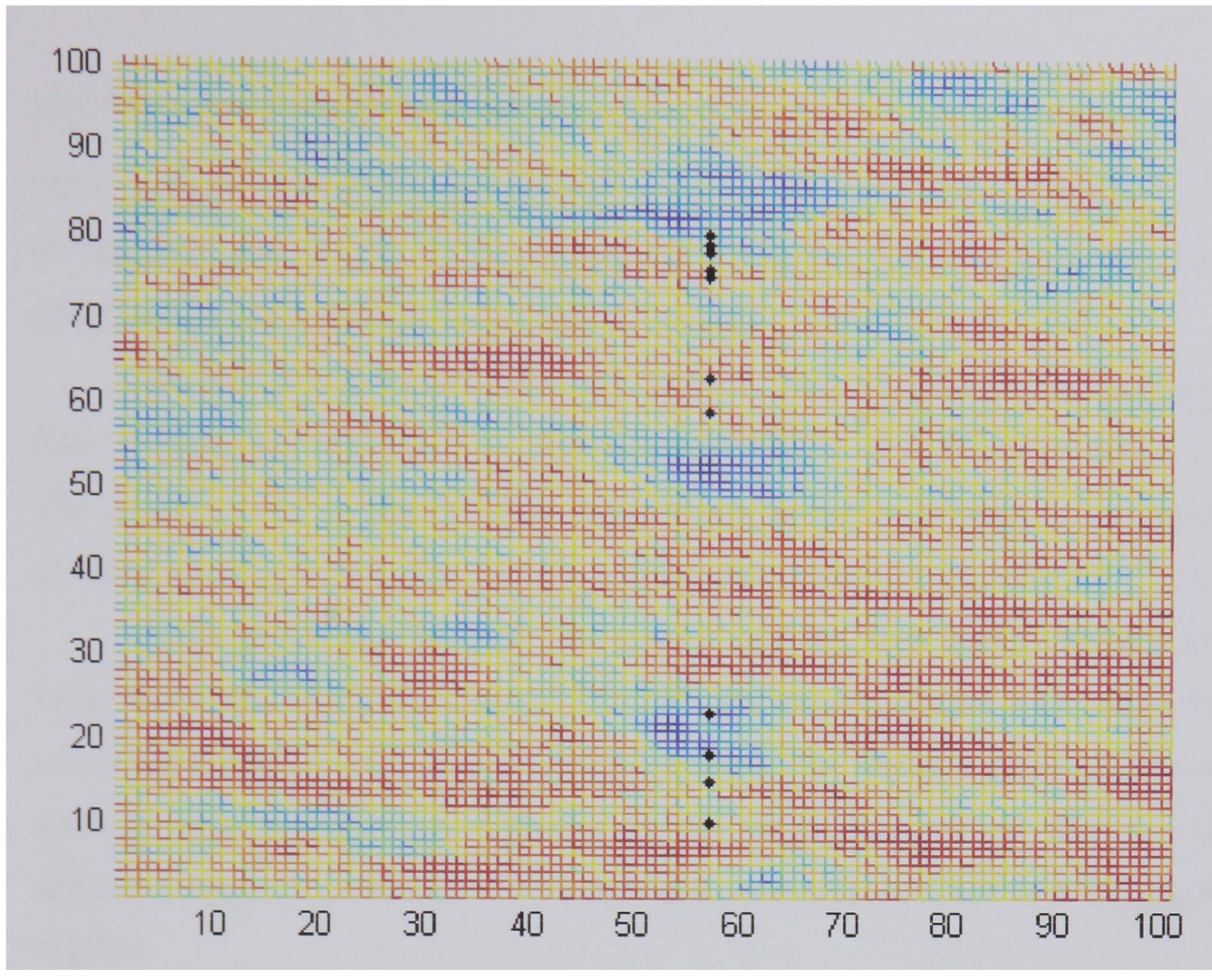


**Figure 6.20** Principal component analysis pre-processing method. Output of the neural network when presented with unseen data. The test set is overlaid with black dots showing the rows that were selected by the network as rows passing through defective sections.

#### 6.5.5.4 Moving window

For the performance evaluation of the moving window technique, a window of 5 x 5 was used.

It should be mentioned, that when using this approach, more data points than the number of elements present in the intensity matrix of the SIP will be processed, this could become a drawback due to the increase in the computational load but it will be determined by the computational power available in the platform were the final system is going to be installed. For instance, for an intensity matrix of 10x100 (1,000 elements), the moving window method will generate (6 x 96) 576 vectors with 25 elements each, giving a total of 14,400 data points.

Because of the high number of points generated by this method, it was required to reduce the training set. Instead of including all the lines covering the

three defects present in the training set, Figure 6.16, just the data points corresponding to the first defect were used (rows 1 to 50). Using 50 rows only 4800 training vectors (signatures) with 25 elements each were generated.

Of the generated vectors, 160 vectors were signatures representing a defect, while the remaining vectors corresponded to non-defective signatures. The targets in the training set that were chosen as representatives of the defects are shown in Figure 6.21(b) overlaid over the training set shown in Figure 6.21(a).

Once the neural network was trained and the error had converged to a value below the given threshold of $1 \times 10^{-6}$, the test set, Figure 6.17, containing unseen data was presented to the neural network. In Figure 6.22(a), the test set and the areas identified as defective by the neural network are shown. The defective areas area presented as black dots overlaid over the test set, Figure 6.22(b).

The test set contained 5,376 signatures from which 299 were identified as defects. Employing the same metric used for the previous cases, there were 323 signatures in the test set that can be identified as signatures representative of defects from which 288 were identified, giving an effectiveness of 89.16%. On the other hand, there were 11 false positives in 5,376 signatures (0.2%).

Because the neural network has learned a series of patterns that represent defective sections and several of these patterns are usually present inside a defective area, when a defect is present in a SIP, it can be expected that a cluster of points will be generated. This has the potential of being used as an additional post processing feature to detect defective areas and to estimate the area of possible defective sections.

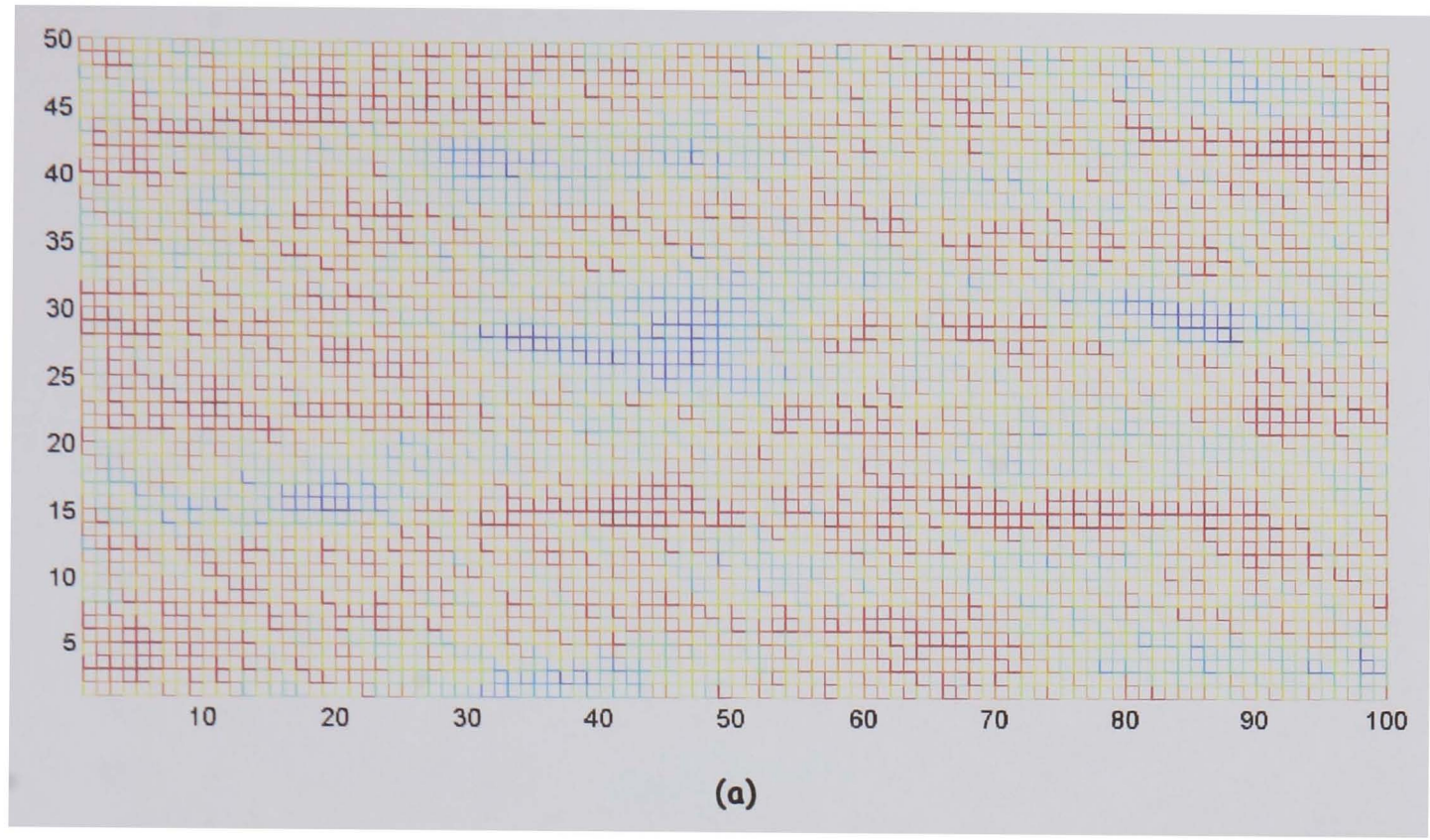


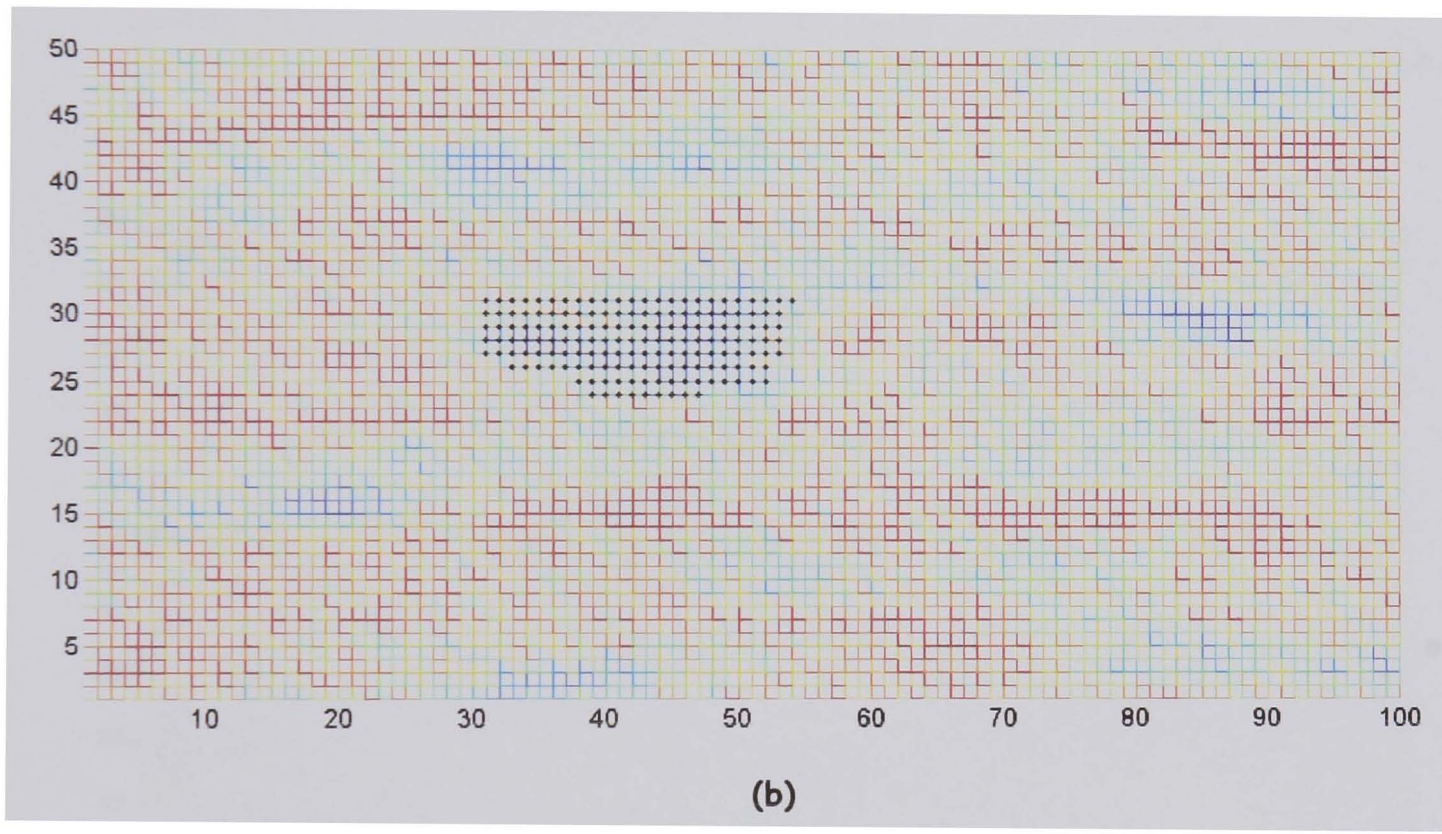


**Figure 6.21** Moving window pre-processing method, training set. (a) Training set (b) training set with elements selected as signatures of defective sections, marked with black dots.

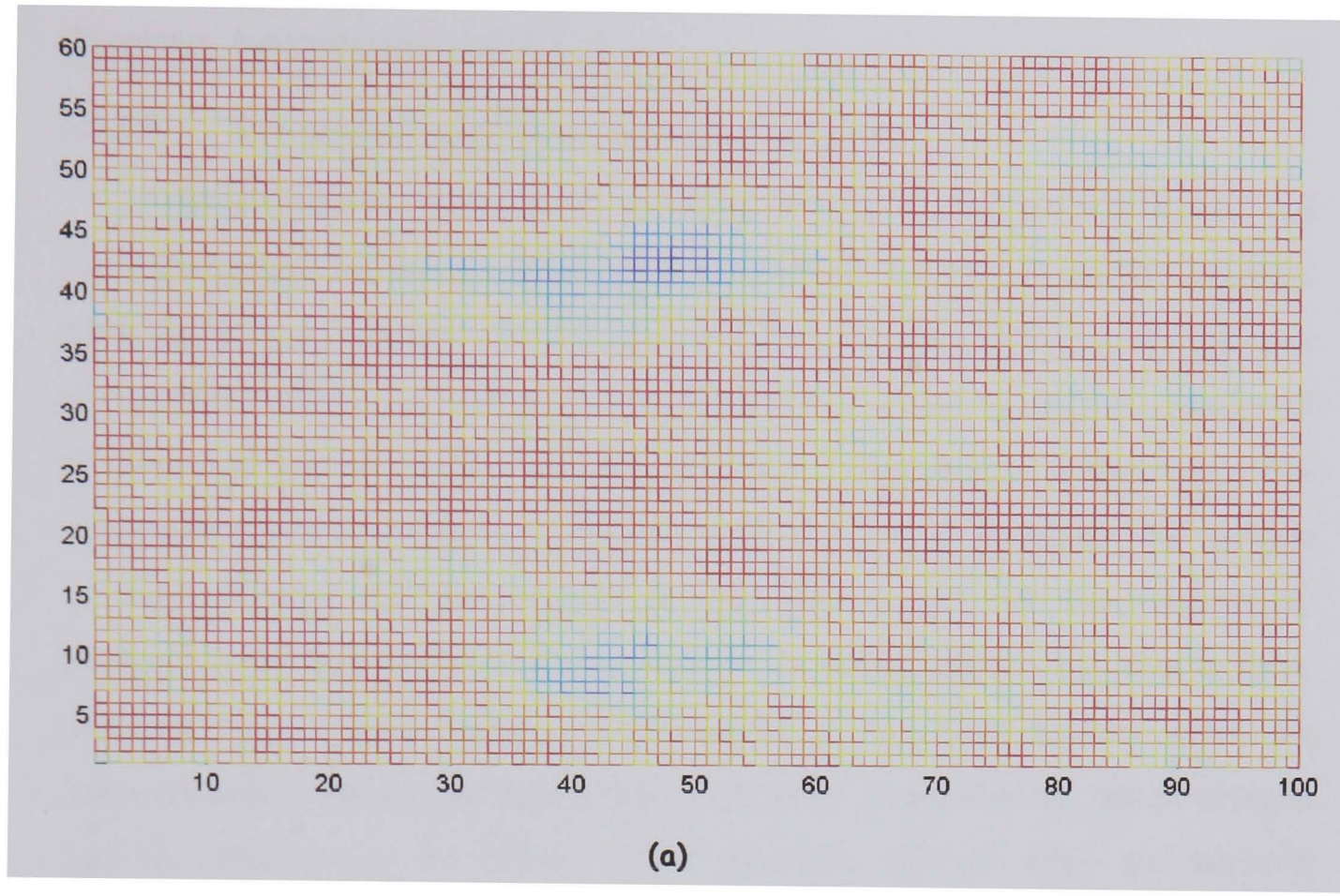


**Figure 6.22** Moving window pre-processing method – test set. (a)The test set used fort testing the capabilities of the trained network. (b) Output of the network superimposed over the test set. Black dots show the elements identified by the network as defective sections.

### 6.5.5.5 Pre-processing method selection - discussion

In sections 6.5.1, 6.5.2, 6.5.3, 6.5.4, 6.5.5.1, 6.5.5.2 6.5.5.3 and 6.5.5.4 four alternatives for pre-processing the intensity information in surface intensity plots have been studied. In this section these pre-processing techniques are compared to each other and the most suitable one chosen. A table is composed showing the four methods with four comparison parameters: Effectiveness for categorising defective and non defective sections in a SIP, as well as the number of false positives and false negatives. The effectiveness will be measured by comparing the defects detected by a trained human by visual inspection to those detected by the neural network. For instance, is the neural network detect the same amount of defects that the human, then it will be said that the neural network has an effectiveness of 100%. False positives will be when the network misclassify non-defective sections as defective, and false negatives just the opposite.

**Table 6.1** Pre-processing methods comparison

| Method | Effectiveness | | False | |
|---|---|---|---|---|
| | Defective | Non-Defective | positives | negatives |
| Sorting Algorithm | 17% | 86% | 11% | 18% |
| FFT | 30% | 100% | 0% | 16% |
| PCA | 17% | 92% | 6% | 18% |
| Moving Window | 88% | 99.8% | 0.2% | 0.7% |

As can be seen in table 6.1, the method with the worst performance is the sorting algorithm. It had the lowest percentage of defects detected and the highest number of false detections. This is followed by the PCA which is as effective as

the sorting algorithm for detecting defective areas but shows a better performance when detecting the non-defective sections.

The FFT is twice as good as the previous two, having an effectiveness of 30% when detecting defective sections with no false positives. It could be said that in some sense, the FFT is retaining more key features than the aforementioned methods.

The moving window approach outperformed all other methods with the best figures in the four selected indicators. As a result, the moving window approach is chosen as the pre-processing methodology for the automatic defect detection system. Another important step is to determine the optimal size of the window for the moving window approach. This will be carried out in the next section.

## *6.6 A Neural network for defect detection*

The problem of creating an automatic defect detection system primarily deals with the issue of producing a very sensitive system which is not prone to false alarms due to noise or slight intensity variations caused by little changes in the inner pipe structure. This is a very difficult task since the local area properties of the intensity in the SIPs such as intensity gradient which serve to identify the defective areas from non-defective ones, can be masked by the aforementioned phenomena mimicing properties of a defect and hence may lead to false positives. Besides in noisy environments, the transition from background to defect can be of similar nature and magnitude as the transitions of noise spikes, potentially masking the presence of defects.

Artificial neural networks are, theoretically, able to simulate any arbitrary mapping [Hertz, 1991]. Hence, they can be employed to solve the problem of defect detection with a minimum of false alarms. A feedforward multi-layer perceptron network, trained using backpropagation, will be used as part of an automatic defect detection system for surface intensity plots.

### 6.6.1 Neural network training

The training of the network is done using data available from previous experiments. The most suitable data for representing the signatures of defectives

areas and non-defective areas was carefully chosen from the different defects, composing a training set which contains the most relevant features of defective as well as non defective areas.

Because of the pre-processing approach chosen for the automatic detection system, defective and non defective targets had to be assigned to points in a SIP. Depending on the size of the defect, a number of signature vectors can lie inside the defective area. However, other areas could be so small that they maybe categorised by one signature vector only. The training set is refined through an optimisation process which depends on the results seen after training the neural network.

The final training set is composed of 3800 vectors from which 108 were defective signatures and the rest were non defective sections representative of the noisy sections seen in the experimental system.

### 6.6.2 Optimisation of the neural network

In section 6.5.5 a multilayer perceptron trained by using the backpropagation algorithm, composed of 3 layers, was used for a comparative study analysing the performance of different pre-processing algorithms aiming to choose the most suitable one. The employed neural network had two hidden layers with 16 nodes and 8 nodes respectively and the output layer had 1 node. In this section, a number of parameters of the base architecture are varied in order to evaluate the capacity of the neural network to separate defective sections from non-defective ones. The generalisation capabilities of the neural network are going to be evaluated as well.

The optimisation of the topology and training patterns of a neural network is a notoriously ill-defined procedure and the rules for the selection of network parameters may be described as being vague at best. In some cases, mainly due to the size of the training set, an exhaustive study involving an in-depth comparison of all parameter combinations is impractical [Lawson, 1996].

The approach adopted here was to independently vary individual parameters of the network and to assess the neural network performance with

respect to binary defects classification when exposed to unseen data. The following parameters are varied:

- Feature vector size (Window size/input nodes)
- Number of hidden layers
- Number of processing elements in the hidden layers

The following feature vector sizes were investigated: 9, 16, 25 and 36. This corresponds to changing the width of a square moving window from 3 to 6 in steps of 1. The number of hidden layers was changed between one and two hidden layers and the processing elements for each layer was varied between 1 and a maximum of 40 hidden nodes per layer. A neural network was considered successfully trained when the sum squared error (between target and network response) was below a threshold of $1x10^{-6}$. Experience showed that for training error below $1x10^{-6}$ an improvement of neural network performance could not be observed.

It was found that a number of different network topologies and training strategies were capable of identifying defects on surface intensity plots with the same efficiency, see table 6.2. Only the neural network with the smallest feature vector did not converge. All other tried architectures converged and achieved 100% success regarding the detection of defects and non-defects.

**Table 6.2** ANN optimization performance comparison table

| **Window size** | **Feature vector width** | **Nodes** | | **Converged** | **Success** | |
|---|---|---|---|---|---|---|
| | | 1st hidden layer | 2nd hidden layer | | defects (%) | non-defects (%) |
| 3 | 9 | 40 | 40 | no | N/A | N/A |
| 4 | 16 | 4 | 4 | yes | 100 | 100 |
| 5 | 25 | 8 | 4 | yes | 100 | 100 |
| 6 | 36 | 8 | 4 | yes | 100 | 100 |

Note, that the table shows a small subset of the conducted study only. For neural network with feature vector sizes 16, 25 and 36 only those results are shown which led to the best performance with the least number of nodes in the hidden layers. In case of the neural network with the smallest feature vector convergence was not achieved for any number of hidden nodes. A table showing the results of the most relevant experiments is attached in appendix C. Table 6.2 gives only limited information about the performance quality of the investigated neural networks, since most of the neural networks achieve 100% success.

Further criteria for selecting a neural network architecture are based on the performance of the neural network and the computational power required to run such network (computational load). Regarding the latter, it should be noted that the size of the feature vector is a key parameter directly impacting on processing time. As a result, the smallest feature vector should be used whenever possible to keep the processing time low.

An analysis on execution time was carried out changing the window size and measuring the time that a Pentium IV with a processing speed of 3.0 GHz needs to calculate the feature vectors from the intensity matrix of a surface intensity plot composed of 110 profiles, each profile containing 100 elements. Results show that the bigger the feature vector is, the longer it takes to compute the classification result. In table 6.3 results are shown. As expected, the relationship between the number of elements in the feature vector and the processing time is virtually linear.

Initially, the smallest neural network and the smallest feature vector are selected. The minimum feature vector size which allowed the neural network to converge was one having 16 elements (window size equal to 4). As a result, a topology with 16 inputs, two hidden layers with 4 hidden nodes on each layer and one output node was chosen. But, when the selected topology was fed with data with similar defects but gathered from pipes made of different material namely PVC, the defect recognition performance was drastically reduced. This was seen as a generalisation detriment in a network with a feature vector with 16 elements.

**Table 6.3** Processing time analysis. Windows size versus processing time.

| Window size | Feature Vector (elements) | Processing time (seconds) |
|---|---|---|
| 3 | 9 | 16 |
| 4 | 16 | 28 |
| 5 | 25 | 44 |
| 6 | 36 | 60 |

It was decided to increment the size of the moving window to 5, leading to a feature vector composed of 25 elements. The neural network was modified, increasing the number of nodes in the input layer from 16 to 25. It was trained using the same training set and tested with the same test sets as the previous one (section 6.6.1). Results show that the defect detection rate of the new neural network, doubled. In Figure 6.23, the output of the neural network, when presented with a SIP created from a PVC pipe with three holes, are presented. Inset (a) shows the output for the neural network using a feature vector with 16 elements. As can be seen, only the biggest hole is detected, while the detection of the medium size defect is somewhat ambiguous with just two individual dots at the lower edge of this defect. Inset (b) shows the output of a neural network using a feature vector with 25 elements. As can be seen the two bigger defects were clearly marked as defective sections (overlaid black dots) by the neural network.

Therefore the optimal network solution adopted for the automatic defect detection system was a network with 25 inputs, two hidden layers with 8 nodes and 4 nodes respectively and an output node.

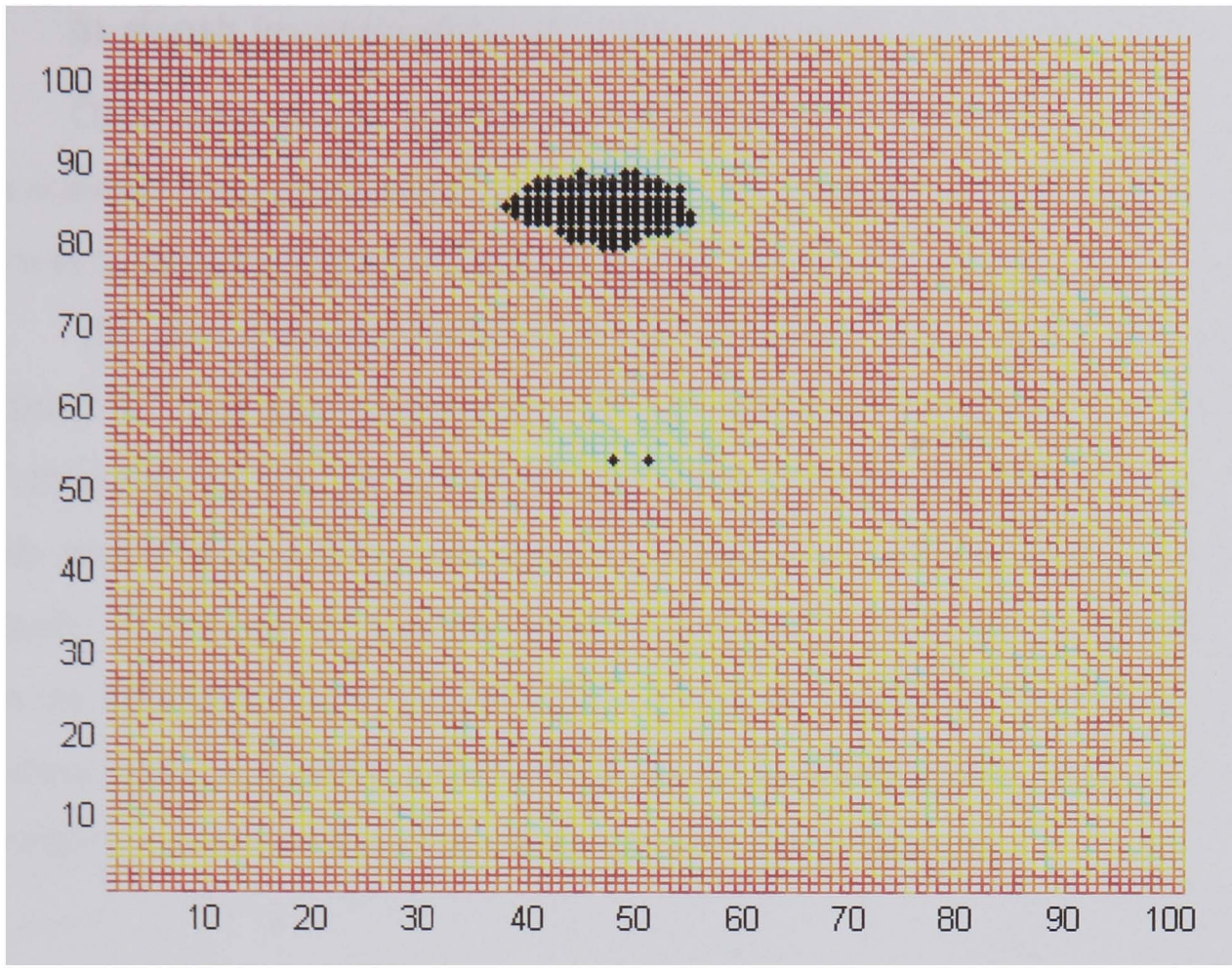


(a)

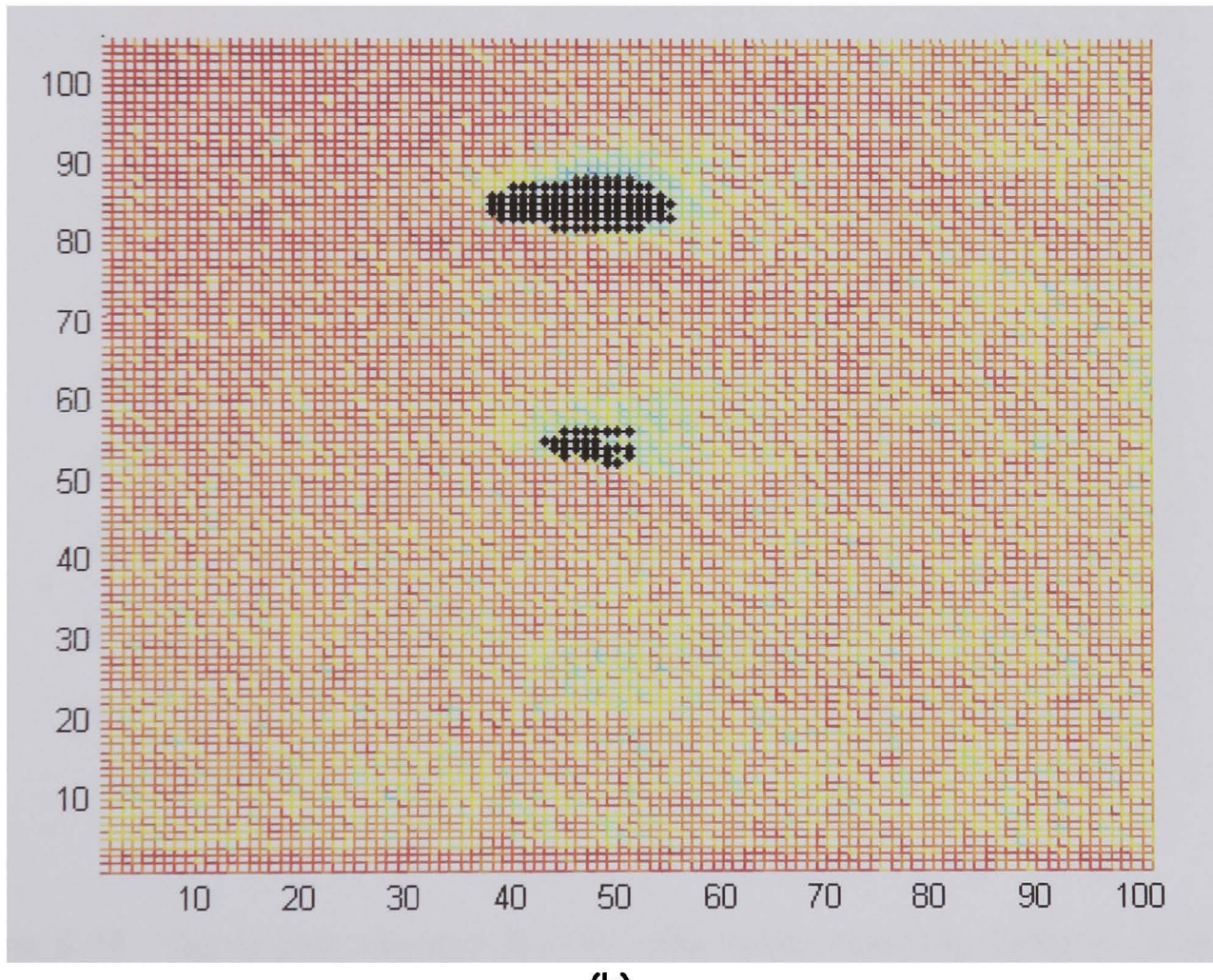


(b)

**Figure 6.23** Surface intensity plots created from scanning a PVC pipe with three perforated holes with diameters from top to bottom: 5, 4 and 3 mm. Black dots show areas classified as defective by the neural network with (a) moving window size of 4 and a (b) moving window size of 5.

## 6.7 *In-depth investigation of chosen classification approach*

Once the network was trained and optimized, it was tested with unseen data scanned from pipes made of materials such as PVC, clay, and Perspex. The aim was to determine the performance and the limits of the proposed system.

The data gathered from the lateral resolution experiment carried out in section 5.4.2 was used in this case. A thin plastic pipe made of Perspex with a wall thickness of 1.0 mm and three rectangular defects with 2.0, 1.0 and 0.5 mm width and 10 mm height, was assessed, Figure 5.12. In Figure 6.24, a surface intensity plot from the scanned pipe is presented. The areas that the neural network identified as probable defective areas are marked by black dots. As can be seen, there are three well defined areas grouping black dots. This areas correspond to the location of the three square holes in the pipe.

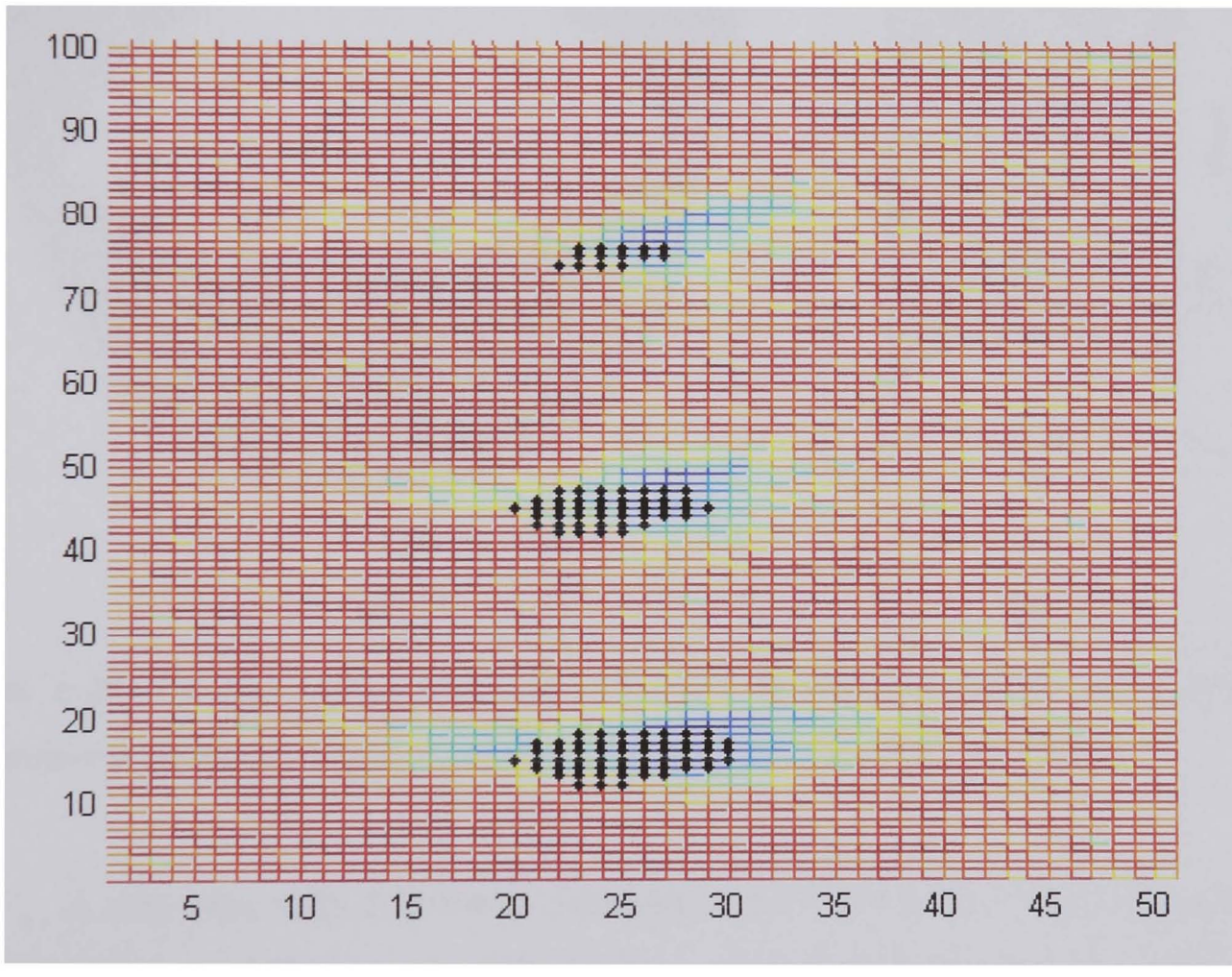


**Figure 6.24** Plastic pipe, thin wall (0.1 mm), with three rectangular defects. Dimensions from top to bottom: 0.5 mm, 1.0 mm and 2.0 mm by 10 mm. Areas classified as defective sections are shown by black dots.

A PVC pipe with a wall thickness of 10 mm having a rectangular section of 70 mm by 10 mm removed was scanned. In Figure 6.26, a surface intensity plot from the scanned pipe is presented. As can be seen, the points identified as defective areas, are forming a cluster inside the area corresponding to the removed section. It should be noted that on the right hand side of the plot are areas where the intensity is decreasing due to noise or artefacts of the measurement that the system correctly classified as a non defective areas, hence, showing a good immunity to these phenomena.

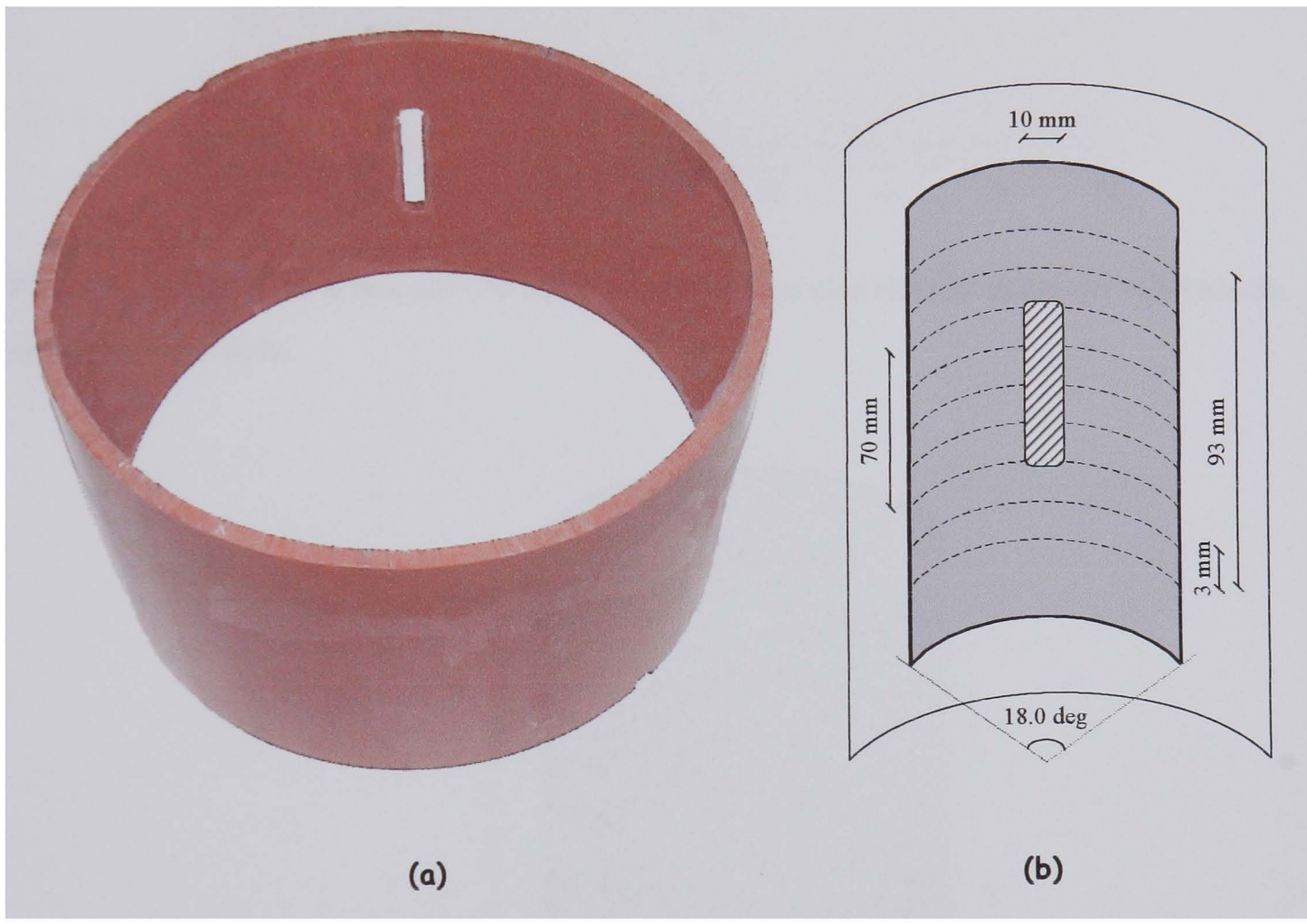


**Figure 6.25** PVC pipe section with a slit (70 mm x 10 mm) used for the neural network experimental validation. (a) picture of the scanned section (b) Schematic diagram

A clay pipe with a nominal diameter of 300 mm with a wall thickness of 34 mm and three different size drilled holes was scanned. The holes were 3 mm, 6 mm and 9 mm in diameter, located next to each other, Figure 6.28. As can be seen in the SIP, Figure 6.29, this scan is distorted by a great amount of noise. In this case the neural network generated ten clusters with more than 4 elements showing them as probable defective areas.

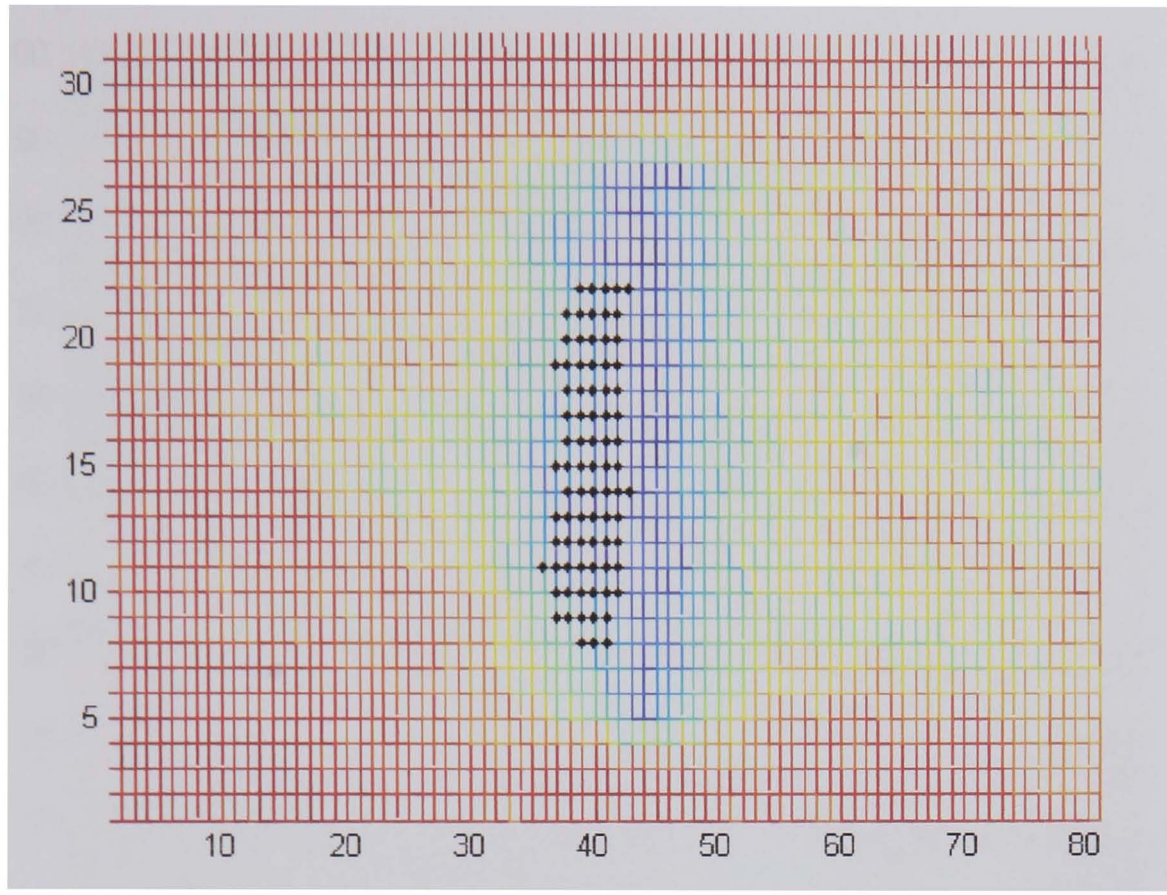


**Figure 6.26** PVC pipe with a slit (70 mm x 10 mm). Areas classified as defective sections are shown by black dots.

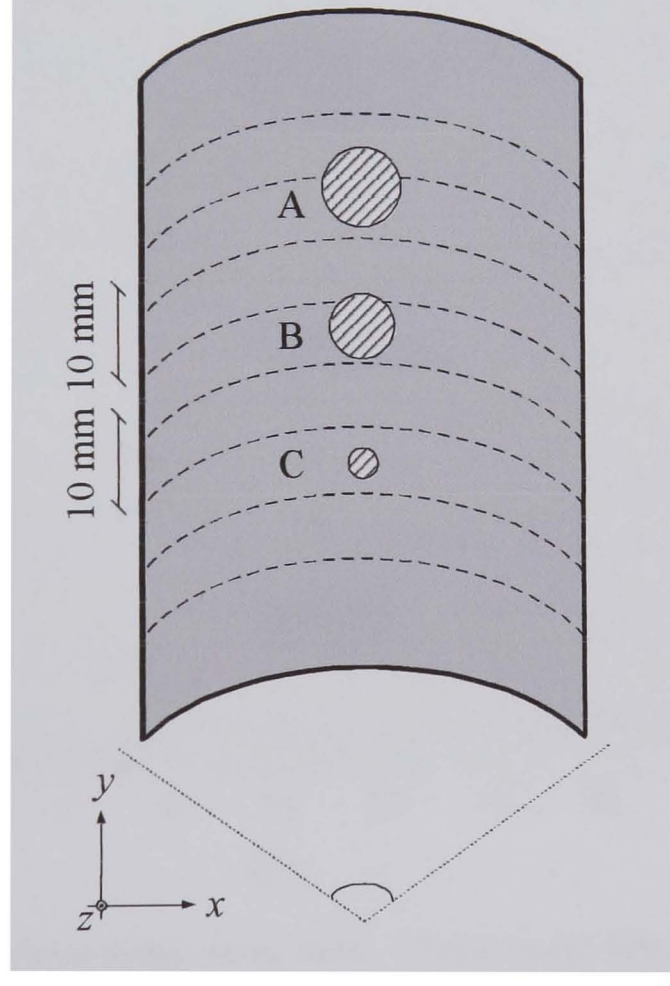


**Figure 6.27** Schematic diagram of a perforated clay pipe used for testing the automatic defect detection system. There are three perforated holes. a) 9 mm, b) 6 mm and c) 3 mm.

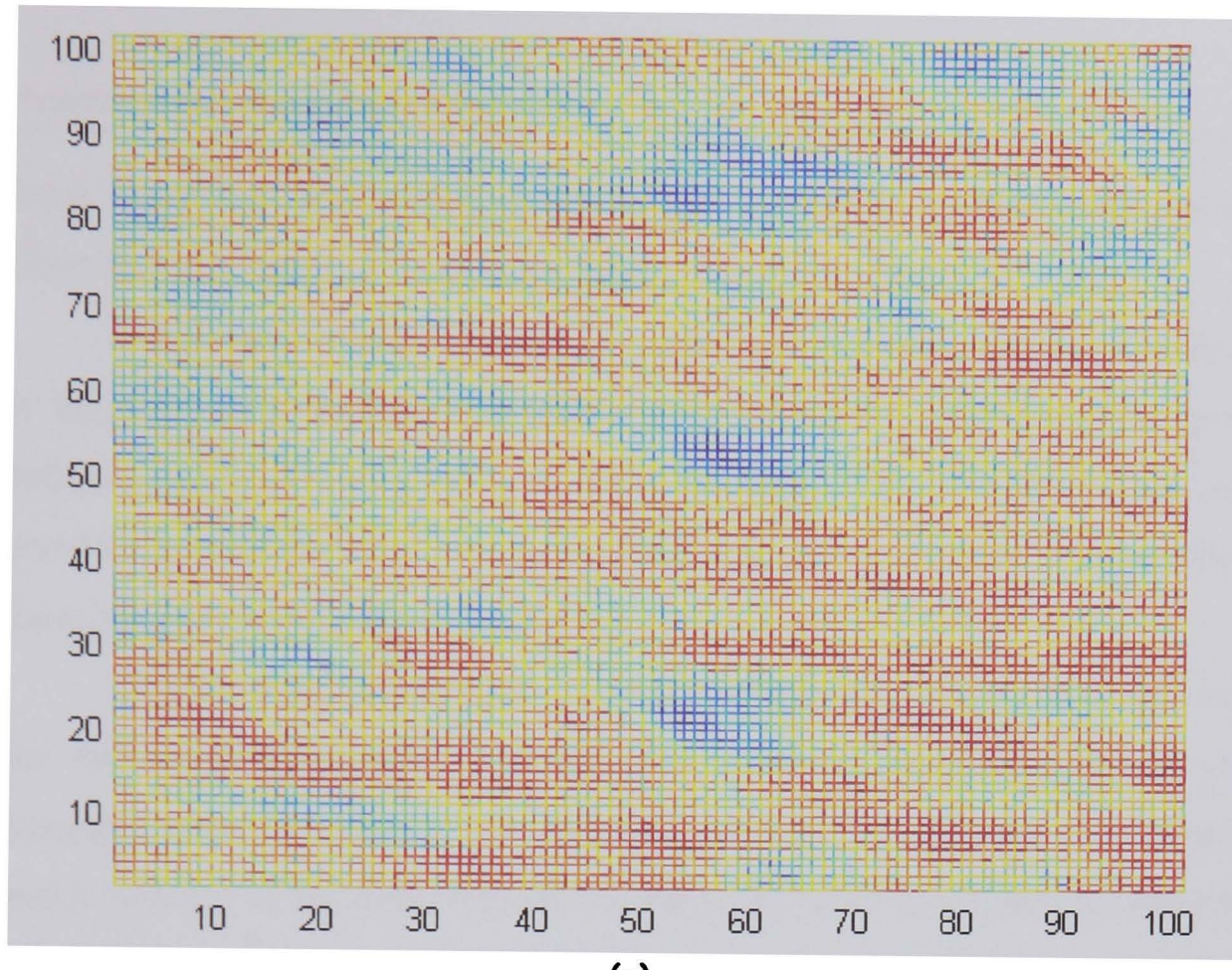


**Figure 6.28** Clay pipe with three holes, noisy data. Three round holes are present in the centre of the surface intensity plot. Defects diameters from top to bottom: 9 mm, 6 mm and 3 mm. (a) Surface intensity plot. (b) Surface intensity plot with defective areas detected by the neural classifier

From those ten, three corresponded to the three holes drilled in the pipe. The other 7 clusters were wrongly classified as defective areas.

This could be caused by a low defect to noise ratio. It looks like the noise in this case is resembling the patterns of the defects. In addition, these non defective areas are so similar to defective ones, that even the author with no previous knowledge of the location of the defects would have wrongly classified those noisy areas as defective sections.

A clay pipe with similar characteristics to the previous one was used for the following experiment. In this case a section presenting defect with an irregular shape is scanned. As shown in section 5.5.2, this pipe contains a hole and a collapse of the inner wall as a result of an induced fracture by compression. The collapsed section can be described as an irregular hollow section of 80 mm x 50 mm size and 10 mm in depth around a drilled hole, Figure 5.20. In the SIP presented in Figure 6.29(a), the defect is easily seen at the centre of the image. The darkest blue area shows the deepest section inside the defect, coinciding with the location of the drilled hole. It is surrounded by a cyan area where the intensity changes depending on the depth of the hollow section and it turns to yellow as the depth decreases until reaching the inner pipe wall. In the area outside the defect, there are yellow shadows or regions that may be caused by noise and slight irregularities in the inner surface of the pipe.

In Figure 6.29(b), the output of the neural network after it was fed with the intensity matrix from the SIP of the scanned section is presented. Black dots overlaid over the image show the areas that were classified by the neural network as defective sections. Due to the size of the image and the proximity of the dots, the area identified as defective is seen as a black section in the centre of the image. As can be seen, the neural network perfectly identified defective and non-defective sections, showing a great immunity to the areas where the intensity is changing due to noise or irregularities. In this experiment, the capability of the created system to identify defective sections from non defective ones is apparent.

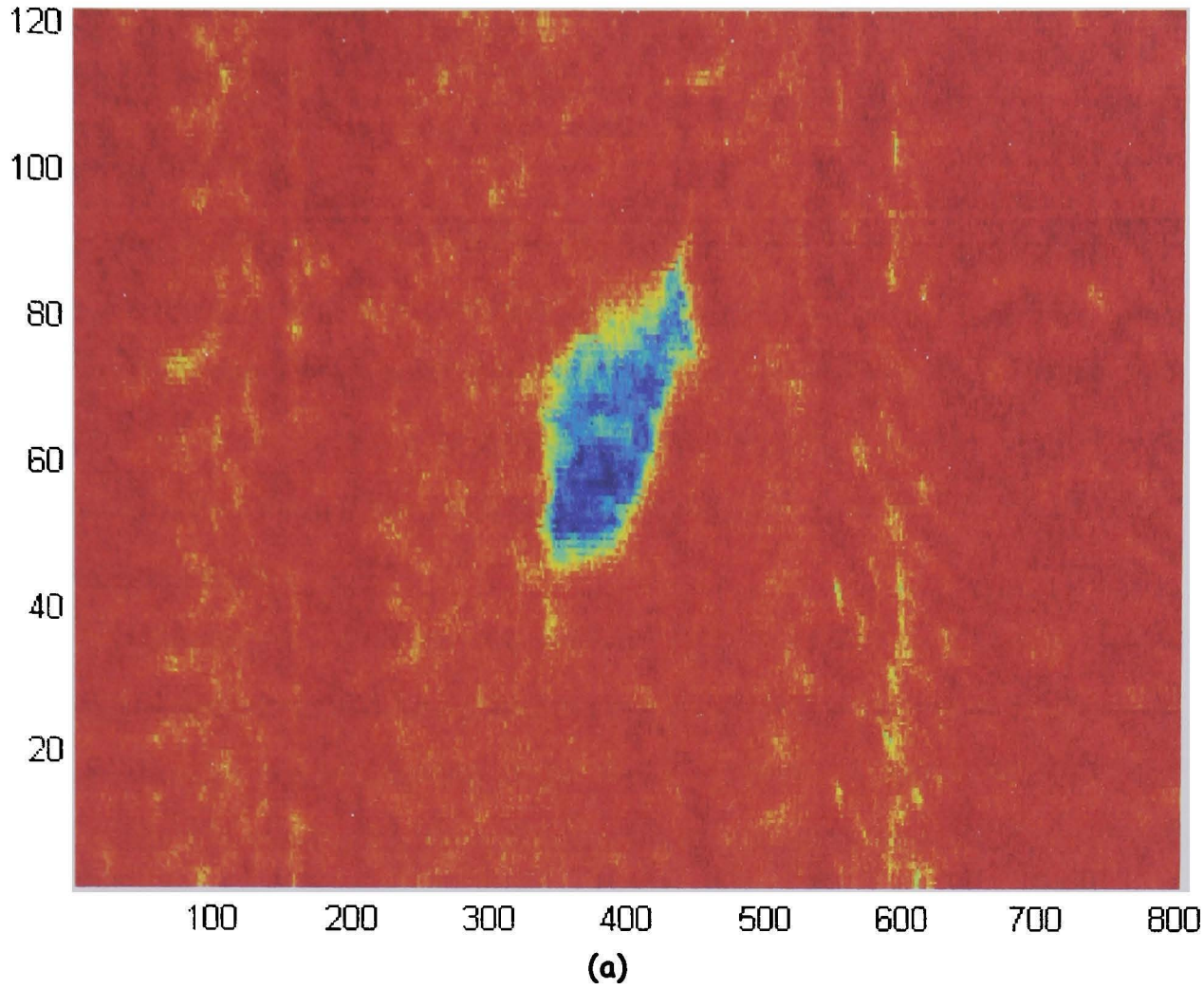


**Figure 6.29** Clay pipe 300 mm diameter with a hole and a collapse in the inner wall. (a) Surface intensity plot (b) Surface intensity plot with defective areas detected by the neural classifier over imposed as black dots.

## 6.8 Summary

An automatic sewer defect recognition and localisation system based on artificial neural network techniques has been successfully developed. The system was implemented by combining a novel imaging technique which enhances the presence of defects and a powerful feature extraction technique that is able to generate a feature vector independent of the size of the surface intensity plot (width and length).

Alternatives such as the sorting algorithm, the fast Fourier transform, principal component analysis and moving windows, were investigated as possible options for the pre-processing stage of the system. It was found that a moving window is the most effective technique for extracting key features from surface intensity plots in order to generate a feature vector.

The pre-processing technique scans the surface-intensity plots with a moving window, creating a feature vector with all the intensities inside the window which later is fed to a multilayer perceptron that was trained by using the backpropagation learning algorithm.

The developed system has been able to identify defects of varying sizes and shapes in real PVC, clay pipes and in experimental Perspex pipes, showing a very good noise immunity. The system has classified non-defective sections as defective ones, only when noise levels in the surface intensity plots are so high that even an expert eye would select those areas as defective ones.

# Chapter 7

## Conclusions

*In this chapter the conclusions of the research work presented in the previous chapters are given. In addition, a discussion on further research in this area is presented.*

## 7.1 Conclusions

This research has focused on investigating ultrasonic profiling methods for the inspection of inner sections of partly filled and fully filled sewer pipes. It aimed to improve the quality of the underwater inspection to a similar level of currently used visual techniques. This work has succeeded in creating an inspection methodology that supersedes the capabilities of current inspection methods.

As part of the investigation, a modelling environment for the simulation of ultrasonic scans inside water filled pipes was implemented in order to study the behaviour of pulse-echo ultrasonic waves inside tubular structures filled with liquid.

An advanced imaging technique that incorporates the intensities of the received ultrasonic echoes to enhance the visualisation of inspected sewer pipes immersed in liquids was formulated. The proposed approach generates images of very high resolution and has the capability of detecting defects of smaller size than existing techniques.

Extending the investigation with regards to the modelling and visualisation work, this research successfully developed an automatic defect recognition and localisation method based on an artificial neural network which allows dissociating the inspection process from the subjectivity of a human operator.

In the following sections, the contributions and conclusions of each of the main parts composing this research are given.

### 7.1.1 Modelling Environment

The simulation of ultrasound fields for medical imaging applications is a mature field, while its application for sewer pipe inspection has been scarcely explored. The novelty of this work has been the development and validation of a simulation platform, oriented towards the generation of simulated data from rotating ultrasonic sensors scanning the inner wall of sewer pipe sections filled with liquid. This allows the creation of simulated two dimensional (B-mode) and three dimensional images of the inspected objects.

A comparative experimental study was carried out to validate the output of the simulation system. Numerical comparisons (beam width and contrast intensity) and visual inspection of inner pipe profiles were used to determine the suitability of the developed environment for the desired aim. Results have shown a good agreement between experimental and simulated data.

Some deviations between the simulated and experimental data were observed. Factors that could affect the performance of real transducers were analysed in depth for the particular case of sewer inspection. It was concluded that such deviations are due to simplification and assumptions used in the development of the ultrasound model. Two aspects have not been included in the modelling environment. First, the modelling environment neglects the effects of the transducer mounting backing material and, second, the insulation oil, in which the transducer is immersed, is not included in the developed model. The conducted analysis has shown that such deviations do not impede the developed simulator to fulfil its goal.

Due to the computational power demanded by the ultrasound modeller, an optimization routine based on the emitted beam of the transducer was investigated in order to avoid the execution of calculations that were not contributing to the final ultrasound images. The reduction of the computational load was achieved by implementing a scatterer reduction routine. The scatterer reduction function was implemented in a way that it can be adjusted to deal with different kinds of transducers with different radiation patterns.

The developed simulation environment can be used to conduct in-depth investigations of ultrasonic based pipe inspection systems, by providing an invaluable tool for studying ultrasound wave propagation in fully filled pipes. It is expected that the present research will facilitate the design of future pipe inspection systems by allowing the execution of a sensitivity analysis before attempting time-consuming measurements in a real-world scenario. In addition, the system can be used to generate artificial data that can be used for purposes of staff training at pipe inspection companies.

### 7.1.2 Enhanced Visualisation of Ultrasound Images

An inspection method for the visualization of defects in structures immersed in liquid, scanned at fixed distance, has been proposed. The method is capable of creating 3D profiles of the inside wall of pipes through the use of consecutives B-mode images acquired by means of rotational ultrasonic sensors. The new approach is capable of detecting anomalous conditions on the surface of the inside pipe wall which could not be detected by employing traditional time-of-flight profiling methods. To the best knowledge of the author, this novel visualisation approach has not been previously applied to the problem of ultrasonic-based inspection of tubular structures.

In simulated experiments, pipe deformations such as indentations or protuberances in the order of 1 mm and square defects as small as 2.5 by 2.5 mm wide were detected using a 3 MHz unfocused transducer. In experiments carried out using a 3 MHz unfocused sensor with a sampling rate of 162 kHz, defects such as a crack as small as 0.5 mm x 12 mm and a 7 mm diameter hole have been successfully detected. The conventional method for sewer pipe inspection is the Time-of-Flight (TOF), when use in combination with the aforementioned sensor, it has a theoretical lateral resolution of 5.76 mm at 150 mm and an axial resolution of 4 mm. Comparing the aforementioned values, with the defect sizes that have been seen when applying the new proposed methodology, an improvement of 11 times in the lateral resolution and 4 times in the axial resolution have been achieved.

During the experimental validation process, it was found that for the inspection of pipes, the scanner has to be located at the centre of the pipe. Suggestions on how to address this problem, will be presented in the future research section (7.2).

### 7.1.3 Automatic Defect Detection

An automatic sewer defect recognition and localisation system based on artificial neural network techniques has been successfully created. The system was implemented by combining a novel imaging technique which enhances the presence of defects (Section 7.1.2) and a powerful feature extraction technique

that is able to generate a feature vector independent of the size of the surface intensity plot (width and length).

Several feature extraction techniques such as the sorting algorithm, the fast Fourier transform, principal component analysis and moving windows were investigated. Their performance was evaluated by using them as pre-processors for a common neural network, and comparing their abilities to classify detective and non-defective sections.

A moving window with a kernel size of five was the most effective technique for generating a feature vector. The moving window technique scans the surface-intensity plots with a square moving window, creating a feature vector with all the intensities inside the window which is fed to a multilayer perceptron that was trained using the backpropagation learning algorithm. An optimisation study was conducted, trying different window sizes and different network architectures, exposing each different case to unseen data sets acquired from pipes made from materials and with different defect types. It was found that the optimal network solution adopted for the automatic defect detection system was a network with 25 inputs, two hidden layers with 8 nodes and 4 nodes respectively and an output node.

The automatic defect detection system has been able to identify defects of varying sizes and shapes in real pipes made of different materials (PVC, clay pipes and Perspex), showing a very good generalisation capability and high immunity to noise. Only when noise levels in the surface intensity plots were extremely high, the system wrongly classified non-defective sections as defective ones.

## *7.2 Future Research*

In this research the capabilities of the investigated techniques for sewer pipe inspection have been successfully investigated in a lab environment. The next step should be to test these new techniques in real sewers or with data gathered from sewers operating under real conditions. In addition there are a few issues that could be explored in order to expand this research work; they are discussed next.

### 7.2.1 Model extension

The developed simulation platform, did not consider the creation of a model for representing the effect of the backing material on which the transducer of the ultrasonic system used for experiments is mounted. This has the disadvantage that the simulator generates a precise pulse with a specified width. But as was explained in section 4.8.1, after being excited by a short-strong electrical pulse, the ultrasound transducer keeps vibrating for some time even though the exciting pulse has diminished. As a result, further work in the modelling of the interaction between backing materials and transducer could be added to the present simulation environment.

Due to the way in which rotational ultrasonic sensing systems are designed, transducers are immersed in transformer oil for protecting them from harsh environments. The Field II simulation routines used for the core of the simulation platform does not allow the simulation of the propagation of ultrasonic fields through adjacent media with different densities. Field two routines could be modified to deal with a multi layer system where each layer has different acoustic characteristics and arbitrary boundary shapes.

By developing these models and integrating them to the existing simulation environment, the accuracy of the resultant images could be improved.

### 7.2.2 Off centre compensation

As mentioned at the end of chapter 5, the proposed visualisation enhancement technique has shown to be sensitive to the location of the transducer inside the pipe. Optimum results were obtained when the transducer was located at the centre of the pipe. It was observed that as the transducer moves away from the centre of the pipe, the intensity of the returning echoes from the points where the incident angle is not normal to the tangent line (at the contact point between the centre of the incident beam and the pipe wall) is drastically reduced, see appendix B.

Two possibilities could be explored to overcome this undesirable phenomenon. The intensity could be compensated by using a software model or

the location of the transducer could be kept in the centre of the pipe by means of a motor-driven mechanism and appropriate control algorithms (motion control).

The first case only functions if the intensity of the signal returning from the pipe wall at every instance is strong enough to be measured by the receiving transducer. This has the advantage that such a system could be used in pipes with liquid levels below the radius of the pipe. Also, this approach could be easily integrated with existing systems, since only the processing software needs to be adapted.

The approach based on a motorised mechanism, is advantageous since it will assure that the transducer is always appropriately aligned with the centre axis of the pipe and, thus, the intensity of the received signal is always measurable, because the signal is always normal to the transducer's surface. However, this approach cannot be used when the liquid level is lower than the radius of the pipe. In addition, the design and implementation of the robotic manipulator will have to be done taking in consideration that they will be working in harsh environments this could lead to costly systems that can be prone to failures due to moving parts.

### 7.2.3 Automatic defect classification

In this work, a binary classification system for separating defective sections from non-defective sections was developed. A natural further step, once a system for identifying faulty conditions in sewer pipes has been implemented, is to implement a system for automatic classifying, the previously identified structural defect by its type (see section 2.3.2). Such classification should be carried out following the guidelines generated by the Water Research Centre in its Sewerage Rehabilitation Manual [WRC, 2004].

A cascade architecture could be used in the final system, where the binary classifier will run continuously, as a first stage. When a faulty section is found, the second classifier will find which type of defect has been detected.

# Appendix A: Matlab functions developed for the project

**circles_intersec.m**

```
area = circles_intersec(R,r,d)
Circle-Circle intersection
Taken from the mathworld worlfram web page:
http://mathworld.wolfram.com/Circle-
CircleIntersection.html
Area = circles_intersec(R,r,d)
   R:  radii biggest circle centred at origing
   r:  radii smallest circle centred at d
   d:  distance between circles
```

**cut_sq_sec.m**

```
positions_new=cut_sq_sec(positions,x_start,
x_end,y_start,y_end,z_start,z_end)
Cut a square from the phantom measurements in
metres.
```

**load_disp.m**

```
load_disp(input_file)
  function to load and display simulations.
```

**mesh_cart_sim_rot.m**

```
mesh_cart_sim_rot(scan,cutoff,angle_start,
angle_step,angle_end,fs,t_base, angle)
Creates a x-y 3-D mesh with the r, theta
coordinates and the amplitudes supplied in the
input matrix modified function to plot and
rotate original data.
parameters:
  angle_start, angle_step, angle_end:  radians
  cutoff:  db
  angle:   deg
```

**mesh_rot_log.m**

```
mesh_rot_log(scan,cutoff,angle_start,angle_step
,angle_end,fs,t_base)
Plot a 3D graph of a rotational image in
logarithmic scale.
```

**mesh_rot_scan.m**

```
plot b-mode ultrasonic image
mesh_rot_scan(scan,angle_start,angle_step,
angle_end,fs,t_base).
```

**model_circle_defect.m**

```
ri_log =
model_circle_defect(T_radii,Def_radii,d)
MODEL_CIRCLE_DEFECT    Reflectivity index model
This function model the changes in the
reflectivity index when a circular transducer
scans a circular defect.  The radiation pattern
of the transducer is assumed to be circular.
   T_radii:  radii of the transducer
   Def_radii:  radii of the defect
   d:  distance between the centre of the
transducer and the defect, can
be a vector with the movement path of the
transducer
        ri_log:  Output in dB
```

**mov_xducer_lin.m**

```
Transducer displacement over x axis
Because the Field II simulator does not let
move the transducer, it is necesary to
Translate the phamtom to simulate the movement
of the transducer.
```

**mov_xducer_rot.m**

```
script rot_xducer(positions)
Rotation of the x-z plane, rotation origin on
positive x-axis.
```

**plot_img_lin.m**

```
plot b-mode ultrasonic image
 created moving the transducer linearly over
the x axis.
```

| | |
|---|---|
| plot_img_rot.m | plot b-mode ultrasonic image |
| plotspec_fg.m | plots spectrum matrix output (polar plots) |
| reflectors.m | create the reflectors to be used in the simulation |
| rot_xducer.m | function RFlines rot_xducer(positions)<br>Rotation on x-y plane theta = width of rotation w.r.t. x |
| rotate_pht.m | positions_new = rotate_pht(positions,angle)<br>Rotates a phantom<br>positions_new = rotate_pht(positions,angle)<br>positions: current positions of the scatterers describing the phantom<br>angle: rotation displacement in degrees<br>positions_new: new postitions of the rotated scatterers<br>Note:<br>The centre of rotation is located at the origin of the coordnate axis |
| scatering.m | Main routine for simulating the ultrasonic pipe inspection process |
| show_3d_pipe.m | Show a B-mode image of an axial cut of a pipe.<br>It uses simulated data. |
| show_xdc.m | creates a 3D plot showing the xducer |
| sim_beamwidth.m | Simulation routine to plot the beamwidth of a transducer averaging the logged intensities of the transmitted pulse<br>scan_db = sim_beamwidth(scan,cutoff,<br>angle_start,angle_step,angle_end,fs,t_base) |
| sim_build_image.m | [scan,t_base]=sim_build_image(RFlines,fs)<br>From the RFlines data, build the b-scan image matrix<br>Returns:<br>scan: b-mode matrix in polar mode angular positions and samples<br>t_base: base time for the first sample real time = sample/fs+base time. |
| sim_clear_vars.m | clear simulation overhead vars. |
| sim_clear_vars_phantom.m | clear simulation overhead vars. |
| sim_clear_vars_results.m | clear simulation overhead vars. |
| sim_db_conv.m | sim_db_conv(input,cutoff)<br>converts the output matrix from the simulator from linear scale to db scale and cut off the values to the specified limit "cutoff". |
| sim_edge_detector_2d.m | This algorithm detect the edge in each A-scan, determining the noise threshold level base using the mean of the signal and adding it up the signal STD<br>The algorithm detect the first value who cross the threshold, and find the maximum amplitude in the returning echoes in that direction. |
| sim_edge_detector_3d.m | edges_3d: Stores the edges detected and the positions of each one, to construct the pipe profile.<br>edgepos: sample where the edge was detected in the (pos) position<br>intensity: max intensity registered in the line where the edge was detected<br>t_base: base time for first sample (current |

| | |
|---|---|
| | sample time= base_t+sample/fs)<br>pos: position of the transducer in the y axis.<br>sk_scan_3D: Stores all the B-mode images scanned. Optional, just for debuging or future use<br>y_pos: position of the transducer in the y axis.<br>scan: B-mode image for the corresponding y position (y_pos).<br>Ex: [edges_3d scan_3d]= sim_edge_detector_3d(xducer_start_y, xducer_end_y, xducer_step_y, fs, noise_thr_log) |
| sim_edge_detector_3d_bigfiles.m | sim_edge_detector_3d_bigfiles(xducer_start_y,xducer_end_y, xducer_step_y,fs,noise_thr_log)<br>Find the edges in a 3D simulation<br>It loads all the RFlines files, normalize the registered values, find the edges and the maximum amplitudes in each 2D scan<br>xducer_start_y: start position of the transducer<br>xducer_end_y: end position of the transducer<br>xducer_step_y: size of the steep used to scan the pipe<br>fs: Sampling frequency (Hz)<br>noise_thr_log: Optional, threshold (dB) to be used for the edge detection, if omitted it will be determined automatically analysing the noise characteristics of the data.<br>This function returns two structs:<br>edges_3d: Stores the edges detected and the positions of each one, to construct the pipe profile.<br>*edgepos: sample where the edge was detected in the (pos) position*<br>*intensity: max intensity registered in the line where the edge was detected*<br>*t_base: base time for first sample (current sample time= base_t+sample/fs)*<br>*pos: position of the transducer in the y axis.*<br>sk_scan_3D: Stores all the B-mode images scanned. Optional, just for debuging or future use.<br>*y_pos: position of the transducer in the y axis.*<br>*scan: B-mode image for the corresponding y position (y_pos.* |
| sim_edge_detector_3d_oc.m | sim_edge_detector_3d<br>Find the edges in a 3D simulation<br>It loads all the RFlines files, find the edges and the maximum amplitudes in each 2D scan by calling to the function edge_detector_sim_2d. This script creates a structure called to store the detected edges<br>edges:<br>*edgepos: sample corresponding to the edge*<br>*intensity: max intensity per dir*<br>*t_base: base time for first sample (current sample time= base_t+sample/fs)*<br>*pos: position of the transducer in the y axis.* |
| sim_edge_detector_3d_OCWT.m | Same as previous but for off centre cases. |
| sim_edge_detector_3d_sr162k.m | Same as sim_edge_detector_3d<br>Reduces de sampling rate from 100 MHz to 162 KHz and find the edges in a 3D simulation. |
| sim_mesh_cart.m | sim_mesh_cart(scan,cutoff,angle_start, angle_step,angle_end,fs,t_base)<br>Creates a x-y 3-D mesh with the r, theta |

| | |
|---|---|
| | cordinates and the amplitudes supplied in the input matrix<br>input parameters:<br>angle_start, angle_step, angle_end: radians<br>cutoff: db |
| sim_scatterers_reduction.m | positions_new=scatterers_reduction(positions, cone_apert,cone_radius)<br>Reduces the number of scatterers to be used for the simulation base in a conic radiation pattern.<br>cone_apert: cone aperture (degrees)<br>cone_radius: cone radius at z = 0 |
| sim_show_pht.m | sim_show_pht(positions)<br>creates a 3D plot showing the phantom and the transducer. |
| sim_surface_3d.m | sim_surface_3d<br>Plot a 3D surface plot of the edges detected and maximum amplitudes found by the script sim_edge_detector_3d. |
| sim_surface_3d_tof.m | Plot a 3D surface plot of the edges detected. |
| sk_beamwidth.m | Plot the beamwidth of a transducer averaging the logged intensities of the transmitted pulse. |
| sk_build_image.m | sk_build_image(t_base,scan,total_samp)From the RFlines data, build the b-scan image matrix<br>Returns:<br>scan: B-mode matrix in polar mode angular positions and samples.<br>t_base: base time for the first sample. |
| sk_db_scaling.m | output=sk_db_scaling(input)<br>Convert the output matrix generated by the SeaKing System from raw counts to db scale. |
| sk_edge_detector_3d.m | Find the edges in a 3D Sea King scan<br>It loads all the B-mode data files, find the edges and the maximum amplitudes in each 2D scan<br>This script creates a structure called sk_edges to store the edges detected:<br>*edgepos: sample corresponding to the edge*<br>*intensity: max intensity per dir*<br>*pos: position of the transducer in the y axis.* |
| sk_mesh.m | sk_mesh_(input,fig_title)<br>Generates a 3D plot, converting the amplitude from counts to db and the samples to time base on a fs=162.5 kHz<br>It labels the plot if desired. |
| sk_mesh_cart.m | sk_mesh_cart(scan,angle_step)<br>Creates a x-y 3-D mesh with the r, theta coordinates and the amplitudes suplied in the input matrix<br>input parameters:<br>scan: data to be mesh<br>angle_step: angle resolution use to scan the data. |
| sk_read_data.m | sk_read_data(filename,samples2zero)<br>It reads a CSV file created with the sonv3 system, cleans it by zeroing the first number of samples specified in the second argument and scale it from raw ADC counts to dB values<br>It returns a matrix with the read values in dB<br>Inputs: |

```
                                filename:  Name of the file to read
                                samples2zero:  Number of samples columns to
                                zeroing.  This is used to removed the
                                undesirable effect created from the reflection
                                inside the protection boot of the SK sensor.

sk_resolution.m                 angle_step=sk_resolution(resolution)
                                returns the angle step for a given resolution
                                of the SeaKing System.
                                Input:
                                   Resolution:  Low, Med, High, Ultra.
                                Output:
                                  angle_step:  1.8, 0.9, 0.45, 0.225.

sk_surface_3d.m                 sk_surface_3d(sk_edges_3d,sk_angle_step)
                                Plot a 3D surface plot using the edges detected
                                and maximum amplitudes stored in the structure
                                sk_edges_3d returned by the sk_edge_detector_3d
                                function.

sk_surface_3d_tof.m             sk_surface_3d_tof(sk_edges_3d,sk_angle_step)
                                Plot a 3D surface plot using the edges detected
                                and stored in the structure sk_edges_3d
                                returned by the sk_edge_detector_3d function.
                                The colour scale is assigned to the depth.

sk_surface_zoom_in.m            sk_edges_3d_zoom=sk_surface_zoom_in(sk_edges_3d
                                ,x_start,x_end,y_start,y_end)
                                This function makes a zoom in previous acquired
                                data.

tangents_norm.m                 [theta_dif,x,y] =
                                tangents_norm(oc,radius,theta_step)
                                fuction to calculate the difference angle
                                between the impingent rays emitted from a
                                rotating transducer and every point of a
                                digital circle.
                                This fuction creates the digital phantom for a
                                complete circle of radius:  "radius" and mesh
                                size of "theta_step".
                                Variables:
                                oc:  off centre offset of the transducer
                                radius:    radius of the circle user to create
                                the digital phantom
                                theta_step: angular mesh dimension to create
                                the digital phantom (polar coordinates)
                                ex:  [theta_dif,x,y] = tangents(-2,148,.9)

xmov_xducer.m                   Transducer displacement over x axis
                                Because the Field II simulator does not let
                                move the transducer, it is necesary to
                                translate the phantom to simulate the movement
                                of the transducer.
```

# Appendix B: Transducer off centre location discussion

Simulations were conducted by rotating an ultrasonic transducer 360 degrees inside a 300 mm pipe diameter (I.D.: 296 mm) at 0.9 degree steps. The transducer was working in a pulse-echo configuration, emitting pulses at 3 MHz with pulse duration of 10 μs. Intensities of the received echoes were logged for every position around the pipe, creating an intensity profile. Once a full rotation was finished, the transducer was moved to a new location farther from the centre of the pipe and another profile was created. Eleven profiles were created by translating the transducer from the centre to 14.8 mm (10% of radius) towards the pipe wall at 1.48 mm steps (1% of radius).

In the Figure A.1, the intensities of the received echoes for a full rotation of the transducer, at each position, have been plotted. The intensity values have been normalised. As can be seen when the transducer moves a distance equivalent to 3% of the radius of the pipe, away from its centre, the intensities for a full rotation decrease below -60 dB.

From figure A.1 it can be seen that regarding the position of the transducer, the intensity is always maximum at the point where angle between the centre of the incident beam and the tangent line at the pipe is normal. This condition occurs twice in a full rotation, one at the shortest distance and one at the largest distance between the transducer and the pipe wall. As the transducer moves away from the point where the maximum intensity occurs, the intensity in all the cases starts decaying until reaching a minimum. When the off centre location of the transducer was 3% of the radius of the pipe, the minimum intensity registered was about -29 dB. The boundary where the intensities reach their minimum, shows a tendency to converge to a sort of asymptote around the point of maximum intensity plus 30 degrees and minus 30 degrees. This behaviour of the intensity seems to have some correlation with the angle formed between the centre of the incident beam and the tangent line at their point of contact. A sensitivity analysis calculating the variations of this angle for each one of the incident points of the emitted beam when the transducer is moved farther away from the centre of the pipe is going to be carried out next.

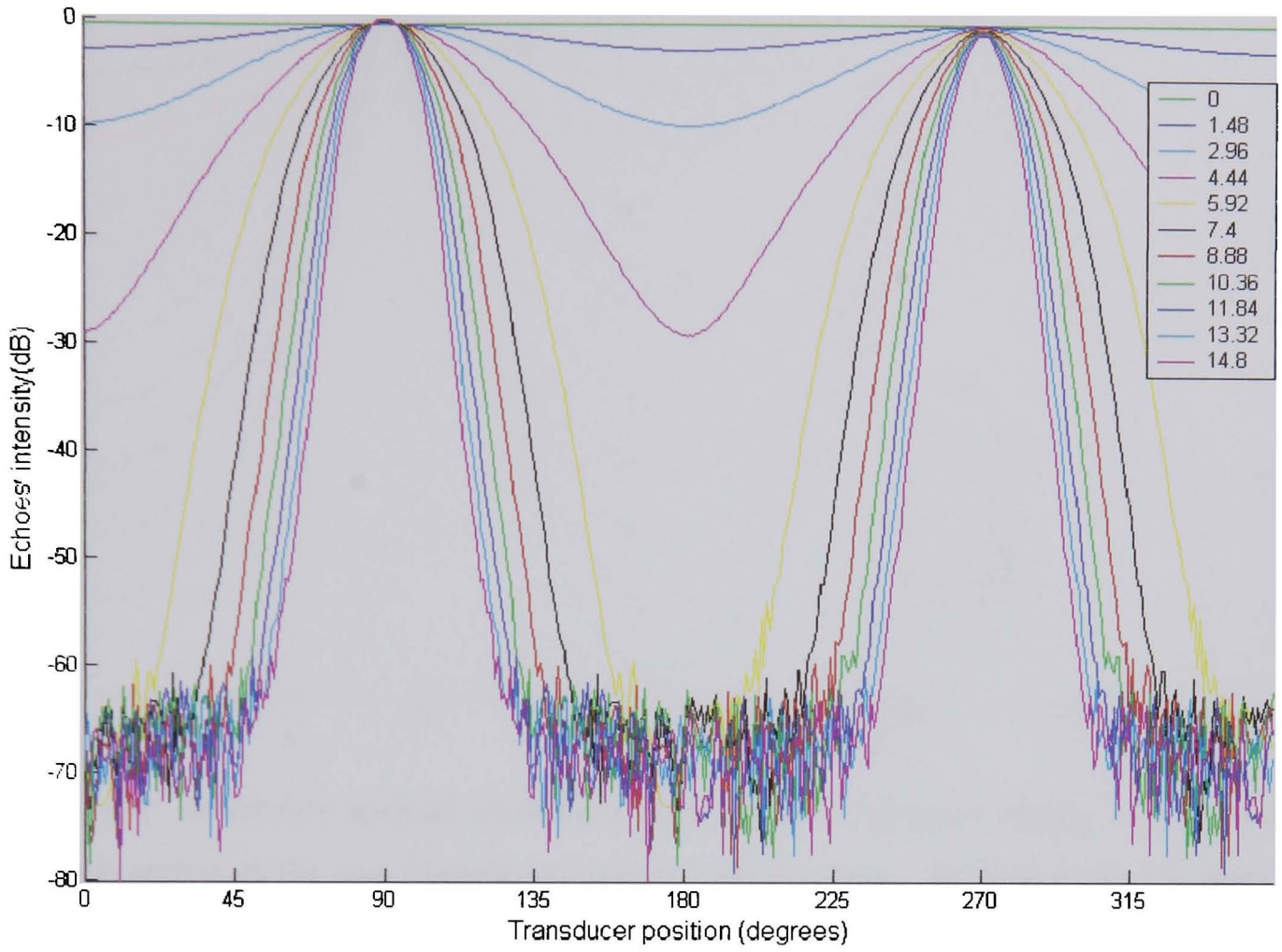


**Figure A.1** Off centre, intensity sensitivity analysis. A 3 MHz transducer was rotated a full rotation at 0.9 degrees steps, registering the intensities of the received echoes at each position and creating intensity profiles. Then the transducer was moved away from the centre of the pipe at intervals equivalent to 1% of the radius of the pipe.

As is shown in Figure A.2, the behaviour of the angle formed between the centre of the incident beam and the tangent, has some similarity with the behaviour of the intensity presented in Figure A.1. For all the studied locations of the transducer, the maximum is always when the angle is normal, and it starts decreasing as the angle move father away from the normal value. This shows that this model has potential in order to be used for compensating for such changes. A quick test was carried out when the transducer is located at an off centre location 3% of the radius, and the tangent model was used for compensating the intensity changes. In Figure A.3, results are shown.

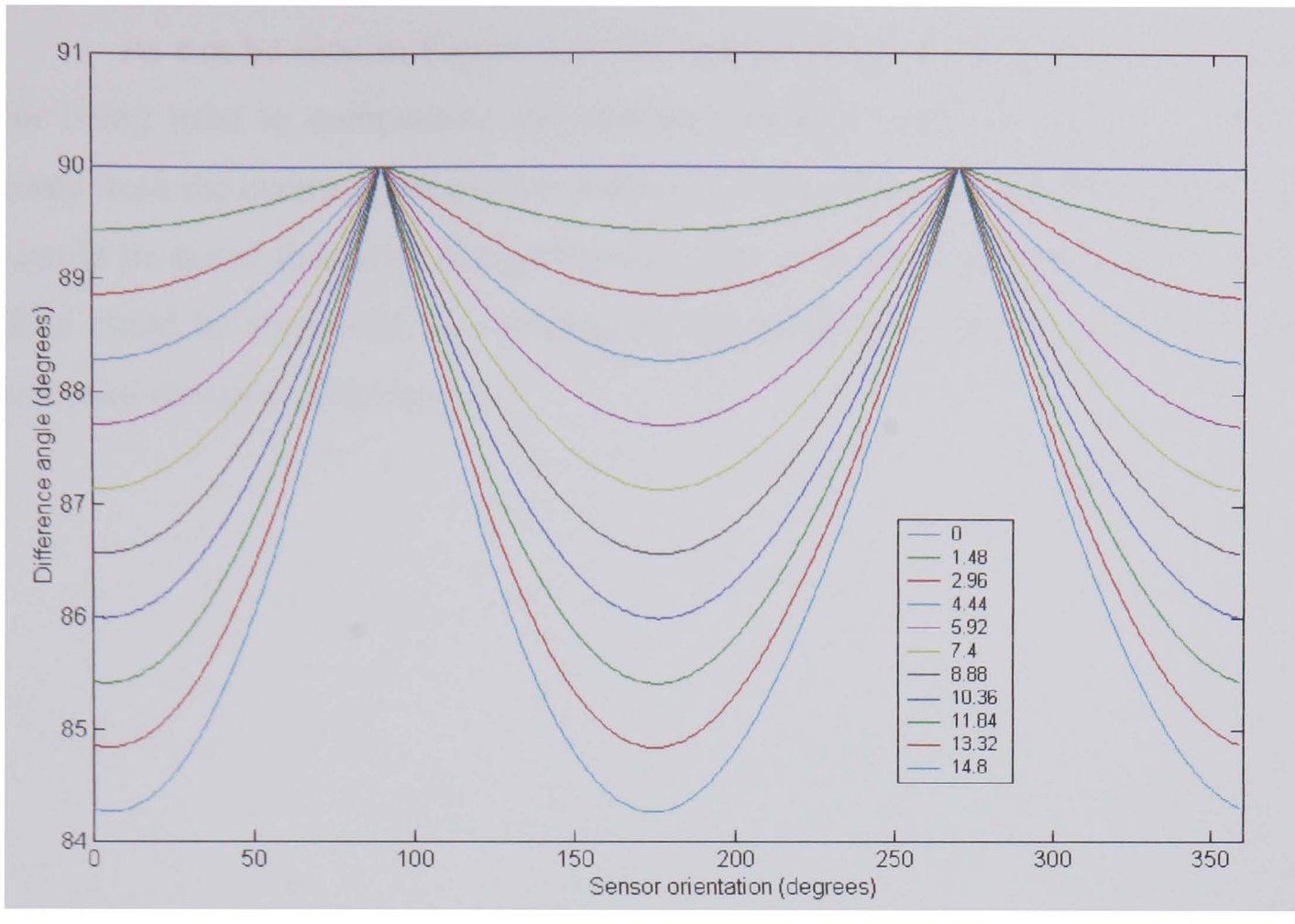


**Figure A.2** Sensitivity analysis difference angle (tangent-impingent angle). Sensor moved from the centre of the pipe towards the wall at 1.48 mm steps. Rotation steps 0.9 degrees. Pipe radius 148 mm.

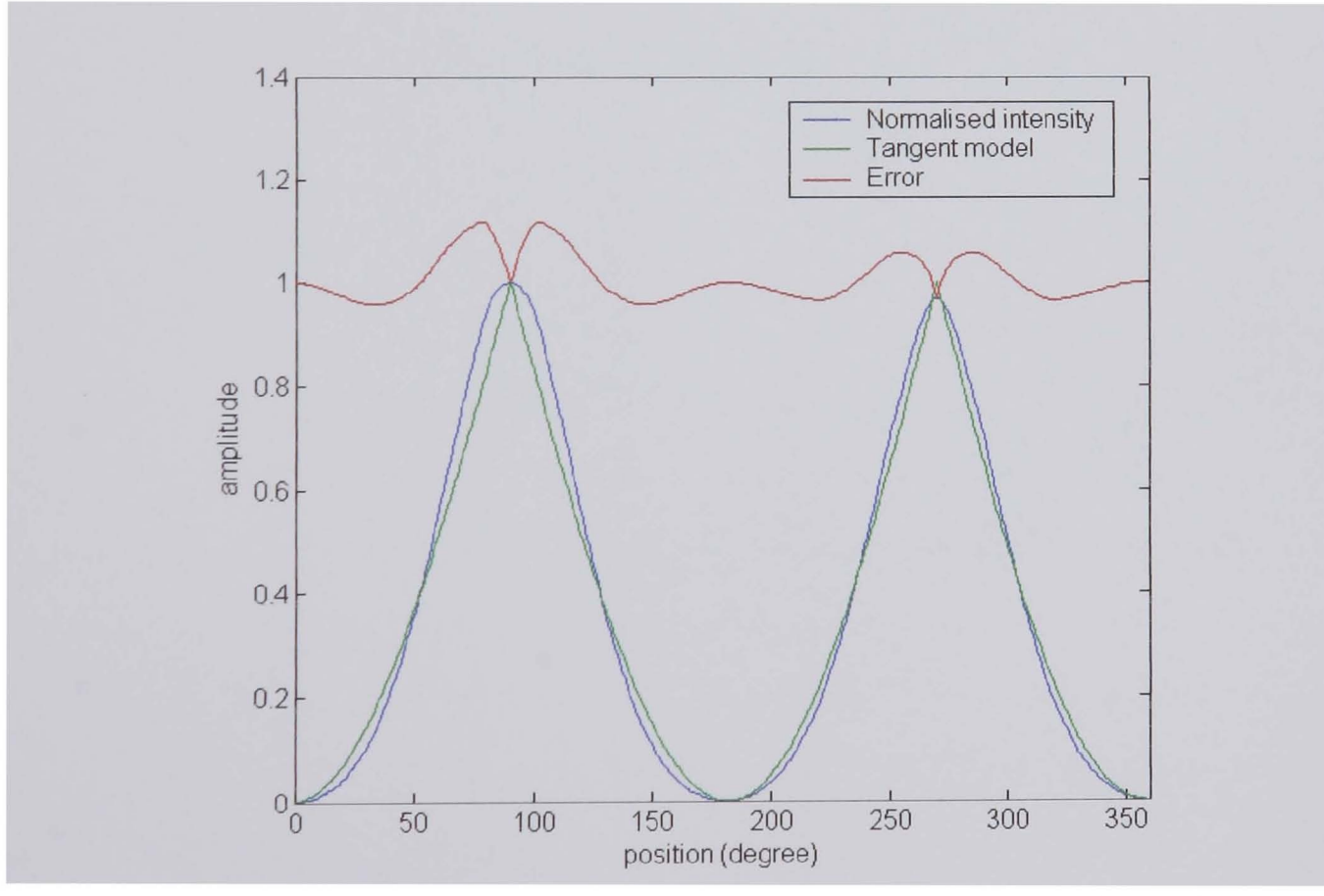


**Figure A.3** Off centre compensation for a transducer located at a 3% of the radius from the centre of the pipe, using a tangent based model. Blue line normalised intensity profile for the transducer. Green line tangent based model. Red line error after software compensation.

As can be seen in Figure A.3, the tangent based model has good potential for being used to compensate the intensity changes when the sensor is moved away from the centre of the pipe, to a distance equivalent to a 3% of the radius. It should be noted that after compensation, there is an error difference about 10%. This could be improved by including in the model the effect of the losses by travelled distance of the beam.

# Appendix C: Automatic defect detection system, neural network additional information

## *Appendix C.1 Neural network optimization*

In the following table a summary of results for the most relevant cases from the optimization stage of the automatic defect detection system are shown.

**Table C.1** Summary of results from neural network optimization

| Window Size | Input layer | Hiden layers | | Performance | Generalisation | Not Converge |
|---|---|---|---|---|---|---|
| | | 1st | 2nd | | | |
| 3 | 9 | 4 | 2 | | | ✓ |
| 3 | 9 | 4 | 4 | | | ✓ |
| 3 | 9 | 40 | 40 | | | ✓ |
| 4 | 16 | 4 | 2 | | | ✓ |
| 4 | 16 | 4 | 4 | Acceptable | Regular | |
| 4 | 16 | 8 | 4 | Acceptable | Regular | |
| 5 | 25 | 2 | 2 | | | ✓ |
| 5 | 25 | 4 | 2 | Acceptable | Regular | |
| 5 | 25 | 4 | 4 | Regular | Regular | |
| 5 | 25 | 8 | 4 | Acceptable | Regular | |
| | | 16 | 8 | Acceptable | Regular | |
| | | 32 | 16 | Regular | Regular | |
| 6 | 36 | 2 | 1 | | | ✓ |
| 6 | 36 | 2 | 2 | | | ✓ |
| 6 | 36 | 8 | 1 | | | ✓ |
| 6 | 36 | 8 | 4 | Acceptable | Regular | |
| 6 | 36 | 10 | 5 | Acceptable | Regular | |
| 6 | 36 | 40 | 40 | Acceptable | Regular | |

It should be noted that the set used for the training of the neural network was composed of 3800 vectors from which 108 were signatures of defective sections and 3692 were signature representing non defective sections mixed with noise levels normally seen in the experimental platform. For testing the generalisation and performance of the neural networks, the network was fed with 14785 signatures from unseen data, containing defects, non-defects and noise.

# Appendix D: Transducer's immersion oil characteristics

# Shell Diala MX

Inhibited mineral insulating oil

## Properties

Shell Diala MX is an inhibited insulating fluid, for use in electrical systems where good oxidation resistance is required. Shell Diala MX is a highly refined naphthenic mineral oil with natural low pour point characteristics.

## Application

Shell Diala MX is intended for use in Transformers, circuit breakers, oil-filled switches
and switchgears. Its gas absorbing characteristic allows the use in those applications where such a performance is required.

## Performance Specifications

Shell Diala MX meets the following specifications:

IEC 296, Class IA and IIA
ASTM D3487 Type II
British Standard BS 148-98, Class IA and IIA

Shell Diala MX is a virgin oil and free of polychlorinated biphenyl's (PCB).

## Typical Physical Characteristics

| | | Method | Shell Diala MX |
|---|---|---|---|
| Appearance | | DIN 57370 | bright and clear |
| Density at 15°C | kg/m³ | ISO 3675 | 889 |
| at 20°C | kg/m³ | ISO 3675 | 886 |
| Kinematic viscosity | | ASTM D445 | |
| at 20°C | mm²/s | | 23.2 |
| at 40°C | mm²/s | | 10.2 |
| at -30°C | mm²/s | | <1800 |
| Flashpoint P.M. | °C | ISO 2719 | 141 |
| Flashpoint COC | °C | ISO 2592 | 148 |
| Pourpoint | °C | ISO 3016 | -51 |
| Neutralisation value | mg KOH/g | DIN 51558-2 | <0.03 |
| Corrosive sulphur | | DIN 51353 | non-corrosive |
| Breakdown voltage (after treatment) | kV | IEC 156 | >50 |
| Dielectric dissipation factor at 90°C (after treatment) | | IEC 247 | 0.002 |
| Gassing tendency | mm³/min | IEC 628 A | < +5 |
| Induction Period | hours | IEC 1125 B | >120 |
| Oxidation stability (164 h/120°C) | | IEC 1125 C | |
| Total acidity | mg KOH/g | | 0.15 |
| Sludge | %m | | 0.012 |
| Oxidation stability (500 h/120°C) | | IEC 1125 C | |
| Total acidity | mg KOH/g | | 0.97 |
| Sludge | %m | | 0.3 |

(*) or technically equivalent methods

These characteristics are typical of current production.
Whilst future production will conform to Shell's specification variations in these characteristics may occur.

## Appendix E: Neural networks tutorial

There is a broad range of Artificial Neural Network models. In general, they can be grouped in three fundamentally different classes [Haykin, 1999]:

Single-Layer Feedforward Networks are the simplest form of a layered network. They have an input layer of source nodes that projects onto an output layer of neurons, i.e. the network is strictly feedforward.

Multilayer feedforward networks, are the second class, it distinguishes itself by the presence of one or more hidden layers, whose computation nodes are correspondingly called hidden units. Their function is to intervene between the external input and the network output in some useful manner. By adding one or more hidden layers, the network is enabled to extract higher order statistics. In a rather loose sense, the network acquires a global perspective despite its local connectivity due to the extra set of synaptic connections and the extra dimension of neural interactions [Churchland and Sejnowski, 1992].

The source nodes in the input layer of the network supply respective elements of the activation pattern (input vector), which constitute the input signals applied to the neurons in the second layer. The output signals of the second layer are used as inputs to the third layer, and so on for the rest of the network. The set of output signals of the neurons in the output layer of the network constitutes the overall response of the network to the activation pattern supplied by the source nodes in the input layer. This kind of networks can be fully connected in the sense that every node in each layer of the network is connected to every other node in the adjacent forward layer, or partially connected, if some of the communication links are missing from the network.

The third class are recurrent neural networks, this class are similar to the feedforward neural networks but they has at least one feedback loop. For instance, a single layer network with each neuron feeding its output signal back to the inputs of all the other neurons.

The presence of feedback loops has a profound impact on the learning capability of the network and on its performance. Moreover, the feedback loops

involve the use of particular branches composed of unit-delay elements, which result in a nonlinear dynamical behaviour.

### 6.1.1 Multilayer perceptron

The type of neural network most widely used as a classifier is the multilayer perceptron, Figure 6.1, which was first introduced by M. Minsky and S. Papert in 1969 and can be trained using the back propagation learning algorithm [Rumelhart and McClelland, 1986].

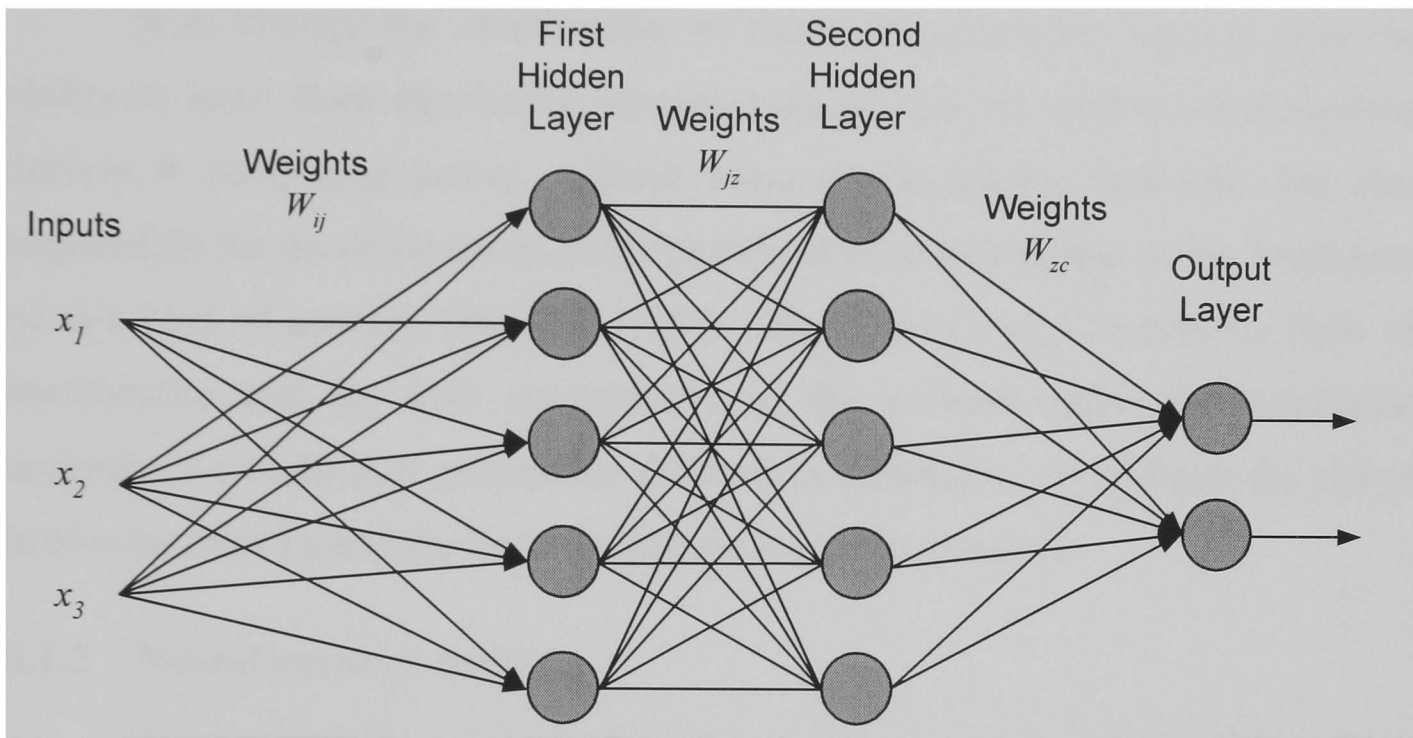


**Figure 6.1** Multilayer Perceptron with two hidden layers

A multilayer perceptron has three distinctive characteristics:

- The model of each neuron in the network includes a nonlinear activation function. It should be noted that the nonlinearity is smooth, i.e., differentiable everywhere. A commonly used form of nonlinearity is a sigmoidal function.
- The network contains one or more layers of hidden neurons that are not part of the input or output of the network.
- The network exhibits a high degree of connectivity, determined by the synapses of the network.

In such a system, each input is coupled onto each of the nodes of the hidden layer with a certain weight factor, and each output is coupled onto each

hidden node also with a certain weight factor. In case of data propagation from input to output (using the network as a classifier of unknown objects), within each node of the hidden layer, an inner product is calculated from input value and weight strength, an offset is added, and the result is fed through an activation function, which normalises the result. The transformation from input to hidden layer represents a remapping of the features to another space usually with another dimension. For the transformation from hidden layer to output layer a transformation from transformed feature space to classification space is obtained.

It is through the combination of these characteristics together with the ability to learn from experience through training that the multilayer perceptron derives it computing power. These same characteristics, however, are also responsible for the deficiencies in the present state of knowledge on the behaviour of this kind of network [Haykin, 1999]. The presence of a distributed form of nonlinearity and the high connectivity of the network make the theoretical analysis of a multilayer perceptron difficult to undertake. In addition the use of hidden neurons makes the learning process harder to visualize.

### 6.1.2 Neural network training

A major task for a neural network is to learn a model of the world in which it is embedded and to maintain the model sufficiently consistent with the real world so as to achieve the specified goals of the application of interest. The knowledge of the world consists of two kinds of information:

- The known world state, represented by facts about what is and what has been known, prior information.
- Observation of the world, obtained by means of sensors designed to probe the environment in which the neural network is supposed to operate. Normally, these observations are inherently noisy, being subject to error due to sensor noise and system imperfections. Such observation provide the pool of information from which the examples to train the neural network are drawn.

A set of input-output pairs, with each pair consisting of an input signal and the corresponding desired response is referred to as a training set. The training process usually proceeds as follows:

- Learning phase: An appropriate architecture is selected. Then a subset of the examples is then used to train the network by means of a suitable algorithm.
- Generalisation phase: The performance of the trained network is tested with data not seen before.

In the learning phase a training data set is presented to the system, the errors from the output are propagated back to the inputs, starting from the output layer to the hidden layer and so on until reaching the input layer. This is an iterative update procedure where weights and offsets are adapted until the error between the class labelled by the expert and the class estimated by the system diminish to zero. However an independent test set should be used to prevent "overlearning". As a consequence, the network will not be able to generalise any more.

Neural network design is based directly on real life data, with the data set being permitted to speak for itself. Thus the neural network not only provides the implicit model of the environment in which it is embedded, but also performs the information-processing function of interest [Haykin, 1999].

#### 6.1.2.1 The back propagation algorithm

Multilayer perceptrons have been applied successfully to solve difficult problems by training them in a supervised manner with the error back propagation algorithm. It basically consists of two passes through the different layers of the network: a forward pass and a backward pass. In the forward pass, an input vector is applied to the sensory nodes of the network, and its effect propagates through the network layer by layer. Finally, a set of outputs is produced as the actual response of the network. During the forward pass the synaptic weights of the networks are all fixed. During the backward pass, on the other hand, the synaptic weights are all adjusted in accordance with an error-correction rule. Specifically, the actual response of the network is subtracted from a desired

response to produce an error signal. This error signal is then propagated backward through the network against the direction of synaptic connections. The synaptic weights are adjusted to make the actual response of the network move closer to the desired response in a statistical sense.

# References

Abolmaesumi P et al. 2001. A User Interface for Robot-Assisted Diagnostic Ultrasound. *IEEE International Conference on Robotics and Automation (ICRA)*, Korea.

Alonso, M. and Finn, E.J. 1983. *Fundamental University Physics*, Vol.1&2, Addison-Wesley, Reading, Mass.

Anastassopoulos A.A. et al. 1999. A Comparative Study of Pattern Recognition Algorithms for Classification of Ultrasonic Signals. *Neural Computing & Applications*, 8:53–66, Springer-Verlag London Limited.

Anderson M. and Trahey G. 200. *A seminar on k-space applied to medical ultrasound*, Technical report, Department of Biomedical Engineering, Duke University, 2000. Available: http://dukemil.egr.duke.edu/Ultrasound/k-space/node11.htm [March 2005]

Andrews M.E. 1998. Large Diameter Sewer Condition Assessment Using Combined Sonar and CCTV Equipment, *APWA International Public Works Congress*, NRCC/CPWA Seminar Series "Innovations in Urban Infrastructure".

Asher R. C. 1997. *Ultrasonic Sensors*, Institute of Physics Publishing, Bristol, UK.

Bishop, C.C. 2003. *Neural Networks for Pattern Recognition*. Oxford University Press, Oxford, UK.

Blake A. and Issard M. 1998. *Active Contours*. Springer-Verlag, New York.

Browne R. and Knott G. 1993. Television and Scanning Sonar in Seattle Metro's Siphons and Brick Sewers, *ASCE International Conference on Pipeline Infrastructure II*, San Antonio, TX. 694–701,.

CERF (Civil Engineering Research Foundation). 2001. *Evaluation of SSET: The Sewer Scanner & Evaluation Technology*. The Civil Engineering Research Foundation, Report: #40551

Chen, C.H. and Wang P.S.P. 2005. *Handbook of pattern recognition and computer vision*. Third Edition. World Scientific.

Chernov L.A. 1960. *Wave Propagation in a Random Medium*. New York: McGraw-Hill.

Christensen C. 1988. *Ultrasonic bioinstrumentation*. New York: John Wiley & Sons.

Churchland, P.S. and Sejnowski T. 1992. *The computational brain.* Cambridge, MA, MIT Press

Connor, Z. M. et al. 1998. Using Scanning Acoustic Microscopy to Study Subsurface Defects and Crack Propagation in Materials, *The Member Journal of The Minerals, Metals & Materials Society*, JOM-e , vol. 50, no. 11

Dasarathy, B. W. 1991. *Nearest Neighbor (NN) Norms: NN Pattern Classification Techniques*. IEEE. Computer Society Press, Los Alamitos, CA.

DEFRA (Department of Environment, Food and Rural Affairs). 2003. *Review of Existing Private Sewers and Drains in England and Wales* – Consultation Paper. Welsh Assembly Government. July.

Duran O., et al. 2003. Pipe inspection using a laser-based transducer and automated analysis techniques. *Transactions on Mechatronics, IEEE/ASME*. Volume: 8, Issue: 3, pages: 401- 409.

Duran O., et al. 2004. Automated pipe inspection using ANN and laser data fusion. *Proc. 2004 IEEE Int. Conf. on Robotics and Automation (ICRA'2004)*, Vol: 5, pp. 4875 - 4880, New Orleans, LA, 26 April - 01 May 2004

Duran, O. et al. 2002a. State of the Art in Sensor Technologies for Sewer Inspection, *IEEE Sensors Journal*, Vol 2, N. 2, pp 63.

Duran, O. et al. 2002b. Automated sewer pipe inspection through image processing. *Proc. 2002 IEEE Int. Conf. on Robotics and Automation (ICRA'2002)*, pp. 2551-2556, Washington, D.C., 11-15 May.

Duran, O. et al. 2002c. Automated Laser-based profiler for Sewer Inspection. *Proceedings of the 7th International Conference on Intelligent Autonomous Systems(IAS-7)*, Marina del Rey, California, USA.

Duran, O., et al. 2002d. Automated sewer inspection using image processing and a neural classifier. *International Joint Conference on Neural Networks, 2002. IJCNN '02*. Honolulu, HI, USA. Proceedings of the 2002. Vol: 2, pags: 1126-1131.

Eiswirth, M. et al. 2001. Sewer assessment by multi-sensor systems. International Water Association - *World Water Congress* 15-19 Oct 2001. Berlin, Germany

Faugeras, O. 1993. *Three-dimensional computer vision*, Cambridge, MA: MIT Press.

Fenner, R.A. 2000. Approaches to sewer maintenance: A review, *Urban Water*, Vol. 2, No. 4, pp 343-356.

Florek, K., Lukaszewicz, J., Perkal, J., and Zubrzycki, S. (1951) Sur la liaison et la division des points d'un ensemble fini. Colloquium Mathematicae, 2, 282–285.

Georg Cybenko. 1988. *Continuous Valued Neural Network with Two Hidden Layers are Sufficient*. Technical report, Department of Computer Science, Tufts University, Medford, MA.

Gomez F., et al. 2003a. Modelling of Rotating Ultrasonic Sensors for Pipe Inspection. *International Conference on Mechatronics (ICOM 2003)*, Loughborough, UK, 19-20 June, 2003.

Gomez F., et al. 2003b. Modeling of Ultrasound Sensor for Pipe Inspection, *Proc. 2003 IEEE Int. Conf. on Robotics and Automation (ICRA 2003)*, pp 2550-2560, Taipei, Taiwan, 12-17 September, 2003.

Gomez F., et al. 2004. An ultrasonic profiling method for sewer inspection, *Proc. 2004 IEEE Int. Conf. on Robotics and Automation (ICRA 2004)*, Volume: 5 , April 26-May 1, 2004, Pages: 4858- 4863, New Orleans, 2004.

Gooch, R.M. et al. 1996. A semi-autonomous sewer surveillance and inspection vehicle. *Proc. IEEE Intelligent Vehicles*, 64-69, Japan.

Gore, J.C. and Leeman, S. 1977. Ultrasonic backscattering from human tissue: A realistic model. *Phys. Med. Biol.*, 22:317–326.

Gustav, K. et al. 1998. *The encyclopaedia of medical imaging*, volume I. Physics, techniques and procedures. NICER Institute. Isis Medical Media.

Harris, J. W. and Stocker, H. 1998. Segment of a Circle. §3.8.6 in *Handbook of Mathematics and Computational Science*. New York: Springer-Verlag, pp. 92-93.

Haykin, S. 1999. *Neural Networks a comprehensive foundation*. 2nd Edition. Prentice Hall, New Jersey, US.

Hayward, P. 2002. Sewerage: Fairytale spending. *Water & Waste Treatment*. 35(8), 30-31.

Hoare, C. A. R. 1962. Quicksort. *Computer Journal*. 5, 10-15.

Holm, S. 2001. Ultrasim - a toolbox for ultrasound field simulation. *Proc. Nordic Matlab Conference*, Oslo, Norway, Oct. 2001.

Hotelling, M. 1933. Analysis of a Complex of Statistical Variables into Principal Components, *Journal of Educational Psychology*, 24, pp. 498-520.

Hsieh, C. 1993. Some Potential Applications of Artificial Neural Systems in Financial Management, *Journal of Systems Management*, v.44 n4, p12(4), April 1993.

Iyer, S. R., et al. 2005. Ultrasonic C-Scan Imaging of Post-Tensioned Concrete Bridge Structures for Detection of Corrosion and Voids. *Computer-Aided Civil and Infrastructure Engineering.* **20,** 79–94.

Jain, A. K. and.Waller, W. G. 1978. On the optimal number of features in the classification of multivariate Gaussian data. *Pattern recognition*, 10:365–374.

Jensen J. A. and Nikolov, S. 2000. Fast simulation of ultrasound images. *Proceedings the IEEE Ultrasonics Symposium*, Puerto Rico, October 2000, pp 1721-1724.

Jensen J.A. 1996. Field: A Program for Simulating Ultrasound Systems, *Medical & Biological Engineering & Computing*, pp. 351-353, Volume 34, Supplement 1, Part 1.

Jensen, J. A. 2001. Speed-accuracy trade-offs in computing spatial impulse responses for simulation medical ultrasound imaging. *Journal of Computational Acoustics*, 9(3):731-744.

Jensen, J.A. 1991. A Model for the Propagation and Scattering of Ultrasound in Tissue. *Journal of Acoustical Society of America*. 89, pp. 182-191.

Jensen, J.A. 1999. A new Calculation Procedure for Spatial Impulse Responses in Ultrasound, *Journal of the Acoustical Society of America*, Vol. 105, pp. 3266-3274.

Jensen, J.A. 1999. *Linear description of ultrasound imaging systems*, Notes for the International Summer School on Advanced Ultrasound Imaging, Technical University of Denmark July 5 to July 9, 1999, Technical University of Denmark.

Jerram D.A. and Cheadle, M.J. 2000. On the cluster analysis of grains and crystals in rocks. *American Mineralogist*, Volume 85, pages 47–67.

John Hertz, et al. 1991. *Introduction to the Theory of Neural Computation.* Addison-Wesley, Redwood City, Califonia, USA, 1. edition. Santa Fe Institute.

Karling Y. and Lewicky M. 2005. *A hierarchical Bayesian model for learning non-linear statistical regularities in non-stationary natural signals*. Neural Computation. Volume 17, pages 397-423

Kaufmann, L. and Rousseeuw, P.J. 1990, *Finding Groups in Data. An Introduction to Cluster Analysis*, Wiley, New York.

Kinsler, L. E. and Frey, A.R. 2000. *Fundamentals of acoustics*. John Wiley and Sons Inc., New York.

Kirchner, F. and Hertzberg, J. 1997. A Prototype Study of an Autonomous Robot Platform for Sewerage System Maintenance. Autonomous Robots.

Kirchner, F. and Hertzberg, J. 1997. A Prototype Study of an Autonomous Robot Platform for Sewerage System Maintenance. Autonomous Robots, Volume 4, Number 4. Page 319-333. Academic Publishers, Netherlands, ISSN: 0929-5593.

Kirkham, R., et al. 2000. PIRAT—A System for Quantitative Sewer Pipe Assessment. *The International Journal of Robotics Research*, Vol. 19, No. 11, 1033-1053.

Kuntze, H.B. and Haffner, H. 1998. Experiences with the development of a robot for smart multisensoric pipe inspection. *Proceedings of the 1998 IEEE International Conference on Robotics and Automation*, Belgium,.

Lawson, S. W. and Parker, G. A. 1996. Automatic detection of defects in industrial ultrasound images using a neural network. *Proceedings of SPIE*, vol 2786, 1996, pp. 37-47.

Maeva E.Y., et al. 2004. Application Of High-Resolution Acoustic Imaging For Adhesive Bond Evaluation. *16th WCNDT 2004 - World Conference on NDT*, CD-ROM Proceedings, Aug 30 - Sep 3, 2004 - Montreal, Canada

Makar, J.M. 1999. Diagnostic Techniques for Sewer Systems, *Journal of Infrastructure Systems*, Vol. 5, No. 2, June 1999, pp. 69-78.

McHugh, et al. 1995. Pixel Based Sonar Imaging. *IEE Colloquium on Recent Developments in Radar and Sonar Imaging Systems: What Next?*

Minsky, M.L. and Papert S. 1969. Perceptrons : an introduction to computational geometry. Cambridge, [Mass.] ; London : M.I.T. Press.

MMC - Monopolies and Mergers Commission. 1996. *Severn Trent plc and South West Water plc: a report on the proposed merger.* London, Stationery Office.

Morse P.M. and Ingard, K.U. 1968. *Theoretical Acoustics*. McGraw-Hill, New York,.

Moselhi, O. and Shehab-Eldeen, T. 1999. Automated detection of surface defects in water and sewer pipes. *Automation in Construction*, 8, 581–588.

Moselhi, O. and Shehab-Eldeen, T. 2000. Classification of Defects in Sewer Pipes Using Neural Networks. *Journal of Infrastructure Systems*, ASCE, 6 (3), 97-105.

NAO – National Audit Office. (2004). *Out of sight - not out of mind: Ofwat and the public sewer network in England and Wales.* Report by the comptroller and auditor general. HC 161 Session 2003-2004: 16 January 2004. London, UK.

OFWAT – Office of Water Wervices. 2000. Serviceability of the water mains and sewer network in England & Wales up to March 1999. Information Note No. 35A. OFWAT, London.

Onda Corporation. 2004. Acoustic Properties Tables, Sunnyvale, California. July. "http://www.ondacorp.com/tables/"

Pace, NG. 1994. Ultrasonic surveying of fully charged sewage pipes, *Electronics and Communications Engineering Journal.* 87-92.

Peneder, M. 2005. Creating Industry Classifications by Statistical Cluster Analysis. *Austrian Institute of Economic Research (WIFO) Working Papers*, No. 257.

Pierce, A. D. 1989. Acoustics, An Introduction to Physical Principles and Applications. *Acoustical Society of America*, New York,.

Powella K. L., et al. 2003. Microbial contamination of two urban sandstone aquifers in the UK, *Water Research* 37, 339–352

Prager R., et al. 1999. Stradx: real-time acquisition and visualisation of freehand three-dimensional ultrasound. *Medical Image Analysis*. **3**, pp. 129–140.

Pratt, W.K. 1991. *Digital Image Processing*, A Wiley-Interscience Publication, New York.

Press W. H., et al. 1992. *Numerical recipes in C. The art of scientific computing*. Cambridge University Press, Cambridge.

Price, T. 1995. Inspecting Buried Plastic Pipe Using A Rotating Sonic Caliper, *Proceedings of the 2nd International Conference on Advances in Underground Pipeline Engineering*. 126–137.

Rao, C.R. 1964. *The Use and Interpretation of Principal Component Analysis in Applied Research. Sankhya* A *26* , 329 -358.

Rens, K.L., et al. 2000. Acoustic Tomographic Imaging Of Concrete Infrastructure. *Journal of Infrastructure Systems*, Volume 6, Issue 1, pp. 15-23.

Revella J.D., et al. 2002. Applied review of ultrasound image feature extraction methods. *The 6th Medical Image Understanding and Analysis Conference*, A Houston and R Zwiggelaar, editors, pages 173--176. BMVA Press, July 2002

Rome E. et al. 2001. A custom IR scanner for landmark detection with the autonomous sewer robot MAKRO, *International Symposium on Intelligent Robotic Systems*.

Rome, E. J. et al. 1999. Towards autonomous sewer robots: the MAKRO project. *Urban Water*. 1. 57-70.

Roth, D.J. et al. 1999. *3-D Surface Depression Profiling Using Focused Air-Coupled Ultrasonic Pulses*. NASA. NASA/TM-1999-209053, 1-22.

Roth, H. and Shilling, K. 1999a Navigation and Control for pipe inspection and repair robots. *Proc. of IFAC world congress*.

Roth, H. et al. 1998. Inspection- and Repair Robots for Waste Water Pipes - A Challenge to Sensorics and Locomotion. *Proceedings IEEE International Symposium on Industrial Electronics*. ISIE '98.

Rumelhart, D. E., and McClelland, J. L. 1986. *Parallel distributed processing: Explorations in the microstructure of cognition* (Vol. 1). Cambridge, MA: MIT Press

Schalkoff R. 1992. *Pattern Recognition: Statistical, Structural and Neural Approaches*. John Wiley & Sons, Inc. ISBN 0-471-52974-5.

Schlaikjer, M., et al. 2003. Trade Off Study on Different Envelope Detectors for B-mode Imaging. *Proceedings of IEEE International Ultrasonics Symposium*, Honolulu, Hawaii.

Schmerr, L.W. 1998. *Fundamentals of Ultrasonic Non-Destructive Evaluation: A Modeling Approach*, Prenum Press, New York.

Seagar A. and Liley D. 2002. *Basic Principles of Ultrasound Imaging System Design (Notes on Biomedical)*, Swinburne University of Technology, School of Biophysical Sciences and Electrical Engineering Imaging.

Serway R. and Beichner R. 2000. *Physics, for scientist and engineers with modern physics*, Fifth Ed., Saunders College Publishing, FL, USA.

Shehab-Eldeen, T. and Moselhi, O. 2002. Automated Inspection of Utility Pipes: A Solution Strategy for Data Management. *International Symposium on Automation and Robotics in Construction*, 19th (ISARC). Proceedings. National Institute of Standards and Technology, Gaithersburg, Maryland. September 23-25, 2002, 531-536 pp.

Shirai, K., et al. 2000. Underwater imaging system using acoustic holography. *Proceedings of the 2000 International Symposium on Underwater Technology*. Tokyo, Japan.

Short C.S. 1988. The Bramham incident 1980 - an outbreak of water borne disease. *Journal of the Institution of Water and Environmental Management*, 2: 383-390.

Silk M.G. 1984. *Ultrasonic transducers for non destructive testing*, Bristol. Hilger.

Sinha S. et al. 2003. Computer Vision Techniques for Automatic Structural Assessment of Underground Pipes, *Computer Aided Civil & Infrastructure Engineering* (18) #2.

Sinha S.K. and Karray F. 2002. Classification of Underground Pipe Scanned Images using Feature-Extraction and Neuro-Fuzzy Algorithm. *IEEE Transactions on Neural Networks*, volume 13, number 2, 393-401.

Sinha, S. K. and Knight M. A. 2004. Intelligent System for Condition Monitoring of Underground Pipelines, *Computer-Aided Civil and Infrastructure Engineering*, Vol. 19, No. 1, 42-53.

Stepanishen P.R. 1971a. The time-dependent force and radiation impedance on a piston in a rigid infinite planar baffle, *Journal of Acoustical Society of America*. 49 (3), pp. 841-849.

Stepanishen P.R. 1971b. Transient radiation from pistons in a infinite planar baffle, *Journal of Acoustical Society of America*. 49, pp. 1627-1638.

Stepanishen P.R. 1981. Pulsed transmit/receive response of ultrasonic piezoelectric transducers, *Journal of Acoustical Society of America*. 69, pp. 1815-1827.

Stremler F. 1990 *Introduction to Communication Systems*, Addison-Wesley, Reading, Mass., 3 edition, January 1.

Tamura, S. and Tateishi, M. 1997. Capabilities of four-layered feed-forward neural networks: Four layers versus three. *IEEE Transactions on Neural Networks*, vol. 8, pp. 251–255.

Tupholme G.E. 1969. Generation of acoustic pulses by baffled plane pistons, *Mathematika* 16, pp. 209-224.

Water Research Centre. 2001. *Sewerage Rehabilitation Manual*. 4th. Edition. Swindon, Wiltshire, UK.

Weaver, H.J. 1983. *Applications of Discrete and Continuous Fourier Analysis*, A Wiley-Interscience Publication, New York.

WEF Manuals & Reports FD-6. 1964. ASCE Manuals and reports on engineering. *Existing sewer evaluation and rehabilitations*, No. 62.

Weisstein, E. W. 2005. Circle-Circle Intersection from *MathWorld*--A Wolfram Web Resource.
http://mathworld.wolfram.com/Circle-CircleIntersection.html

Wirahadikusumah, R. et al. 1998. Assessment technologies for sewer system rehabilitation, *Automation in Construction*, 7, 259–270.

Zemp R.J. et al. 2003. Linear System Models for Ultrasonic Imaging: Application to Signal Statistics. *IEEE Ultrasonics, Ferroelectrics And Frequency Control Society*, 50(6):642-654.

Zhuang, B. H. et al. 1998. Non-contact laser sensor for pipe inner wall inspection. *Optical Engineering*. Vol. 37, pp. 1643–1647.